SATELLITE RETRIEVALS OF
TOTAL COLUMN WATER VAPOUR AND SURFACE EMISSIVITY
DURING ARCTIC WINTER

by

Christopher Perro

Submitted in partial fulfillment of the requirements
for the degree of Doctor of Philosophy

at

Dalhousie University
Halifax, Nova Scotia
September 2017

TABLE OF CONTENTS

LIST OF TABLES

LIST OF FIGURES

ABSTRACT

A new water vapour column retrieval using passive microwave satellite measurements is presented for use during the Arctic winter. The retrieval, named PLDC16 (Perro Lesins Duck Cadeddu 2016), uses measurements at the strong 183 GHz water vapour absorption line together with an auxiliary temperature profile and water vapour profile shape. The retrieval can be applied to several microwave instruments providing up to 25 years of Arctic water vapour column measurements.

PLDC16 is evaluated using simulations and real brightness temperatures from the Microwave Humidity Sounder (MHS). RMS deviations from the G-Band Vapor Radiometer (GVR) at Barrow, Alaska were smaller than for other retrieval techniques and satellite instruments. Swath measurements show fine structure that is not seen in reanalyses.

Surface emissivity and reflectance ratios are also retrieved using microwave measurements from the Advanced Technology Microwave Sounder (ATMS), and are validated with aircraft campaign measurements. Maps of reflectance ratio show large spatial and temporal variations across the different Arctic surfaces, particularly over Greenland.

The assumption of specular surface reflection for microwaves is investigated. Differences between large satellite zenith angle and nadir satellite zenith angle water vapour retrievals indicate Lambertian reflection occurs over land and sea ice surfaces while a mixture of specular and Lambertian reflection occurs over open ocean and is applied in PLDC16.

The PLDC16 retrieval is used together with maps of reflectance ratio to obtain pan-Arctic maps of water vapour column. Good agreement is seen with the Arctic radiosonde network and ERA-interim reanalysis, although ERA-interim shows a significant dry bias with respect to PLDC16. Enhanced water vapour over ice leads is also seen.

ACKNOWLEDGEMENTS

First I'd like to thank my supervisor Prof. Thomas J. Duck. I am very grateful for the opportunity to be a graduate student under your supervision. Your insight, patience, and support was extremely helpful during my research and during the writing of this thesis. I'd also like to thank Prof. Glen Lesins and Prof. James Drummond for being a part of my thesis committee and for all the meetings we had during my Ph.D. I'd also like to thank Dalhousie University and the NSERC Create Training Program run by Dr. Kimberly Strong for supporting my work financially.

I'd like to give the biggest thank you to Danielle Cox for helping me deal with all the stresses that go along with writing a thesis. I would not have been able to do it without you! I want to thank my parents, who supported me in everything I've done in my life. I'd also like to thank Jonathan Franklin, Jason Hopper, Colin Pike-Thackray, Ryan Robski, Stephen D'Andrea, and Ben Beck for being great office mates. You were all very helpful by relieving my stress.

CHAPTER 1

INTRODUCTION

Global mean surface temperatures have increased markedly during the last few decades with an average rate of $0.12°C$ per decade over the last 60 years (IPCC, 2014). The warming across the planet has been attributed to the emission of greenhouse gases through human activity, the primary cause being CO_2 from fossil fuel combustion accounting for approximately 60% of the increase in radiative forcing from well-mixed greenhouse gases (IPCC, 2014). Since pre-industrial times, CO_2 has increased by approximately 40% (IPCC, 2014).
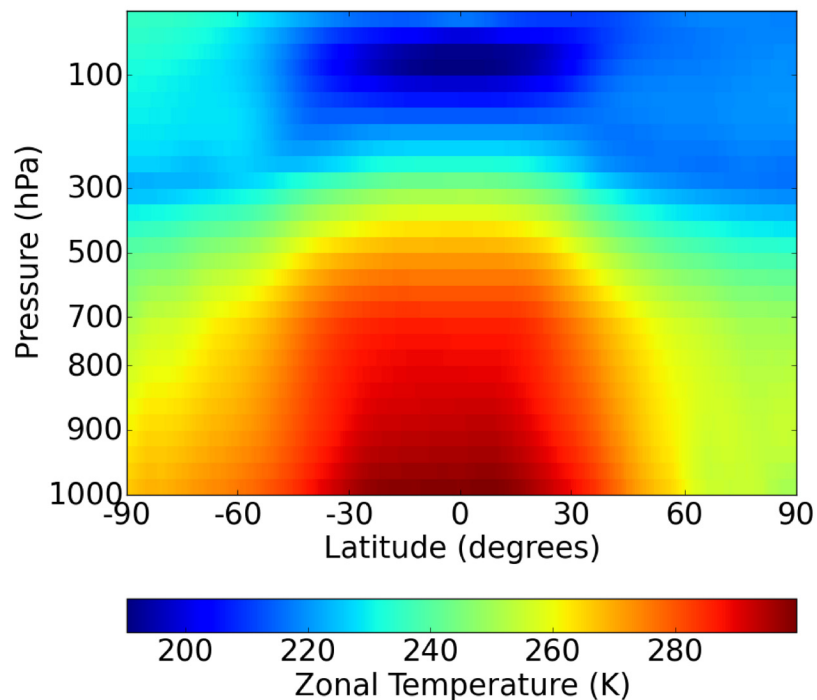
Figure 1.1: Zonal atmospheric temperatures from ERA-interim reanalyses for the month of January 2013.

The warming caused by anthropogenic emission is amplified by various feedbacks, the

most important of which is due to water vapour (Curry et al., 1995; Ghatak and Miller, 2013). Increasing global temperatures leads to increased water vapour saturation pressure, thereby increased water vapour concentrations. An increase in water vapour further increases temperatures due to water vapour being a greenhouse gas. Water vapour is also the largest contributing greenhouse gas.

Global temperature changes occur on top of the background temperature distribution. Global surface temperatures on average decrease with absolute latitude as shown in Fig. 1.1. Figure 1.1 also shows that atmospheric temperatures typically decrease with altitude in the troposphere.

Surface Temperature Anomaly (°C) (1951-1981 baseline)
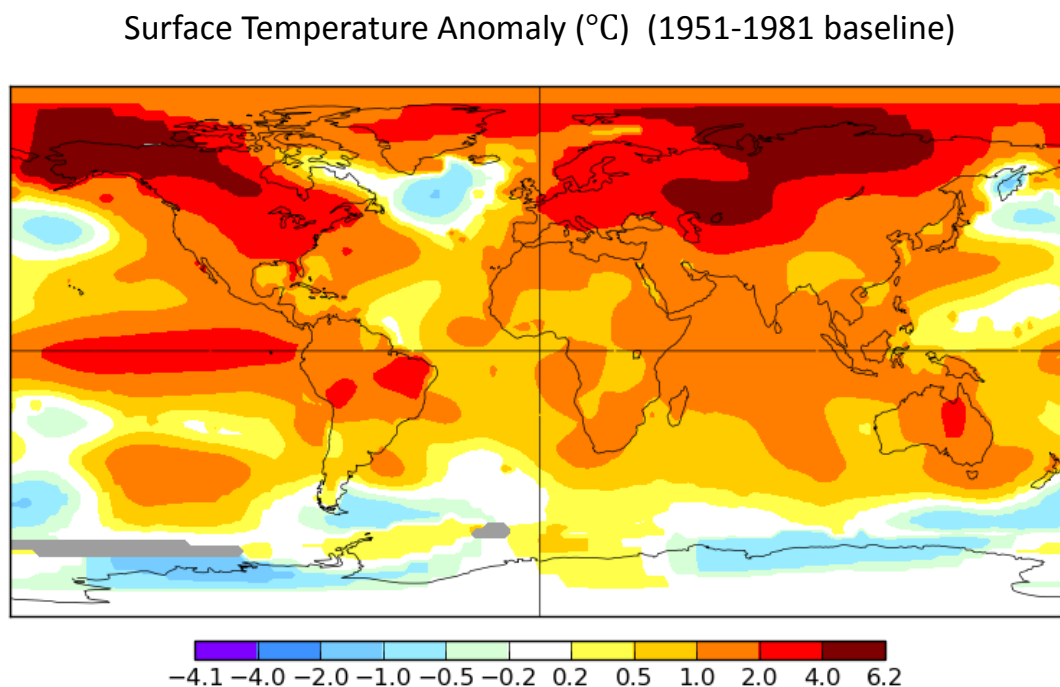
Figure 1.2: Global temperature anomaly compared to 1951-1981 temperatures during the winter season (November-April, 2016). (Hansen et al., 2010; GISTEMP Team, 2017)

Warming in the Arctic is more pronounced than for the planetary average. For the past 60 years, a warming trend of 0.88°C per decade is seen at Eureka, Nunavut (Lesins et al., 2010). A similar trend is observed across the Arctic. Figure 1.2 shows a 3.5°C wintertime anomaly with respect to a 1951-1981 baseline (Hansen et al., 2010; GISTEMP Team, 2017) at high latitudes. Compared to any other part of the Earth, the surface temperature increase

is at least twice as large in the Arctic according to Fig. 1.2.
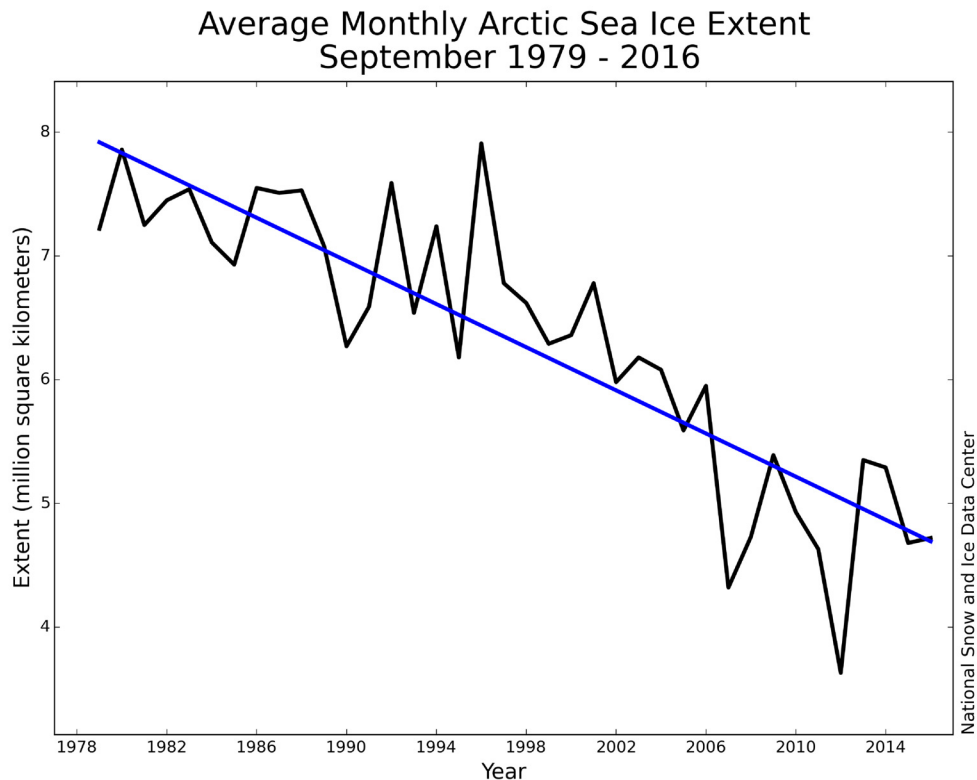
Figure 1.3: Arctic sea ice extent for the month of September ranging from 1979 to 2016. (NSIDC, 2017)

The larger temperature increase in the Arctic is referred to as the Arctic amplification. Factors contributing to the amplification include a greater sensitivity at colder temperatures (Planck feedback), the decreased albedo from lost snow and ice, stratification from thermal inversions, increased meridional transport, and albedo effects from cloud cover and black carbon aerosols (Serreze and Barry, 2011; Lesins et al., 2010; Pithan and Mauritsen, 2014).

The high albedo in the Arctic is due to sea-ice and snow. The increase in temperatures has caused the sea ice to recede within the last few decades, as seen in Fig. 1.3 (NSIDC, 2017). This leads to a reduction in the albedo of the Arctic since the open ocean absorbs solar radiation more efficiently than sea ice. The deterioration of the Arctic sea ice also exposes a large source of water vapour.

The impact of water vapour on longwave radiation is substantial for the Arctic. Figure 1.4 shows two measured downwelling surface infrared spectra, one at Barrow, Alaska, the other for the tropics, both during the winter season (Petty, 2006). Windows with near

zero radiance from 8 μm to 13 μm in the Barrow spectrum indicate high transmission allowing surface radiation to escape to space and cool the planet. The potentially dominant absorber in this particular radiative window is water vapour. Any increase in water vapour content will partially close these windows (such as occurs in the tropics) and so reduce cooling. Careful monitoring of water vapour is therefore important for understanding radiative transfer.
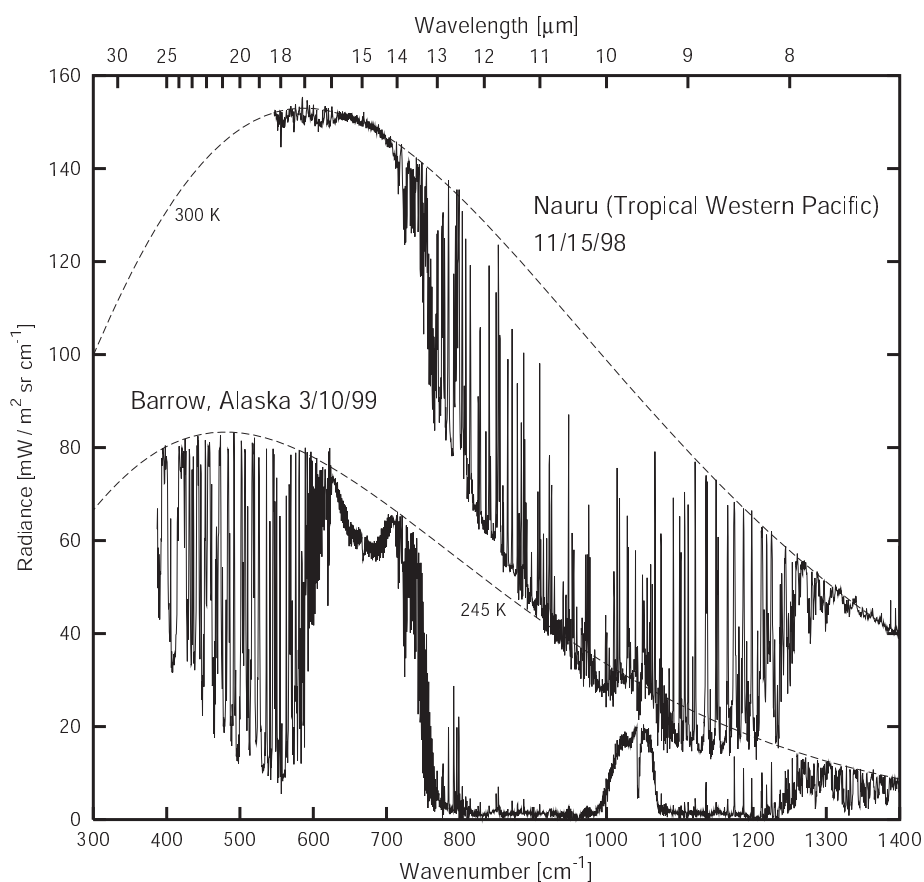
Figure 1.4: Measured Downwelling Surface Infrared Absorption spectrum for Arctic (Barrow, Alaska March 10, 1999) and lower-latitude (Nauru, November 15, 1998) atmospheric profiles viewed from the surface. Dashed lines correspond to black body spectra at the surface temperature for each profile. (Petty, 2006)

There are few measurements of water vapour in the Arctic. Ground based measurements include radiosondes, G-band Vapor radiometer (GVR), and lidar measurements are spatially sparse due to the difficulty of operating instrumentation in remote, harsh environments. Satellite measurements can fill in some of the gaps, but can be limited due to many techniques using infrared wavelengths which are blocked by clouds. Clouds occur with a

frequency greater than 50% during the winter in the Arctic (Curry et al., 1996).

Microwaves are relatively unaffected by clouds when compared to visible and infrared wavelengths. In the microwave spectrum, there is a strong, relatively isolated, water vapour absorption line at 183 GHz created by a pure rotation line from state 2 to 3 (Kakar, 1983). It is so strong that it may be used to obtain accurate measurements in low water vapour conditions, which predominantly occur during the Arctic winter. For this reason, passive microwave satellite measurements are used for this thesis.

There are several different 183 GHz passive microwave satellite instruments, most of which are currently in operation. These include the Microwave Humidity Sounders (MHS), Advanced Technology Microwave Sounder (ATMS), Special Sensor Microwave Imager/Sounder (SSMIS), and the MicroWave Humidity Sounder (MWHS). Previously operating instruments include the Advanced Microwave Sounding Unit-B (AMSU-B) and the Special Sensor Microwave/Temperature-2 (SSM/T-2). The instruments have footprints as small as 15 x 15 km^2 at nadir. Each instrument type is also on board multiple satellites. This combination of data sets may be used to provide high temporal resolution and 25 years of continuous measurements.

There are few retrieval techniques of water vapour using passive microwave measurements in the Arctic. They include techniques by Miao (1998), Melsheimer and Heygster (2008), and the Microwave Integrated Retrieval System (MIRS) (Boukabara et al., 2011). The techniques by Miao (1998) and Melsheimer and Heygster (2008) are optimized for Arctic conditions and use 183 GHz measurements from SSM/T-2 and AMSU-B, respectively. Numerous approximations are used, and vertical variations of temperature and water vapour are ignored.

MIRS uses a 1-dimensional variational approach to determine water vapour, and other atmospheric and surface quantities with measurements from the MHS and Advanced Microwave Sounding Unit-A (AMSU-A). The retrieval doesn't take advantage of the fact that surface properties change slowly by only using single instantaneous measurements which increases the error in retrieved quantities. The MIRS algorithm uses all channels from both instruments to determine water vapour globally; however very few of those channels provide useful data during the dry Arctic winter. Profile information in the retrieval is encoded using a small number of empirical orthogonal functions. This thesis presents a retrieval for water vapour that uses detailed auxiliary atmospheric profiles and slowly changing surface

properties, targeted for use during the Arctic winter.

Currently there are few measurements in the literature of surface emissivity near 183 GHz. Aircraft campaigns have been undertaken (Hewison and English, 1999; Selbach, 2003; Harlow, 2009) which provide a small, spatially sparse set of measurements. A small number of satellite measurements have been published, but are limited to particular surface types, lower frequencies, and assume simplistic surface properties (Yan et al., 2008; Guedj et al., 2010; Mathew et al., 2008; Karbou et al., 2014; Kongoli et al., 2011).

This thesis provides a new water vapour retrieval based upon the formula from Miao (1998) and Melsheimer and Heygster (2008). Using a similar formulation, surface emissivity is determined in low water vapour conditions. Retrievals of both water vapour and surface emissivity will be shown.

Chapter 2 provides a background on atmospheric and surface radiative transfer. The radiative transfer equation for a passive microwave satellite is derived. The three microwave polar orbiting satellites used in the thesis are described.

Chapter 3 introduces the new water vapour column retrieval technique, named PLDC16, it was evaluated using simulations and Microwave Humidity Sounder (MHS) measurements. The PLDC16 retrieval applied to MHS brightness temperatures was compared to the G-band Vapour Radiometer (GVR). Reanalyses were also compared to the GVR to evaluate the PLDC16 retrieval.

Chapter 4 describes two retrieval techniques for surface emissivity and reflectance ratio. A modification to the radiative transfer algorithm in Chapter 2 was shown to allow the choice of specular and Lambertian surface reflection. The surface emissivity retrievals were evaluated using simulations and brightness temperature measurements from the Advanced Technology Microwave Sounder (ATMS). ATMS surface emissivities were shown in the form of pan-Arctic maps and probability densities over different surface types.

Chapter 5 presents an analysis of pan-Arctic water vapour retrievals. Two updates are made to improve the PLDC16 retrieval: a) PLDC16 is modified to use reflectance ratio maps; and b) the choice of specular, Lambertian, or a mixture of surface reflection is allowed. Corrections to ensure consistent measurements regardless of satellite viewing angle and instrument channels used are implemented. The updated PLDC16 retrieval is evaluated using the GVR. A comparison of water vapour column from the Arctic radiosonde network, ERA-interim reanalyses, and a time series of pan-Arctic water vapour column

are presented. Finally, PLDC16 retrievals in the vicinity of ice leads are used to measure the impact on local water vapour. To conclude, Chapter 6 summarizes the results from the previous chapters and discusses future work.

In this thesis, I designed and implemented the PLDC16 water vapour retrieval and used it to obtain water vapour columns from simulated and real satellite measurements. PLDC16 was built upon a previous water vapour retrieval created by Miao (1998) and Melsheimer and Heygster (2008). The name PLDC16 refers to the publication in which the retrieval was introduced (Perro et al., 2016). The contribution from each author was as follows. Dr. Glen Lesins initially explored the application of the technique of Melsheimer and Heygster (2008) to MHS measurements and suggested improvements could be made. Dr. Thomas J. Duck provided feedback and discussion which aided in the production of the new water vapour retrieval. Dr. Maria Cadeddu (Argonne National Laboratory, Argonne, IL, 60439, USA) provided water vapour column measurements from the G-band Vapor Radiometer at Barrow Alaska. The paper was written by myself. The PLDC16 retrieval uses a 1-dimensional radiative transfer model known as RTTOV, provided by EUMET-SAT Numerical Weather Prediction (Matricardi and Saunders, 1999). MHS, ATMS, and AMSU-B brightness temperatures were obtained from National Oceanic and Atmospheric Administration (NOAA) Comprehensive Large Array-Data Stewardship System (CLASS).

I calculated surface emissivity and reflectance ratios using simulated and real satellite measurements. The techniques were given by Hewison and English (1999) and Selbach (2003) which I applied to the simulated and real satellite measurements. The technique from Selbach (2003) was previously applied to aircraft measurements. The OSI-403-c product, provided by EUMETSAT Ocean and Sea Ice Satellite Application Facility ice type product (Breivik et al., 2012), was used to distinguish between different surface types. Published aircraft campaign measurements from Hewison and English (1999), Selbach (2003), and Harlow (2009, 2011) were used to compare to my satellite surface emissivity retrievals and I determined reflectance ratios of the published results from their surface emissivities.

I performed the comparisons between PLDC16, ERA-interim, National Centers for Environmental Prediction (NCEP), Japanese 55-year Reanalysis (JRA-55), MIRS, Atmospheric Infrared Sounder (AIRS), and Arctic System Reanalysis (ASR) datasets with GVR water vapour column at Barrow, Alaska. I performed the comparison of PLDC16 with

radiosonde measurements at Barrow, Alaska. I also performed the comparison between PLDC16 and Advanced Very High Resolution Radiometer (AVHRR) measurements. ERA-interim data were obtained from the European Center for Medium range Weather Forecasting (ECMWF). NCEP data were obtained from the NOAA Earth System Research Laboratory Physical Sciences Division. JRA-55 data were obtained from the Japan Meteorological Agency Climate Prediction Division. MIRS and AVHRR data were obtained from NOAA CLASS. AIRS data were obtained from the NASA Jet Propulsion Laboratory and ASR data were obtained from the Byrd Polar Research Center Polar Meteorology Group.

CHAPTER 2

BACKGROUND

In this chapter, equations describing radiative transfer between the atmosphere and surface are introduced, and their relevance to passive microwave satellite retrieval theory is discussed. A brief introduction to the microwave instruments used for this thesis is given.

2.1 Atmospheric Radiative Transfer

Three types of processes influence the propagation of radiation in the atmosphere: absorption, emission, and scattering. The following subsections describe each.

2.1.1 Absorption

Absorption is the process whereby a molecule or particle interacts with radiation by removing and converting radiative energy to internal energy. Absorption occurs when the energy of an incident photon equals the difference between energy states of a molecule or particle. Absorption lines are not infinitely small in width: a single transition can occur over a range of wavelengths due to pressure and Doppler broadening.

Figure 2.1 shows the absorption spectrum at the microwave frequencies. Oxygen absorption is centred at 118 GHz for one line, while a series of absorption features between 49 GHz and 70 GHz combine to form a second line. The two water vapour absorption lines are centred at 22 GHz and 183 GHz.

The background absorption in Fig. 2.1 is produced by the water vapour continuum. The continuum is a range of frequencies where there is continuous absorption that is not characterized by absorption lines. The cause of the continuum is not well understood. Theories include formation by the far wings of absorption lines accumulating near these frequencies

and water molecule clusters which potentially have a large number of absorption lines close to one another (Petty, 2006; Cormier et al., 2005).

Liquid water cloud absorption in the microwave spectrum is relatively small when compared to the features previously described. The optical depth from a liquid cloud with a liquid water path (LWP) of 100 g/m^2 is shown in Fig. 2.1. The optical depth is significantly smaller than the total clear sky optical depth. Near absorption lines, the difference is at least a magnitude larger. Average monthly LWPs at Barrow, Alaska are no larger than 90 g/m^2 (Cadeddu et al., 2013). During the winter months, the average LWP is less than 50 g/m^2 (Cadeddu et al., 2013), indicating the absorption due to typical liquid water clouds would be less than shown in Fig. 2.1.
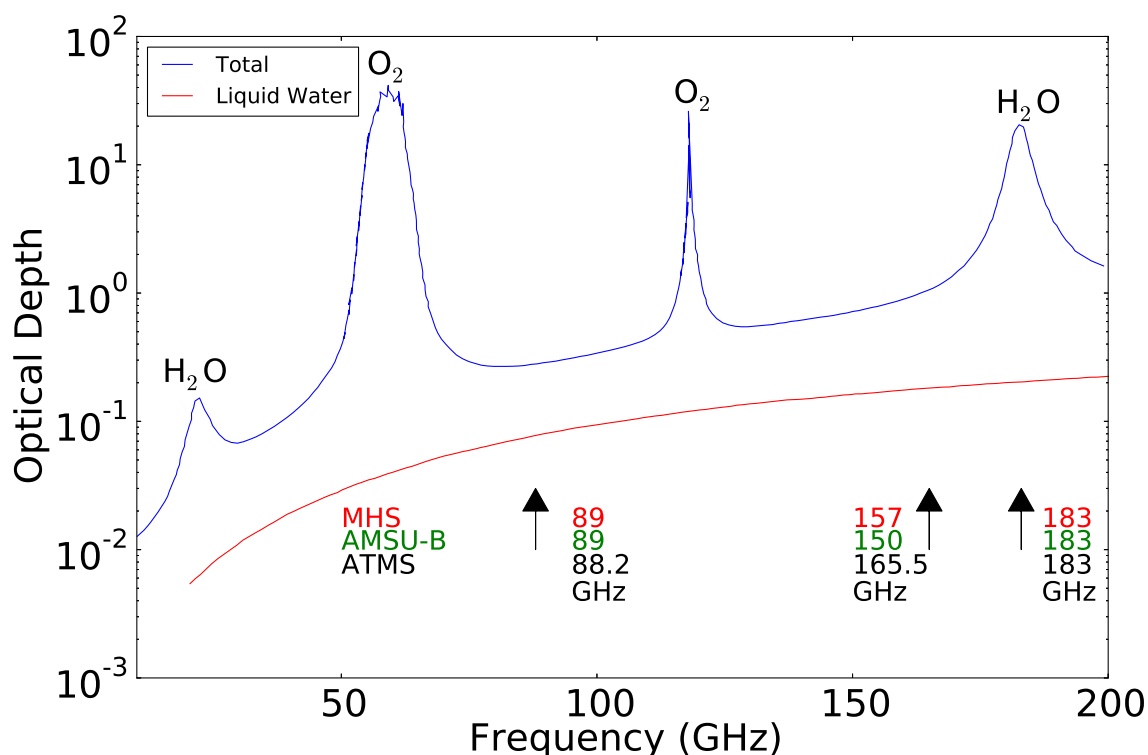
Figure 2.1: Microwave spectrum optical depths showing two water vapour and two oxygen absorption lines (Cadeddu et al., 2013). Measurement frequencies for the MHS, AMSU-B, and ATMS instruments are given. The blue line is the total clear sky (no clouds) Optical Depth and the red line is the Optical depth from a liquid water cloud with a liquid water path (LWP) of 100 g/m^2. See also Payne et al. (2011).

Ice clouds are considered to have a smaller effect on absorption when compared to liquid water clouds and are assumed to have negligible effects on absorption in the microwave

spectrum (Kneifel, 2010). Scattering of microwaves due to ice clouds has a larger effect on microwave radiation than absorption (Liu, 2008) and is discussed in Sect. 2.1.2. For most Arctic winter conditions, atmospheric absorption on microwave radiation due to clouds can be safely neglected.

2.1.2 Scattering

Scattering of photons may be classified as elastic and inelastic. For elastic scattering, the exchange of energy between the scatterer and photon is negligible. For inelastic scattering, a photon may gain or lose energy resulting in a wavelength shift.

Elastic scattering theory may broken up into three regimes: Rayleigh, Mie, and geometric optics scattering. The intensity and distribution of the scattered radiation by the three regimes of elastic scattering are dependent on the wavelength and polarization of the incident radiation, size, refractive index, and shape of the scattering particle (Liou, 2002). The regimes are delineated by the size parameter,

$$x = \frac{2\pi R}{\lambda},$$ (2.1)

where R is the radius of the particle, and λ is the wavelength of the incident radiation. Rayleigh scattering occurs for $x \ll 1$, Mie scattering for $x \geq 1$ and geometric optics scattering for $x \gg 1$ (Liou, 2002).

Consider microwave radiation with a frequency of 200 GHz. For water molecules (radius 0.3 nm (McGowan, 2000)) the size parameter is approximately 1.25×10^{-6}, for an aerosol (radius: 100μm or less (Seinfeld and Pandis, 2016) it is approximately 0.4 and smaller, for a water cloud droplet from a thin supercooled water cloud (effective radius: 5-40μm (Bourdages et al., 2009)) it is approximately between 0.02 and 0.16, for an ice crystal (effective radius: 15-220μm (Bourdages et al., 2009)) it is approximately between 0.06 and 0.9, and for rain droplets (radius: 0.2-2.5 mm (Stull, 2016) it is approximately between 0.8 and 10. Rain droplets are in the Mie regime, but are unexpected during the Arctic winter. Thus, microwave scattering in Arctic winter conditions occurs in the Rayleigh regime.

The total scattering intensity of radiation is proportional to the scattering cross section, σ_{sc}, which is the effective area of scattering for a single particle, in units of area. Scattering efficiency is the ratio of the effective area of scattering with the geometric cross-sectional
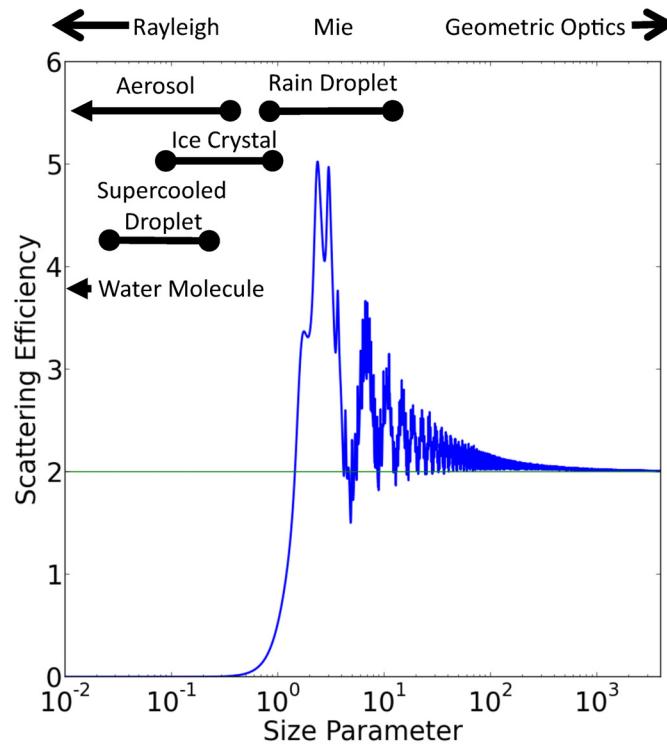
Figure 2.2: Scattering efficiency plot using Mie scattering code with varying size parameter (Bohren and Huffman, 1983). The green line represents the value the scattering efficiency converges to for large size parameters. The black bars in the figure represent ranges of size parameters for different particles. Above the figure are labels for the different scattering regimes.

area of the particle,

$$Q_{sc} = \frac{\sigma_{sc}}{\pi R^2}. \tag{2.2}$$

Figure 2.2 shows the scattering efficiency, Q_{sc}, for a range of size parameters with no absorption. The three scattering regimes are identified. The scattering cross-section is dependent on which regime is being considered. The scattering cross section for the Rayleigh regime is proportional to λ^{-4}. For Mie and geometric optics, the scattering cross section is proportional to the size of the scatterer (Liou, 2002). Note, the scattering efficiency approaches 2 for large size parameters meaning the scattering cross section is twice as large than the physical area of the particle, this is due to diffraction of light around the scatterer (Liou, 2002).

Figure 2.2 identifies the scattering efficiency for water molecules, aerosols, thin super-cooled water cloud droplets, ice crystals, and rain droplets. The scattering efficiency is small for aerosols, droplets in thin super-cooled water clouds, ice crystals and also water molecules. For most Arctic winter conditions, atmospheric scattering of microwave radiation can be safely neglected.

2.1.3 Transmittance

Radiation is lost due to scattering and absorption by particles or molecules along a path. The change in intensity of radiation as it goes through a medium can be determined using the Beer-Bougher-Lambert law (Liou, 2002),

$$I_1 = I_0 e^{-\tau_s} = I_0 e^{-\int \alpha_{ext} ds}, \tag{2.3}$$

where I_0 and I_1 are the intensities before and after the radiation passes through the medium and α_{ext} is the extinction coefficient. The extinction coefficient represents the fraction of radiation lost per unit length traveled through the medium. The distance traveled through the medium is s, and τ_s is the optical depth for path s. The extinction coefficient may be split into scattering and absorption components as,

$$\alpha_{ext} = \alpha_{sc} + \alpha_a \tag{2.4}$$

where α_{sc} and α_a are the scattering and absorption coefficients, respectively. As discussed in Sect. 2.1.2, scattering in the Arctic winter atmosphere is negligible at microwave frequencies, so $\alpha_{ext} = \alpha_a$.

If horizontal variations in the atmosphere can be taken as small, then the plane-parallel approximation may be applied (Petty, 2006). In this approximation, the distance r and altitude z are related by,

$$s = z \sec \theta \tag{2.5}$$

where θ is the observation angle with respect to zenith. Applying this to Eq. 2.3 gives,

$$I_1 = I_0 e^{-\sec \theta \int \alpha_{ext} dz} = I_0 e^{-\tau \sec \theta}. \tag{2.6}$$

where τ is the nadir optical depth for the path z.

2.1.4 Emission

Emission occurs when a molecule or particle converts some of its internal energy into radiation. For local thermodynamic equilibrium (LTE), emission is characterized by Planck's Function,

$$B(\lambda, T) = \frac{2hc^2}{\lambda^5 (e^{hc/k_B \lambda T} - 1)} \tag{2.7}$$

where B is the spectral radiance that is emitted by the object in units of W/m^2/μm/sr, c is the speed of light, h is Planck's constant, λ is the wavelength of radiation, T is the temperature of the object, and k_B is Boltzmann's constant. Planck's function gives the maximum spectral radiance that can be emitted by an object with a particular temperature and for a particular wavelength.

For radiation in the microwave spectrum, Planck's Function can be simplified. For microwave wavelengths, $hc/k_B \lambda T \ll 1$, and this allows Planck's Function to become

$$B(\lambda, T) = \frac{2ck_B T}{\lambda^4}, \tag{2.8}$$

which is the Rayleigh-Jean approximation.

The emissivity, ε, accounts for the deviation from Planck's Function,

$$I(\lambda, \theta, T) = \varepsilon(\lambda, \theta) B(\lambda, T) \tag{2.9}$$

where $I(\lambda, \theta, T)$ is the spectral radiance of the object. The emissivity can range from 0 for an object that does not emit radiation at the wavelength and temperature specified to 1 for a blackbody. Kirchhoff's law states that the emissivity is equal to the fraction of radiation absorbed at a given equal wavelength and angle of incidence.

2.1.5 Upwelling and Downwelling Radiation

The amount of radiation from the atmosphere viewed by an observer is dependent on the distribution of emission and transmittance. The spectral radiance viewed by an observer at

the top of the atmosphere from altitude, z, emitted from layer dz, is given by

$$dI_u = \sec\theta \, \alpha_a B(\lambda, T) e^{-\tau(z,H)\sec\theta} dz \qquad (2.10)$$

where $\tau(z, H)$ is the optical depth between the altitude, z, and the observer at altitude H (Petty, 2006). Similarly, the spectral radiance viewed by an observer at the surface, from altitude z, emitted from layer dz, is represented by,

$$dI_d = \sec\theta \, \alpha_a B(\lambda, T) e^{-\tau(0,z)\sec\theta} dz \qquad (2.11)$$

where $\tau(0, z)$ is the optical depth between the surface observer and altitude, z.

2.2 Surface Radiation Properties

The surface has a significant impact on radiative transfer, particularly in the microwave spectrum. The following section discusses the effect of polarization, surface reflectance, surface emission, and penetration depth on radiation.

2.2.1 Polarization

For microwave satellite-based remote sensing, each channel measures incident radiation in a particular polarization. For microwave radiation, polarization is typically induced by surface reflection of unpolarized emitted radiation from the atmosphere. The polarization of radiation for remote sensing is described in terms of horizontal and vertical components (Martin, 2014). Horizontal polarization refers to an electric field with a polarization perpendicular to the plane of incidence, and vertical polarization refers to an electric field that is parallel to the plane of incidence. The plane of incidence is the plane perpendicular to the scattering surface and parallel to the incident ray of radiation. The microwave satellite instruments used in the following chapters measure radiation at horizontal, vertical, or mixed polarization. Specific instrument polarizations will be discussed in Sect. 2.4.

2.2.2 Surface Reflection

Reflectance is the fraction of radiation incident on a surface that is reflected in a particular direction. The reflectance of radiation is dependent on both the angle of incidence and the angle of reflection. In general, the amount of radiation reflected from one direction to another is described by the bidirectional reflectance distribution function (BRDF) (Nicodemus, F., 1965). For the purposes of a retrieval algorithm, simplified geometries are needed.

Figure 2.3 shows examples of different extreme types of surface reflection. Specular reflection occurs for surfaces that are smooth and flat relative to the wavelength of the radiation; the angle of incidence equals the angle of reflection. Radiation that reflects equally in all directions from a rough surface is a special case of diffuse reflection called Lambertian reflection (Maxwell, 1974; Chuvieco et al., 2009; Matzler, 2005). Lambertian surface reflection is also depolarized (Maxwell, 1974). In general, reflectance can be represented as a mixture of specular and Lambertian reflection.
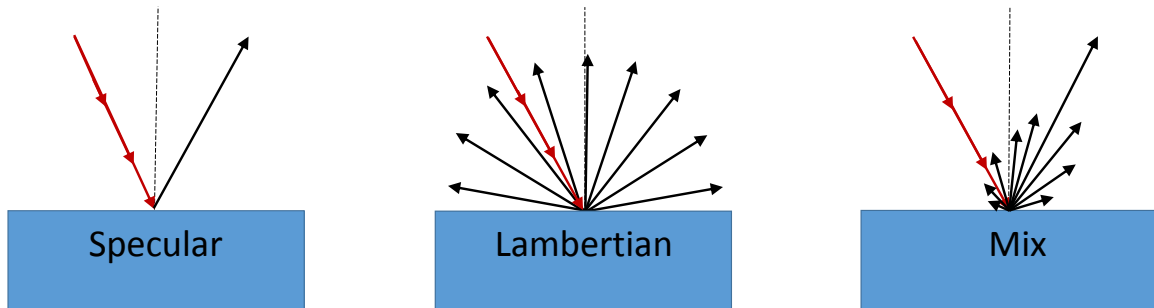
Figure 2.3: Distributions of surface reflection for specular, mix, and Lambertian. The red ray is the incoming radiation and the black rays are the reflected rays of radiation.

The reflectance at a surface can be calculated using the Fresnel equations from the theory of classical electromagnetic radiation (Petty, 2006). For a specular surface,

$$r_V(\lambda) = \left| \frac{\cos\theta_t - N_2(\lambda)/N_1(\lambda)\cos\theta_i}{\cos\theta_t + N_2(\lambda)/N_1(\lambda)\cos\theta_i} \right|^2 \qquad (2.12)$$

$$r_H(\lambda) = \left| \frac{\cos\theta_i - N_2(\lambda)/N_1(\lambda)\cos\theta_t}{\cos\theta_i + N_2(\lambda)/N_1(\lambda)\cos\theta_t} \right|^2 \qquad (2.13)$$

where $N_1(\lambda)$ and $N_2(\lambda)$ are the complex refractive indices of the incoming and transmitting

materials respectively at the interface, θ_i and θ_t are the incoming and transmission angles of the radiation, and r_V and r_H are the reflectances at the surface for vertical and horizontal polarizations.

Emission from the atmosphere is randomly polarized; however, as shown by Eq. 2.12 and Eq. 2.13, reflection from the surface can induce a polarization. Figure 2.4 gives reflectivity from the Fresnel relations for a liquid water surface at vertical and horizontal polarizations for visible and microwave wavelengths.

At visible wavelengths the reflectance is nearly zero until large incident angles. There is also a small difference in the reflectance for each polarization until large incident angles where the difference maximizes near 70° with a difference of approximately 0.1. For microwave radiation at ν=176 GHz, the reflectance is much larger and it is comparable to the emissivity of the surface. As the incident angle increases at the surface, the reflectance for vertical polarization decreases and for horizontal polarization it increases. The difference between the two polarizations maximizes at 80° with a difference of approximately 0.5. The large variation of surface reflectance with polarization and incident angle implies that the surface must be properly characterized when dealing with microwave radiation that has interacted with a surface.
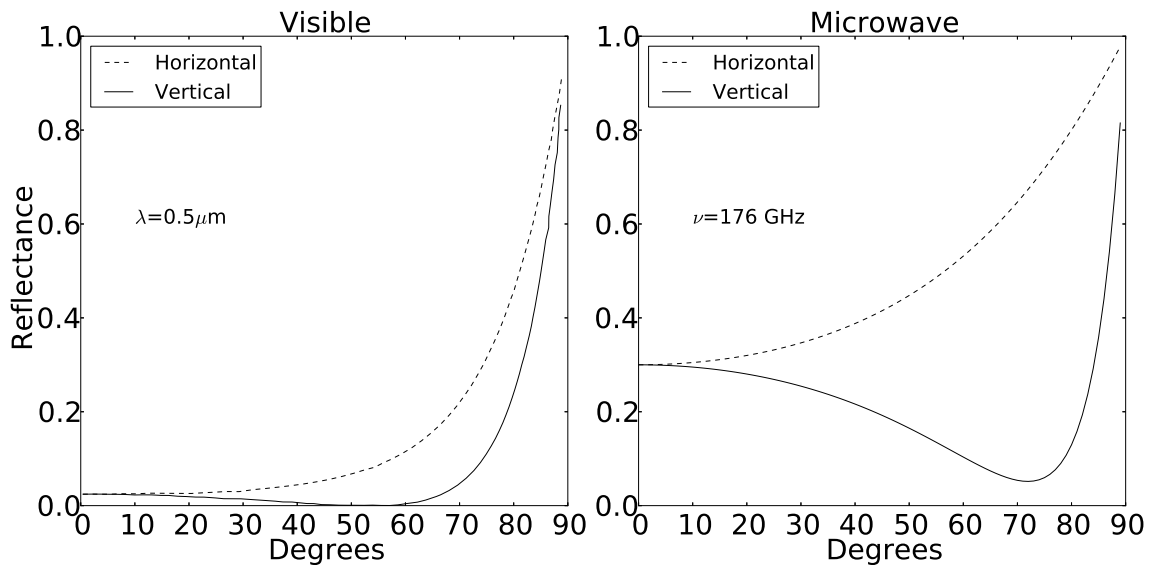
Figure 2.4: Reflectance at various angles of incidence for open water at visible and microwave wavelengths (Petty, 2006; Hasted et al., 1987).

2.2.3 Surface Emission

The surface emits radiation according to

$$I_S(\lambda, \theta, T_s) = \varepsilon(\lambda, \theta)B(\lambda, T_s), \tag{2.14}$$

where $I_S(\lambda, \theta, T_s)$ is the spectral radiance of the surface, ε is the surface emissivity, and T_s is the skin temperature.

For radiation at a particular polarization and incident angle to an opaque surface, the sum of the reflectance and the absorption is equal to 1. Kirchhoff's law gives

$$a_{P,a}(\lambda, \theta) + r_P(\lambda, \theta) = \varepsilon_P(\lambda, \theta) + r_P(\lambda, \theta) = 1, \tag{2.15}$$

where $a_{P,a}$ is the absorptance for polarization P, and ε_P is the emissivity at polarization P (Guissard and Sobieski, 1994).

2.2.4 Penetration depth

Surface emissivity varies with frequency, especially in the microwave. Surface emissivity is related to the penetration depth, which is the depth at which $1/e$ of the radiation at a particular wavelength is absorbed when incident on a surface. The penetration depth, d, may be calculated using the absorption coefficient of the surface or the imaginary component of the index of refraction, n_i, for the surface material using,

$$d = \frac{1}{\alpha_a} = \frac{\lambda}{4\pi n_i}. \tag{2.16}$$

Figure 2.5 shows the change in penetration depth for snow, younger (first-year) and older (multi-year) sea ice in part of the microwave spectrum. Penetration depths tend to decrease with increasing frequency in the microwave. The depth also varies significantly for the different surface types. Multi-year ice has a larger penetration depth than first-year ice due to decreasing salinity with increasing age of the sea ice (Shokr and Sinha, 2015). This decreases the absorption coefficient and increases the penetration depth of the sea ice.

In terms of radiative transfer, the skin temperature is the emitting temperature of the surface. The penetration depth of a surface provides the depths which radiation is being emitted from the surface. The skin temperature can be determined using the emission
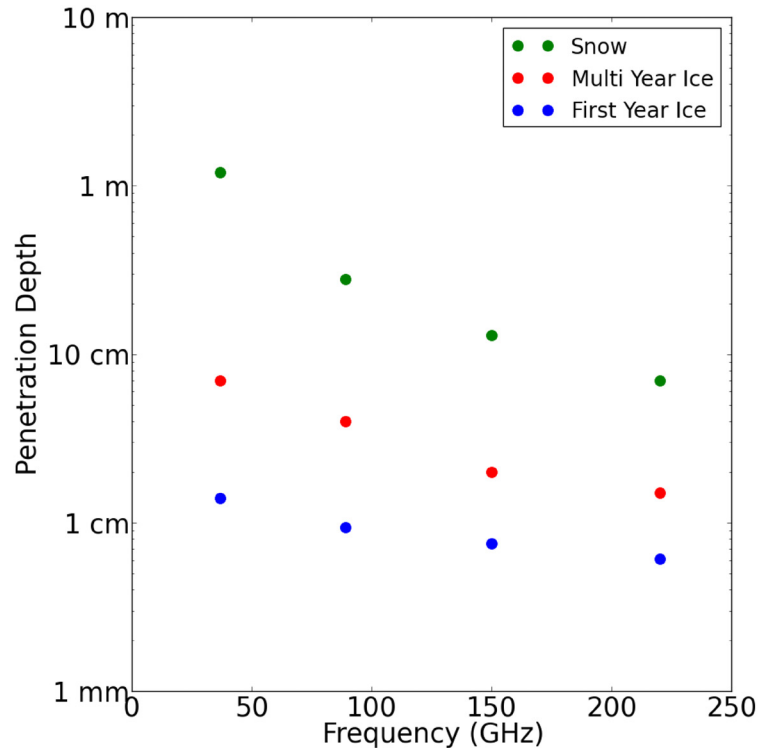
Figure 2.5: Theoretical penetration depth of radiation within the microwave spectrum for Snow, First-Year Ice, and Multi-Year Ice (Haggerty and Curry, 2001).

depths and surface temperature profile. Since penetration depth is wavelength dependent, the same is true for skin temperature.

2.3   Microwave Satellite Radiative Transfer

Microwave radiative transfer processes relevant for arctic winter remote sensing are illustrated in Fig. 2.6. As shown, the general radiative transfer equation must account for atmospheric absorption, emission, scattering, surface scattering, and surface emission. For the microwave spectrum, atmospheric scattering will be ignored as stated in Sect. 2.1.2. This simplification is evaluated in Chapter 3.

The radiation measured by a passive microwave satellite has four components: a) cosmic microwave background radiation, I_c, that was reflected at the surface in the direction of the satellite; b) radiation emitted by the atmosphere towards the surface, I_d, that is reflected in the direction of the satellite; c) radiation emitted by the surface, I_S; d) radiation emitted by the atmosphere in the direction of the satellite, I_u. Each component is subject to
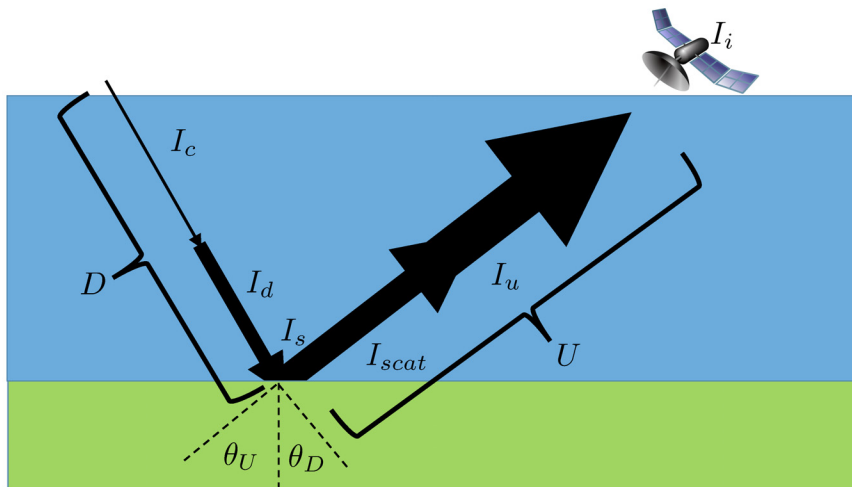
Figure 2.6: Atmospheric contributions of satellite-measured brightness temperature for the microwave spectrum. Symbols are defined in the text. D is the path for downwelling radiation and U is the path for upwelling radiation.

absorption along the way.

The total downwelling spectral radiance (i.e. the sum of components a) and b)) is given by

$$I_D = I_c e^{-\tau(0,H)\sec\theta_D} + \int_0^H \sec\theta_D \alpha_a B(\lambda,T) e^{-\tau(0,z)\sec\theta_D} dz, \qquad (2.17)$$

where I_c is the spectral radiance along path D towards the surface at the top of the atmosphere, H, θ_D is the angle of incidence on the surface with respect to zenith, and $e^{-\tau(0,H)\sec\theta_D}$ is the transmission of radiation along path D. The second term represents the sum of the atmospheric emission towards the surface, along the path D.

The fraction of I_D reflected at the surface towards the satellite is represented by I_{scat}. Specular reflection is commonly assumed for the microwave spectrum (Hewison and English, 1999; Guissard and Sobieski, 1994). In this case, I_{scat} may be written as

$$I_{scat} = rI_D = (1-\varepsilon)I_D. \qquad (2.18)$$

where r is the reflectance of the surface.

Component c) is described by Eq. 2.14. The upwelling spectral radiance (i.e. component d)) is given by

$$I_u = \int_0^H \sec \theta_U \alpha_a B(\lambda, T) e^{-\tau(z,H)\sec \theta_U} dz, \tag{2.19}$$

where θ_U is the angle of the satellite with respect to zenith and $e^{-\tau(z,H)\sec \theta_U}$ is the transmission of radiation along path U. The integral represents the sum of the atmospheric emission towards the satellite, along the path U. From the specular reflection assumption, $\theta_U = \theta_D = \theta$.

Combining all the components from Fig. 2.6 gives the formula for spectral radiance observed by a satellite viewing a specularly reflecting surface,

$$I_i = I_u + e^{-\tau(0,H)\sec \theta}(\varepsilon I_S + I_{scat}), \tag{2.20}$$

where I_i is the spectral radiance measured by channel i of the satellite instrument. I_S and I_{scat} are multiplied by the transmittance to represent the attenuation of the radiation while traveling from the surface to the satellite.

For the microwave spectrum spectral radiances can be represented as brightness temperatures with the application of the Rayleigh-Jean approximation, which has $I \propto T$. Equation 2.20 becomes

$$T_i = T_u + e^{-\tau(0,H)\sec \theta}(\varepsilon T_S + (1-\varepsilon)T_D), \tag{2.21}$$

where T_i is the brightness temperature measured by the satellite and T_u and T_D are the upwelling and total downwelling brightness temperatures. Eq. 2.19 and Eq. 2.17 become

$$T_u = \int_0^H \sec \theta \alpha_a T_a(z) e^{-\tau(z,H)\sec \theta} dz \tag{2.22}$$

and

$$T_D = T_c e^{-\tau(0,H)\sec \theta} + \int_0^H \sec \theta \alpha_a T_a(z) e^{-\tau(0,z)\sec \theta} dz \tag{2.23}$$

where $T_a(z)$ is the atmospheric temperature at altitude, z.

Substituting T_u and T_D from Eq. 2.22 and Eq. 2.23 respectively into Eq. 2.21 yields (after considerable algebraic manipulation shown in Appendix A) the radiative transfer

formula used for the work in Chapter 3. It is

$$T_i = m_p T_s - (T_0 - T_c)(1 - \varepsilon)e^{-2\tau(0,H)\sec\theta} \tag{2.24}$$

where T_0 is the surface air temperature. m_p is a term that contains all vertical profile infor-
mation and is given by

$$m_p = 1 + \left((1 - \varepsilon e^{-\tau(0,H)\sec\theta}) \frac{T_0 - T_s}{T_s} - \frac{1}{T_s} \left(\int_0^H -(1 - e^{-\tau(z,H)\sec\theta}) \frac{dT}{dz} dz + \right. \right.$$

$$\left. \left. (1 - \varepsilon)e^{-\tau(0,H)\sec\theta} \int_0^H (1 - e^{\tau(z,H)\sec\theta}) \frac{dT}{dz} dz \right) \right). \tag{2.25}$$

Equations 2.24 and Eq. 2.25 are from Guissard and Sobieski (1994).

2.4 Microwave Satellite Instrumentation

Three microwave instruments are used for the water vapour and surface emissivity re-
trievals in the following chapters. They are the Advanced Microwave Sounding Unit-B
(AMSU-B), Microwave Humidity Sounder (MHS), and Advanced Technology Microwave
Sounder (ATMS). There are three AMSU-B instruments on board the NOAA-15, NOAA-
16, NOAA-17 satellites, four MHS instruments on board the NOAA-18, NOAA-19, MetOP-
A/B satellites, and one ATMS instrument on board the Suomi-npp satellite. Other mi-
crowave satellite instruments that are not used for the following work include the Mi-
croWave Humidity Sounder (MWHS), Special Sensor Microwave Imager/Sounder (SS-
MIS), and Special Sensor Microwave/Temperature-2 (SSM/T-2) and are left for future
work. ATMS is the successor to MHS and MHS is the successor to AMSU-B, making
the three similar to one another.

The frequencies and polarizations used by AMSU-B, MHS, and ATMS are similar as
shown in Table 2.1. Near 183 GHz, each instrument samples a series of paired frequency
bands. The channels are labeled in Fig. 2.7, which shows the microwave absorption spec-
trum at 183 GHz and the channel locations for each instrument in that frequency range.
The AMSU-B has three paired frequency bands near the 183 GHz water vapour absorption
line, MHS has two paired frequency bands and one single band at 190 GHz, and ATMS
has five paired frequency bands at 183 GHz. The other frequencies for AMSU-B, MHS,

Table 2.1: AMSU-B, MHS, and ATMS instrument specifications including frequencies and nadir polarization orientations (Kleepsies and Watts, 2006) (Kim et al., 2014).

Frequencies (GHz)			Polarizations			Noise(K)		
AMSU-B	MHS	ATMS	AMSU-B	MHS	ATMS	AMSU-B	MHS	ATMS
89	89	88.2	Vertical	Vertical	Vertical	0.40	0.32	0.29
150	157	165.5	Vertical	Vertical	Horizontal	0.80	0.53	0.46
183.31 ± 1	183.311 ± 1	183.31 ± 1	Vertical	Horizontal	Horizontal	0.80	0.50	0.73
		183.31 ± 1.8			Horizontal			0.59
183.31 ± 3	183.311 ± 3	183.31 ± 3	Vertical	Horizontal	Horizontal	0.75	0.41	0.54
		183.31 ± 4.5			Horizontal			0.46
183.31 ± 7	190.311	183.31 ± 7	Vertical	Vertical	Horizontal	0.80	0.55	0.38

and ATMS include window frequencies (150, 157, 165.5 GHz) and another frequency between the oxygen absorption lines (89, 89, 88.2 GHz). The central frequencies are labeled in Fig. 2.1. Between the three instruments there are only small changes in frequencies and polarization excluding the additional two frequencies for ATMS.

The satellites are polar orbiting (inclination angle 98°) with periods of approximately 100 minutes at altitudes of approximately 800 km. At nadir, each channel has a spatial resolution of approximately 15 km which increases to approximately 50 km at the largest viewing angle. The instruments scan across the orbital path with a total of 90 steps equating to ±49.5 degrees in viewing angle for AMSU-B and MHS, and 96 steps equating to ±52.725 degrees in viewing angle for ATMS. The instruments measure pure horizontal or vertical polarization with respect to the plane of incidence at nadir. The measured polarization varies with increasing scan angle (Miao et al., 2001) according to

$$\varepsilon_M(\theta) = \varepsilon_V(\theta)\cos^2\Theta + \varepsilon_H(\theta)\sin^2\Theta \tag{2.26}$$

where ε_M is the surface emissivity due to the mixed polarization, ε_V and ε_H are the surface emissivity for purely vertical and horizontal polarizations respectively, and θ and Θ are the satellite local zenith angle and satellite scan angle respectively. Figure 2.8 shows a diagram labeling θ and Θ. Equation 2.26 is for an instrument channel that measures vertically polarized radiation at nadir. For horizontal polarization at nadir, ε_V and ε_H are reversed.

The first AMSU-B launched in 1998 and the final instrument stopped data collection in 2012. The first MHS launched in 2005 and all four instruments are still online. The ATMS launched in 2011 and is also still online. Between these three instruments there is a total of approximately 20 years of data.
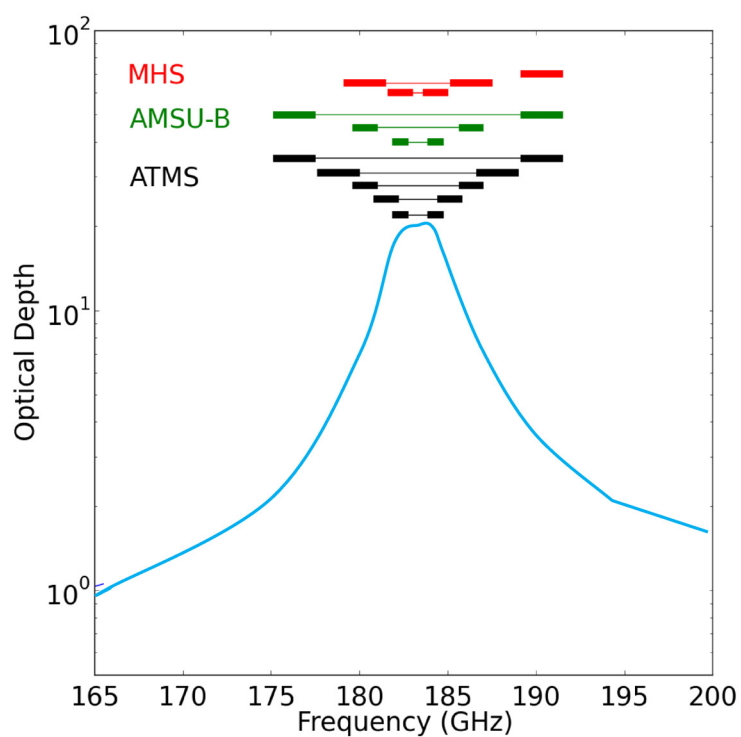
Figure 2.7: Microwave Optical Depth Absorption spectrum showing the 183 GHz water vapour absorption line with 183 GHz channels labeled for AMSU-B (green), MHS (red), and ATMS (black). Lines connect the double sideband channels
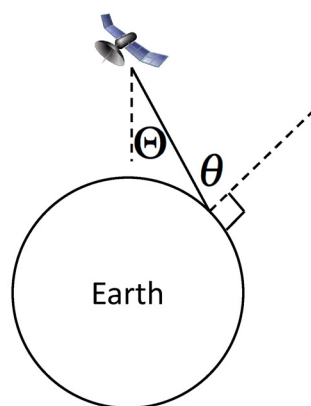
Figure 2.8: Viewing geometry of satellite with respect to the Earth's surface with satellite viewing angle, Θ, and satellite local zenith angle, θ. Note, this is the actual viewing geometry of the satellite with respect to the Earth, however, a plane parallel approximation is used for the following retrieval algorithms.

CHAPTER 3

WATER VAPOUR COLUMN RETRIEVAL TECHNIQUES

This chapter describes a retrieval method for determining water vapour column in the Arctic using microwave satellite instrumentation. Perro et al. (2016) is a published paper that describes and evaluates the new retrieval of water vapour column, PLDC16, for use during the Arctic winter and is included in Sect. 3.1.

The paper initially describes two previous microwave water vapour column retrievals, M98 and MH08, which use similar formulations, but have a large number of simplifications and parameterizations in Sect. 3.1.3.1 -3.1.3.2. PLDC16 removes a number of these and instead uses auxiliary temperature and water vapour profiles as shown in Sect. 3.1.3.3-3.1.4. PLDC16 is evaluated using simulations and comparisons to measurements made at Barrow, Alaska in Sect. 3.1.5-3.1.7.2. Finally, a discussion of possible uncertainties in the retrieval is shown in Sect. 3.1.7.3.

A number of topics were not included in the published paper which describe issues that were encountered when developing the PLDC16 retrieval and some topics that were included, but only briefly described. An appendix is included in this Chapter in Sect. 3.2 to discuss these issues and give a full description of these topics.

The structure of the appendix is as follows. Section 3.2.1 describes a previous iteration of the water vapour column retrieval. The method built upon the MH08 retrieval by including an extra term and using a least squares regression to determine coefficients. The approach was found to have certain deficiencies which will be discussed. Section 3.2.2 discusses the influence of clouds on the PLDC16 retrieval. Micro pulse lidar, radiosonde measurements, and MHS overpasses are used to evaluate this. Comparison of PLDC16 water

vapour column for the MetOP-A and NOAA-18 MHS instruments were done to investigate any discrepancies between them in Sect. 3.2.3. Further discussion of the simplifications and resultant errors in the PLDC16 retrieval is given in Sect. 3.2.4.

3.1 A Microwave Satellite Water Vapour Column Retrieval for Polar Winter Conditions

3.1.1 Abstract

A new microwave satellite water vapour retrieval for the polar winter atmosphere is presented. The retrieval builds on the work of Miao et al. (2001) and Melsheimer and Heygster (2008), employing auxiliary information for atmospheric conditions and numerical optimization. It was tested using simulated and actual measurements from the Microwave Humidity Sounder (MHS) satellite instruments. Ground truth was provided by the G-band vapour radiometer (GVR) at Barrow, Alaska. For water vapour columns less than $6\,\mathrm{kg\,m^{-2}}$, comparisons between the retrieval and GVR result in a root mean square (RMS) deviation of $0.39\,\mathrm{kg\,m^{-2}}$ and a systematic bias of $0.08\,\mathrm{kg\,m^{-2}}$. These results are compared with RMS deviations and biases at Barrow for the retrieval of Melsheimer and Heygster (2008), the AIRS and MIRS satellite data products, and the ERA-Interim, NCEP, JRA-55, and ASR reanalyses. When applied to MHS measurements, the new retrieval produces a smaller RMS deviation and bias than for the earlier retrieval and satellite data products. The RMS deviations for the new retrieval were comparable to those for the ERA-Interim, JRA-55, and ASR reanalyses; however, the MHS retrievals have much finer horizontal resolution ($15\,\mathrm{km}$ at nadir) and reveal more structure. The new retrieval can be used to obtain pan-Arctic maps of water vapour columns of unprecedented quality. It may also be applied to measurements from the Special Sensor Microwave/Temperature 2 (SSM/T2), Advanced Microwave Sounding Unit B (AMSU-B), Special Sensor Microwave Imager/Sounder (SS-MIS), Advanced Technology Microwave Sounder (ATMS), and Chinese MicroWave Humidity Sounder (MWHS) instruments.

Table 3.1: AMSU-B and MHS instrument specifications including frequencies, noise equivalent differential temperature, and nadir polarization orientations (Kleepsies and Watts, 2006). Entries like 183.31 ± 1 GHz imply that two frequency bands at 182.31 and 184.31 GHz are combined. Vertical and horizontal polarization refers to cross-track and along-track polarization respectively.

Frequencies (GHz)		Noise (K)		Polarizations	
AMSU-B	MHS	AMSU-B	MHS	AMSU-B	MHS
89	89	0.40	0.32	Vertical	Vertical
150	157	0.80	0.53	Vertical	Vertical
183.31 ± 1	183.311 ± 1	0.80	0.50	Vertical	Horizontal
183.31 ± 3	183.311 ± 3	0.75	0.41	Vertical	Horizontal
183.31 ± 7	190.311	0.80	0.55	Vertical	Vertical

3.1.2 Introduction

The polar winter troposphere is very dry, with water vapour columns typically near $3 \, \mathrm{kg \, m^{-2}}$ (Serreze et al., 1995). Climate change is expected to increase absolute humidity and alter the polar radiative balance (Stamnes et al., 1998) with consequences for sea ice and global climate. Accurately monitoring polar humidity variations is necessary, but is difficult to do because of the small water vapour concentrations and the few ground-based stations from which observations can be made. Infrared and visible satellite measurements have better spatial coverage but are challenged by scattering and absorption from clouds and the lack of solar radiation during polar winter.

Microwave satellite measurements overcome many of the difficulties. Microwaves have a strong water vapour absorption line at 183 GHz that is useful for dry conditions, with emissions that can be observed during any part of the diurnal cycle. Microwaves are less affected by scattering and absorption from clouds, allowing for water vapour measurements in most weather conditions (Miao et al., 2001). Microwave instruments aboard a series of polar-orbiting satellites since 1991 (F11 to 19, NOAA-15 to 19, MetOP-A and B, FY3-A to C, and NPP) already provide a substantial data set for water vapour studies. Planned missions include JPSS-1 and 2, MetOP-C, MetOP-SG, and DMSP-S20.

This paper introduces a modified technique for retrieving water vapour columns from microwave satellite measurements in polar winter conditions that are characterized by low optical depths. The retrieval uses the microwave signal formulation given by Miao (1998, hereafter M98). M98's retrieval technique involves several approximations that were somewhat relaxed in a variation by Melsheimer and Heygster (2008, hereafter MH08). Our

retrieval (hereafter referred to as PLDC16) employs fewer approximations but requires auxiliary data for the atmospheric conditions. The results are more accurate, but come at the cost of increased computational complexity.

MH08 and PLDC16 are tested against simulated signals in order to determine the impacts of different sources of error. Their performance is also assessed using Microwave Humidity Sounder (MHS) measurements from MetOP-A and NOAA-18 in comparison with surface based G-band vapour radiometer (GVR) measurements at Barrow, Alaska ($71.3°\,$N, $156.8°\,$W). MHS measurements were chosen because they provide the longest period of overlap with the GVR, with continuous water vapour column measurements since 2005 (Cadeddu et al., 2009). The GVR measures brightness temperatures at four double-sideband frequencies near the $183\,$GHz water vapour absorption line. The water vapour column is estimated to have $5\,\%$ error for values between 2 and $7\,\mathrm{kg\,m^{-2}}$ (Cadeddu et al., 2009). Comparisons for water vapour columns less than $8\,\mathrm{kg\,m^{-2}}$ between the GVR and Vaisala radiosondes launched from the ARM Climate Research Facility in Barrow, Alaska have an RMS deviation of $0.23\,\mathrm{kg\,m^{-2}}$. The continuous measurements, relatively low uncertainties, and availability of complementary measurements (most notably a micro pulse lidar) make the GVR an ideal instrument against which to test satellite retrievals.

Similar to the GVR, MHS measures microwave radiances at five frequencies near the $183\,$GHz water vapour absorption line. MHS is the successor to AMSU-B, the target instrument for MH08's analysis. The specifications for both instruments are summarized in Table 3.1. The instruments have slightly different frequencies and there is decreased noise for MHS.

The structure of this paper is as follows. Section 3.1.3 introduces M98's microwave signal formulation and the three techniques (M98, MH08, and PLDC16) for retrieving water vapour columns. Section 3.1.4 describes how different water vapour column regimes are treated. The application of PLDC16 and MH08 to simulated signals is examined in Sect. 3.1.5. Section 3.1.7 follows by comparing the PLDC16 MHS retrieval with the GVR, other satellite data products (AIRS and MIRS) and atmospheric reanalysis data sets (ERA-Interim, NCEP, ASR, and JRA-55). The results are discussed in Sect. 3.1.7.3.

3.1.3 Satellite microwave signal formulation and retrieval techniques

The brightness temperature T_i measured at frequency ν_i by channel i of a satellite-borne microwave instrument is parameterized by (Guissard and Sobieski, 1994)

$$T_i = m_p(\nu_i)T_s - (T_o - T_c)(1 - \varepsilon_i)e^{-2\tau_i \sec\theta}, \tag{3.1}$$

where T_s is the skin temperature, T_o is the surface air temperature, T_c is the cosmic background temperature, ε_i is the surface emissivity, $\tau_i \equiv \tau_i(0,\infty)$ is the total optical depth, θ is the zenith viewing angle of the satellite, and m_p is a factor incorporating the vertical structure of the atmosphere. Equation (3.1) is a combined form of the upwelling and downwelling brightness temperature equations that includes a contribution from cosmic microwave background radiation. Microwave contributions are assumed to be identical in both polarizations, and the surface is assumed to be a perfect specular reflector.

The common idea of M98 and subsequent retrieval schemes is to combine brightness temperatures T_1, T_2, and T_3 from three channels with $\tau_1 < \tau_2 < \tau_3$ to obtain

$$\frac{\Delta T_{12} - b_{12}}{\Delta T_{23} - b_{23}} = \frac{r_1}{r_2}\left(\frac{e^{-2\tau_1 \sec\theta} - (r_2/r_1)e^{-2\tau_2 \sec\theta}}{e^{-2\tau_2 \sec\theta} - (r_3/r_2)e^{-2\tau_3 \sec\theta}}\right), \tag{3.2}$$

where $\Delta T_{12} = T_1 - T_2$ and $\Delta T_{23} = T_2 - T_3$ are brightness temperature differences, and r_1, r_2, and r_3 are surface reflectances with $r_i = 1 - \varepsilon_i$. The factors b_{12} and b_{23} are bias coefficients given by

$$\begin{aligned}
b_{ij} &= \int_0^\infty \left(e^{-\tau_j(z,\infty)\sec\theta} - e^{-\tau_i(z,\infty)\sec\theta}\right)\frac{dT(z)}{dz}dz \\
&\quad + (T_o - T_s)\left(\varepsilon_j e^{-\tau_j \sec\theta} - \varepsilon_i e^{-\tau_i \sec\theta}\right) \\
&\quad + r_j e^{-2\tau_j \sec\theta}\int_0^\infty \left(1 - e^{\tau_j(z,\infty)\sec\theta}\right)\frac{dT(z)}{dz}dz \\
&\quad - r_i e^{-2\tau_i \sec\theta}\int_0^\infty \left(1 - e^{\tau_i(z,\infty)\sec\theta}\right)\frac{dT(z)}{dz}dz,
\end{aligned} \tag{3.3}$$

where $\tau_i(z,\infty)$ is the optical depth above altitude z.

The three retrieval techniques (M98, MH08, and PLDC16) used to solve for the water vapour column are described next. The retrieval techniques are subject to water vapour column regimes with different frequencies and reflectance choices, and these are discussed

in Sect. 3.1.4.

3.1.3.1   M98

The M98 retrieval simplifies the formulation of Eqs. (3.2) and (3.3). It is assumed that the frequencies for each measurement are similar enough that $r_1 = r_2 = r_3$, and all but the first term in Eq. (3.3) is neglected. It is also assumed that water vapour is the only significant absorber in the frequency range of interest and that the total optical depth depends linearly on the water vapour column. This allows a series expansion of Eq. (3.2) to yield

$$W \sec \theta = C_0 + C_1 \log \left(\frac{\Delta T_{12} - b_{12}}{\Delta T_{23} - b_{23}} \right), \tag{3.4}$$

where W is the water vapour column, and C_0 and C_1 are coefficients that combine integrated mass absorption coefficients. Notice that the dependence on surface reflectance is eliminated.

M98 assumed constant coefficients b_{12}, b_{23}, C_0, and C_1, and determined them using the 1-D radiative transfer model Microwave Model (MWMOD Fuhrhop et al., 1998) with radiosonde profile inputs. A separate calibration is required for each frequency triplet v_1, v_2, v_3.

3.1.3.2   MH08

MH08 proposed a variation of the M98 retrieval for cases with water vapour columns greater than $8 \, \text{kg} \, \text{m}^{-2}$. Instead of assuming all surface reflectances to be the same, they allow for the possibility that r_1 differs from $r_2 = r_3$. Following M98, a series expansion of Eq. (3.2) results in

$$W \sec \theta = C_0 + C_1 \log \left[\frac{r_2}{r_1} \left(\frac{\Delta T_{12} - b_{12}}{\Delta T_{23} - b_{23}} + C \right) - C \right]. \tag{3.5}$$

MH08 found C to be constant for the range of water vapour columns under consideration. The coefficients b_{12}, b_{23}, C_0, and C_1 were determined using the same approach as in M98 except with a viewing angle dependency. A separate calibration is required for each frequency triplet v_1, v_2, v_3. Aircraft measurements of sea ice emissivity were used to establish a constant value for r_2/r_1.

3.1.3.3 PLDC16

Our approach is to employ Eqs. (3.2) and (3.3), but with fewer assumptions. Unlike M98 and MH08, auxiliary information for the atmospheric conditions is required. This information may be obtained from atmospheric reanalyses or other sources.

As a practical matter, the second term in Eq. (3.3) is ignored[1]. It is proportional to the difference between the skin and surface air temperatures, and comparisons between atmospheric reanalysis products for this factor show considerable disagreement. We also take $r = r_i = r_j$ in the third and fourth terms of Eq. (3.3), leaving

$$
\begin{aligned}
b_{ij} \approx & \int_0^\infty \left(e^{-\tau_j(z,\infty)\sec\theta} - e^{-\tau_i(z,\infty)\sec\theta} \right) \frac{\mathrm{d}T(z)}{\mathrm{d}z}\mathrm{d}z \\
& + r \left[e^{-2\tau_j\sec\theta} \int_0^\infty \left(1 - e^{\tau_j(z,\infty)\sec\theta} \right) \frac{\mathrm{d}T(z)}{\mathrm{d}z}\mathrm{d}z \right. \\
& \left. - e^{-2\tau_i\sec\theta} \int_0^\infty \left(1 - e^{\tau_i(z,\infty)\sec\theta} \right) \frac{\mathrm{d}T(z)}{\mathrm{d}z}\mathrm{d}z \right].
\end{aligned}
\tag{3.6}
$$

A constant value for r is assumed, and auxiliary information is used to determine $\mathrm{d}T(z)/\mathrm{d}z$. The sensitivity of our retrieval to these approximations is discussed in Sect. 3.1.5.5.

Next, suppose that the true optical depth profile $\tau_i(z,\infty)$ is related to a trial optical depth profile $\tau_{i,n}(z,\infty)$ by

$$
\tau_i(z,\infty) = x_n \tau_{i,n},
\tag{3.7}
$$

where x_n is a scaling factor and $n = \{0,1,2,3,\ldots\}$ is the trial number. The trial optical depth profile is given by

$$
\tau_{i,n}(z,\infty) = \int_z^\infty k_i(p(z),T(z))w_n(z)\mathrm{d}z + \tau_i^o(z,\infty),
\tag{3.8}
$$

where $p(z)$ and $T(z)$ are pressure and temperature profiles, respectively, w_n is the trial water vapour mass density profile, k_i is the mass absorption coefficient, and $\tau_i^o(z,\infty)$ is the optical depth profile for other constituents (most notably O_2 for the 89 GHz channel). We determine $\tau_{i,n}(z,\infty)$ for each trial using the RTTOV 1-D radiative transfer model (Matricardi and Saunders, 1999). Pressure and temperature profiles are taken from the auxiliary

---

[1]The second term in Eq. 3.3 is shown to be small and is further discussed in Sect. 3.2.4

Table 3.2: MHS frequencies for the low, mid, and extended regimes for the retrievals of water vapour column with typical water vapour column (W) ranges. The frequencies v_1, v_2 and v_3 in each regime are ordered so that $\tau_1 < \tau_2 < \tau_3$.

Regime	MHS frequencies (GHz)			W range
	v_1	v_2	v_3	$(\mathrm{kg\,m^{-2}})$
Low	190.311	183.311 ± 3	183.311 ± 1	0–2.5
Mid	157	190.311	183.311 ± 3	1.5–9
Extended	89	157	190.311	8–15

information.

The calculation begins with a trial water vapour profile $w_0(z)$ taken from the auxiliary estimate. The scaling factor x_n is the only unknown variable. It is determined for each trial by solving Eqs. (3.2), (3.6) and (3.7) with a numerical nonlinear optimizer. Trial water vapour profiles for iterations $n > 0$ are determined using

$$w_{n+1}(z) = x_n w_n(z). \tag{3.9}$$

Iterating gradually re-balances the contributions in Eq. (3.8) between water vapour and other atmospheric constituents.

Having obtained a scaling factor, the water vapour column for iteration $n + 1$ is given by

$$W_{n+1} = x_n \int_0^\infty w_n(z)\mathrm{d}z. \tag{3.10}$$

Note that the final result depends on the shape of the auxiliary water vapour profile but not on its column amount.

Unlike M98 or MH08 there is no need to perform a separate frequency calibration. We stop iterating when the change in the water vapour column is less than 0.1% between iterations. The number of iterations varies for each measurement, and a maximum of 20 iterations is applied. Figure 3.1 summarizes the PLDC16 retrieval process.

Although it is not inherently required by the formulation above, for the remainder of this paper we shall assume that the influence of liquid clouds and ice crystals on the retrieval is negligible. The mass absorption coefficient for liquid water in particular is almost constant across the frequencies of interest (Miao et al., 2001). The impact of this assumption is explored in Sect. 3.1.7.3.
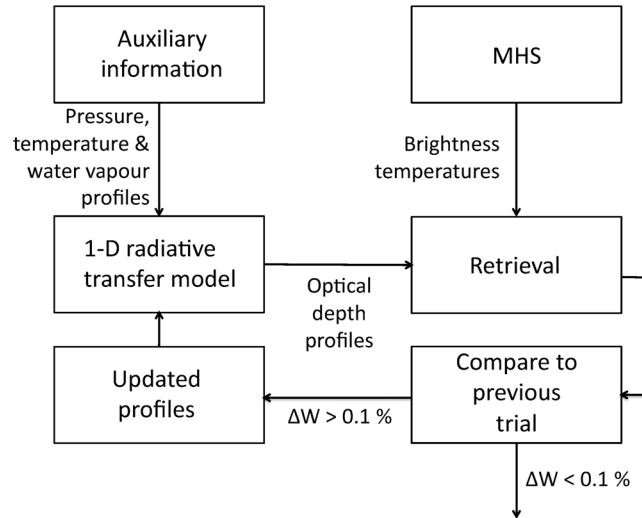
Figure 3.1: PLDC16 retrieval flow chart. The retrieval starts with auxiliary temperature, pressure, and water vapour profiles as input to a 1-D radiative transfer model. Optical depth profiles are produced for each channel. These are used together with satellite brightness temperatures and Eqs. (3.2), (3.6) and (3.7) to retrieve the scaling factor x_n for each trial n. x_n is used to scale the trial water vapour profile through Eq. (3.9) and produce a water vapour column using Eq. (3.10). If the change ΔW in the water vapour column between trials is greater than the threshold then the scaled water vapour column is used in the next trial. The process is repeated until convergence is achieved.

3.1.4 Regime selection

Three sets of frequencies are used for MHS retrievals, giving rise to the "low", "mid", and "extended" regimes, as summarized in Table 3.2. These correspond to measurements at highly, moderately, and weakly absorbed frequencies. M98 applies to only the low and mid regimes while MH08 and PLDC16 apply to all three. The retrievals use different criteria for choosing between regimes.

Brightness temperatures typically increase with increasing water vapour column, but decrease for larger columns as the weighting function peaks at higher (and therefore colder) altitudes. M98 therefore switches from the low to mid regime when $\Delta T_{12} > 0$ or $\Delta T_{23} > 0$. MH08 switches to a higher regime if $\Delta T_{12} - b_{12} > 0$ or $\Delta T_{23} - b_{23} > 0$.

A difficulty with the above approach is that brightness temperatures are strongly affected by temperature profile structure, and in particular by surface temperature inversions that are ubiquitous during polar winter (e.g. Lesins et al., 2010, 2012). This causes regime selection artifacts, as will be seen in Sect. 3.1.5.1.

We take a different approach. The slant water vapour column is determined from auxiliary information, with the slant given by the instrument's viewing angle. The low regime is used for slant water vapour columns between 0 and $2.5\,\mathrm{kg\,m^{-2}}$, the mid regime is used from 1.5 to $9\,\mathrm{kg\,m^{-2}}$, and the extended regime is used above $8\,\mathrm{kg\,m^{-2}}$. The boundaries of the regimes were chosen by comparing multiple GVR and PLDC16 water vapour columns. When a regime becomes too moist for its strongest absorbing frequency, the retrieval shows a decrease in sensitivity with increasing water vapour. By comparing the RMS deviation and bias for adjacent regimes the optimal regime for a particular range of water vapour column was chosen. Weighted averages are used where regimes overlap in order to smooth the transition. Measurements near the lower boundary of a regime sometimes do not have a solution, and in this case the nearest regime in terms of the slant water vapour column is used.

MH08 retrievals in the low and mid regimes assume $r_1 = r_2 = r_3$, and as such it is equivalent to M98 in those regimes. For the extended regime, the reflectance r_1 is taken to be different from $r_2 = r_3$ because of the separation in frequencies. MH08 found a ratio $r_2/r_1 = 1.22$ from the Surface Emissivities in Polar Regions Polar Experiment (SEPOR/POLEX) aircraft campaign measurements. It is important to note that this value is fixed in their retrieval because it is used in the determination of the constants C_0 and C_1 in Eq. (3.5).

For the PLDC16 retrieval, we assume $r_1 = r_2 = r_3$ in the low regime, r_1 different from $r_2 = r_3$ in the mid regime, and all three reflectances different in the extended regime. Because there are no pre-determined coefficients in our retrieval, we are able to set the reflectance ratios as required. Different assumptions were made for the simulations and measurement retrievals, as will be explained.

3.1.5   *Retrieval performance with simulated measurements*

To test the retrieval techniques, we used the RTTOV 1-D radiative transfer model to simulate brightness temperature measurements, employing operational radiosonde profiles from Barrow, Alaska as inputs. A total of 1490 profiles between December and March for 2008 to 2014 were used. The maximum water vapour column allowed was $15\,\mathrm{kg\,m^{-2}}$.

All simulations assumed nadir satellite measurements, and the surface air and skin temperatures were taken to be equal. The surface reflectance was set to 0.2 for all frequencies

in both the simulations and retrievals. Simulations at different viewing angles show insignificant differences in the retrieval of the water vapour column.
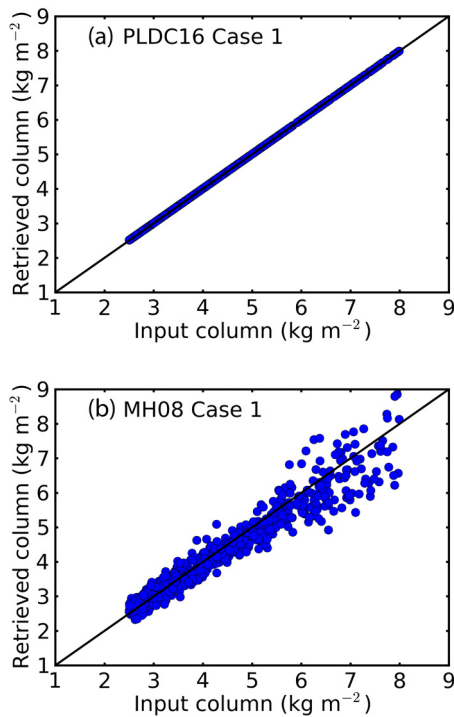
Figure 3.2: Comparisons of mid regime retrievals (excluding overlap) from simulated signals against the input water vapour columns for **(a)** PLDC16 and **(b)** MH08. The simulated signals are noiseless and perfect auxiliary information is provided. The black line represents a perfect retrieval.

RTTOV was used to provide cloud-free brightness temperatures for both the MHS and AMSU-B instruments. We used AMSU-B simulations for MH08's retrieval given that their retrieval coefficients are calibrated for that instrument. MHS simulations were used for our retrieval.

The retrieval techniques were tested against three different cases, with results given in Sects. 3.1.5.1–3.1.5.3:

1. simulated signals with no detector noise and perfect auxiliary information;

2. simulated signals with detector noise and perfect auxiliary information;

3. simulated signals with detector noise and climatological auxiliary information.

In each case we compare the retrieved water vapour columns against the input columns. The simulations are also used in Sect. 3.1.5.5 to evaluate the impacts of our assumptions,

Table 3.3: Root mean square deviation (RMSD) and bias ($\mathrm{kg\,m^{-2}}$) for PLDC16 and MH08 retrievals from simulated signals for the low, mid and extended regimes (excluding overlap). Results from three cases are provided. Case 1 uses noiseless simulated brightness temperatures with perfect auxiliary information. Case 2 uses simulated brightness temperatures with Gaussian noise and perfect auxiliary information. Case 3 uses simulated brightness temperatures with Gaussian noise and a climatological auxiliary profile. Case 3 does not include a column for combined measurements because regime selection requires better auxiliary information.

	Low		Mid		Extended		Combined	
	RMSD	Bias	RMSD	Bias	RMSD	Bias	RMSD	Bias
Case 1								
PLDC16	0.00	0.00	0.00	0.01	0.00	0.07	0.01	0.01
MH08	0.08	0.10	0.35	−0.10	0.57	−0.67	0.67	0.13
Case 2								
PLDC16	0.10	0.00	0.23	0.03	0.34	0.11	0.19	0.02
MH08	0.13	0.10	0.41	−0.07	0.68	−0.63	0.64	0.12
Case 3								
PLDC16	0.13	0.05	0.44	−0.13	0.59	−1.24	n/a	n/a
MH08	0.13	0.10	0.41	−0.07	0.68	−0.63	n/a	n/a

and in Sect. 3.1.6 to evaluate the possibility of applying the MH08 retrieval to MHS measurements. All three cases assume perfect knowledge of the surface reflectance.

3.1.5.1 Case 1

The intrinsic accuracy of each retrieval is tested by using noiseless simulated signals and perfect auxiliary information. Figure 3.2 compares mid regime retrievals (2.5 to $8\,\mathrm{kg\,m^{-2}}$, excluding overlap) to simulated water vapour columns. RMS deviation and bias values are given in Table 3.3. The PLDC16 retrieval has negligible RMS deviations and biases. This is expected given the ideal conditions for the test, with non-zero values arising from the small disagreements between RTTOV and our radiative transfer parameterization. The greater scatter and bias values for MH08 are due to the inherent error in that retrieval's constant coefficients. The reduction of standard error by PLDC16 over MH08 is due entirely to the calculation of bias coefficients. Iterations have an insignificant effect on the retrieval.

Figure 3.3 shows results for the three combined regimes. The MH08 retrieval shows significant bias at the boundary between the low and mid regimes (2.5–$3\,\mathrm{kg\,m^{-2}}$). It can also be seen that the mid regime extends up to approximately $10\,\mathrm{kg\,m^{-2}}$, which is where the extended regime should be used.

Table 3.3 summarizes the low, mid, and extended regime results for both retrievals. Similar to the mid regime, the standard deviation for the PLDC16 low and extended regimes is significantly less than for MH08. There is a positive bias in the extended regime of the PLDC16 retrieval, and this is due again to the small disagreement between RTTOV and our parameterized radiative transfer.
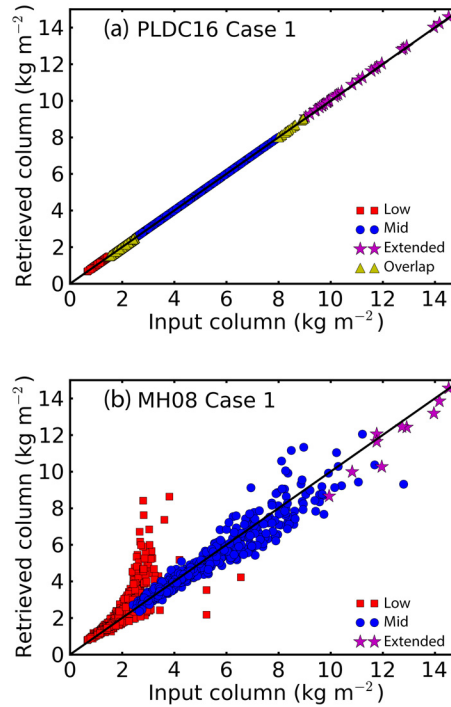
Figure 3.3: Comparisons of combined regime retrievals from simulated signals against the input water vapour columns for **(a)** PLDC16 and **(b)** MH08. The simulated signals are noiseless and perfect auxiliary information is provided. The black line represents a perfect retrieval.

3.1.5.2   Case 2

Gaussian-distributed noise with a standard deviation of $0.5\,\mathrm{K}$ was added to the simulated brightness temperatures for this second case. The value was chosen to be consistent with the noise equivalent differential temperature for the MHS instruments (see Table 3.1). Perfect auxiliary information was provided to the retrievals.

Figure 3.4 compares the PLDC16 and MH08 mid regime retrievals to the input water vapour column. The RMS deviations are increased compared to case 1, but more so for PLDC16 (see Table 3.3). Nevertheless, the RMS deviation for MH08 is 78 % greater than
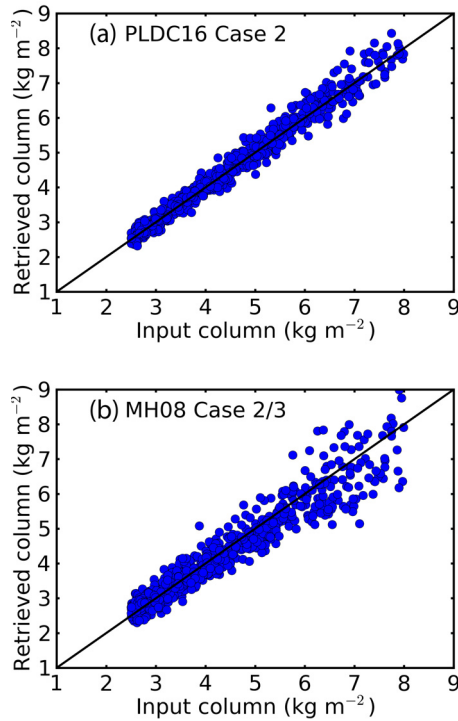
Figure 3.4: Comparisons of mid regime retrievals (excluding overlap) from simulated signals against the input water vapour columns for **(a)** PLDC16 and **(b)** MH08. The simulated brightness temperatures include Gaussian noise with a $0.5\,\text{K}$ standard deviation, and perfect auxiliary information is provided. The black line represents a perfect retrieval.

for PLDC16. The reduction of standard error by PLDC16 over MH08 is due primarily to the calculation of bias coefficients. In the extended regime, however, iterations account for $24\,\%$ of the overall correction.

Table 3.3 summarizes the results for the low, mid, and extended regimes. In each case the PLDC16 retrieval has a smaller standard deviation and bias. PLDC16's RMS deviation is significantly lower for combined regimes, although this is partly due to the improved regime selection of PLDC16. The results indicate that the PLDC16 retrieval is more accurate if there is perfect auxiliary information.

3.1.5.3 Case 3

In the third case climatological auxiliary information is used, which represents severely degraded knowledge of the atmospheric conditions. The climatological water vapour and temperature profiles were obtained by averaging the profiles from all 1490 measurements considered in this study. The noise and MH08 retrievals are the same as for Case 2.
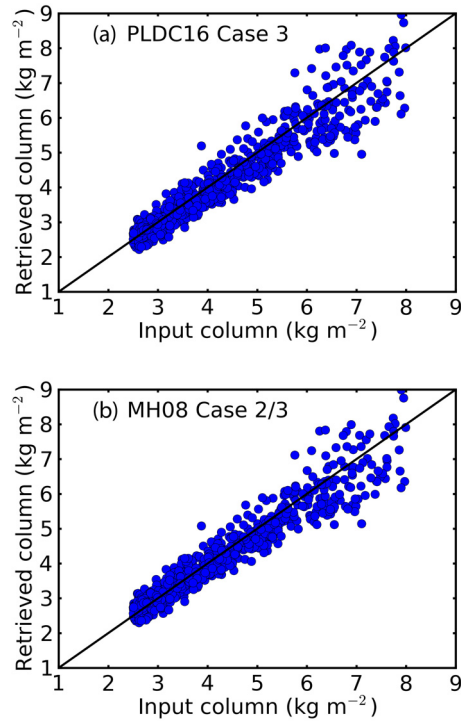
Figure 3.5: Comparison of the mid regime retrieval (excluding overlap) from simulated signals against the input water vapour columns for PLDC16. The simulated brightness temperatures include Gaussian noise with a $0.5\,\mathrm{K}$ standard deviation, and climatological auxiliary information is used. The black line represents a perfect retrieval.

Figure 3.5 compares the PLDC16 retrieval to the input water vapour column for the mid regime. The RMS deviation is $0.21\,\mathrm{kg\,m^{-2}}$ larger than for Case 2, and $0.03\,\mathrm{kg\,m^{-2}}$ larger than for MH08. The low regime results (not shown) are nearly the same. For the extended regime (not shown), PLDC16 performs slightly better in terms of RMS deviation, but has significantly larger bias. The results show that when the auxiliary information is severely degraded, the PLDC16 retrieval can be expected to perform comparably to MH08 for the low and mid regimes.

3.1.5.4 Discussion

Three test cases were given to theoretically evaluate the PLDC16 and MH08 retrievals. Case 1 tests their intrinsic accuracy for noiseless brightness temperatures and perfect auxiliary information. Both retrievals performed as expected, with the PLDC16 retrieval faithfully reproducing the model water vapour data. Case 2 included randomized noise as found in the MHS instruments. Given perfect auxiliary information, the PLDC16 retrieval more

Table 3.4: Root mean square deviation (RMSD) and bias ($\mathrm{kg\,m^{-2}}$) for MH08 retrievals from simulated signals for the low, mid and extended regimes (excluding overlap). The AMSU-B results are the same as in Case 1 from Table 3.3.

	Low		Mid		Extended	
Retrieval	RMSD	Bias	RMSD	Bias	RMSD	Bias
AMSU-B	0.08	0.10	0.35	−0.10	0.57	−0.67
MHS	0.08	0.06	0.37	0.11	0.64	1.96

accurately reproduced the model water vapour. Case 3 employed climatological auxiliary information, which represents a worst-case scenario for PLDC16. The test yielded comparable errors for the two retrievals for the low and mid regimes.

We expect that reanalysis data will always be available to provide auxiliary information. As such, the most realistic retrieval comparison is given by Case 2. Notwithstanding, there are uncertainties in reanalyses (Serreze et al., 2012), spatiotemporal variations in water vapour distribution (Behler et al., 2012; Tobin et al., 2006), and systematic uncertainties which are difficult to treat quantitatively in simulations. Results from testing in real-world conditions are given in Sect. 3.1.7.

3.1.5.5 Assessment of PLDC16 assumptions

Simulations may also be used to assess the impact of two approximations made in the development of the PLDC16 retrieval.

i. The second term of Eq. (3.3), which contains the difference between the surface air and skin temperatures, was ignored.

ii. A constant value for $r = r_i = r_j$ must be assumed in Eq. (3.6) and may be in error.

Case 1 simulations were performed so that we could completely isolate the effects of each item.

To evaluate the impact of (i), we ran simulations with $T_\mathrm{o} - T_\mathrm{s} = \pm 5\,\mathrm{K}$ and $\pm 2\,\mathrm{K}$. Note that although atmospheric reanalyses often disagree on $T_\mathrm{o} - T_\mathrm{s}$, values up to $2\,\mathrm{K}$ are typical for multi-year Arctic sea ice (Melsheimer and Heygster, 2008). As such, the $\pm 5\,\mathrm{K}$ test represents an extreme case.

We found that inclusion of $T_\mathrm{o} - T_\mathrm{s}$ in the simulations caused a bias in the retrieved water vapour columns. The bias was positive for $T_\mathrm{o} - T_\mathrm{s} > 0$ and negative for $T_\mathrm{o} - T_\mathrm{s} < 0$. The

bias varied for each regime in the retrieval. The low regime bias for $T_o - T_s = \pm 5\,\mathrm{K}$ ranged from 3 to 5 % with increasing water vapour column. Similarly the mid regime bias ranged from 3 to 7 % and the extended regime bias ranged from 3 to 4 %. For the more typical case with $T_o - T_s = 2\,\mathrm{K}$, we found a bias in all regimes of less than 3 %.

To assess the impact of (ii), we performed separate simulations using surface reflectance values of 0.05 and 0.35, which represent extremes in the Arctic (Selbach, 2003), for all channels. Assuming $r = 0.12$ in Eq. (3.6) provides the best retrieval. We found that a maximum random error of less than 3 % in the water column was introduced. The error is largest for the low-humidity end of each regime.

3.1.6   Evaluation of MH08 as applied to MHS measurements

The MH08 retrieval was designed for application to AMSU-B measurements. Section 3.1.7, however, applies the MH08 retrieval to MHS measurements instead. The error due to the application of MH08 to MHS can be assessed using the simulations from Case 1.

Table 3.4 shows the results when MH08 is applied to simulated MHS and AMSU-B brightness temperatures for each regime. In the low regime both the RMS deviation and bias are small. The mid regime's bias effectively changes sign and the RMS deviation increases by 6 %. For the extended regime the RMS deviation increases by 12 %, whereas the absolute bias increases by 193 %. We conclude that the MH08 retrieval can be reasonably applied to MHS measurements for the low and mid regimes.

The simulations do not account for the difference in polarization measured by the two instruments. This has an unknown effect on the retrieved columns.

3.1.7   Measurements

This section examines PLDC16 water vapour columns retrieved from MHS overpasses of Barrow, Alaska. The retrievals are compared with simultaneous GVR measurements and a variety of other data sets. Swath data are used to illustrate the spatial distribution of retrieved water vapour columns.
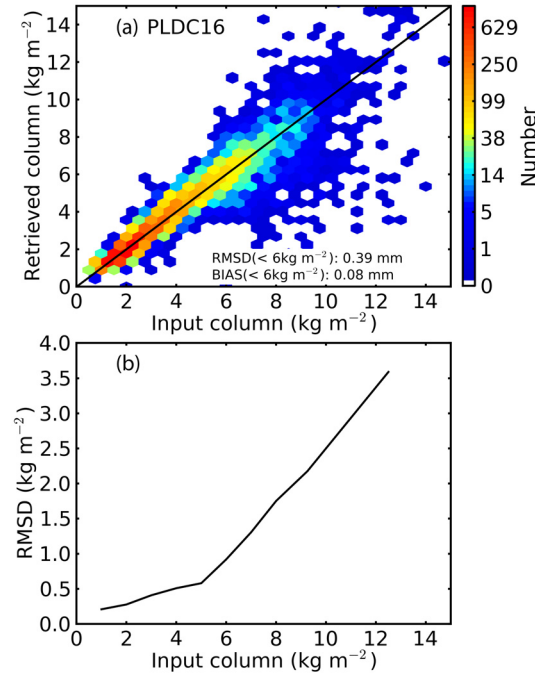
Figure 3.6: **(a)** PLDC16 retrieval of water vapour column from MHS brightness temperatures compared to GVR retrievals at Barrow, Alaska. **(b)** The corresponding root mean square deviations (RMSDs).

3.1.7.1 Assessment of water vapour column using GVR

A total of 11 333 MHS measurements from MetOP-A and NOAA-18 within 50 km of Barrow, Alaska were obtained for the same time period as in Sect. 3.1.5. We retrieved water vapour columns from these data using PLDC16 with the ERA-Interim reanalysis providing auxiliary information. ERA-Interim data have an 80 km resolution in latitude and are provided four times per day.

For the reflectance ratio in the mid regime we chose $r_1/r_2 = 1.12$ from SEPOR/POLEX data which is representative of ice and open water (Selbach, 2003). For the extended regime, we chose $r_1/r_2 = 1.19$ for a mixture of coastal ice and snow-covered land using MACSI aircraft campaign data (Hewison and English, 1999). The second ratio was chosen to be $r_2/r_3 = 1.12$ as these are the same frequencies as r_1/r_2 from the mid regime.

Figure 3.6 shows the results of the PLDC16 retrieval compared to coincident GVR measurements in terms of water vapour column. The GVR obtains four measurements per minute (Pazmany, 2007), and these are averaged over 3 min to reduce noise.

For the full data set the RMS deviation is $0.72\,\mathrm{kg\,m}^{-2}$ and the bias is $0.02\,\mathrm{kg\,m}^{-2}$.

Table 3.5: Water vapour column root mean square deviations (RMSDs) for various data sets against GVR measurements for columns less than $6\,\mathrm{kg\,m^{-2}}$. Values in brackets give the deviations and biases as a fraction of the mean column amount.

Data set/retrieval		Nadir resolution (km)	Samples	RMSD $(\mathrm{kg\,m^{-2}})$	Bias $(\mathrm{kg\,m^{-2}})$
Reanalyses					
NCEP		280	2693	0.79 (29.9%)	−0.04 (−1.6%)
JRA-55		140	2694	0.39 (14.8%)	−0.49 (−18.7%)
ASR ($\leq$ 2012)		30	4047	0.40 (15.6%)	−0.18 (−6.9%)
ERA-Interim		80	2694	0.42 (15.8%)	−0.11 (−4.3%)
Satellite					
AIRS	combined	45	10774	1.03 (38.9%)	−0.34 (−12.8%)
	infrared			1.10 (41.6%)	−0.22 (−8.3%)
	microwave			1.05 (39.6%)	0.11 (4.1%)
MIRS (MHS DJFM 2013/4)		15	1002	0.69 (22.0%)	−0.18 (−5.7%)
MH08 (AMSU-B $\leq$ 2009)		15	4277	0.95 (39.2%)	0.20 (8.1%)
MH08 (MHS)		15	9739	0.71 (27.2%)	0.23 (8.6%)
PLDC16 (MHS)		15	9741	0.39 (14.9%)	0.08 (3.2%)

Note, however, that the error is larger at water vapour columns greater than $6\,\mathrm{kg\,m^{-2}}$. The RMS deviation and bias for GVR-measured columns less than $6\,\mathrm{kg\,m^{-2}}$ are reduced to 0.39 and $0.08\,\mathrm{kg\,m^{-2}}$, respectively. During the dry Arctic winter the water vapour column is typically less than $6\,\mathrm{kg\,m^{-2}}$ (Przybylak, 2015).

Table 3.5 provides a statistical comparison of various water vapour data sets with the GVR, all for GVR-measured columns less than $6\,\mathrm{kg\,m^{-2}}$. Reanalysis data sets include the European Centre for Medium-Range Weather Forecasts (ECMWF) ERA-Interim product (Dee et al., 2011), the National Centers for Environmental Prediction (NCEP; Kalnay et al., 1996) product, the Arctic System Reanalysis (ASR; Bromwich et al., 2010), and the Japanese 55 year Reanalysis (JRA-55; Kobayashi et al., 2015). Satellite products included were the Atmospheric Infrared Sounder (AIRS) Divakarla et al., 2006), Microwave Integrated Retrieval System (MIRS) (Boukabara et al., 2010), MH08 retrieval, and PLDC16 retrieval. AIRS satellite data included three different products: infrared measurements, microwave measurements (using AMSU-A), and combined (infrared and microwave) measurements. MIRS is a data product that uses a one dimensional variational inversion scheme (1D-VAR) in conjunction with satellite measurements from MHS and AMSU sensors to determine atmospheric quantities such as water vapour column. MH08 was applied to both the MHS and AMSU-B instruments and PLDC16 was applied to MHS.

Table 3.5 shows that the RMS deviation and bias for PLDC16 MHS retrievals is smaller than for the other satellite data products. The MH08 retrievals from MHS measurements

also have smaller RMS deviations than most of the other satellite data products. The comparison between the PLDC16 and MH08 results is consistent with our conclusions from Sect. 3.1.5.

The PLDC16 retrieval has similar RMS deviations to the ASR, ERA-Interim, and JRA-55 reanalyses; NCEP, on the other hand, has RMS deviations that are twice as large. The JRA-55 bias is significantly larger than every other reanalysis and satellite product in this comparison. The biases are negative for each of the reanalyses ranging from -0.04 to $-0.49\,\mathrm{kg\,m^{-2}}$. The excellent performance of the reanalyses is not surprising given that they incorporate data from radiosonde launches at Barrow. It is unclear how the measurements and analyses compare away from the radiosonde anchor points, and this is the subject of ongoing study.

3.1.7.2 *Spatial distributions of water vapour column*

As an example of how PLDC16 can be applied to swath data, Fig. 3.7a shows the retrieval for the NOAA-18 MHS measurement from 31 January 2008. The area chosen is centred over the Chukchi Sea north of Alaska. The ERA-Interim reanalysis was used to provide auxiliary information, and the reflectance ratios from Sect. 3.1.7.1 were used for simplicity. A detailed analysis of the Arctic-wide, reflectance-dependent PLDC16 retrieval is left for future work.

The plot shows individual footprints which vary in size due to the MHS's viewing angle. For comparison, Fig. 3.7b shows the equivalent ASR water vapour column for the same period. The ASR resolution is 30 km in latitude. The comparison reveals PLDC16 applied to MHS data has the finer intrinsic resolution. The ASR reanalysis tends to smooth out fine details in the water vapour column.

3.1.7.3 *Uncertainties*

The PLDC16 errors in the measurements of Sect. 3.1.7 were greater than were obtained for the simulations in Sect. 3.1.5. This is not unexpected. Sources of error that exist in measurements that are not simulated include:

   i. differences in the scene viewed by GVR and MHS;

  ii. uncertainties in the reflectance ratio terms in the mid and extended regimes;
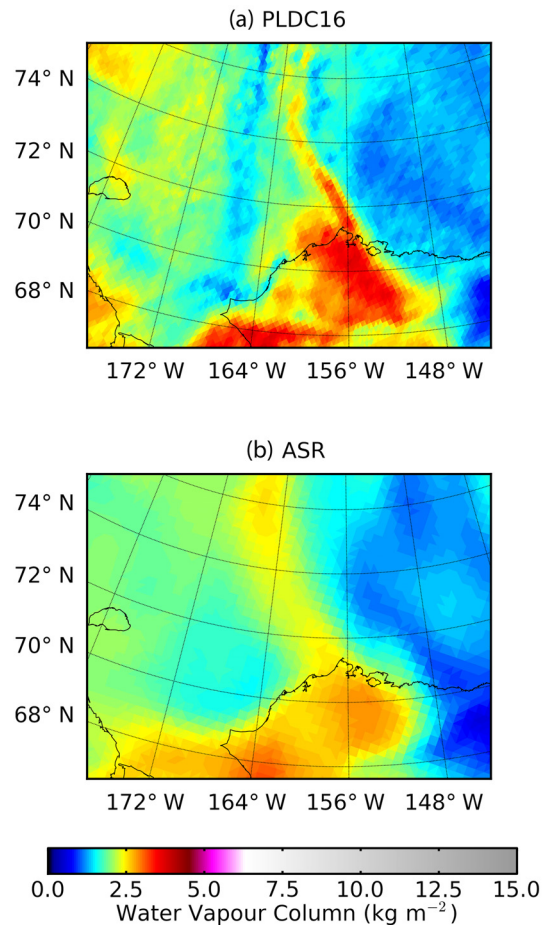
Figure 3.7: The spatial distribution of water vapour column centred over the Chukchi Sea north of Barrow, Alaska: **(a)** the PLDC16 retrieval from NOAA-18 MHS brightness temperature measurements on 31 January 2008 at 23:09 UTC; and **(b)** the Arctic System Reanalysis (ASR) product for 1 February 2008 at 00:00 UTC.

iii. uncertainties in the auxiliary temperature profile (Serreze et al., 2012);

iv. optically thick ice crystal and liquid water clouds;

v. removal of the second term in Eq. (3.3);

vi. changes with time in MHS noise;

vii. polarization in the MHS measurements for different frequencies;

viii. uncertainties in the GVR measurements;

ix. the assumption of a purely specular reflecting surface.

Table 3.6: Water vapour column root mean square deviations (RMSDs) for PLDC16 retrievals using different auxiliary data sets against GVR measurements for columns less than $6\,\mathrm{kg\,m^{-2}}$.

Auxiliary	RMSD $(< 6\,\mathrm{kg\,m^{-2}})$	Bias $(< 6\,\mathrm{kg\,m^{-2}})$
AIRS Combined	0.41	−0.02
NCEP	0.52	0.20
JRA-55	0.44	0.16
ASR (≤ 2012)	0.46	0.08
ERA-Interim	0.39	0.08
ERA-Interim (monthly mean)	0.46	0.09

The error in (i) arises from the GVR being a stationary zenith-pointing instrument, while the satellite-borne MHS has varying downward-pointing viewing angles. The criteria for an overpass match in Sect. 3.1.7 allows the centre of the MHS footprint to be up to 50 km from Barrow, Alaska. Any geophysical variation in the water vapour field can be expected to result in differences between the two measurements. The viewing geometry error can potentially be larger than the random error from either instrument. Behler et al. (2012) estimated the error to vary from 0.66 to $1.05\,\mathrm{kg\,m^{-2}}$ for the AMSU-B's largest footprints. The impact of elevation differences at Barrow for the various data products were tested using the Case 3 simulations. The terrain around Barrow ranges from heights of 7 to 20 m with small amounts of vegetation. Our calculations indicate differences in water vapour columns of less than 1 % owing to elevation variations.

The error in (ii) depends on the regime and frequencies selected. SEPOR/POLEX data show a high correlation for the 157 and 183 GHz surface emissivity measurements over different sea ice types. The high correlation corresponds to a small range of 0.96 to 1.13 for the reflectance ratio (r_1/r_2 for mid, r_2/r_3 for extended) over different types of sea ice and water surfaces. The 89 and 157 GHz surface emissivity measurements have very little correlation and produce a large range of 0.56 to 1.26 for the reflectance ratio (r_1/r_2 for extended regime). The range of r_1/r_2 for the mid regime term translates to a variation in the water vapour column of 25 %. Similarly, in the extended regime, the range of r_2/r_3 results in a variation of 2 %, and the large range of r_1/r_2 yields a variation of 143 %.

For (iii), Table 3.6 provides RMS deviations from GVR measurements for the PLDC16 retrieval using different reanalyses for the auxiliary information. Only GVR water vapour columns of less than $6\,\mathrm{kg\,m^{-2}}$ were considered. The results from Table 3.6 show the RMS

deviation varies only slightly depending on the data set used to provide auxiliary information. The ERA-Interim auxiliary information provides the smallest RMS deviation while the NCEP auxiliary information gives the largest. Even the ERA-Interim monthly mean profile provides a good retrieval, indicating that the monthly mean provides a reasonable representation of the profile shape. Note, however, that the daily ERA-Interim reanalysis was still used for the regime selection.

For (iv), MHS measurements at Barrow were separated into cases with liquid water clouds, ice clouds, and clear skies by using micro pulse lidar (MPL) backscatter and depolarization data. The PLDC16 retrieval was applied to each set of measurements and then compared to radiosonde measurements that came within $1\,h$ of the MHS measurements. Radiosonde measurements were used because the GVR and MHS might observe similar effects given that they are both microwave instruments. The liquid water and ice cloud cases had increases in the RMS deviation of 0.06 and $0.05\,kg\,m^{-2}$, respectively, when compared to the clear sky cases. The bias did not change significantly between the three cases. This indicates that clouds do not present a large source of error in the retrieval.

For (v), the removal of the second term in the retrieval equation typically translates to a change of $3\,\%$ in water vapour column (as discussed in Sect. 3.1.5.5). The error of the GVR measurements in (viii) is $\pm 5\,\%$. Other sources of error are difficult to quantify.

3.1.8 Conclusions

A new retrieval based on the microwave formulation developed by Miao et al. (2001) was introduced. Simulations show that the new technique reduces errors compared to earlier approaches when good auxiliary information for the atmospheric conditions is used. In a comparison with ground-truth measurements, the new PLDC16 retrieval provides more accurate water vapour columns than other satellite measurements.

Maps of water vapour can be created that reveal fine structure that reanalyses do not discern. Pan-Arctic water vapour charts can be created twice per day using the combination of overpasses from NOAA-18 and MetOP-A alone. Temporal resolution may be further improved by including additional instruments. Given historical satellite data sets and planned launches, microwave water vapour measurements may provide new insights into changing Arctic conditions. Complications arising from varying microwave surface emissivity were not treated in this paper, which only examines the retrieval at a single location. A follow-on

paper that applies the retrieval in a pan-Arctic context will explore this important topic.

3.2   Appendix

The following section describes issues in the development of PLDC16 and some topics that were not fully described the previous sections, as described at the beginning of Chapter 3.

3.2.1   Least Square Retrieval

Previous to the PLDC16 retrieval, another method was used in an attempt to improve the MH08 water vapour retrieval using MHS measurements known as the Least Square Regression (LSR) retrieval. LSR used a variation of the MH08 technique. An extra term was included in the series expansion of Eq. 3.4, giving

$$C_0 + C_1 W \sec \theta + C_2 (W sec \theta)^2 = \log \left(\frac{\Delta T_{12} - b_{12}}{\Delta T_{23} - b_{23}} \right). \tag{3.11}$$

Similarly, the series expansion for Eq. 3.5 gives

$$C_0 + C_1 W \sec \theta + C_2 (W sec \theta)^2 = \log \left[\frac{r_2}{r_1} \left(\frac{\Delta T_{12} - b_{12}}{\Delta T_{23} - b_{23}} + C \right) - C \right] \tag{3.12}$$

The coefficients b_{12}, b_{23}, C_0, C_1, and C_2 were determined using a least square regression with MHS brightness temperature measurements using the GVR water vapour column as the ground truth. Note, the coefficients were constant in the LSR retrieval, therefore, no auxiliary information was provided, which is also why this technique was initially pursued. As in Melsheimer and Heygster (2008), C was taken to be 1.1 and r_2/r_1 to be 1.22. A separate calibration was required for each frequency triplet v_1, v_2, v_3.

Table 3.7: MHS frequencies for the low-mid and extended regimes for the LSR retrieval of water vapour column with typical water vapour column ranges.

Regime	Frequencies (GHz) (MHS)			W Range ($kg \, m^{-2}$)
	v_1	v_2	v_3	
Low-Mid	157	190.311	183.311 ± 3	0–8
Extended	89	157	190.311	8–15

The LSR retrieval employed two regimes, a low-mid regime and extended regime. The low-mid regime used the mid regime frequencies of M98 and MH08 and the extended

regime frequencies were the same as MH08 as summarized in Table 3.7. The regime selection for MH08 was used for the LSR retrieval. Preliminary LSR results showed similar results in terms of RMS deviation whether the low regime or the mid regime frequency triplet were used for the smallest water vapour columns at Barrow, Alaska. Removing the low regime frequency triplet simplified the regime selection and removed any bias induced due to the selection process in MH08 as discussed in Sect. 3.1.4.

Table 3.8: Calibration coefficients for the low-mid regime of the LSR retrieval and the mid regime for the MH08 retrieval at nadir.

Technique	C_0	C_1	C_2	b_{12}	b_{23}
LSR (low-mid)	0.01	0.37	-0.02	27.29	11.12
MH08 (mid-nadir)	1.62	2.45	n/a	5.99	6.55

Table 3.8 displays the calibration coefficients that were found for the low-mid regime. Extended regime coefficients were not determined. For comparison, the MH08 calibration coefficients are displayed for the mid regime at nadir. The LSR coefficients are considerably different than those for MH08. The reason for this will be discussed later in this section.
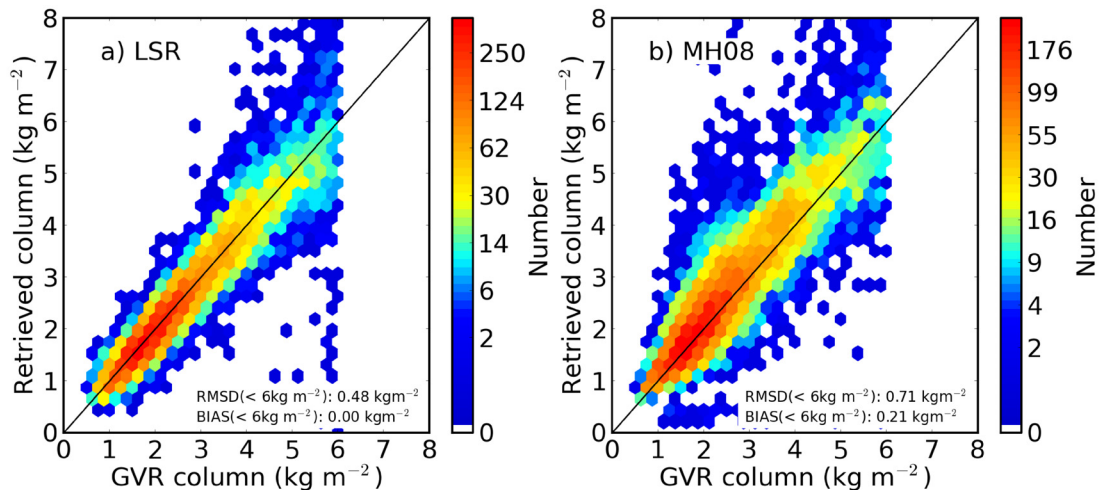
Figure 3.8: Comparison of water vapour column retrievals with GVR measurements less than $6\,\mathrm{kg\,m^{-2}}$ slant water vapour column for a) LSR and b) MH08.

Figure 3.8 shows the LSR and MH08 retrievals compared to GVR water vapour measurements for GVR water vapour column less than $6\,\mathrm{kg\,m^{-2}}$. The LSR retrieval had a smaller RMS deviation and bias compared to the MH08 retrieval. This suggested the LSR technique had promise.

Table 3.9: RMS deviation and bias of LSR and MH08 retrievals for different water vapour column ranges.

W range ($\mathrm{kg\,m^{-2}}$)	Technique	SD ($\mathrm{kg\,m^{-2}}$)	Bias ($\mathrm{kg\,m^{-2}}$)
0 - 1.5	LSR	0.23	0.03
	MH08 (low)	0.37	0.20
2.5 - 6	LSR	0.57	0.00
	MH08 (mid)	0.69	0.23
0 - 6	LSR	0.48	0.00
	MH08	0.71	0.21

Table 3.9 includes the RMS deviation and bias of the LSR and MH08 low regime for water vapour columns less than 1.5 $\mathrm{kg\,m^{-2}}$ and the LSR and MH08 mid regime for water vapour columns greater than 2.5 $\mathrm{kg\,m^{-2}}$ and less than 6 $\mathrm{kg\,m^{-2}}$. The difference in RMS deviation between MH08 and LSR is smaller when comparing the 2.5 $\mathrm{kg\,m^{-2}}$ to 6 $\mathrm{kg\,m^{-2}}$ range of water vapour column to the 0 $\mathrm{kg\,m^{-2}}$ to 1.5 $\mathrm{kg\,m^{-2}}$ and 0 $\mathrm{kg\,m^{-2}}$ to 6 $\mathrm{kg\,m^{-2}}$ ranges. This is due to the MH08 retrieval selection process. The bias was smaller for LSR due to the fact that it was calibrated with GVR measurements and because MH08 calibration coefficients were created for the AMSU-B instrument as discussed in Sect. 3.1.6.
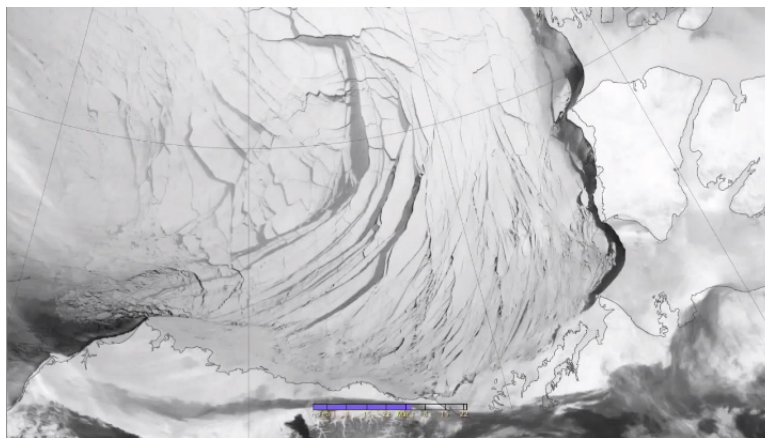
Figure 3.9: Map of AVHRR raw 11.5-12.5 μm measurements on March 2, 2013 North of Barrow Alaska.

An issue with the LSR retrieval was discovered when maps of water vapour column were produced. Figure 3.9 shows raw 11.5-12.5 μm measurements from the AVHRR satellite instrument on March 2, 2013. The AVHRR measurement show distinct leads in the ice during this time period. Figure 3.10 shows the MH08 retrieval and LSR retrieval for the
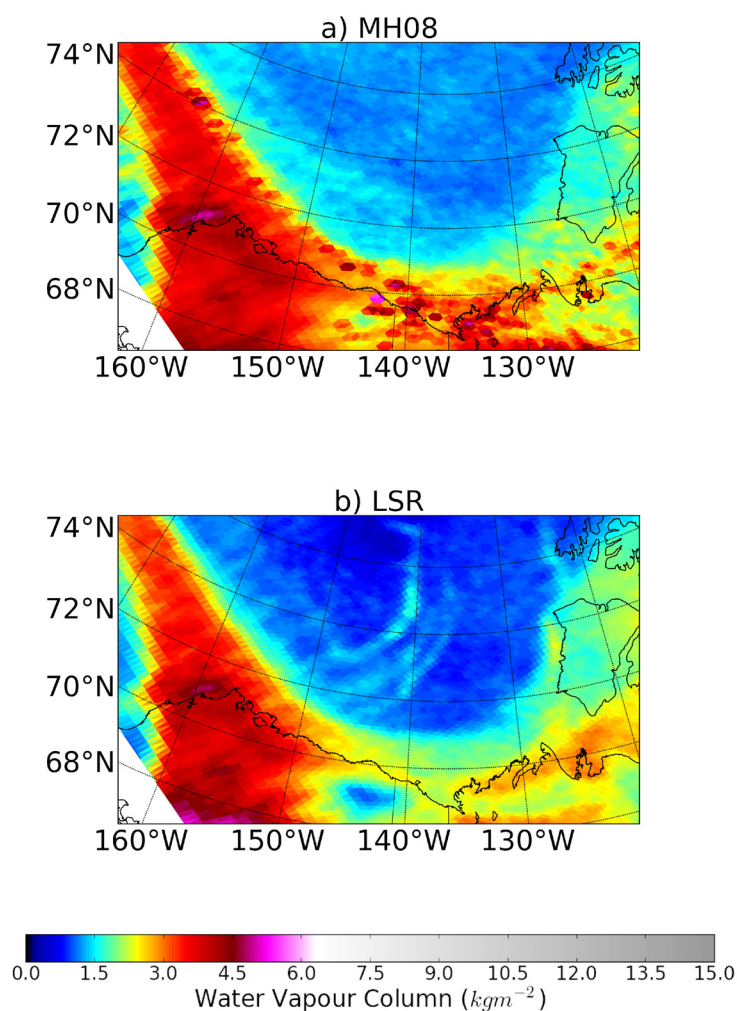
Figure 3.10: Maps of water vapour column using the MH08 and LSR retrievals on March 2, 2013 North of Barrow Alaska.

same date and location. The LSR retrieval also showed an increase in water vapour corresponding to the location of the lead. But, MH08 showed no change in the water vapour column over that region. As will be shown, the enhanced water vapour column for LSR is an artifact owing to differing surface emissivity over the leads.

To test for an artifact owing to variations in surface emissivity, simulations were produced using the same assumptions and radiosonde measurements from Sect. 4.3 except with surface emissivity varied. Simulations were produced for a series of surface emissivities ranging from 0.5 to 0.99. The PLDC16 retrieval used climatological profiles as in Sect. 3.1.5.3 for the purpose of evaluating the worst case scenario. The results are shown in Fig.
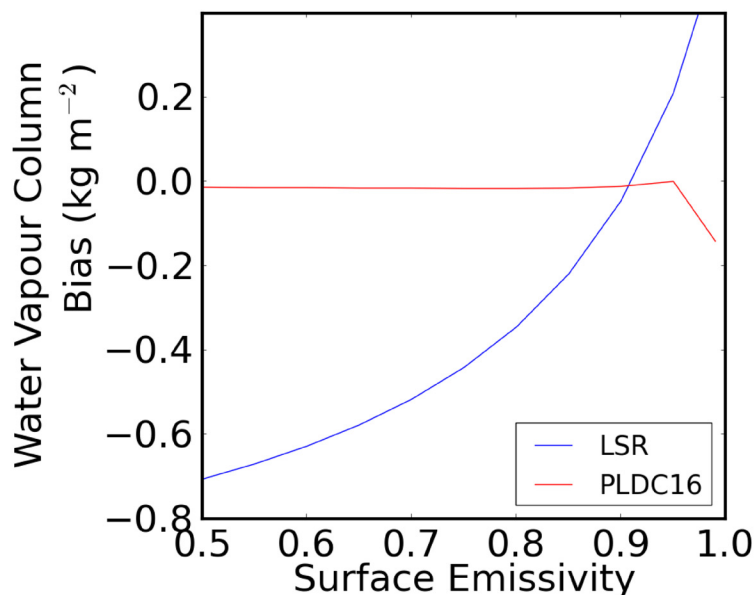
Figure 3.11: Water vapour bias of LSR and PLDC16 retrievals with respect to model input compared to surface emissivity for simulated brightness temperatures derived from radiosonde measurements at Barrow, Alaska.

3.11. The results show a large variation in the bias of the water vapour column retrieved using the LSR while the PLDC16 retrieval shows very little change in the bias except at the largest surface emissivities. Younger ice, which is likely beginning to form over leads, typically has large surface emissivities in comparison with other types of sea ice (Hewison and English, 1999). The positive bias seen in Fig. 3.10 corresponds with the positive bias of the LSR retrieval for large surface emissivities Fig. 3.11.

From simulations in Sect. 4.3, b_{12} ranges from -1.82K to 2.57K and b_{23} ranges from -2K to 6.12K for the low-mid regime. Comparing to the LSR coefficients from Table 3.8 shows significantly larger LSR coefficients when compared to the calculated bias coefficients. The least square regression did not account for the physical meaning of the calibration coefficients, and produced unphysical values. MH08 did not have these problems owing to more physical coefficients.

The results from the LSR technique showed that carefully treating coefficients was important for minimizing water vapour column variations with surface emissivity. This was not possible with the LSR technique given the single calibration point and led to the PLDC16 retrieval.

3.2.2   Cloud Contamination

Clouds can have a significant effect on satellite atmospheric measurements. The visible and infrared spectra are especially affected while the microwave spectra not as strongly. In most cases, clouds are opaque in visible and infrared measurements making it impossible to sample the entire atmospheric column, resulting in large uncertainties and biases. While this is not the case for the microwave region, they may still induce errors in the measurements. Their impact is evaluated in this section

Clouds cover approximately 50% of the Arctic at any time during the winter season (Curry et al., 1996). They can be classified as two types for the purpose of this work: ice clouds and supercooled thin water clouds.

Section 3.1.7.3 briefly described the effect of clouds on MHS measurements. This section more fully explains the analysis.

To determine the effect of clouds on the PLDC16 retrieval, micropulse lidar (Spinhirne, 1993) measurements at Barrow, Alaska, were used to classify MHS overpasses from MetOP-A as cases that are a) cloud-free, b) contain ice water clouds, c) contain liquid water clouds (with or without ice precipitation), or d) unclassified cloud cases. Cases of unclassified clouds arose from total lidar signal attenuation before a cloud was completely sampled. The MHS overpasses chosen were the same as Sect. 3.1.7 during which the MPL was operating continuously. The MPL transmits and receives at 532 nm measuring backscatter (MHz) and depolarization ratio (%).

Table 3.10: MPL measurement visual cloud classification

Atmospheric Condition	Altitude Corrected Backscatter	Depolarization Ratio
Cloud-free	small	small
Ice Cloud	large	large
Water Cloud	large	small

Figure 3.12 shows an example of an MPL measurement with a portion containing a period of cloud-free measurements, containing ice cloud measurements, and containing liquid water cloud measurements. Table 3.10 summarizes the method of classifying each case. Cloud-free cases only have aerosol and molecular backscatter giving a relatively smaller backscatter when compared to larger backscatter from ice or water clouds. Water clouds have small depolarization ratios due to the spherical structure of the water droplet while ice crystals have large depolarization ratios owing to a highly complex structure.
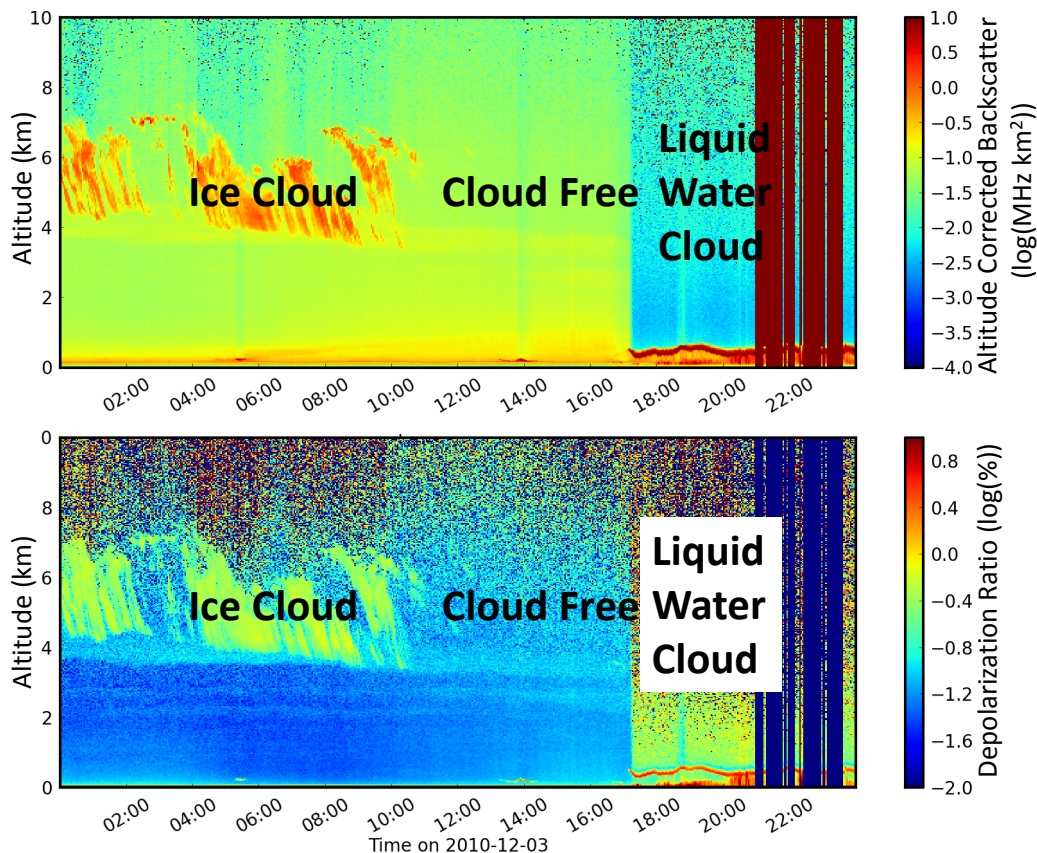
Figure 3.12: MPL measurements on 2010-12-03 with ice clouds upto 10:00 UTC, cloud-free from 10:00 UTC to 17:00 UTC and a ice precipitating water cloud from 17:00 UTC to 23:59 UTC. The altitude corrected backscatter (MHz km^2) is shown in the top plot and depolarization ratio (%) is shown in the bottom.

From 00:00 UTC to 10:00 UTC an ice cloud between 4 km and 7 km is shown with large backscatter and depolarization ratio. The cloud-free portion of the measurement occurs between 10:00 UTC and 17:00 UTC with relatively small backscatter and depolarization ratio. The liquid water cloud begins at 17:00 UTC and was approximately between 0.5 km and 0.7 km having a large backscatter and small depolarization ratio. The bottom of the cloud had a large depolarization ratio due to the liquid water cloud precipitating ice.

The PLDC16 retrieval was applied to each set of MHS overpasses and compared with operational radiosonde measurements of water vapour column from Barrow. Radiosonde measurements were used instead of GVR measurements to isolate the effects of clouds. The GVR and MHS would suffer from the same cloud absorption and scattering as they operate at similar frequencies. MHS measurements were only chosen for the comparison if they were within 1 hour of the radiosonde launch time. This reduced the number of
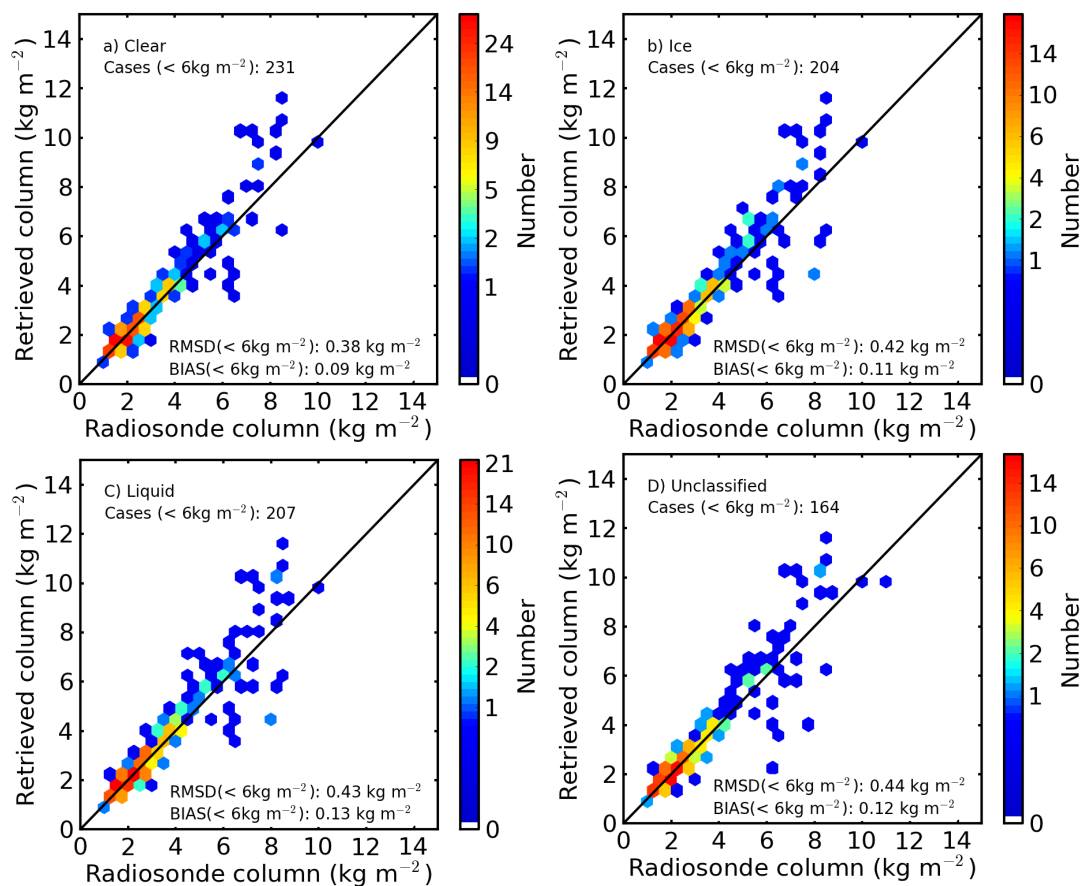
Figure 3.13: PLDC16 retrieval compared to radiosonde measurements with MHS overpasses no further than 1 hour from the radiosonde launch for A) cloud-free cases, B) purely ice cloud cases, C) liquid water cloud cases, and D) unclassified cloud cases.

measurements to approximately 250 for each cloud classification.

The comparisons of the PLDC16 retrieval with radiosonde measurements of water vapour column are shown in Fig. 3.13. The RMS deviation was 0.04 $kg\,m^{-2}$ larger for ice water clouds and 0.05 $kg\,m^{-2}$ for liquid water clouds compared to the cloud-free cases. The difference in the bias between cloud-free and ice cloud cases was 0.02 $kg\,m^{-2}$ and the difference was 0.04 $kg\,m^{-2}$ between cloud-free and liquid cloud cases. Unclassified cloud cases had a RMS deviation and bias 0.06 $kg\,m^{-2}$ and 0.03 $kg\,m^{-2}$ larger than cloud-free cases respectively.

Unclassified cases had the largest RMS deviation since the clouds were mostly optically thick in these cases. This is also why the RMS deviations are 0.01 $kg\,m^{-2}$ smaller than in Sect. 3.1.7.3 since the unclassified values were either considered ice or liquid water clouds in that section. However, the bias for liquid water clouds was largest while the unclassified

cases were $0.01\ \mathrm{kg\,m^{-2}}$ smaller. The influence of clouds on the RMS deviation and bias could be due to other cloud parameters besides optical depth, such as cloud height, cloud particle size, and cloud type.

The PLDC16 retrieval displayed a small increase in the RMS deviation and bias when compared to radiosonde measurements. The results show there was no need to remove or mask MHS measurements with clouds in the PLDC16 retrieval.

3.2.3   Satellite Dependencies
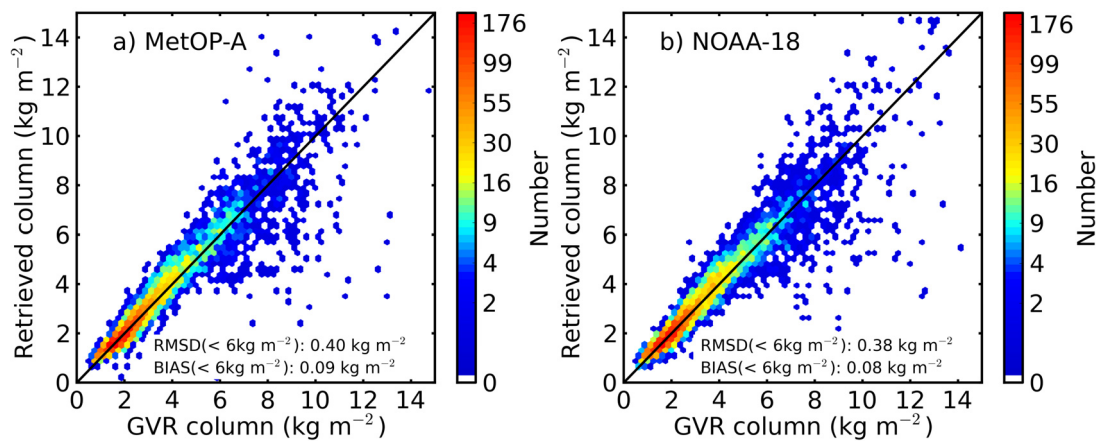
Figure 3.14: PLDC16 retrieval compared to GVR measurements for MHS overpasses at Barrow, Alaska, for A) MetOP-A and B) NOAA-18.

For the comparison of MHS overpass measurements with GVR measurements at Barrow, Alaska, two satellites were used: MetOP-A and NOAA-18. The PLDC16 retrieval was applied to each satellite and compared to the GVR water vapour column in Fig. 3.14 in order to identify differences. The RMS deviation and bias between the two instruments differed by only $0.02\ \mathrm{kg\,m^{-2}}$ and $0.01\ \mathrm{kg\,m^{-2}}$ respectively. This difference is considered negligible.

3.2.4   Evaulation of approximations in PLDC16

Two approximations were introduced into the PLDC16 retrieval. First was the removal of the second term in Eq. 3.3. Second was the assumption of a constant reflectance value in Eq. 3.6. The following sections will describe why each approximation was applied and the associated uncertainties.

3.2.4.1   Second Bias Term
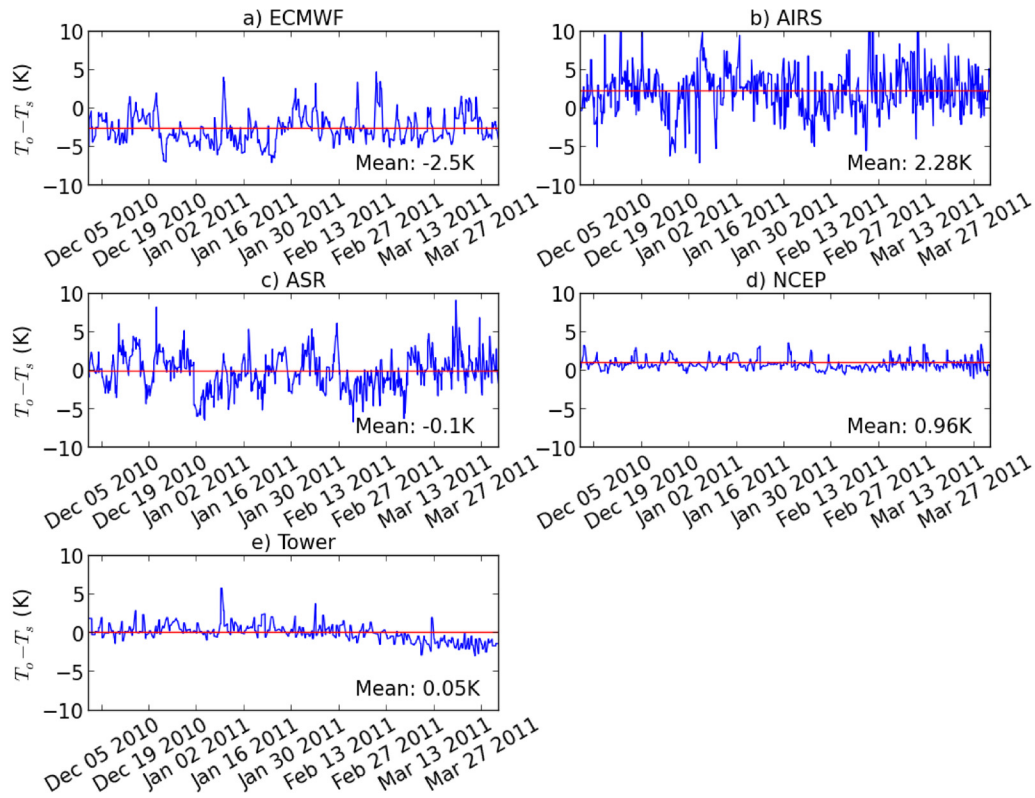
Figure 3.15: $T_0 - T_s$ values in K for the winter 2011 season using a) ERA-interim, b) AIRS, c) ASR, d) NCEP, and e) Tower measurements. Note: JRA-55 is not included due to skin temperatures being produced only for land surfaces with the Barrow pixel being coastal.

The neglected second term is,

$$(T_{\mathrm{o}} - T_{\mathrm{s}}) \left(\varepsilon_j e^{-\tau_j \sec \theta} - \varepsilon_i e^{-\tau_i \sec \theta} \right). \tag{3.13}$$

Later in this section, it is shown that the influence of this term on water vapour column is small and can be safely ignored. The factor $T_0 - T_s$ is difficult to evaluate. The auxiliary data sets from Sect. 3.1.7.3 did not correlate or agree with one another. Figure 3.15 shows $T_0 - T_s$ for ERA-interim, ASR, JRA-55, NCEP, AIRS, and flux tower measurements during the winter 2011 season at Barrow, Alaska. Each data set shows a different magnitude and variation in the structure. This was confirmed in Fig. 3.16 where correlation plots for each data set were produced and showed little correlation with other data sets.
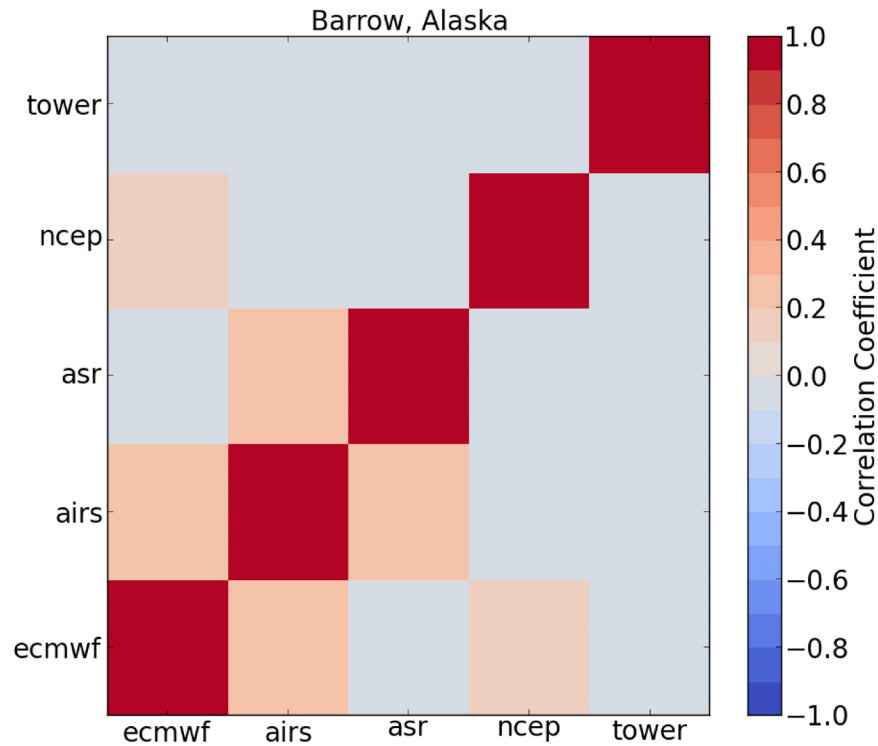
Figure 3.16: Correlation plots of ERA-interim, ASR, JRA, NCEP, AIRS, and tower measurements of $T_0 - T_s$ in units of K. Note: JRA-55 is not included due to skin temperatures being produced only for land surfaces with the Barrow pixel being coastal.

To confirm the results are not exclusive at Barrow, Alaska, pan-Arctic maps of $T_0 - T_s$ were produced for each of the reanalyses as shown in Fig. 3.17. The land and sea ice regions showed significant variations in the structure, magnitude, and sign of $T_0 - T_s$ between each reanalysis. Agreement was only seen over open sea-water. Due to the disagreement between the reanalyses, it was deemed necessary to remove this term from Eq. 3.3 for the PLDC16 retrieval.

To evaluate the effect of the removal of the second bias term on the PLDC16 retrieval, simulated brightness temperatures from Sect. 3.1.5.1 were modified to vary $T_0 - T_s$. Typically, $T_0 - T_s$ is not larger than $2K$ for multi-year sea ice (Melsheimer and Heygster, 2008). For the simulations, values of $\pm 2K$ and $\pm 5K$ were simulated to represent the typical and extreme temperature differences in the Arctic. The simulated brightness temperatures were applied to the PLDC16 retrieval with the results are shown in Fig. 3.18.

A bias in the PLDC16 retrieval was induced for $T_0 - T_s \neq 0$. The results from Fig 3.18
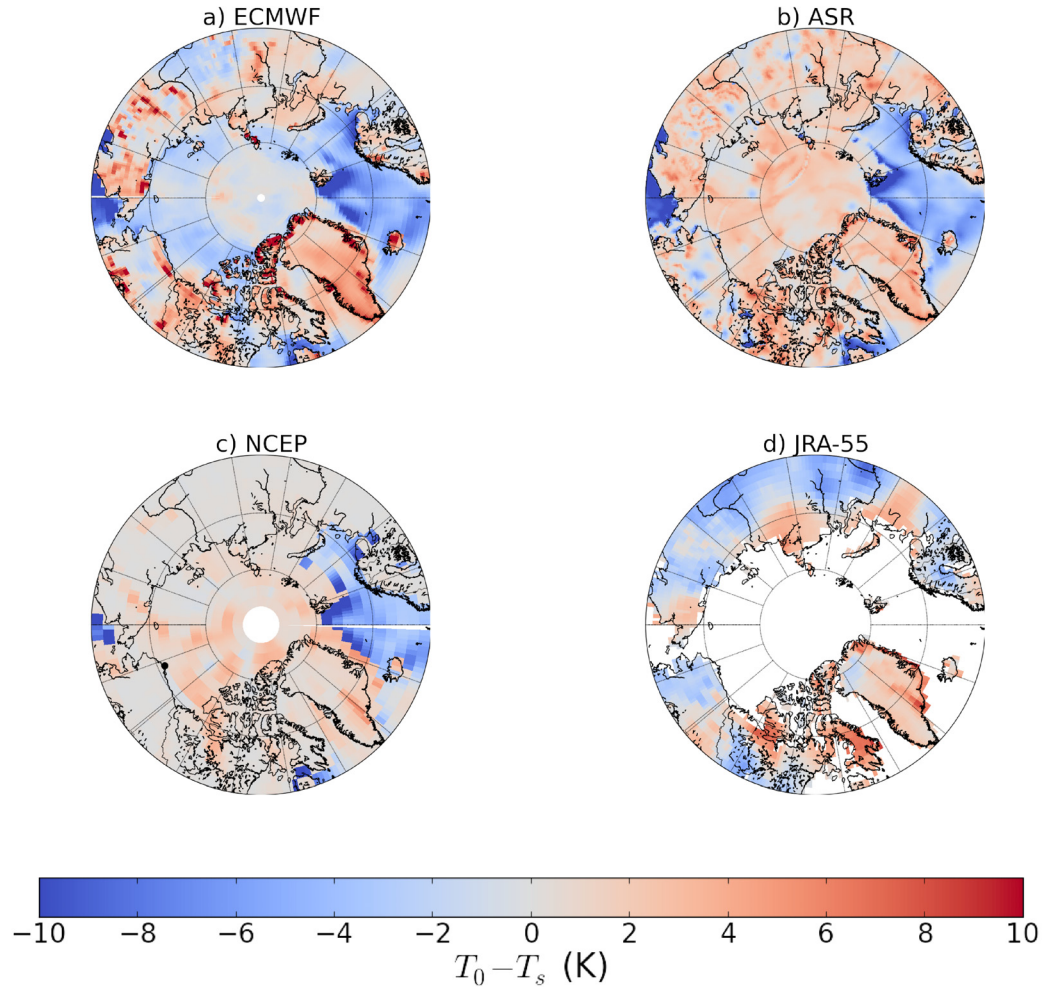
Figure 3.17: Pan-Arctic maps of $T_0 - T_s$ using a) ERA-interim, b) ASR, c) NCEP, and d) JRA reanalyses. Note: JRA-55 reanalyses only produce surface skin temperature over land surfaces.

show the relative change in water vapour column for the typical case of $T_0 - T_s = 2K$ and the extreme case of $T_0 - T_s = 5K$. The change in water vapour column was smallest at the beginning of each regime and grew with increasing water vapour column. The water vapour column change was no larger than 7% for the extreme $5K$ case and 3% for the typical $2K$ case. The corresponding $T_0 - T_s < 0$ results were equal in magnitude. Therefore, it is reasonable to remove the second bias term from Eq. 3.3 until better skin temperature measurements can be determined.
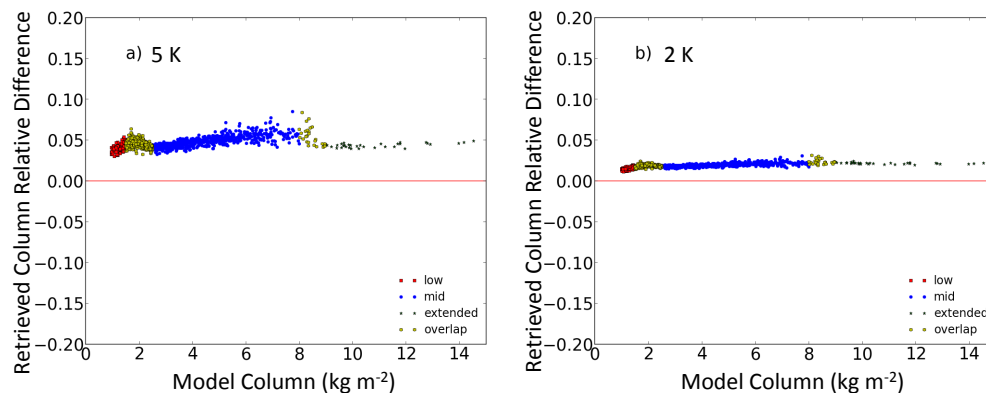
Figure 3.18: Relative change in water vapour column without the second bias term when the difference between the surface air and skin temperature is A) *5K* and B) *2K*.

3.2.4.2   Reflectance Term in Bias Equation

Eq. 3.6 contains a single term with the surface reflectance, r. A constant value for r can be chosen without appreciably increasing error. This section will describe the process of approximating the best value for r.

To determine an optimal value for r, simulated brightness temperatures from Sect. 3.1.5.1 were modified to have surface reflectances of 0.05 and 0.35. Those values represent the extremes for the range of surface reflectances in the Arctic (Selbach, 2003). For each extreme, the PLDC16 retrieval was applied to the resulting simulated brightness temperatures while varying r in Eq. 3.6.
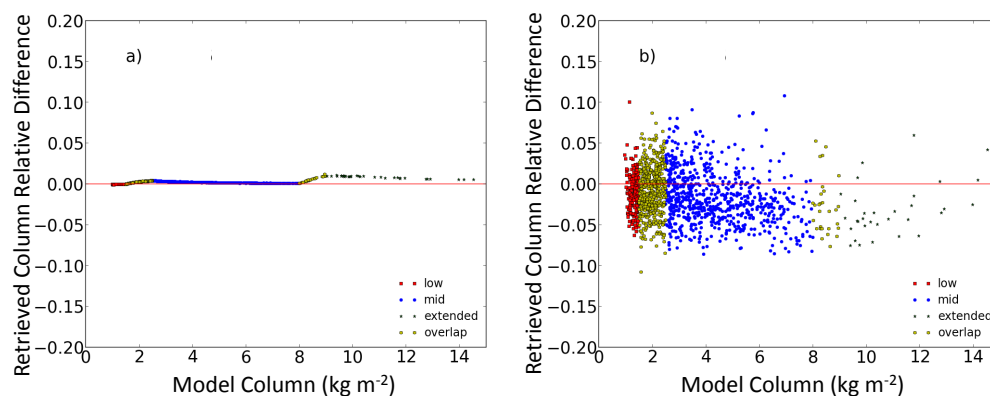
Figure 3.19: Relative change in water vapour column assuming r in Eq. 3.6 is 0.35 for modeled brightness temperatures with surface reflectances of a) 0.35 and b) 0.05.

It was important to choose a value of r that produced minimum errors for each extreme value of surface reflectance. Figure 3.19 shows the results for when a value of 0.35 was

assumed for *r* for each set of simulated brightness temperatures. The random error was insignificant for the case where the simulated reflectance was equal to the reflectance in the PLDC16 retrieval. A small bias was shown in the extended regime which is due to differences between RTTOV and the parameterized radiative transfer in the PLDC16 retrieval as discussed in Sect. 3.1.5.1. However, the random error induced in the PLDC16 retrieval for simulated brightness temperatures at the other extreme was up to 10%.
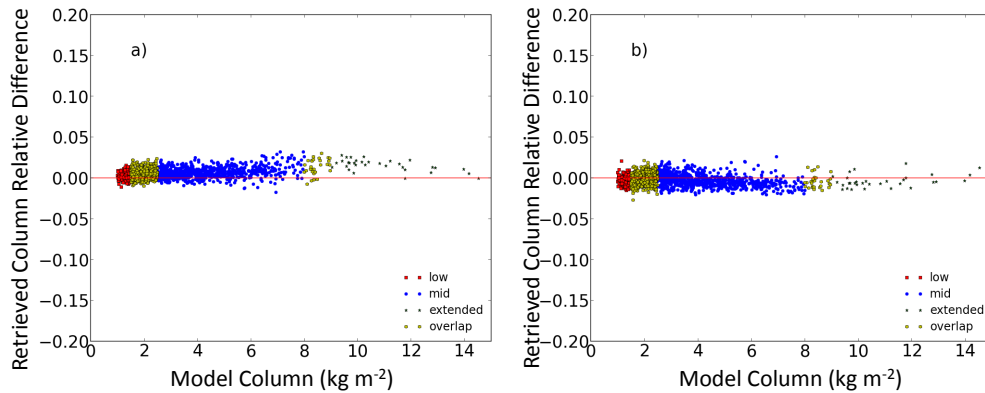
Figure 3.20: Relative change in water vapour column assuming *r* in Eq. 3.6 is 0.12 for modeled brightness temperatures with surface reflectances of a) 0.35 and b) 0.05.

The value of *r* that minimized the random error for each extreme was 0.12. Figure 3.20 shows the relative difference in water vapour column between the PLDC16 retrieval and simulations. The error induced at each extreme was no more than 3%. The value of 0.12 for *r* was applied to all current and future PLDC16 retrievals.

3.3 Summary

A new water vapour retrieval technique for microwave satellite measurements was created, building upon two previous techniques, M98 and MH08. The first iteration of a new retrieval, LSR, used a least squares regression to calibrate MHS measurements with a ground truth of water vapour column. However, it was not independent of surface emissivity. This led to the PLDC16 retrieval which used auxiliary estimates for temperature and water vapour profile shape.

The PLDC16 retrieval was evaluated using simulated and real brightness temperatures from the MHS instrument on board the MetOP-A and NOAA-18 satellites. The simulated results of the PLDC16 retrieval showed significantly less intrinsic noise than the MH08.

Random noise applied to the simulated brightness temperatures showed improved retrievals of water vapour column with the PLDC16 when compared to MH08. For the worst case scenario where auxiliary information is a climatological profile from several winter seasons, the PLDC16 retrieval performed equally to MH08 for most situations. Real measurements of brightness temperature from MHS showed a reduction in RMS deviation and bias with respect to GVR for PLDC16 when compared to MH08. RMS deviations and biases were nearly equal or smaller for PLDC16 when compared to reanalyses and were smaller than AIRS satellite measurements for water vapour column less than $6 \, \mathrm{kg \, m^{-2}}$. PLDC16 and reanalyses showed similar RMS deviations but PLDC16 showed small scale structure that was not seen by the reanalyses.

Several assumptions and uncertainties in the PLDC16 retrieval were evaluated. Small uncertainties were induced due to simplifications in the PLDC16 retrieval and insignificant differences were seen in the retrievals from the MetOP-A and NOAA-18 satellites. Cloud contamination was evaluated using real MHS measurements and lidar measurements at Barrow, Alaska, and minimally impacted the PLDC16 retrieval.

CHAPTER 4

SURFACE REFLECTION AND EMISSIVITY

In this chapter, a surface emissivity retrieval is introduced and used to determine pan-Arctic surface emissivities and reflectance ratios. Surface emissivity is calculated using the brightness temperature formulation of Chapter 2 subject to either specular or Lambertian surface reflection. Two techniques are used to determine surface emissivity. One technique uses multiple instrument channels and the other uses a single instrument channel.

The surface emissivity retrievals are evaluated using simulations and real measurements. Simulations show a reduction in error for the surface emissivity retrieved in atmospheric conditions with small water vapour columns. Also, a reduction in error is seen when the multiple frequency technique uses channel combinations with more weakly absorbed frequencies or a larger number of frequencies/channels. Maps of surface emissivity and reflectance ratio using ATMS measurements throughout the winter season are produced. The maps show anomalous values in reflectance ratio over Greenland which are investigated in Sect.4.4.

Aircraft campaigns provide validation data for measurements of surface emissivity. There have been several aircraft campaign results (Selbach, 2003; Hewison and English, 1999; Harlow, 2009, 2011); however, these campaigns were limited in scope. While there have been measurements using the AMSU-B 89 GHz and 150 GHz channels for either land (Yan et al., 2008; Guedj et al., 2010) or sea-ice (Mathew et al., 2008; Karbou et al., 2014; Kongoli et al., 2011) surfaces in the Arctic, there is a dearth of such measurements at MHS and ATMS frequencies. The MIRS algorithm uses all MHS and ATMS frequencies for measurements of surface emissivity over sea-ice but relies on a 1-D variational

assimilation scheme (Kongoli et al., 2011) that does not take into account the day-to-day stability of surface properties. Currently there is no product producing surface emissivities from satellite measurements at 183 GHz with minimal model involvement over all Arctic surfaces.

The various aircraft campaigns used different surface reflection assumptions. Specular reflection was favoured by older campaign results from Selbach (2003) and Hewison and English (1999) while newer publications by Harlow (2009, 2011) have been using Lambertian. The AMSU-B measurements over land (Yan et al., 2008) and sea-ice (Mathew et al., 2008; Karbou et al., 2014; Kongoli et al., 2011) surfaces only assumed specular reflection. Guedj et al. (2010) evaluated measurements of surface emissivity over Antarctica for both specular and Lambertian but this was only applied to 89 GHz measurements using AMSU-A.

Comparisons of retrieved satellite surface emissivity with aircraft campaign measurements show good agreement for open ocean, land, FYI, and MYI surfaces. Retrievals of surface emissivity at various satellite zenith angles show minimal variation over Lambertian surfaces (land, FYI, and MYI) while specular surfaces (open ocean) vary which is expected. Surface emissivity variations with increasing water vapour column are also investigated and showed Lambertian surfaces having minimal variation.

Section 4.1 introduces diffuse surface reflection to the brightness temperature formulation in Chapter 2. The surface emissivity and reflectance ratio retrieval techniques are described in Sect. 4.2. Simulations are used to evaluate the surface emissivity retrievals using 5 different scenarios in Sect. 4.3. Section 4.4 shows surface emissivities and reflectance ratios derived from ATMS and MHS measurements. They are shown in the form of pan-Arctic maps in Sect. 4.4.1 and comparisons to aircraft campaign measurements for individual surface types in Sect. 4.4.2. The viewing angle and water vapour column dependence are also investigated in Sect. 4.4.4 and Sect. 4.4.5.

4.1   Surface Reflection

The PLDC16 retrieval from Chapter 3 and brightness temperature formulation from Chapter 2 assumed specular reflection from the surface. However, real surface reflection is typically more complicated as described in Sect. 2.2.2. A Lambertian (diffuse) scheme is introduced for the purpose of providing a better representation of surface reflection for

some surface types. To include a Lambertian component, the downward component of radiation reflected from the surface to the satellite needs to be reformulated for use in Eq. 2.21.
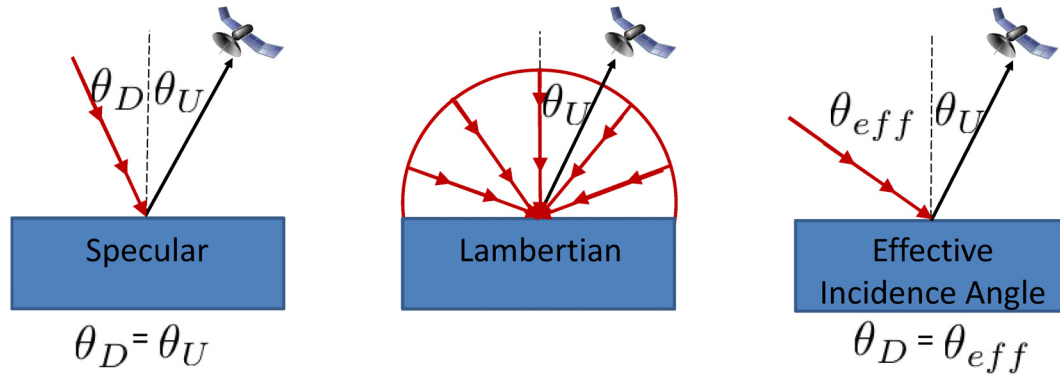
Figure 4.1: Examples for specular, Lambertian, and effective angle surface reflection for a satellite viewing the surface. Red lines are the downward component of radiation and black lines are reflected radiation in the view of the satellite.

Figure 4.1 shows examples of specular reflection, Lambertian reflection, and a parameterization for Lambertian reflection. For specular reflection, the downward component of radiation that is reflected to the satellite has an angle of incidence that is equal to the local zenith angle of the satellite. For Lambertian reflection, the reflected component of radiation to the satellite encompasses downward radiation from all directions in the entire hemisphere above the surface. The calculation is simplified for use in Eq. 2.24 by parameterizing Lambertian surface reflection in terms of an effective incidence angle (Matzler, 2005) as shown in Fig. 4.1. The effective incidence angle is derived in Matzler (1987) and given as,

$$\theta_{eff} = \cos^{-1}\left(\frac{-\tau}{\ln(2E_3(\tau))}\right), \qquad (4.1)$$

where E_3 is the exponential integral of the third order. This is also referred as the diffusivity factor (Wallace and Hobbs, 2006) or effective zenith angle (Petty, 2006). Figure 4.2 shows the variation of the effective incident angle with optical depth. The effective incident angle is $60°$ for optical depths near 0 and decreases nonlinearly with increasing optical depth.

To account for the introduction of θ_{eff} into the brightness temperature formulation from Chapter 2, Eq. 2.18 is modified to use a path D with an angle of incidence that does not equal the satellite local zenith angle. Completing the derivation from Sect. 2.3 for the
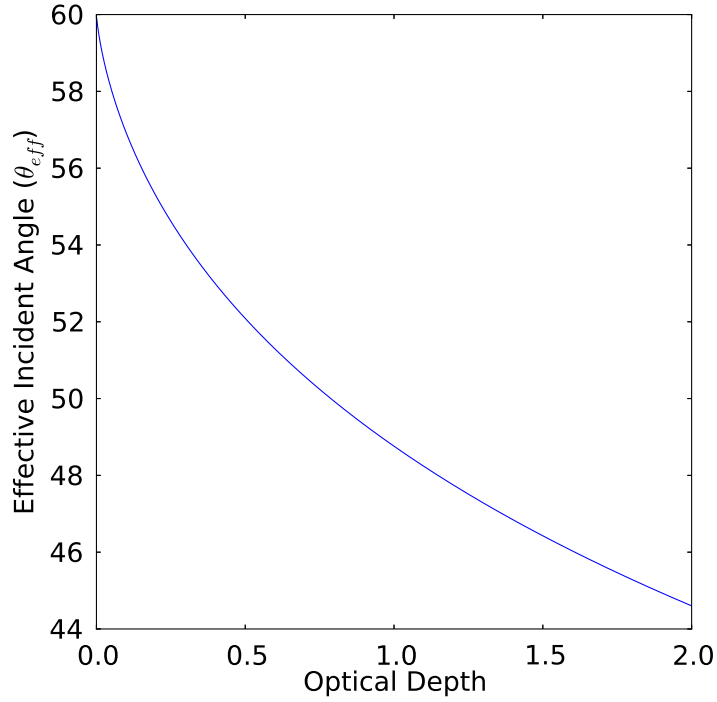
Figure 4.2: Effective incident angle compared to optical depth.

brightness temperature measured by a satellite with this change gives,

$$T_i = T_s m_p - (T_0 - T_c)(1 - \varepsilon)t_D t_U \tag{4.2}$$

where t_D and t_U are the transmittances for the atmospheric paths from the surface to the top of the atmosphere along the path D and from the surface to the satellite respectively as seen in Fig. 4.1. The factor, m_p, takes the form of

$$m_p = 1 + \left((1 - \varepsilon_i t_U) \frac{T_0 - T_s}{T_s} - \right.$$

$$\left. \frac{1}{T_s} \left(\int_0^H -(1 - t_U(z,H)) \frac{dT}{dz} dz + (1 - \varepsilon_i) t_D t_U \int_0^H (1 - t_D(z,H)^{-1}) \frac{dT}{dz} dz \right) \right). \tag{4.3}$$

where $t_D(z,H)$ and $t_U(z,H)$ are the transmittance from altitude, z, to the altitude of the satellite, H, in the D and U direction respectively. This form of T_i can be used for specular or Lambertian surface reflection. Under the plane parallel approximation, for specular reflection $t_D = t_U$ and for Lambertian reflection $t_D = t_{eff}$ where $t_{eff} = e^{-\tau \sec \theta_{eff}}$.

4.2 Surface Emissivity Formula

The surface reflectance ratio is a required quantity for the PLDC16 water vapour column retrieval. In Chapter 3, constant values were used for each regime which were determined from previously published surface emissivity measurements (Selbach, 2003; Hewison and English, 1999). However, different surfaces have different surface emissivities and therefore have different reflectance ratios. Also, surface emissivity can change temporally due to physical changes of the surface. Calculating the surface emissivity and reflectance ratio over different surfaces temporally will provide better estimates for the PLDC16 retrieval. In this chapter, two methods are used to calculate surface emissivity: the Hewison technique, and the Selbach technique.

4.2.1 Hewison Technique

The first method applies the same approach from the aircraft technique of Hewison and English (1999) to Eq. 4.2. This method substitutes Eq. 4.3 into Eq. 4.2 to solve for surface emissivity, ε,

$$\varepsilon_i(\theta) = \frac{T_i - T_0 + I_1 + t_U t_D I_2 + (T_0 - T_c) t_U t_D}{t_U t_D I_2 + (T_0 - T_c) t_U t_D - t_U (T_0 - T_s)} \tag{4.4}$$

$$\text{where } I_1 = -\int_0^H [1 - t_U(z,H)] \frac{dT_a(z)}{dz} dz$$

$$\text{and } I_2 = \int_0^H \frac{dT_a(z)}{dz} (1 - \frac{1}{t_D(z,H)}) dz.$$

Similar to the PLDC16 retrieval, auxiliary temperature and water vapour profiles, and skin temperature are needed. Note that only a single frequency is used in this technique.

4.2.2 Selbach Technique

The second method to calculate surface emissivity also gives a retrieval method for skin temperature. This is accomplished by using multiple frequencies which are close enough in terms of frequency to assume the surface emissivity and penetration depth are equal. This is assumed to be true for the 183 GHz frequencies of the microwave satellite instruments

used in this thesis.

The second method, introduced by Selbach for aircraft measurements (Selbach, 2003), defines a cost function, F_c, which minimizes the squared difference of measured and modeled brightness temperatures for at least two channels as,

$$F_c = \sum_i (T_{b,i} - T_{m,i})^2,$$

(4.5)

where $T_{m,i}$ is the modeled brightness temperature and $T_{b,i}$ is the measured brightness temperature for channel, i. The modeled brightness temperature is derived from the auxiliary information given to the retrieval. The cost function is minimized by setting the derivative with respect to surface emissivity and skin temperature to zero.

Rearranging for surface emissivity and skin temperature for each cost function derivative respectively gives an expression for both variables. Substituting one equation into the other gives independent expressions for both surface emissivity and skin temperature. The equations are,

$$\varepsilon_i(\theta) = \frac{\sum_i t_{U,i}^2 \sum_i T_{D,i}(T_{b,i} - T_{U,i} - T_{D,i}t_{U,i})t_{U,i} - \sum_i T_{D,i}t_{U,i}^2 \sum_i (T_{b,i} - T_{U,i} - T_{D,i}t_{U,i})t_{U,i}}{(\sum_i T_{D,i}t_{U,i}^2)^2 - \sum_i t_{U,i}^2 \sum_i T_{D,i}^2 t_{U,i}^2},$$

(4.6)

and,

$$T_s = \frac{\sum_i (T_{b,i} - T_{U,i} - T_{D,i}t_{U,i})t_{U,i} \sum_i T_{D,i}^2 t_{U,i}^2 - \sum_i T_{D,i}(T_{b,i} - T_{U,i} - T_{D,i}t_{U,i})t_{U,i} \sum_i T_{D,i}t_{U,i}^2}{\sum_i T_{D,i}t_{U,i}^2 \sum_i (T_{b,i} - T_{U,i} - T_{D,i}t_{U,i})t_{U,i} - \sum_i t_{U,i}^2 \sum_i T_{D,i}(T_{b,i} - T_{U,i} - T_{D,i}t_{U,i})t_{U,i}},$$

(4.7)

where $T_{U,i}$ and $T_{D,i}$ are the upwelling and downwelling contributions of radiation to $T_{m,i}$. From Eq. 2.22 and Eq. 2.23 and in terms of the Lambertian reflection formulation from Sect. 4.1 they are,

$$T_{U,i} = \int_0^H T_a(z) \frac{\partial t_{U,i}(z,H)}{\partial z} dz$$

(4.8)

and,

$$T_{D,i} = - \int_0^H T_a(z) \frac{\partial t_{D,i}(0,z)}{\partial z} dz + t_{D,i}(0,H) T_c. \tag{4.9}$$

To calculate the surface emissivity, auxiliary temperature and water vapour profiles are needed.

4.2.3 Discussion

The differences between the Hewison and Selbach techniques are that Selbach uses at least two channels while Hewison uses a single channel. Also, the Selbach technique produces a value for T_s while Hewison needs an auxiliary estimate.

As discussed in Chapter 3, the skin temperature information provided by reanalyses was not reliable due to the variation between datasets. Therefore, the surface air temperature, T_0, was set equal to the skin temperature, T_s for the PLDC16 retrieval. This can induce an error in the surface emissivity retrieved by the Hewison technique. Therefore, it is best to use the Selbach technique for the surface emissivity retrievals when possible.

The Selbach retrieval can only be used for the 183 GHz frequency in the following work because it is the only set of frequencies that have equal surface emissivity. However, the surface emissivity needs to be retrieved for 88 (89) GHz, 165 (157) GHz, and 183 GHz for the ATMS (MHS). Equation 4.5 from the Hewison technique will be used to calculate the 88 (89) GHz and 165 (157) GHz surface emissivities. The skin temperature derived from the 183 GHz Selbach retrieval will be used as auxiliary information at 88 (89) GHz and 165 (157) GHz. An error will be induced due to T_s varying with frequency due to changes in the penetration depth. However, the error is still smaller than when T_0 is assumed to be equal to T_s. This source of error will be investigated in the following section.

4.3 Theoretical Evaluation of Surface Emissivity Retrieval

To test the surface emissivity retrieval, modeled brightness temperatures were derived from a variety of atmospheric profiles. Similar to Chapter 3, radiosonde profiles from Barrow, Alaska, were used. The model uses the same inputs as in Chapter 3: nadir viewing angle, surface emissivity of 0.8 for all frequencies, cloud-free, unpolarized radiation, specular

surface reflection, and equal surface air and skin temperatures. Simulations were produced for the ATMS instrument. The surface emissivity retrieval was tested against simulated signals with:

1. No detector noise and perfect auxiliary information;

2. Detector noise and perfect auxiliary information;

3. No detector noise and a systematic bias water vapour (and temperature) auxiliary information;

4. No detector noise, perfect auxiliary information, and incorrect surface scattering assumption; and

5. No detector noise and a deviation of auxiliary skin temperature from model skin temperature.

In each case, the calculated surface emissivity and reflectance ratio are plotted against water vapour column for 183 GHz, 165 GHz, and 88 GHz for the ATMS instrument. MHS results are not shown because results for the three 183 GHz channels on MHS closely resemble those from the ATMS 183 GHz channels. Comparisons of the calculated and input surface emissivity will also be shown in terms of bias and standard deviation for different combinations of channels for the 183 GHz retrievals. Unphysical skin temperatures and retrieved surface emissivities are masked. For the simulations, this includes skin temperatures outside 0 K and 400 K and surface emissivities outside 0 and 1.

The sets of channels used for the Selbach technique in the simulations are shown in Table 4.1. For the two, three, four, and five channel combinations, the most strongly and weakly absorbed frequency sets were chosen. Choosing the most strongly and weakly absorbed frequencies for a particularly sized set shows the full range surface emissivity can vary for that set size. Also, all the ATMS channel combinations that coincide with MHS are shown in each case for the purpose of optimizing the channels used for MHS.

The model results are used to aid in evaluating the real surface emissivity retrieval results. The model results help to determine the frequencies near 183 GHz to be used for the surface emissivity and reflectance ratio retrieval, and the ideal atmospheric conditions for the retrievals.

Table 4.1: ATMS 183 GHz channel combinations used in model case studies for sets of two, three, four, and five channels. Matching MHS channels are combinations of ATMS channels that are similar to the MHS.

	ATMS Channels		Matching MHS Channels	
	Weakly Absorbed	Strongly Absorbed	Weakly Absorbed	Strongly Absorbed
two	$\pm$ 7, 4.5	$\pm$ 1.8, 1	$\pm$ 7, 3	$\pm$ 3, 1
three	$\pm$ 7, 4.5, 3	$\pm$ 3, 1.8, 1	$\pm$ 7, 3, 1	$\pm$ 7, 3, 1
four	$\pm$ 7, 4.5, 3, 1.8	$\pm$ 4.5, 3, 1.8, 1	n/a	n/a
five	$\pm$ 7, 4.5, 3, 1.8, 1	$\pm$ 7, 4.5, 3, 1.8, 1	n/a	n/a

4.3.1 Case 1

The intrinsic accuracy of the surface emissivity retrieval is tested by using noiseless simulated signals and perfect auxiliary information. Figure 4.3 compares the surface emissivity retrieval to water vapour column input into the model for the ATMS frequencies. The 183 GHz retrieval uses the 183 $\pm$ 1, 3, 7 GHz channels, which are also similar channels to MHS. The retrieved surface emissivity has negligible deviation from the input surface emissivity up to 7 $\mathrm{kg\,m^{-2}}$ of water vapour column for the 183 GHz retrieval. The 88 GHz and 165 GHz frequencies show no deviation except near 10 $\mathrm{kg\,m^{-2}}$.
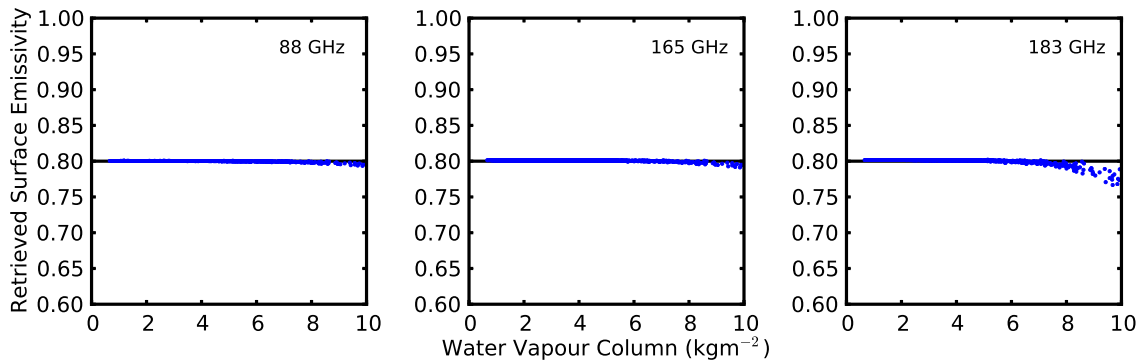
Figure 4.3: Retrieval of surface emissivity compared to water vapour column at nadir for simulated ATMS signals at 88 GHz, 165 GHz, and 183 GHz ($\pm$ 1, 3, 7). The simulated signals are noiseless and perfect auxiliary information is provided. Retrieved values are masked for unphysical skin temperatures and surface emissivities.

Figure 4.4: Bias of retrieved surface emissivity with respect to model input compared to water vapour column for 88 GHz, 165 GHz, and 183 GHz using simulated signals with different combinations of 183 GHz channels for the ATMS satellites. The simulated signals are noiseless and perfect auxiliary information is provided. Retrieved values are masked for unphysical skin temperatures and surface emissivities.

The deviation at 183 GHz is due to the large atmospheric absorption from water vapour. The 88 GHz and 165 GHz retrievals do not have this issue. However, the 88 GHz and 165 GHz retrievals deviate near $10 \ \mathrm{kg\,m^{-2}}$ due to the error in the skin temperature retrieval at 183 GHz (recall the skin temperature from the 183 GHz retrieval is input into the 88 and 165 GHz retrievals).

Two factors determine the water vapour column at which the 183 GHz surface emissivity retrieval deviates from the model input. The first factor is the selection of channels used in the retrieval. Figure 4.4 shows the bias of the retrieved surface emissivity with respect to the model input for increasing water vapour column for the various combinations of channels near 183 GHz for the ATMS instrument and the corresponding 88 GHz and 165 GHz surface emissivity retrievals. The bias is smaller at larger water vapour columns when more frequencies are used. Also, the deviation occurs at larger water vapour column for more weakly absorbed frequencies. Using a pair of more weakly absorbed frequencies further reduces the bias compared to using a greater number of frequencies; this can be seen when comparing $\pm$ 7, 3 GHz to $\pm$ 7, 3, 1 GHz. The 88 GHz and 165 GHz retrievals are weakly dependent on the frequency combination used in the 183 GHz retrieval except when the 183 GHz retrieval approaches unphysical values of skin temperature or surface emissivity.

The second factor is the local zenith angle of the satellite. Figure 4.5 shows the same simulation from Fig. 4.3 except with a satellite local zenith angle of 60 degrees. The longer path through the atmosphere causes the deviation of retrieved surface emissivity to occur at smaller water vapour columns.
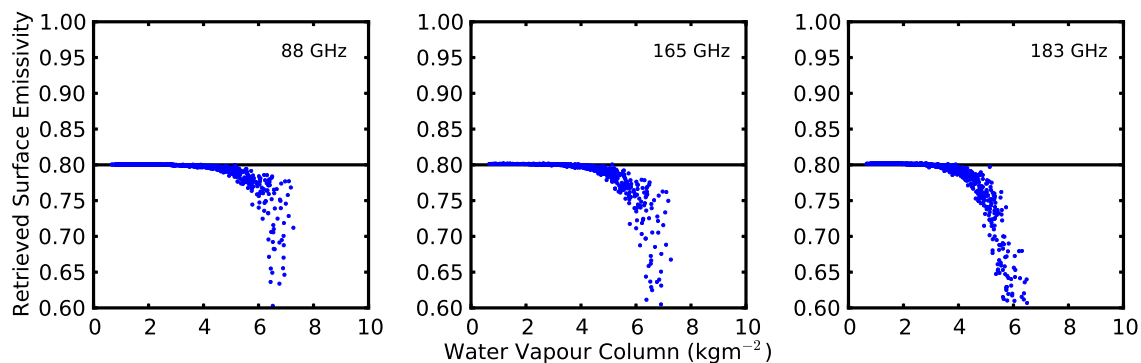
Figure 4.5: Retrieval of surface emissivity compared to water vapour column at a satellite local zenith angle of 60 degrees for simulated ATMS signals at 88 GHz, 165 GHz, and 183($\pm$ 1, 3, 7) GHz. The simulated signals are noiseless and perfect auxiliary information is provided. Retrieved values are masked for unphysical skin temperatures and surface emissivities.

The reflectance ratios, r_{88}/r_{165} and r_{165}/r_{183}, are derived from the surface emissivity retrievals and are shown in Fig. 4.6 for the 183 $\pm$ 1, 3, 7 GHz channels. The reflectance ratios do not deviate from the expected value of 1 except for larger water vapour columns which can be explained by the weak surface contribution to the brightness temperature.
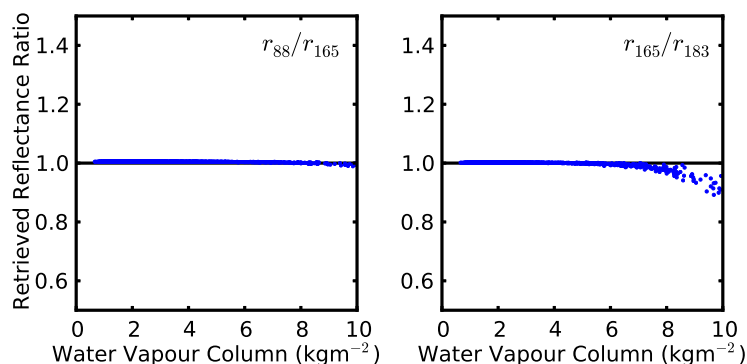
Figure 4.6: Ratio of reflectance compared to water vapour column at nadir for r_{88}/r_{165} GHz and r_{165}/r_{183} (183 $\pm$ 1, 3, 7) from simulated ATMS signals. The simulated brightness temperatures are noiseless and perfect auxiliary information is provided. Retrieved values are masked for unphysical skin temperatures and surface emissivities.
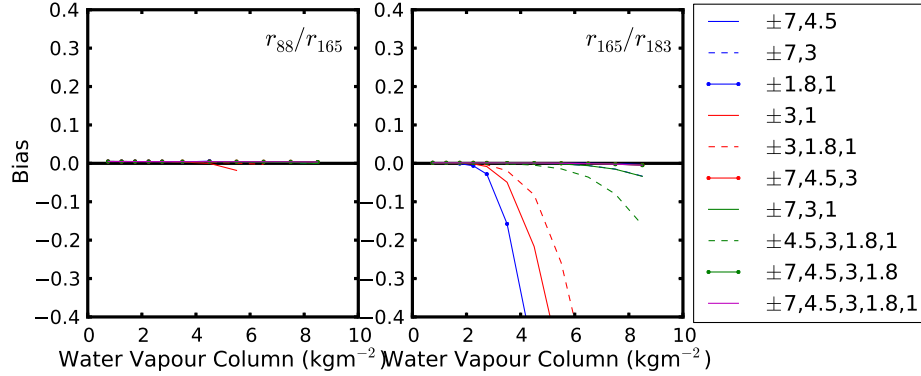
Figure 4.7: Bias of r_{88}/r_{165} GHz and r_{165}/r_{183} with respect to model input compared to water vapour column using simulated signals with different combinations of 183 GHz channels for the ATMS instrument. The simulated signals are noiseless and perfect auxiliary information is provided. Retrieved values are masked for unphysical skin temperatures and surface emissivities.

Similar to the surface emissivity retrievals, the reflectance ratio deviates when the surface contribution of the brightness temperature becomes small. Figure 4.7 shows the bias of the reflectance ratio with respect to the input value for increasing water vapour column for the various combinations of channels near 183 GHz. The reflectance ratio deviates at slightly smaller water vapour columns when compared to the surface emissivities in Fig. 4.4.

The simulations from testing intrinsic retrieval noise show an insignificant bias for the 183 GHz surface emissivity compared to the model input for water vapour columns greater than 10 $\mathrm{kg\,m^{-2}}$ depending on the channel frequencies used. The results show that using the surface emissivity and reflectance ratio for measurements with smaller water vapour columns reduce or remove the bias. Using 183 GHz combinations with a larger number of channels or more weakly absorbed frequencies extend the range of water vapour columns without a bias. The best channel combination at 183 GHz for the surface emissivity and reflectance ratio retrievals is $\pm$ 7, 4.5 GHz.

4.3.2   Case 2

For this case, Gaussian-distributed noise with a standard deviation of 0.5 K was added to the simulated brightness temperatures. The noise applied is the approximate noise equivalent differential temperature for each channel of the instrument as shown in Table 2.1. Perfect auxiliary information was provided to the surface emissivity retrieval.

Figure 4.8: Retrieval of surface emissivity compared to water vapour column at nadir for simulated ATMS signals at 88 GHz, 165 GHz, and 183 ($183 \pm 1, 3, 7$)GHz. The simulated signals include Gaussian noise with the 0.5 K standard deviation and perfect auxiliary information is provided. Retrieved values are masked for unphysical skin temperatures and surface emissivities.

Figure 4.8 compares the surface emissivity retrievals to the water vapour column input for the ATMS frequencies. The 183 GHz retrieval uses the $183 \pm 1, 3, 7$ GHz channels. A scatter is induced in the retrieved surface emissivity that increases with increasing water vapour column for all three retrievals. The more weakly absorbed frequencies at 88 GHz and 165 GHz have a scatter that is similar to that at 183 GHz for smaller water vapour columns due to a combination of the noise induced in those channels and the error skin temperature provided from the 183 GHz retrieval. Without the skin temperature retrieval from 183 GHz, the 88 GHz and 165 GHz retrieval scatter is reduced (not shown), given that the skin temperature is perfectly known in the simulation. Also, at larger water vapour columns the scatter is larger for 183 GHz.

The amount of scatter depends on the choice of frequencies used in the surface emissivity retrieval. Figure 4.9 shows the standard deviation of the retrieved surface emissivity with respect to the model input with increasing water vapour column for the various combinations of channels near 183 GHz and the corresponding 88 GHz and 165 GHz retrievals. The standard deviation decreases for the same reasons as the bias decreased in Case 1: an increase in the number of channels used, and the use of more weakly absorbed frequencies with respect to water vapour.
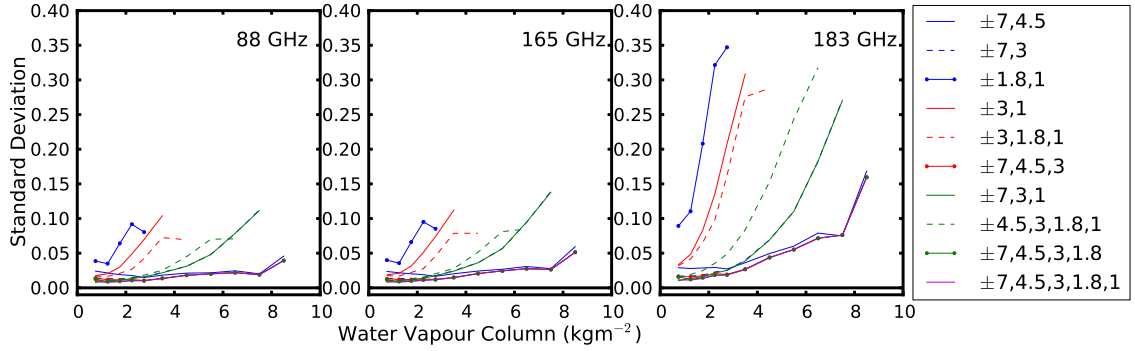
Figure 4.9: Standard deviation of retrieved surface emissivity with respect to model input compared to water vapour column for simulated signals with all combinations of 183 GHz channels for the ATMS instrument at 88 GHz, 165 GHz, and 183 GHz. The simulated signals include Gaussian noise with the 0.5 K standard deviation and perfect auxiliary information is provided. Retrieved values are masked for unphysical skin temperatures and surface emissivities.

Figure 4.10: Reflectance ratio compared to water vapour column at nadir for r_{88}/r_{165} and r_{165}/r_{183} (using $183 \pm 1, 3, 7$ GHz) from simulated ATMS signals. Simulated ATMS signals have Gaussian distributed noise with a standard deviation of 0.5 K and perfect auxiliary information is provided. Retrieved values are masked for unphysical skin temperatures and surface emissivities.

For the combination of $183 \pm 7, 4.5$ GHz and the corresponding 88 GHz and 165 GHz retrievals, there is an increase in scatter for smaller water vapour columns compared to $183 \pm 7, 3$ GHz. From Case 1, the bias was induced at larger water vapour columns for $183 \pm 7, 4.5$ GHz when compared to $183 \pm 7, 3$ GHz due to its weaker absorption by water vapour. The standard deviation is larger for $183 \pm 7, 4.5$ GHz because the proximity of the two channels to each other with respect to frequency. The difference between nearby brightness temperatures is small causing the simulated noise to have a larger effect.

Table 4.2: ATMS 183 GHz channel combinations surface emissivity and reflectance ratios standard deviation (SD) with respect to the model input. Standard deviations were computed using simulations with water vapour column less than $1.5\ \mathrm{kg\,m^{-2}}$.

Channels 183 (GHz)	Surface Emissivity SD			Reflectance Ratio SD	
	88 GHz	165 GHz	183 GHz	r_{88}/r_{165}	r_{165}/r_{183}
$\pm$ 7, 4.5	0.022	0.022	0.028	0.018	0.040
$\pm$ 1.8, 1	0.035	0.036	0.108	0.019	16.506
$\pm$ 7, 3	0.013	0.013	0.017	0.018	0.029
$\pm$ 3, 1	0.020	0.021	0.047	0.019	0.236
$\pm$ 7, 4.5, 3	0.012	0.012	0.016	0.018	0.029
$\pm$ 3, 1.8, 1	0.017	0.017	0.041	0.018	0.190
$\pm$ 7, 3, 1	0.010	0.010	0.013	0.018	0.028
$\pm$ 7, 4.5, 3, 1.8	0.009	0.009	0.013	0.018	0.027
$\pm$ 4.5, 3, 1.8, 1	0.011	0.011	0.019	0.018	0.051
$\pm$ 7, 4.5, 3, 1.8, 1	0.008	0.008	0.011	0.018	0.026

Table 4.2 shows standard deviations of surface emissivity for water vapour columns less than $1.5\ \mathrm{kg\,m^{-2}}$. The standard deviations are similar for most combinations with more weakly absorbed frequencies but is smallest when all the ATMS channels are used. The standard deviations show only a small difference between the 183 GHz retrievals and the 88 GHz and 165 GHz retrievals for most channel combinations except for combinations of channels that are more strongly absorbing water vapour. The values in Table 4.2 are used in Sect. 4.4.2 to differentiate between geophysical variability and instrument noise.
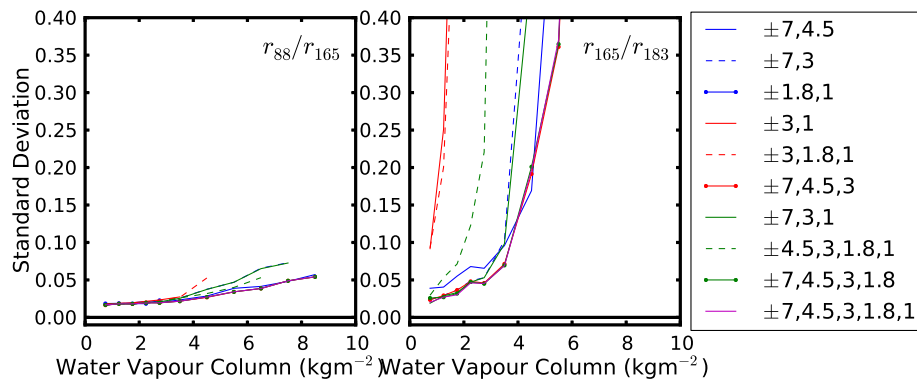
Figure 4.11: Standard deviation of r_{88}/r_{165} and r_{165}/r_{183} with respect to model input compared to water vapour column for simulated signals with different combinations of 183 GHz channels for the ATMS instrument. The simulated signals include Gaussian noise with the 0.5 K standard deviation and perfect auxiliary information is provided. Retrieved values are masked for unphysical skin temperatures and surface emissivities.

Figure 4.10 gives reflectance ratios determined from the retrieved emissivities. For the reflectance ratios, the 183 ± 1, 3, 7 GHz channels were used. A scatter is induced in the retrieved reflectance ratios that increases with increasing water vapour column similar to what is seen in the surface emissivities. The scatter is approximately the same for both reflectance ratios at small water vapour columns but for r_{165}/r_{183} it increases at a faster rate with respect to increasing water vapour when compared to that for r_{88}/r_{165}.

Figure 4.11 shows the standard deviation of the reflectance ratios with respect to the model input with increasing water vapour column for the various combinations of channels near 183 GHz. The standard deviation is decreased with the use of more 183 GHz channels, particularly when they are more weakly absorbed. The same increase in standard deviation from the surface emissivity retrievals for 183 ± 7, 4.5 GHz compared to 183 ± 7, 3 GHz is seen for the reflectance ratios.

Table 4.2 also shows standard deviations of reflectance ratios for water vapour columns less than 1.5 kg m^{-2}. Similar to the surface emissivity standard deviations, the reflectance ratio standard deviations are approximately the same for most combinations with more weakly absorbed frequencies and is smallest when all the 183 GHz ATMS channels are used. The sensitivity of the standard deviation to channel combination for the reflectance ratios is different when compared to surface emissivity. The standard deviation of r_{165}/r_{183} is more sensitive to channel combinations while there is almost no variation in standard deviation of r_{88}/r_{165} with different channel combinations when compared to the surface emissivity standard deviations. The standard deviation for r_{165}/r_{183} using ± 1.8, 1 GHz is significantly larger due to it using the two most strongly absorbing frequencies.

The simulations from the addition of Gaussian distributed noise show increased scatter in the surface emissivity and reflectance ratio retrievals which increases with increasing water vapour column. The results show that using small water vapour columns reduces the amount of scatter in the surface emissivity and reflectance ratio retrievals. The amount of scatter is further reduced when all channels are used in the 183 GHz retrieval. Using more weakly absorbed frequencies also produces comparable results while more strongly absorbed frequencies having significantly more scatter. The best channel combination at 183 GHz for the surface emissivity and reflectance ratio retrievals is ± 7, 4.5, 3, 1.8, 1 GHz, which is a different channel combination than what was most optimal for Case 1 ($\pm$ 7, 4.5 GHz). A resolution to this conflict is given in Sect. 4.3.6.

4.3.3   Case 3

The third case introduces a +25% systematic bias to the water vapour column in the auxiliary information. Noiseless simulated signals are used to isolate the error induced by the increase in water vapour column. The purpose of this test is to determine the effect of an error in the auxiliary information of water vapour (reanalysis data set) on the surface emissivity retrieval.

Figure 4.12: Retrieval of surface emissivity compared to water vapour column at nadir for simulated ATMS signals at 88 GHz, 165 GHz, and 183 (183 ± 1, 3, 7) GHz. The simulated signals are noiseless and a +25% systematic bias to the water vapour column is applied to the auxiliary information. Retrieved values are masked for unphysical skin temperatures and surface emissivities.

Figure 4.12 compares the surface emissivity retrieval to water vapour column for the ATMS instrument. The 183 GHz retrieval uses the 183 ± 1, 3, 7 GHz channels. A scatter is induced to the surface emissivity retrieval and the surface emissivity decreases with increasing water vapour column. The scatter in surface emissivity with respect to water vapour column is due to differences in the auxiliary temperature and water vapour profiles between each simulated measurement. Notice also that, the surface emissivity retrieval is greater than the model input for the smallest water vapour columns. The 88 GHz and 165 GHz retrievals behave the same as the 183 GHz retrieval but with a smaller decrease in surface emissivity with increasing water vapour column.

The rate of decrease with respect to water vapour column depends on the channels used near 183 GHz. Figure 4.13 shows the bias of the retrieved surface emissivity compared to water vapour column for various channel combinations near 183 GHz. When more weakly absorbed frequencies are used, the rate of decrease for surface emissivity is smaller. The initial bias of the retrieved surface emissivity at the smallest water vapour columns also

depends on the 183 GHz channels used. The more weakly absorbed channel combinations have a larger bias for the smallest water vapour columns than the more strongly absorbed channel combinations. When more channels are used, the initial bias decreases but not to a large degree.
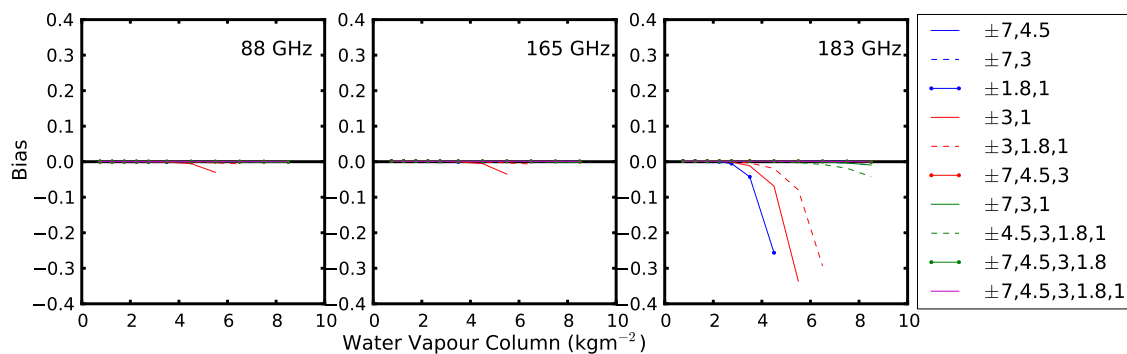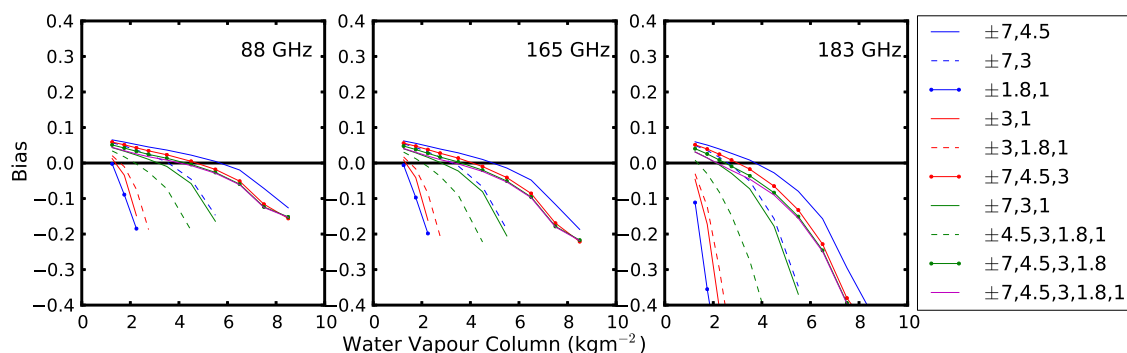

Figure 4.13: Bias of retrieved surface emissivity with respect to model input compared to water vapour column for 88 GHz, 165 GHz, and 183 GHz using simulations with all combinations of 183 GHz channels for the ATMS instrument. The simulated signals are noiseless and a 25% increase in water vapour column is applied to the auxiliary information. Retrieved values are masked for unphysical skin temperatures and surface emissivities.

For the case where the auxiliary water vapour column is decreased, the trend is reversed. The surface emissivity for small water vapour columns are smaller than the model input and increases with increasing water vapour column for the 183 GHz retrieval (not shown).

A ± 5 K systematic bias to the temperature profile in the auxiliary information was also applied to noiseless simulated signals. The purpose of this test was to determine the effect of an error in the auxiliary information for the temperature profile (reanalysis data set) on the surface emissivity retrieval. The results show the same trend as seen with a systematic bias in the water vapour column: Errors were negligible for small water vapour columns. The induced surface emissivity bias is smaller when comparing a ± 5 K temperature profile bias to a $\pm 25\%$ water vapour column bias.

The reflectance ratios for the ATMS instrument are shown Fig. 4.14 using the 183 $\pm$ 1, 3, 7 GHz channels. The reflectance ratios decrease with increasing water vapour column and do not have the bias at low water vapour columns that was shown in the surface emissivity retrievals. The bias from the model input is minimized for the smallest water vapour columns and increases with increasing water vapour. The r_{88}/r_{165} rate of decrease with increasing water vapour column is smaller than for r_{165}/r_{183}. With a 25% decrease

for the ancillary information of water vapour column, the reflectance ratios increase with increasing water vapour column (not shown).
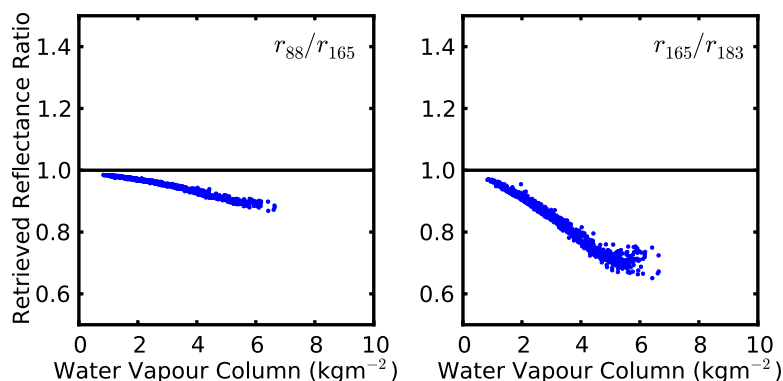
Figure 4.14: Reflectance ratio compared to water vapour column at nadir for r_{88}/r_{165} GHz and r_{165}/r_{183} (183 $\pm$ 1, 3, 7) from simulated ATMS signals. Simulated ATMS signals are noiseless and a 25% increase in water vapour column for the auxiliary information. Retrieved values are masked for unphysical skin temperatures and surface emissivities.
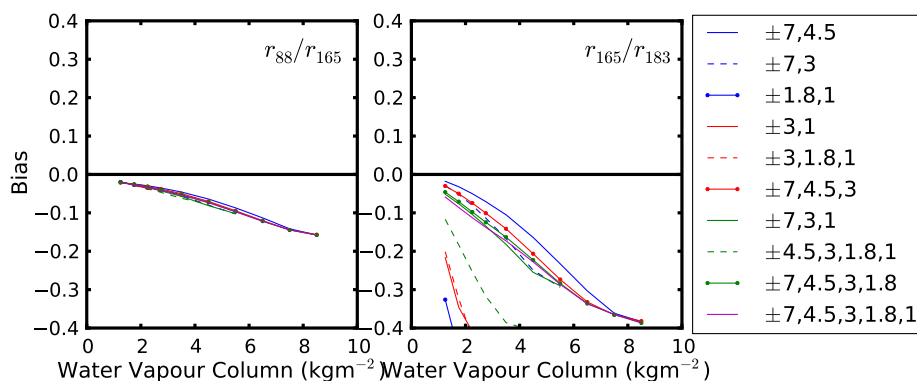
Figure 4.15: Bias of r_{88}/r_{165} GHz and r_{165}/r_{183} with respect to model input compared to water vapour column for simulated signals with different combinations of 183 GHz channels for the ATMS satellite. The simulated signals are noiseless and a 25% increase in water vapour column is applied to the auxiliary information. Retrieved values are masked for unphysical skin temperatures and surface emissivities.

Figure 4.15 shows the bias of the reflectance ratios with respect to the model input compared to water vapour column for the various combinations of channels near 183 GHz. The bias for r_{165}/r_{183} is smallest when fewer channels are used in the 183 GHz retrieval of surface emissivity. The addition of extra channels to the more weakly absorbed frequencies increases the bias, but the resulting bias is still smaller than more strongly absorbed channel

combinations. r_{88}/r_{165} does not vary significantly with a change in the channels used in the 183 GHz surface emissivity retrieval.

The simulations using a systematic bias of $+$ 25% to the auxiliary water vapour induced a bias in 88 GHz, 165 GHz, and 183 GHz surface emissivity retrievals that changes with increasing water vapour column. The initial positive bias was larger for more weakly absorbed channel pairs but decreased with increasing the number of channels. Using all the 183 GHz channels produced the best results. The initial bias is further reduced for more strongly absorbed frequencies but the slope of decrease is significantly larger with increasing water vapour column. The best channel combination at 183 GHz for the surface emissivity retrieval is $\pm$ 7, 4.5, 3, 1.8, 1 GHz which is the same combination optimal for Case 2 but not Case 1. For the reflectance ratios, more weakly absorbed pairs of channels had the smallest bias. Adding channels to the more weakly absorbed frequency pairs increased the bias. The best channel combination at 183 GHz for the reflectance ratio retrieval is $\pm$ 7, 4.5 GHz which is not the same as the results from Case 2 but equal to the results from Case 1.

4.3.4 Case 4
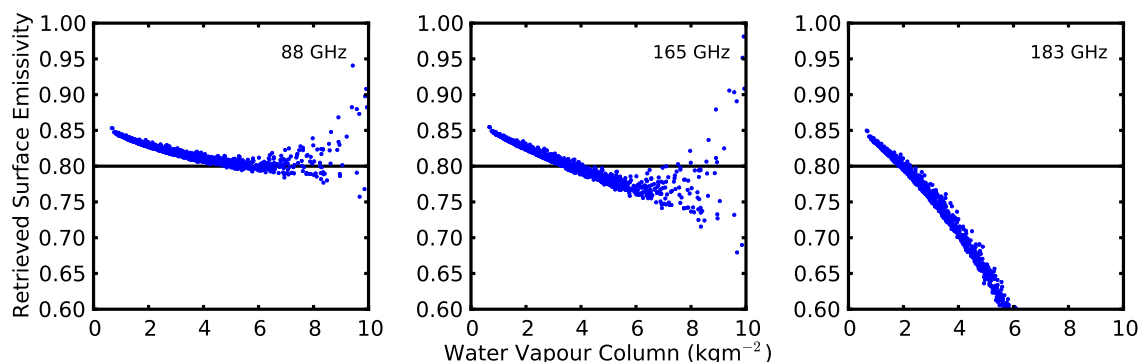
Figure 4.16: Retrieval of surface emissivity compared to water vapour column at nadir for simulated ATMS signals at 88 GHz, 165 GHz, and 183 GHz. The simulated signals are noiseless and perfect auxiliary information is provided. The surface scattering assumption in the retrieval is Lambertian but the model assumes specular. Retrieved values are masked for unphysical skin temperatures and surface emissivities.

The fourth case assumes Lambertian surface reflection in the surface emissivity retrieval, while the simulation uses specular surface reflection. Noiseless simulated signals

and perfect auxiliary information were used to isolate the error induced by the surface reflection assumption. The purpose of this test is to evaluate the effect of assuming the incorrect type of surface reflection for a particular surface.

Figure 4.16 compares the surface emissivity retrievals to water vapour column input for ATMS. The 183 GHz retrieval uses the 183 $\pm$ 1, 3, 7 GHz channels. A decrease in the retrieved surface emissivity with increasing water vapour column, similar to Case 3, is shown for the 183 GHz retrieval. For 88 GHz and 165 GHz retrievals, a decrease with increasing water vapour column is also shown, but the rate of change is significantly smaller. At small water vapour columns, the surface emissivity retrieved is larger than the value input into the model.
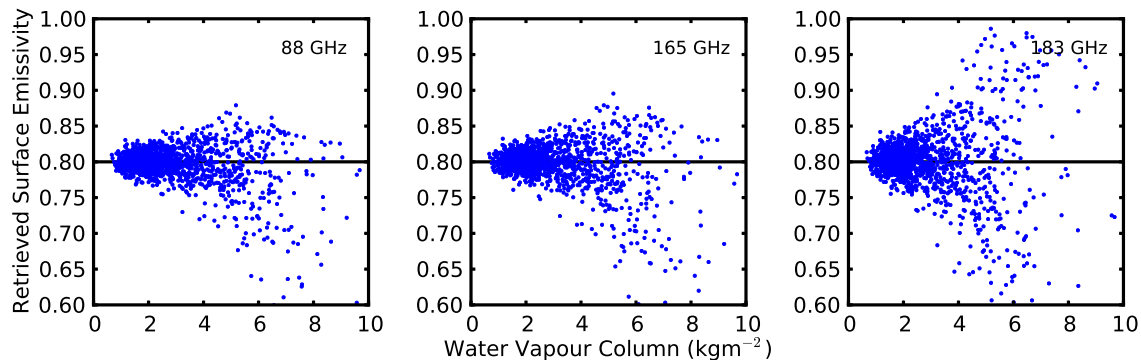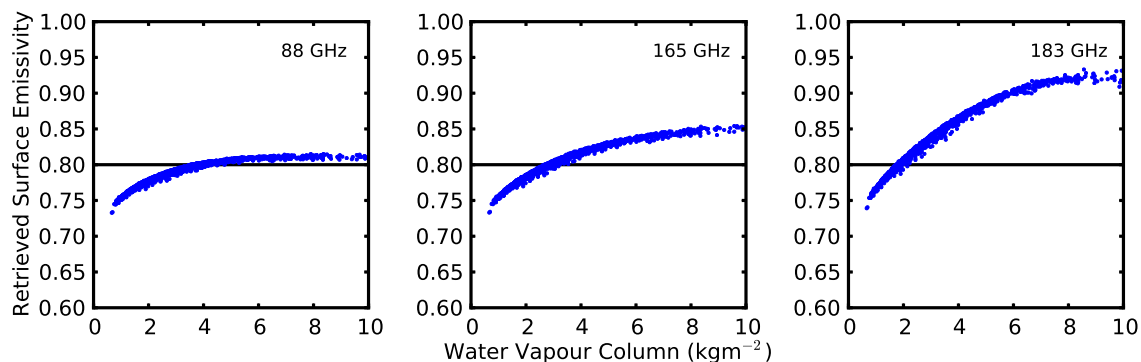

Figure 4.17: Retrieval of surface emissivity compared to water vapour column at nadir for simulated ATMS signals at 88 GHz, 165 GHz, and 183 GHz. The simulated signals are noiseless and perfect auxiliary information is provided. The surface scattering assumption in the retrieval is specular but the model assumes Lambertian. Retrieved values are masked for unphysical skin temperatures and surface emissivities.

For the case where the satellite zenith angle is not at nadir (not shown), the bias is reduced. As satellite zenith angle increases from the nadir position, the difference between the satellite zenith angle and effective incident angle decreases, which reduces the induced bias in the retrieved surface emissivity. The nadir case represents the maximum possible error induced by assuming the incorrect type of surface reflection.

When Lambertian surface reflection is assumed by the model and specular surface reflection is assumed in the retrieval of surface emissivity, the error in surface emissivity retrieved is reversed. Figure 4.17 compares the surface emissivity retrievals to water vapour column input for ATMS for the case of the simulation using Lambertian reflection while the retrieval uses specular reflection. The surface emissivity for small water vapour columns

is less than the model input, but increases with increasing water vapour column until it is larger than the model input.

The rate of decrease for the surface emissivity retrieved with respect to water vapour column varies depending on the channel combination used in the retrieval. Figure 4.18 shows the bias of the retrieved surface emissivity that assumes specular reflection with respect to Lambertian model input compared to water vapour column for the various combinations of channels near 183 GHz. As in the previous cases, the use of more weakly absorbed frequencies reduces the rate of decrease for surface emissivity. The more weakly absorbed channel combinations have a larger bias for the smallest water vapour columns when compared to more strongly absorbed channel combinations. When more channels are used, the initial bias decreases, but not to a large degree. The channel combination results for specular simulations and the retrieval assuming Lambertian are the same but with a negative bias for more weakly absorbed frequencies at small water vapour columns (not shown).
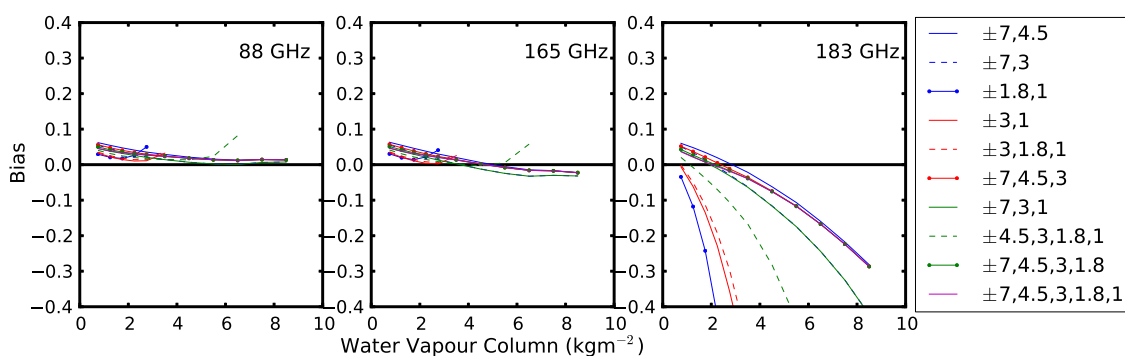
Figure 4.18: Bias of retrieved surface emissivity with respect to water vapour column for 88 GHz, 165 GHz, and 183 GHz (183 $\pm$ 1, 3, 7) using simulated signals with a number of combinations of 183 GHz channels for ATMS. The simulated signals are noiseless and perfect auxiliary information is provided. The model assumes specular surface reflection while the emissivity retrieval assumes Lambertian surface reflection. Retrieved values are masked for unphysical skin temperatures and surface emissivities.

Figure 4.19 shows the reflectance ratios using the 183 $\pm$ 1, 3, 7 GHz channels. The results are similar to Case 3 where the reflectance ratios decrease with increasing water vapour column and the reflectance ratio are closest to 1 for the smallest water vapour column while the surface emissivity retrieval has a positive bias. The results for specular simulations and the retrieval assuming Lambertian reflection are similar except for having an increasing reflectance ratio with increasing water vapour column (not shown).
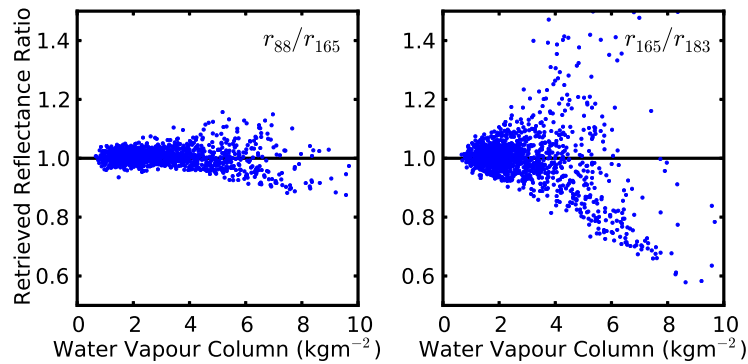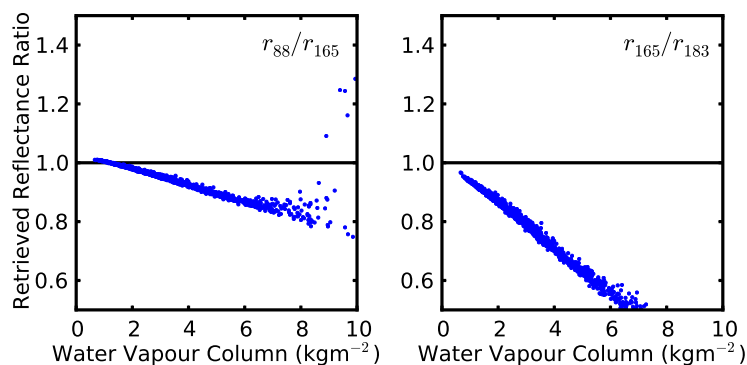
Figure 4.19: Reflectance ratio compared to water vapour column at nadir for r_{88}/r_{165} and r_{165}/r_{183} ($183 \pm 1, 3, 7$) from simulated ATMS signals. The simulated signals are noiseless and perfect auxiliary information is provided. The retrieval assumed Lambertian surface reflection while the model assumed specular surface reflection. Retrieved values are masked for unphysical skin temperatures and surface emissivities.

Figure 4.20 shows the bias of the reflectance ratios with respect to the model input compared to water vapour column for a number of combinations of channels near 183 GHz. The reflectance ratio biases follow a pattern similar to Case 3, where the bias of r_{165}/r_{183} is smallest when fewer more weakly absorbed frequencies are used in the 183 GHz surface emissivity retrieval and r_{88}/r_{165} does not vary significantly with different 183 GHz channels. The channel combination results for specular simulations and the retrieval assuming Lambertian are the same but with a positive bias (not shown).
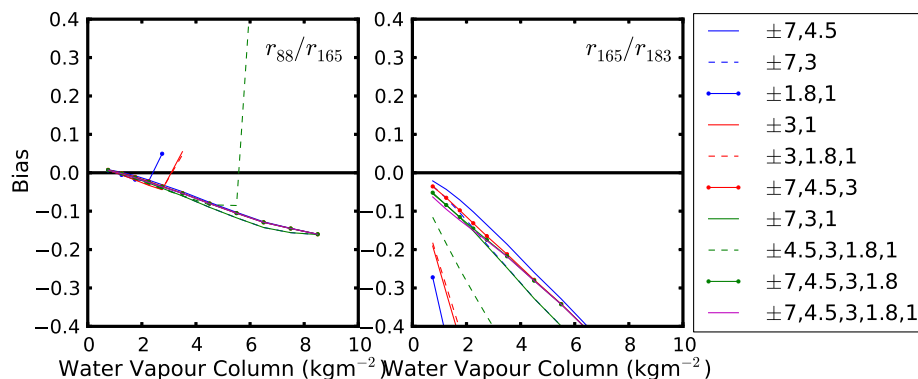
Figure 4.20: Bias of reflectance ratio with respect to model input compared to water vapour column for r_{88}/r_{165} and r_{165}/r_{183} using simulated signals with different combinations of 183 GHz channels for ATMS. The simulated signals are noiseless and perfect auxiliary information is provided. The model assumes specular surface reflection while the emissivity retrieval assumes Lambertian surface reflection. Retrieved values are masked for unphysical skin temperatures and surface emissivities.

Simulations that assumed the incorrect surface reflection in the surface emissivity and reflectance ratio retrievals induced a bias in the 88 GHz, 165 GHz, and 183 GHz surface emissivity retrievals that changes with increasing water vapour column. The initial bias was larger for more weakly absorbed channel pairs but decreased as the number of channels was increased. Using all the 183 GHz channels produced the best results. The initial bias is further reduced for more strongly absorbed frequencies but the slope of decrease is significantly larger with increasing water vapour column. The best channel combination at 183 GHz for the surface emissivity retrieval is ± 7, 4.5, 3, 1.8, 1 GHz. This is the same combination that is optimal for surface emissivity retrievals in Case 2 and Case 3 but not Case 1. For the reflectance ratios, more weakly absorbed pairs of channels had the smallest bias. Adding channels to the more weakly absorbed channel pairs increased the bias. The best channel combination at 183 GHz for the reflectance ratio retrieval is ± 7, 4.5 GHz. This is the optimal combination used for Case 3 and Case 1 but not the same as Case 2.

4.3.5 Case 5

The final simulation introduces a difference between the skin temperature in the auxiliary information and the skin temperature of the simulation. Noiseless simulated signals were used to isolate the error induced by the change in skin temperature. The purpose of this case is to evaluate the change in surface emissivity due to the skin temperatures wavelength dependence as discussed in Sect. 2.2.4.

Modeling of penetration depth and temperature profiles from SHEBA measurements (Mathew et al., 2008) of sea ice and snow show that the skin temperature can be 2 K to 20 K larger than the surface air temperature at 89 GHz. For 157 GHz, the skin temperature can range from 1 K to 7 K larger than the surface air temperature. The simulation increases the auxiliary skin temperature by 20 K and 7 K for the 88 GHz and 165 GHz frequencies respectively to represent the upper bound of error in the surface emissivity retrieval.

Figure 4.21 compares the surface emissivity retrieval to water vapour column input into the model using the $183 \pm 1, 3, 7$ GHz frequencies. The 88 GHz surface emissivity retrieval has a positive bias of 0.07 and the 165 GHz retrieval has a positive bias of 0.03 due to the respective 20 K and 7 K changes to skin temperature. The surface emissivity retrieved does not vary significantly with increasing water vapour column or channel combinations used in the 183 GHz retrieval.
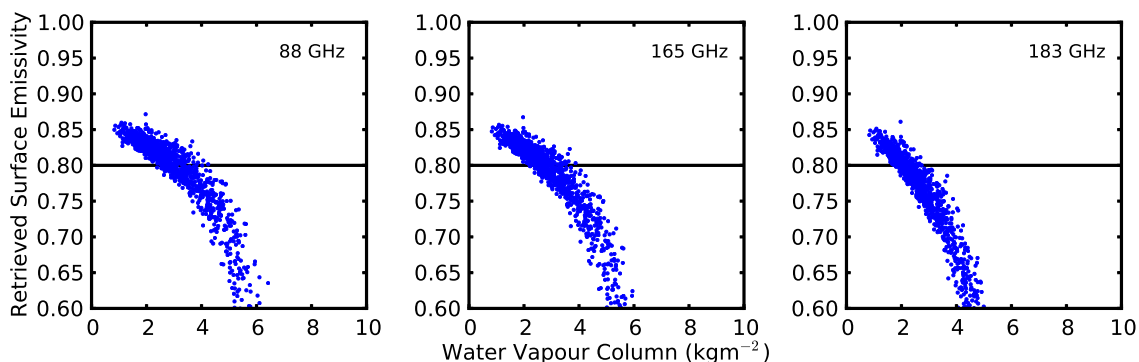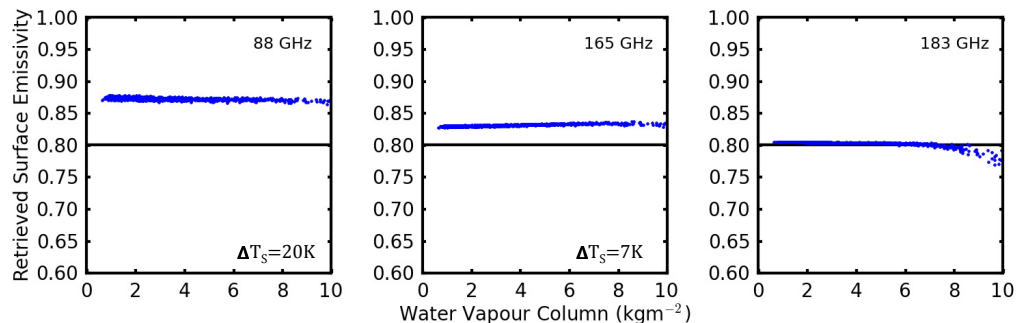
Figure 4.21: Retrieval of surface emissivity compared to water vapour column at nadir for simulated ATMS signals at 88 GHz, 165 GHz, and 183 GHz ($183 \pm 1, 3, 7$). The simulated signals are noiseless and the skin temperature in the model is 7 K and 20 K larger for 165 GHz and 88 GHz respectively when compared to the auxiliary information. Retrieved values are masked for unphysical skin temperatures and surface emissivities.
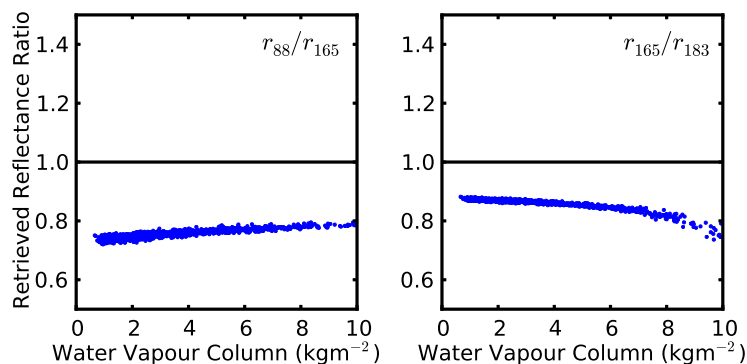
Figure 4.22: Reflectance ratio with respect to model input compared to water vapour column at nadir for r_{88}/r_{165} and r_{165}/r_{183} ($183 \pm 1, 3, 7$) for simulated ATMS signals. The simulated signals are noiseless and the skin temperature in the model is 20 K and 7 K larger for 88 GHz and 165 GHz respectively when compared to the auxiliary information. Retrieved values are masked for unphysical skin temperatures and surface emissivities.

The reflectance ratios are shown in Fig. 4.22. A decrease of greater than 0.2 is shown for r_{88}/r_{165} and greater than 0.1 for r_{165}/r_{183}. The bias of the reflectance ratio is approximately constant for variations in water vapour column and frequencies used in the 183 GHz surface emissivity retrieval.

The simulations of adding a 7 K and 20 K offset to the skin temperature at 165 GHz and 88 GHz respectively showed a positive bias of approximately 0.03 and 0.07 for the surface emissivity retrievals. The reflectance ratios had similar results but with a negative bias of approximately 0.2 and 0.1 for r_{88}/r_{165} and r_{165}/r_{183} respectively. The bias was

independent of the channel combinations for both surface emissivity and reflectance ratio meaning there is no optimal channel combination for this simulation. Also, note that the simulations induce the maximum error according to Mathew et al. (2008), measurements would not frequently have skin temperature differences of this magnitude over the range of 88 GHz and 183 GHz.

4.3.6 Discussion

The five test cases were given to theoretically evaluate the surface emissivity retrieval at 88 GHz, 165 GHz, and 183 GHz. Case 1 tested the intrinsic accuracy of the retrieval. Case 2 included randomized noise to the brightness temperatures. Case 3 imposed a +25% systematic bias to the auxiliary profile of water vapour. Case 4 evaluated the error induced by an incorrect surface reflection assumption. Finally, Case 5 evaluated the maximum error induced by using the 183 GHz skin temperature at 88 GHz and 165 GHz.

The simulations from all the cases indicate it is best to use the surface emissivity and reflectance ratio retrievals at small water vapour columns to reduce error. The case results either showed an increase in scatter or an increase in the bias with larger water vapour columns.

For the surface emissivity simulations, Case 2, Case 3, and Case 4 showed that the use of all five 183 GHz channels produce the best results while Case 1 showed that the best result was produced when using the two most weakly absorbed frequencies. For Case 1, the induced biases using $\pm$ 7, 4.5, 3, 1.8, 1 GHz and $\pm$ 7, 4.5 GHz were the same up to at least 10 kg m^{-2} at nadir. For large viewing angles (not shown), there was a small deviation beginning at approximately 6 kg m^{-2} between the previous channel combinations. This is insignificant compared to the differences seen in the other cases. Therefore, it's optimal to use the $\pm$ 7, 4.5, 3, 1.8, 1 GHz frequencies for the ATMS instrument.

For the reflectance ratio simulations, Case 2 showed that the best results were produced when all five 183 GHz channels were used, while Case 1, Case 3, and Case 4 showed the best results when the two most weakly absorbed frequencies were used. For Case 2, the standard deviation was less than double for $\pm$7,4.5 GHz when compared to $\pm$ 7, 4.5, 3, 1.8, 1 GHz for water vapour columns less than 1.5 kg m^{-2}, as shown in Table 4.2. However, the absolute difference in standard deviation is small. It is preferred to have a small increase in standard deviation than to have larger systematic offsets in reflectance ratio retrieved.

Therefore, it's optimal to use the $\pm$ 7, 4.5 GHz for the ATMS instrument.

These case results can also be applied to the MHS instrument. The possible channel combinations from MHS for 183 GHz are $\pm$ 7, 3 GHz, $\pm$ 3, 1 GHz, $\pm$ 7, 1 GHz, and $\pm$ 7, 3, 1 GHz. For the same reasons above, the most optimal surface emissivity channel combination would use all the MHS frequencies, $\pm$ 7, 3, 1 GHz. The optimal reflectance ratio channel combination would use the two most weakly absorbed frequencies, $\pm$ 7, 3 GHz.

4.4   Retrievals from Real Brightness Temperatures

The criteria developed from simulations can be applied to retrievals of surface emissivity calculated from real brightness temperature measurements. In the following section, ATMS and MHS overpasses in the Arctic are shown in the form of pan-Arctic maps to compare surface emissivity and reflectance ratio over different surface types. Measurements from the different Arctic surface types are examined individually and compared to previously published results. Comparisons of surface emissivities to water vapour column and satellite local zenith angle are produced to evaluate the retrievals.

Microwave radiation has historically been assumed to reflect specularly from most surfaces (Matzler, 2005). However, recent work shows certain surfaces are Lambertian or at least a mixture of specular and Lambertian (Harlow, 2011). For this chapter, ice and land surfaces are assumed to be Lambertian (Harlow, 2011) while the open ocean will be assumed to be specular (Matzler, 2005). This will be re-evaluated in Sect. 5.5 using the PLDC16 water vapour column retrieval.

As determined from Sect. 4.3.6, ATMS measurements should use $\pm$ 7, 4.5, 3, 1.8, 1 GHz channels for the surface emissivity retrieval and $\pm$ 7, 4.5 GHz for the reflectance ratio retrieval. However, the optimal frequencies determined in Sect. 4.3.6 will not be used for MHS.

MHS measures 183 GHz brightness temperature at different polarizations as described in Table 2.1. The $\pm$ 3, 1 GHz channels are horizontally polarized while the 190 GHz channel is vertically polarized. The channel combination used in the Selbach retrieval must have the same polarization for measurements that are not at nadir. Therefore, at 183 GHz, the $\pm$ 3, 1 GHz channels must be used. In terms of error and noise, these channels are not optimal as discussed in Sect. 4.3, but they have the same polarization as the 183 GHz

channels of ATMS.

For the MHS reflectance ratio, the Hewison technique at 190 GHz will be used to determine surface emissivity by using the skin temperature from the Selbach technique using $\pm$ 3, 1 GHz. The reason for this is to produce a reflectance ratio with a single polarization since the 157 GHz channel is vertically polarized.

Note, the ATMS $\frac{r_{88}}{r_{165}}$ is a mixed polarization where 88 GHz is vertically polarized and 165 GHz is horizontally polarized. For $\frac{r_{88}}{r_{165}}$, mixed polarization reflectance ratios are required by the water vapour retrieval. From this point forward, polarization will be labeled on surface emissivities and reflectance ratios. For example, the ATMS 88 GHz and 165 GHz reflectance ratio becomes $\frac{r_{88v}}{r_{165h}}$. Similarly, frequencies are labeled as 88v GHz and 165h GHz for ATMS.

4.4.1   *Surface Emissivity and Reflectance Ratio Maps*

Pan-Arctic maps of surface emissivity and reflectance ratio were produced by binning measurements in a 30 km x 30 km grid for latitudes greater than $60°$. The mode of the probability densities from a maximum of 50 measurements with the smallest water vapour column were used for each grid cell to reduce the effects from instrument noise as simulated in Sect. 4.3. A minimum of 10 measurements is used for each grid cell. Monthly maps were produced for the purpose of using measurements with small water vapour columns. Measurements with satellite local zenith angles between $0°$ and $20°$ were used to minimize any variation of surface emissivity with satellite local zenith angle.

Figure 4.23 shows maps of surface emissivity at 88v GHz, 165h GHz, and 183h GHz. For land surfaces, there is a large range of values. Relatively small values are seen over eastern Russia and over central Greenland while larger values are seen in northern Europe and southern Greenland. The range of surface emissivities is relatively smaller at 183h GHz and 165h GHz when compared to 88v GHz.

88v GHz 165h GHz

183h GHz

Surface Emissivity
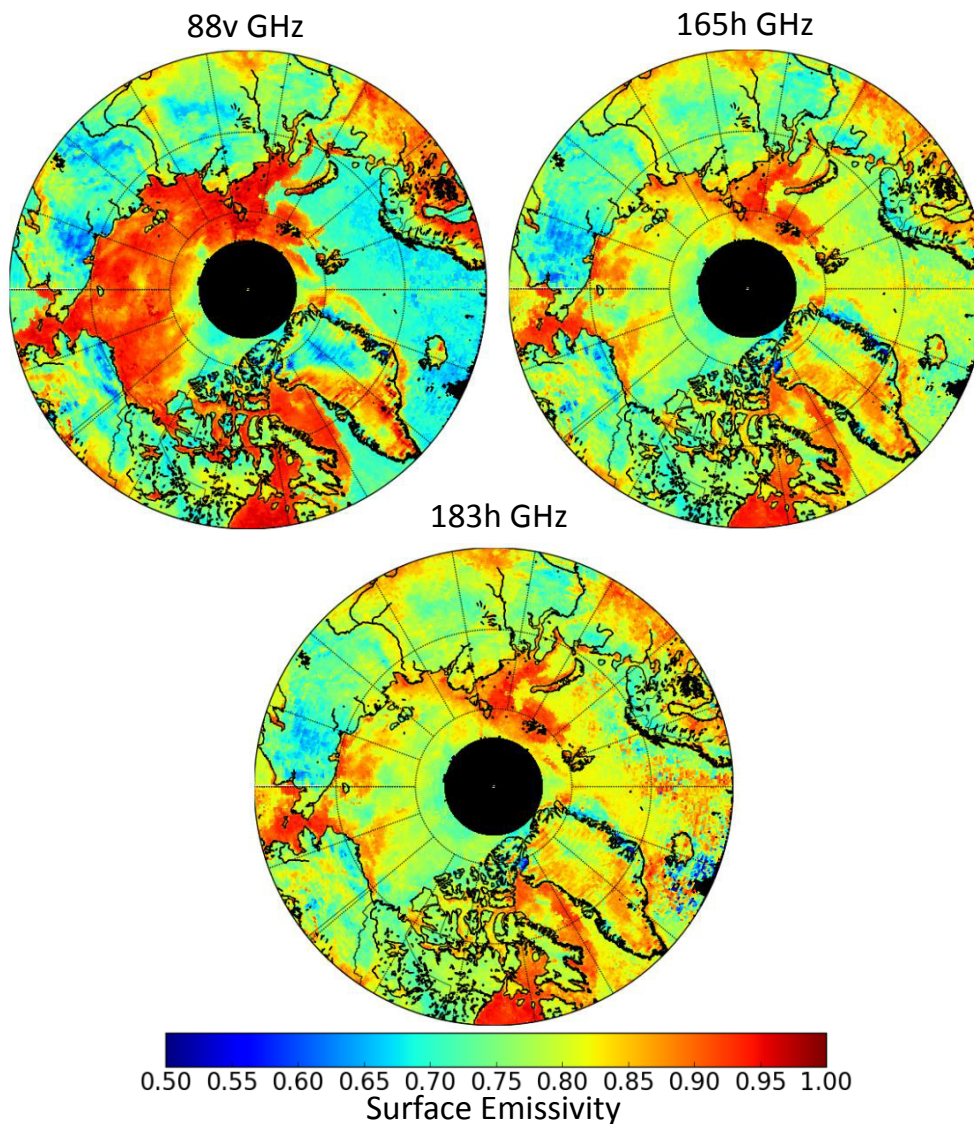
Figure 4.23: Surface emissivity retrieval maps over the Arctic for December 2012 at 88v GHz, 165h GHz, and 183h GHz using the ATMS instrument.

Over the ocean, particularly at 88v GHz, there are distinct features and boundaries. To identify different surfaces, EUMETSAT Ocean and Sea Ice Satellite Application Facility ice type product (OSI-403-c) (Breivik et al., 2012) was used. This product uses data from two instruments, SSMIS and the Advanced Scatterometer (ASCAT). The classification is produced using the SSMIS 19 GHz, 37 GHz, and 89 GHz channels to calculate ratios of the difference to the sum for various combinations of frequencies and polarizations. Also, ASCAT backscatter at 5.255 GHz is used (Aaboe et al., 2015).
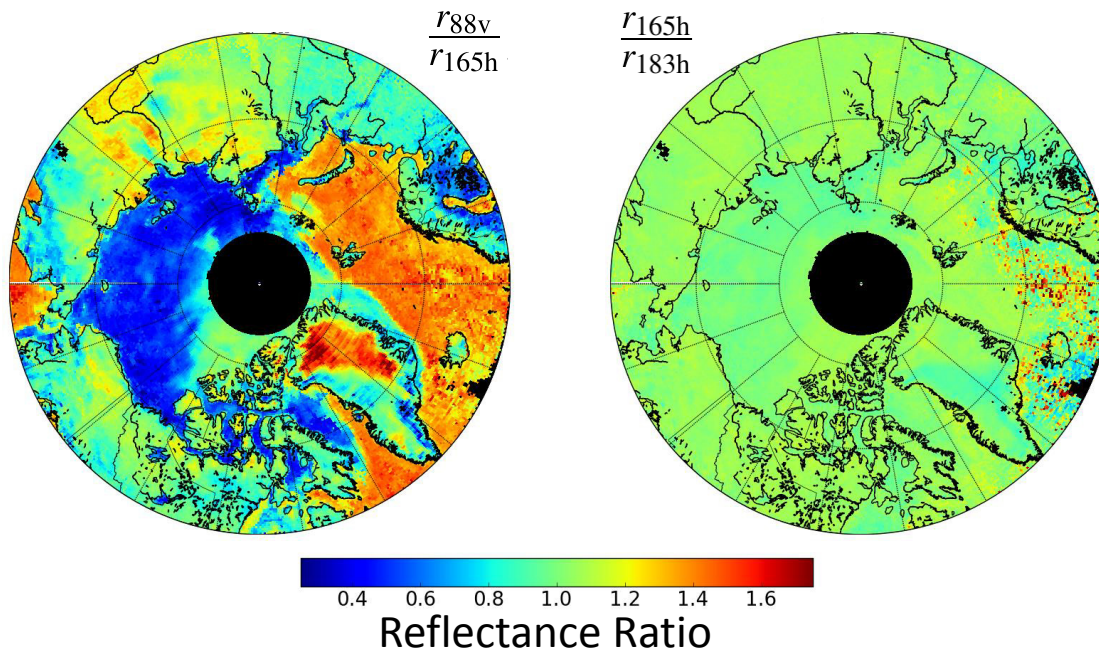
Figure 4.24: Reflectance ratio retrieval maps over the Arctic for December 2012 at $\frac{r_{88v}}{r_{165h}}$ and $\frac{r_{165h}}{r_{183h}}$ using the ATMS instrument.

Figure 4.25 shows ice type derived from the OSI-403-c product for December 15, 2012. At 88v GHz, surface emissivities are relatively large north of Alaska and Russia which correspond to first-year ice (FYI) according to Fig. 4.25. North of Canada, closer to the North pole, values are relatively smaller corresponding with regions of multi-year ice (MYI) as seen in Fig. 4.25. Surface emissivities are even smaller over the open Atlantic Ocean.

Surface emissivities at 165h GHz and 183h GHz show relatively small values when compared to FYI at 88v GHz. Open ocean has relatively large values when compared to measurements at 88v GHz. The relative difference between the surface emissivities at 165h GHz and 183h GHz over different surface types is smaller than at 88v GHz. Significant noise can be seen over open ocean at lower latitudes in the Atlantic ocean for 183h GHz surface emissivities; values should not be trusted in this region.

Figure 4.24 shows maps of reflectance ratio for $\frac{r_{88v}}{r_{165h}}$ and $\frac{r_{165h}}{r_{183h}}$. The $\frac{r_{88v}}{r_{165h}}$ easily distinguishes the surface types with large values over open ocean and part of Greenland, low values over FYI, and values near 1 for MYI and other land surfaces. Similar to the 88v GHz surface emissivities, significant structure can be seen over land. The $\frac{r_{165h}}{r_{183h}}$ shows very little structure in comparison to $\frac{r_{88v}}{r_{165h}}$. This reflectance ratio is nearly the same over most surface types with slightly larger values over land and open water compared to sea-ice.
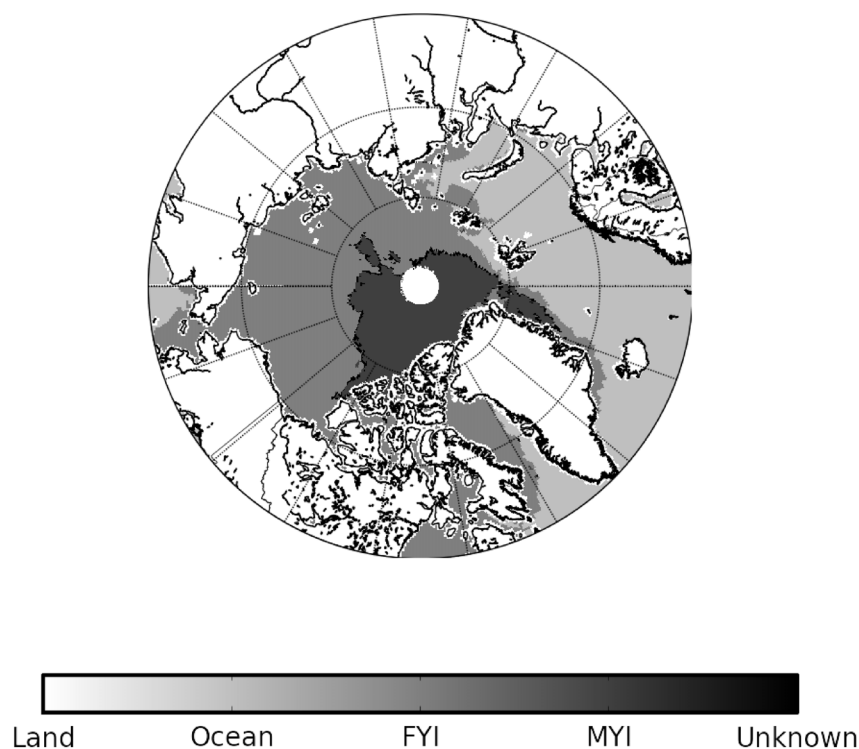
Figure 4.25: Ice type from the OSI-403-c product for Dec. 15, 2012. Surface types are split up as land, ocean, FYI, MYI, and unclassified.

As mentioned previously, over land there is large amount of structure in the reflectance ratios and surface emissivities, particularly over eastern Russia, Norther Europe, and Greenland. The reflectance ratios in Northern Europe could be affected by error induced by large water vapour columns. The features over eastern Russia could be associated with geophysical variations in the land surface. Figure 4.26 shows a surface elevation map for the Arctic from ERA-interim. The relatively small $\frac{r_{88v}}{r_{165h}}$ values in eastern Russia correspond to a region south of a mountain range. Some of the other $\frac{r_{88v}}{r_{165h}}$ structure over Russia also matches with the regions of low and high elevation. For Greenland, the elevated values of $\frac{r_{88v}}{r_{165h}}$ could be associated with old glacial ice. Figure 4.27 shows the total melt extent for Greenland for the melt season of 2010 (Mernild et al., 2011). The areas with no melt nearly match the $\frac{r_{88v}}{r_{165h}}$ feature over Greenland. Also, Hall et al. (2009) showed an elevated
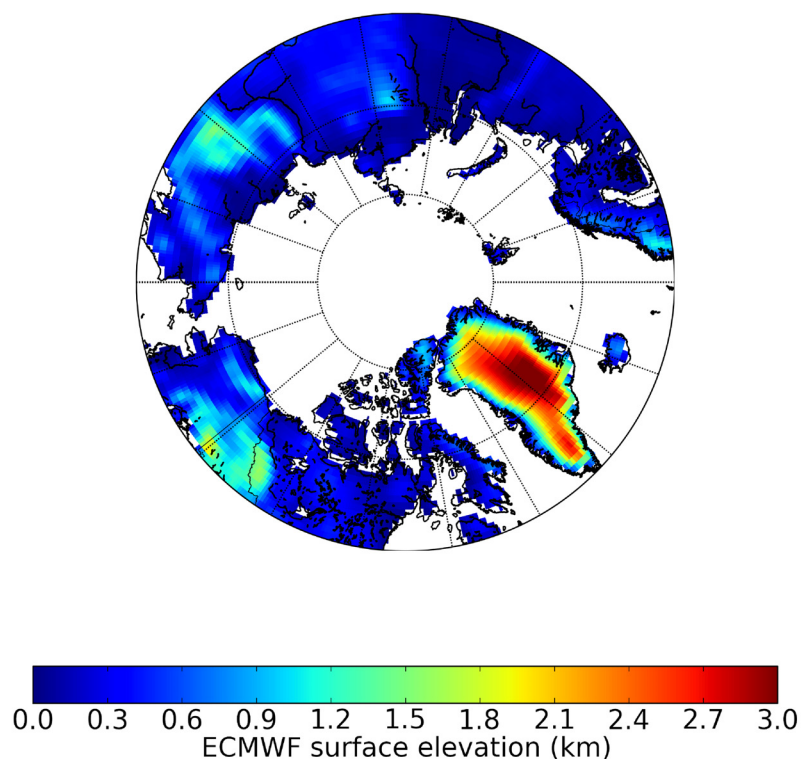
Figure 4.26: ERA-interim pan-Arctic surface elevation map.

albedo using MODIS over Greenland that was associated with the melt extent of glacial ice in Greenland. The MODIS product uses wavelengths in the range of 0.4 to 0.25 μm. Other factors might also be associated with this feature including surface elevation, surface roughness, and snow and ice properties over Greenland.

The lack of validation data makes it difficult to determine whether these features are geophysical or due to systematic errors in the retrieval. More measurements (e.g. from aircraft campaigns) are needed.

Figure 4.27: Greenland simulated and measured melt extent for 2010. Red and white regions are where there was or was not melt respectively according to the simulations. The black boundary was the boundary of melt and melt-free regions according to satellite measurements (Mernild et al., 2011).

Using a series of monthly reflectance ratio maps, the temporal change of reflectance ratio can be examined. Figure 4.28 shows pan-Arctic maps of reflectance ratio for $\frac{r_{88v}}{r_{165h}}$ for the months between November 2012 and April 2013. The maps show increasing sea ice extent as seen by the increasing extent of low $\frac{r_{88v}}{r_{165h}}$ values over the ocean. It is also possible to see lakes freeze when comparing the months of November and December in Northern Canada. The MYI extent grows as FYI ages as seen by the extension of typical MYI values north of Alaska. FYI values slowly increase later in the winter season as well. The increasing FYI values could be associated with FYI aging.

The $\frac{r_{88v}}{r_{165h}}$ anomaly over Greenland initially has a spatial extent that slowly decreases later in the winter season. However, the value of $\frac{r_{88v}}{r_{165h}}$ in the anomaly increases during the winter season. The decreasing spatial extent of the anomaly over Greenland could be associated with snow fall covering the old glacial ice near the margins.
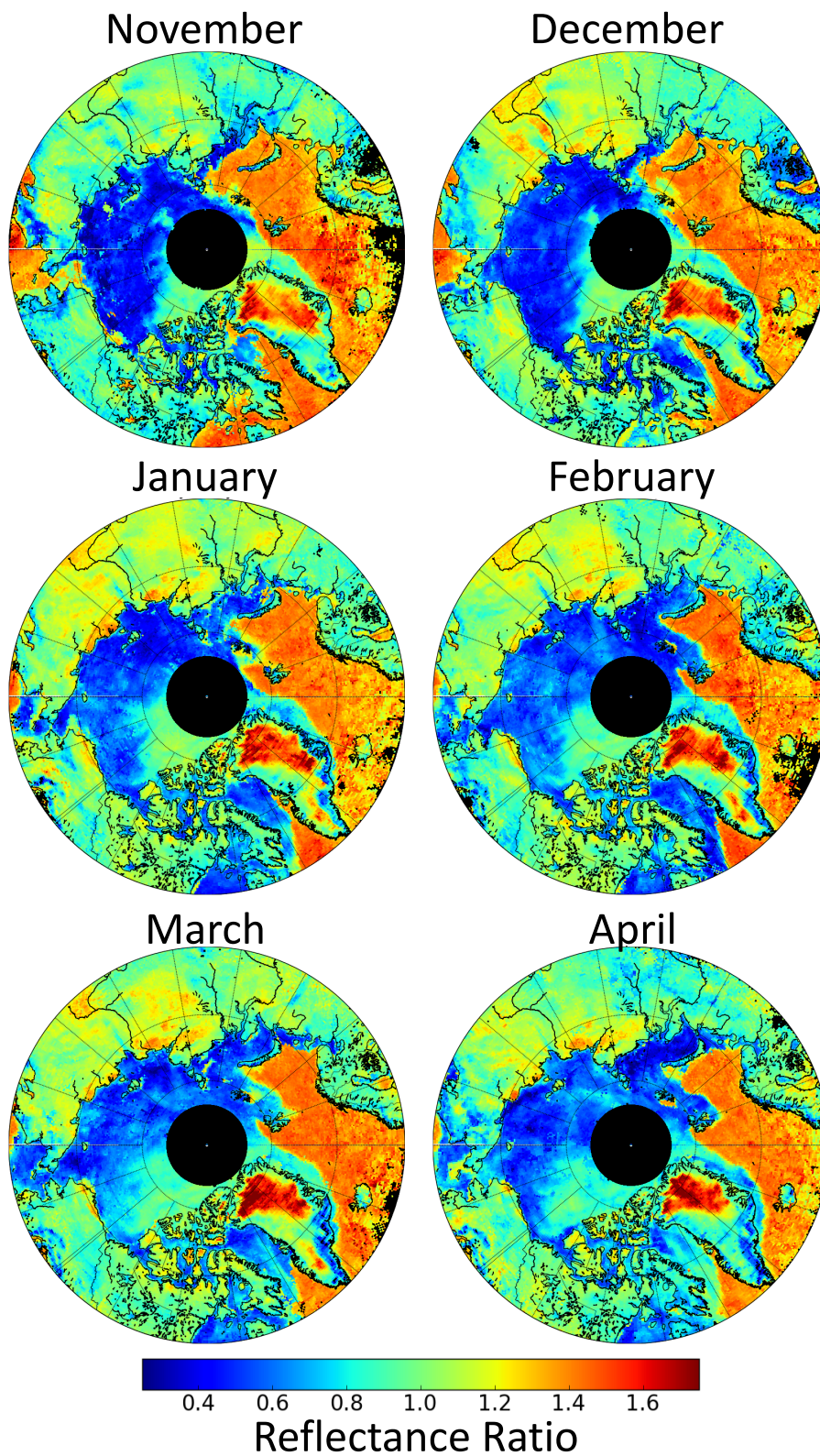
Figure 4.28: Monthly $\frac{r_{88v}}{r_{165h}}$ maps over the Arctic for November 2012 to April 2013 using the ATMS instrument.
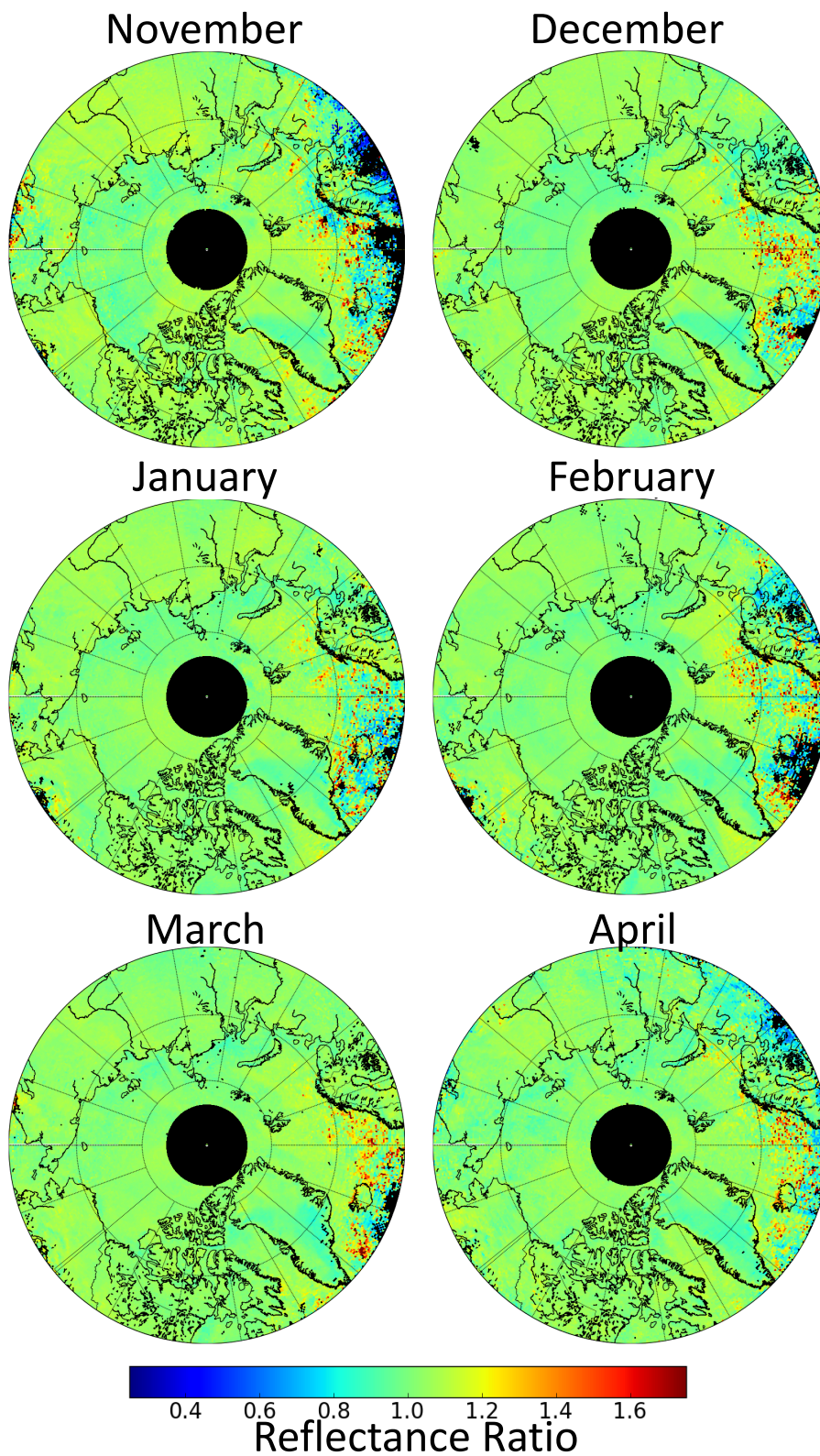
Figure 4.29: Monthly $\frac{r_{165h}}{r_{183h}}$ maps over the Arctic for November 2012 to April 2013 using the ATMS instrument.

Low $\frac{r_{88v}}{r_{165h}}$ values over eastern Russia increase later into the winter season to the point where it is equal to the surrounding region. Significant structure in $\frac{r_{88v}}{r_{165h}}$ over other parts of Russia are also persistent for multiple months. The long lifetime suggests that these are real surface features. If the features were from error induced by the auxiliary information, the features would likely not be persistent over long periods of time.

A large amount of noise over the open ocean is apparent in November 2012 compared other months later in the season. This is due to larger water vapour columns in the month of November.

Figure 4.29 shows maps of reflectance ratio for $\frac{r_{165h}}{r_{183h}}$ for the months of November 2012 to April 2013. Very little change can be seen in $\frac{r_{165h}}{r_{183h}}$ during the winter season. The noise decreases near the Atlantic Ocean after November as was seen for $\frac{r_{88v}}{r_{165h}}$. The enhancement over Greenland decreases slightly in size later in the winter season as well. There are also relatively small elevated regions of $\frac{r_{165h}}{r_{183h}}$ over land surfaces, particularly in November.

Pan-Arctic maps of surface emissivities and reflectance ratios showed significant differences over different surface types and within each surface type, particularly over land. The features were persistent over long periods of time suggesting the features are likely real and not artifacts due to the auxiliary information. Also, the features aligned with surface elevation in certain regions. Regions of different elevation likely have different surfaces in terms of roughness and vegetation. A feature with anomalously high reflectance ratios over Greenland was also shown that was likely associated with old glacial ice. The $\frac{r_{165h}}{r_{183h}}$ values were relatively equal over all surfaces when compared to $\frac{r_{88v}}{r_{165h}}$.

4.4.2 Validation

The following section examines surface emissivity and reflectance ratio distributions from open ocean, land, Greenland, first-year ice (FYI) and multi-year ice (MYI). Both measurements from ATMS and MHS are shown for each surface type and are compared to previously published results (Selbach, 2003; Hewison and English, 1999; Harlow, 2009, 2011). Surface emissivity and reflectance ratio retrievals are applied to ATMS and MHS overpasses from December 2012 to March 2013 for latitudes greater than 60°N. OSI-403-c was used to separate the surfaces, as described in the previous section.

The published surface emissivities from Hewison and English (1999), Selbach (2003),

and Harlow (2009, 2011) are from aircraft campaign measurements. The Microwave Airborne Radiometer Scanning System (MARSS) instrument (McGrath and Hewison, 2001) was used for each campaign. MARSS measures at 5 frequencies which are 88.992 GHz, 157.075 GHz, 183.248 ± 1.0 GHz, 183.248 ± 3.0 GHz, and 183.248 ± 7.0 GHz. At 88.992 GHz, the polarization is the same as the 89 GHz AMSU-B channel. The other frequencies have a mixed polarization which is horizontally polarized at one end of the scan angle and becomes vertically polarized with increasing scan angle.

Each publication used measurements from different campaigns except for Harlow (2009, 2011). These two papers, however, did use data from different overpasses. Hewison and English (1999) used the Hewison technique from Sect. 4.2.1 and assumed specular reflection at the surface. Selbach (2003) and Harlow (2009, 2011) used the Selbach technique from Sect. 4.2.2. Selbach (2003) assumed specular surface reflection, while Harlow (2009, 2011) assume Lambertian surface reflection. For specular reflection, nadir measurements were used and for Lambertian, all viewing angles were used. Harlow (2009) and Harlow (2011) use assumptions most compatible with this study.

The retrieved surface emissivities for satellites (MHS and ATMS) and aircraft campaigns are provided over different spatial ranges. The satellite measurements used in the comparison are over the entire Arctic surface while aircraft campaigns are from single flight paths. By comparing different spatial representations, differences are introduced between the satellite and aircraft data sets and is further discussed Sect. 4.4.3.

The local zenith angles of the satellite measurements are limited to values less than $10°$ to match other published results which employed nadir measurements (Hewison and English, 1999; Selbach, 2003). Also, measurements with water vapour columns less than $1.5\,\mathrm{kg\,m^{-2}}$ are used for the comparisons, which follows from the simulations in Sect. 4.3.

The ATMS and MHS have some channels with similar frequencies but different polarizations. Therefore, some surface emissivities and reflectance ratios from each instrument have different polarizations, i.e. the 165h and 157v GHz frequencies for ATMS and MHS. ATMS $\frac{r_{88v}}{r_{165h}}$ is a mixture of vertical and horizontal polarization and $\frac{r_{89v}}{r_{157v}}$ for MHS is vertically polarized. Also, ATMS $\frac{r_{165h}}{r_{183h}}$ is horizontally polarized and $\frac{r_{157v}}{r_{183v}}$ for MHS is vertically polarized.

The differences in polarization can cause differences in the retrieved surface emissivity or reflectance ratio. However, for specular reflection, the difference is minimized by

Table 4.3: Mode and standard deviations (SD) of surface emissivity and reflectance ratio distributions from measurements between December 2012 and March 2013 for ATMS and MHS. Mean surface emissivities from aircraft campaign measurements from Hewison and English (1999), Selbach (2003), and Harlow (2009, 2011) are also presented and are used to produce reflectance ratios.

	Emissivity Mode/Mean (SD)			Reflectance ratio Mode/Mean (SD)	
	88v/89v GHz	165h/157v GHz	183h GHz	$\frac{r_{88v}}{r_{165h}} / \frac{r_{89v}}{r_{157v}}$	$\frac{r_{165h}}{r_{183h}} / \frac{r_{157v}}{r_{183v}}$
Land					
MHS	0.741(0.078)	0.758(0.062)	0.761(0.097)	1.048(0.193)	0.985(0.094)
ATMS	0.750(0.073)	0.769(0.058)	0.778(0.052)	1.075(0.222)	1.049(0.050)
Harlow (2009)	0.757	0.694	0.676	0.794	0.944
Harlow (2009)	0.677	0.735	0.747	1.219	1.047
Greenland					
MHS	0.737(0.076)	0.835(0.059)	0.839(0.082)	1.507(0.342)	1.009(0.125)
ATMS	0.742(0.074)	0.854(0.053)	0.855(0.047)	1.597(0.419)	1.049(0.085)
Open Ocean					
MHS	0.690(0.049)	0.763(0.044)	0.807(0.081)	1.291(0.093)	1.118(0.159)
ATMS	0.676(0.043)	0.757(0.031)	0.777(0.033)	1.305(0.080)	1.076(0.032)
Selbach (2003)	0.638	0.712	0.732	1.257	1.075
Hewison and English (1999)	0.660	0.743	n/a	1.323	n/a
FYI					
MHS	0.893(0.055)	0.787(0.063)	0.789(0.097)	0.613(0.145)	0.912(0.087)
ATMS	0.913(0.051)	0.796(0.062)	0.793(0.058)	0.563(0.179)	1.016(0.052)
Harlow (2011)	0.864	0.763	0.753	0.570	0.960
Harlow (2011)	0.854	0.783	0.764	0.673	0.919
Harlow (2011)	0.799	0.759	0.761	0.834	1.008
Harlow (2011)	0.789	0.747	0.735	0.834	0.955
MYI					
MHS	0.747(0.045)	0.735(0.041)	0.754(0.093)	0.955(0.080)	0.982(0.082)
ATMS	0.751(0.043)	0.744(0.040)	0.755(0.036)	0.974(0.100)	1.048(0.039)
Harlow (2011)	0.693	0.701	0.717	1.027	1.057
Harlow (2011)	0.724	0.747	0.753	1.091	1.024

using near nadir angles. For Lambertian reflection, the surface emissivity is constant with changes in viewing angle and polarization (Maxwell, 1974; Matzler, 2005; Chuvieco et al., 2009) as discussed in Sect. 2.2.2. If the surfaces are not purely specular or Lambertian, polarizations may have an influence on surface emissivity at nadir. This is investigated in the following section.

4.4.2.1   Open Ocean

Open ocean brightness temperature measurements were classified using the OSI-403-c mask for latitudes greater than $60°$ and water vapour columns less than $1.5\ \mathrm{kg\,m^{-2}}$. The

resulting surface emissivity calculations from ATMS (MHS) are shown as probability densities in Fig. 4.30 for 88v (89v) GHz, 165h (157v) GHz, and 183h GHz. The surface emissivity modes from Table 4.3 for MHS at 89v GHz and 157v GHz are approximately 0.01 greater than ATMS at 88v GHz and 165h GHz. Similarly, the MHS mode is 0.03 greater for 183h GHz when compared to ATMS. For both instruments, the surface emissivities increase with increasing frequency.

Figure 4.30: Probability densities for the surface emissivity over open water using the ATMS (MHS) on board the Suomi-npp (MetOP-A) at 88v (89v) GHz, 165h (157v) GHz, and 183h GHz. Overpasses from December 2012 to March 2013 were used for latitudes greater than 60 $^\circ$ and less than 1.5 $\mathrm{kg\,m^{-2}}$ water vapour column. Vertical cyan lines represent results from Selbach (2003) and red lines are from Hewison and English (1999).

The surface emissivity distributions are similar in terms of shape and width between ATMS and MHS except at 183h GHz, where the MHS distribution is more than twice as wide in terms of standard deviation when compared to ATMS. The difference in the modes and distribution widths would be due to the MHS 183h GHz measurement being more sensitive to retrieval errors due to the more strongly absorbed frequencies. The offset between the modes of ATMS at 88v GHz and MHS at 89v GHz are due to the use of skin temperatures from the 183h GHz retrieval. This is also true for the offset between ATMS at 165h GHz and MHS at 157v GHz.

For the ATMS measurements, instrument noise accounts for about 25% of the distribution width (see Table 4.2). For MHS, the instrument noise can account for up to 40% of the distribution width at 89v GHz and 157v GHz, while at 183h GHz it accounts for approximately 50%. This difference is due to instrument noise having a larger effect for more strongly absorbed frequencies.

The other sources of error from Sect. 4.3 may account for part of the remaining distribution width. Polarization does not seem to influence the retrievals over open ocean near nadir. ATMS and MHS have equal polarizations except for the 165h and 157v GHz. The ATMS surface emissivity is slightly larger at 165h GHz when compared to MHS at 157v GHz, but this is also true when comparing ATMS at 88v GHz and MHS at 89v GHz. This indicates the offset between the instruments is not due to polarization. Also, the OSI-403-c classification could produce a small error due to misclassification of surface types for the ocean. However, it is difficult to quantify the other sources of error. For open ocean, surface emissivity distributions are expected to have little geophysical variation. Any geophysical variation would be caused by waves. Therefore, the standard deviations for open ocean represents an estimate of the maximum retrieval noise.

Figure 4.31: Probability densities for the reflectance ratio over open water surfaces using the ATMS (MHS) on board the Suomi-npp (MetOP-A) for $\frac{r_{88v}}{r_{165h}}$ ($\frac{r_{89v}}{r_{157v}}$) and $\frac{r_{165h}}{r_{183h}}$ ($\frac{r_{157v}}{r_{183v}}$). Overpasses from December 2012 to March 2013 were used for latitudes greater than $60\,°$ and less than $1.5\,\mathrm{kg\,m^{-2}}$ water vapour column. Vertical cyan lines represent results from Selbach (2003) and red lines are from Hewison and English (1999).

Mean surface emissivities from Selbach (2003) and Hewison and English (1999) are shown in Fig. 4.30 and Table 4.3 for open ocean. The published results are within the distributions of the ATMS and MHS surface emissivities. The mean surface emissivities from Hewison and English (1999) are approximately 0.5 SD less than the ATMS (MHS) retrieval modes for 88v (89v) GHz and 165h (157v) GHz. Hewison and English (1999) did not have measurements at 183h GHz. Selbach (2003) mean surface emissivities are greater than 1 SD less than ATMS and MHS modes for all frequencies. The differences between Selbach (2003) and Hewison and English (1999) are either due to the differences in retrieval methods or differences in their data sets.

The $\frac{r_{88v}}{r_{165h}}\left(\frac{r_{89v}}{r_{157v}}\right)$ and $\frac{r_{165h}}{r_{183h}}\left(\frac{r_{157v}}{r_{183v}}\right)$ for ATMS (MHS) were calculated using the previous surface emissivity calculations for open ocean and are shown as probability densities in Fig. 4.31. The $\frac{r_{88v}}{r_{165h}}$ and $\frac{r_{165h}}{r_{183h}}$ modes for ATMS are 0.14 greater and 0.042 less than $\frac{r_{89v}}{r_{157v}}$ and $\frac{r_{157v}}{r_{183v}}$ for MHS respectively. While the standard deviations and shape for ATMS and MHS are approximately equal for $\frac{r_{88v}}{r_{165h}}$ and $\frac{r_{89v}}{r_{157v}}$ respectively, the standard deviation of $\frac{r_{165h}}{r_{183h}}$ for ATMS is five times smaller for $\frac{r_{157v}}{r_{183v}}$ for MHS. This is due to retrieval error being larger for more strongly absorbed frequencies. The width of the $\frac{r_{165h}}{r_{183h}}$ distribution for ATMS is significantly smaller than $\frac{r_{157v}}{r_{183v}}$ for MHS and is due to the instrument noise having a larger effect on more strongly absorbed frequencies. Most of the ATMS and MHS distributions span the same reflectance ratio range.

The mean surface emissivities from the published results were used to derive $\frac{r_{89}}{r_{157}}$ and $\frac{r_{157}}{r_{183}}$. The published results are within the ATMS and MHS distributions. For both reflectance ratios, the published results nearly match the ATMS and MHS modes.

ATMS and MHS surface emissivity and reflectance ratios modes were similar for all frequencies over open ocean. MHS surface emissivities were consistently slightly larger than those of ATMS. The reflectance ratio, $\frac{r_{88v}}{r_{165h}}$ was slightly greater than $\frac{r_{89v}}{r_{157v}}$ and $\frac{r_{165h}}{r_{183h}}$ was smaller than $\frac{r_{157v}}{r_{183v}}$ when comparing ATMS to MHS. Published aircraft campaign measurements show good agreement as they were well within the ATMS and MHS distributions of surface emissivity and reflectance ratio. This justifies that the retrievals performed on ATMS and MHS measurements were accurate.

4.4.2.2 Land

Land brightness temperature measurements were identified using the OSI-403-c mask for latitudes greater than $60°$ and water vapour columns less than $1.5\ \mathrm{kg\,m^{-2}}$. Measurements over Greenland are treated separately owing to the anomalous behaviour shown in Sect. 4.4.1.

Surface emissivity probability densities are shown in Fig. 4.32 at 88v (89v) GHz, 165h (157v) GHz, and 183h GHz for ATMS (MHS). At each frequency, the surface emissivities span a range of values producing a near Gaussian distribution for each instrument. The modes from Table 4.3 for MHS are approximately 0.01 less at all frequencies when compared to ATMS. The surface emissivities increase slightly with increasing frequency for both instruments.

The surface emissivity distributions are similar in terms of shape and width between ATMS and MHS except at 183h GHz. The MHS distribution width at 183h GHz in terms of standard deviation is twice as large when compared to ATMS. The difference in the modes and distribution widths is due to the MHS 183h GHz measurement being more sensitive to retrieval errors due to the more strongly absorbed frequencies. The offset between the modes of ATMS at 88v GHz and MHS at 89v GHz are due to the use of skin temperatures from the 183h GHz retrieval. This is also true for the offset between the ATMS at 165h GHz and MHS at 157v GHz.

Figure 4.32: Probability densities for the surface emissivity over land surfaces using the ATMS (MHS) on board the Suomi-npp (MetOP-A) for 88v (89v) GHz, 165h (157v) GHz, and 183h GHz. Overpasses from December 2012 to March 2013 were used for latitudes greater than $60\,^\circ$ and less than $1.5\,\mathrm{kg\,m^{-2}}$ water vapour column. Vertical green lines represent other published results.

For the ATMS measurements, instrument noise only accounts for about 15% of the distribution width when compared to Table 4.2. For MHS, instrument noise accounts for up to 25% of the distribution width at 89v GHz and 157v GHz, while at 183h GHz it accounts for approximately 50%. The differences in relative noise contribution to ATMS and MHS distributions of surface emissivity is due to the more strongly absorbed frequencies used for the MHS 183h GHz retrieval.

The difference in surface emissivity distribution width for land and open ocean can give an estimate for how much of the distribution is caused by retrieval noise and geophysical variation. The land distribution widths for ATMS in terms of standard deviation are 0.032 larger for 88v GHz, 0.027 larger for 165h GHz, and 0.019 larger for 183h GHz and for MHS they are 0.029 larger for 89v GHz, 0.018 larger for 157v GHz, and 0.016 larger for 183h GHz. These differences are likely due to geophysical variation. The surface emissivity

distribution difference is largest at 88v (89v) GHz for ATMS (MHS), which agrees with the Arctic surface emissivity maps that showed larger variation in surface emissivity over land surfaces at that frequency when compared to other frequencies.

Polarization does not seem to influence the retrievals over land surfaces near nadir. ATMS and MHS have equal polarizations except for the 165h and 157v GHz. As described earlier, the ATMS surface emissivity is slightly larger at 165h GHz when compared to MHS at 157v GHz, but this is also true when comparing ATMS at 88v GHz and MHS at 89v GHz. This indicates the offset between the instruments is not due to polarization.

Figure 4.33: Probability densities for the reflectance ratio over land surfaces using the ATMS (MHS) on board the Suomi-npp (MetOP-A) for $\frac{r_{88v}}{r_{165h}}$ ($\frac{r_{89v}}{r_{157v}}$) and $\frac{r_{165h}}{r_{183h}}$ ($\frac{r_{157v}}{r_{183v}}$). Over-passes from December 2012 to March 2013 were used for latitudes greater than $60\,^\circ$ and less than $1.5\,\mathrm{kg\,m^{-2}}$ water vapour column. Vertical green lines represent published results from Harlow (2009).

Mean surface emissivities from two flight paths over land from Harlow (2009) are over-laid in Fig. 4.32. Both of Harlow's measurements are within the ATMS and MHS distri-butions. The first flight path from Harlow (2009) nearly matched the modes from ATMS (MHS) at 88v (89v) GHz. At 88v (89v) GHz, the second flight path was approximately 1 SD less. At 165h (157v) GHz, the first flight path from Harlow (2009) was more than 1 SD less than ATMS (MHS) modes while the second flight path was approximately 0.5 SD less. For 183h GHz, the second flight path was close to the ATMS (MHS) modes, but the first flight path result was 1 SD less than the mode of the MHS distribution and approxi-mately 2 SD from the ATMS mode. The first flight path result at 183h GHz is closer to the MHS result in terms of standard deviation due to the larger standard deviation caused by increased retrieval error.

The $\frac{r_{88v}}{r_{165h}}$ ($\frac{r_{89v}}{r_{157v}}$) and $\frac{r_{165h}}{r_{183h}}$($\frac{r_{157v}}{r_{183v}}$) for ATMS (MHS) were calculated using the previous

surface emissivity calculations over land and are shown as probability densities in Fig. 4.33. The reflectance ratio modes for ATMS $\frac{r_{88v}}{r_{165h}}$ and $\frac{r_{165h}}{r_{183h}}$ are 0.027 and 0.064 greater than $\frac{r_{89v}}{r_{157v}}$ and $\frac{r_{157v}}{r_{183v}}$ for MHS respectively. The standard deviation for ATMS and MHS is approximately equal for $\frac{r_{88v}}{r_{165h}}$ and $\frac{r_{89v}}{r_{157v}}$ while ATMS is twice as small as MHS for $\frac{r_{165h}}{r_{183h}}$ and $\frac{r_{157v}}{r_{183v}}$, which is due to the instrument noise having a larger effect on more strongly absorbed frequencies. Most of the ATMS and MHS distributions span the same reflectance ratio range.

The mean surface emissivities from the published results were used to derive $\frac{r_{89}}{r_{157}}$ and $\frac{r_{157}}{r_{183}}$. The published results are within the ATMS and MHS distributions. For $\frac{r_{88v}}{r_{165h}}$ ($\frac{r_{89v}}{r_{157v}}$) from ATMS (MHS), the modes are greater than 1 SD apart from the published results. The $\frac{r_{165h}}{r_{183h}}$ mode for ATMS is approximately 2 SD larger for the first flight path, but almost equal to the second flight path. Due to the large distribution width of MHS $\frac{r_{157v}}{r_{183v}}$, the two flight paths are much less than 1 SD from the MHS mode.

ATMS and MHS surface emissivity and reflectance ratios modes were similar for all frequencies over land with a small difference where ATMS is slightly larger than MHS for all frequencies. Published aircraft campaign measurements show good agreement as they were well within the ATMS and MHS distributions of surface emissivity and reflectance ratio. This suggests that the retrievals performed on ATMS and MHS measurements were accurate.

4.4.2.3 Greenland

The results for surface emissivity and reflectance ratio over Greenland are different from other surfaces in the Arctic. Figure 4.34 shows probability densities for surface emissivity over Greenland. At each frequency, the surface emissivities span a similar range of values as over land. As in the previous section, ATMS modes are 0.01 greater than MHS at all frequencies.

The modes of the surface emissivity distributions at 165h (157v) GHz and 183h GHz for ATMS (MHS) are larger than other land surfaces. The surface emissivities at 88v (89v) GHz are approximately 0.01 less than over land, but, at 165h (157v) GHz and 183h GHz, the surface emissivities are approximately 0.01 greater than the other land surfaces as shown in Table 4.3.

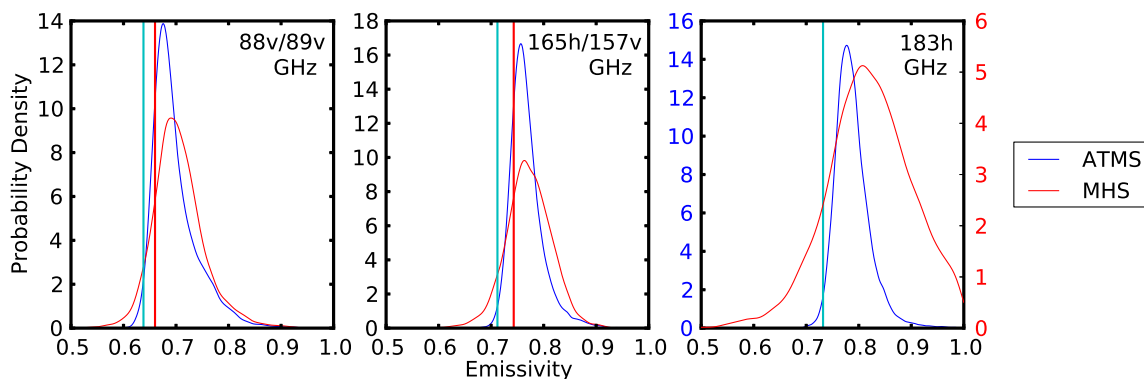The surface emissivity distributions are similar in terms of shape and width between
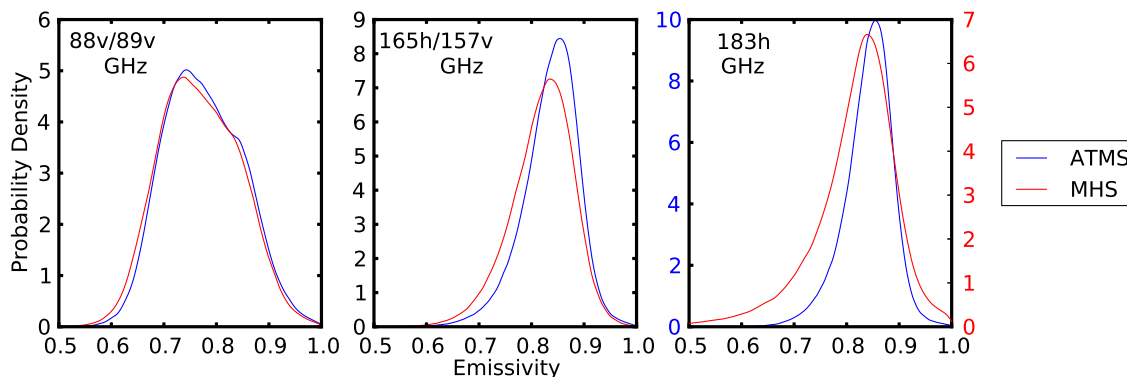
Figure 4.34: Probability densities for the surface emissivity over Greenland using the ATMS (MHS) on board the Suomi-npp (MetOP-A) for 88v (89v) GHz, 165h (157v) GHz, and 183h GHz. Overpasses from December 2012 to March 2013 were used for latitudes greater than 60 ° and less than 1.5 kg m^{-2} water vapour column.

ATMS and MHS except at 183h GHz. The MHS distribution at 183h GHz has a standard deviation that is almost twice as large as the ATMS distribution. The difference in the modes and distribution widths is due to the MHS 183h GHz measurement being more sensitive to retrieval errors due to the more strongly absorbed frequencies. The offset between the modes of ATMS at 88v GHz and MHS at 89v GHz are due to the use of skin temperatures from the 183h GHz retrieval. This is also true for the offset between the ATMS at 165h GHz and MHS at 157v GHz.

For the ATMS measurements, instrument noise accounts for about 15% of the distribution width when compared to Table 4.2. For MHS, the instrument noise can account for up to 25% of the distribution width at 89v GHz and 157v GHz while at 183h GHz it accounts for approximately 50%. The difference between ATMS and MHS is due to the more strongly absorbed frequencies used for the MHS 183h GHz retrieval. The different polarizations for ATMS and MHS at 165h GHz and 157v GHz respectively do not seem to influence the retrievals for Greenland near nadir since the difference between 165h GHz and 157v GHz is similar in size to the other frequencies.

Comparing the distribution widths to open ocean show Greenland distribution widths for ATMS are 0.031 larger for 88v GHz, 0.022 larger for 165h GHz, and 0.014 larger for 183h GHz and for MHS they are 0.027 larger for 89v GHz, 0.015 larger for 157v GHz, and 0.001 larger for 183h GHz. These differences are likely due to geophysical variation. The small difference for MHS at 183h GHz is likely due to retrieval error masking the geophysical variation. The change in width of the surface emissivity distribution is largest

for 88v (89v) GHz, which agrees with the Arctic surface emissivity maps that showed larger variation in surface emissivity over Greenland at that frequency when compared to other frequencies.
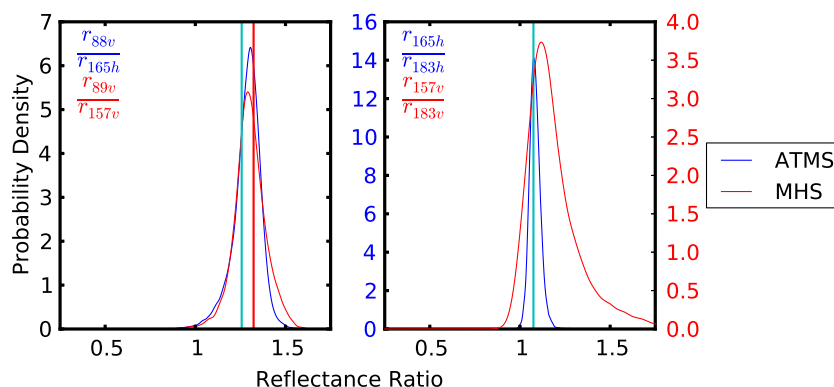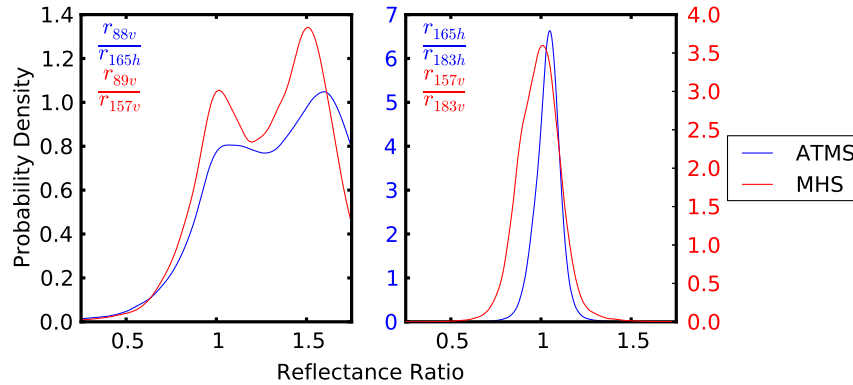

Figure 4.35: Probability densities for the reflectance ratios over Greenland using the ATMS (MHS) on board the Suomi-npp (MetOP-A) for $\frac{r_{88v}}{r_{165h}}$ ($\frac{r_{89v}}{r_{157v}}$) and $\frac{r_{165h}}{r_{183h}}$ ($\frac{r_{157v}}{r_{183v}}$). Overpasses from December 2012 to March 2013 were used for latitudes greater than $60\,^\circ$ and less than $1.5\,\mathrm{kg\,m^{-2}}$ water vapour column.

Figure 4.35 shows probability densities for reflectance ratios over Greenland. For $\frac{r_{88v}}{r_{165h}}$ ($\frac{r_{89v}}{r_{157v}}$) from ATMS (MHS), two modes are seen by both instruments. The first mode represents values from the region of Greenland that has similar reflectance ratios to other land surfaces, while the second mode represents the anomalous values mentioned in Sect. 4.4.1 which could be associated with old glacial ice. For $\frac{r_{165h}}{r_{183h}}$ ($\frac{r_{157v}}{r_{183v}}$), the values are approximately the same as other land surfaces shown in Table 4.3. ATMS $\frac{r_{88v}}{r_{165h}}$ and $\frac{r_{165h}}{r_{183h}}$ are 0.09 and 0.04 greater than $\frac{r_{89v}}{r_{157v}}$ and $\frac{r_{157v}}{r_{183v}}$ for MHS respectively. The width of the $\frac{r_{165h}}{r_{183h}}$ distribution for ATMS is significantly smaller than $\frac{r_{157v}}{r_{183v}}$ for MHS and is due to the instrument noise having a larger effect on more strongly absorbed frequencies. Most of the ATMS and MHS distributions span the same reflectance ratio range.

There were no published values to compare to over Greenland. An aircraft campaign over Greenland would be beneficial in determining if the anomalous surface emissivities and reflectance ratios over Greenland are valid. A published result using the Moderate-Resolution Imaging Spectroradiometer (MODIS) measurements showed larger reflectances over Greenland as well (Hall et al., 2009) indicating the previous results could be real, but these measurements were in the visible and infrared spectrum. Overall, ATMS and MHS surface emissivity and reflectance ratios modes were similar for all frequencies for Greenland with ATMS being slightly larger than MHS for all frequencies.

4.4.2.4   First-Year and Multi-Year Sea Ice

Sea-ice measurements were classified using the OSI-403-c mask for latitudes greater than $60°$ and water vapour columns less than $1.5 \ kg\,m^{-2}$. The OSI-403-c mask is also used to distinguish first-year ice (FYI) and multi-year ice (MYI).

Surface emissivity probability densities from ATMS (MHS) are shown in Fig. 4.36 for FYI at 88v (89v) GHz, 165h (157v) GHz, and 183h GHz. At each frequency, the surface emissivities span a larger range of values than open ocean, but smaller than land surfaces. FYI surface emissivity decreases with increasing frequency and the surface emissivity mode for 88v (89v) GHz is large compared to the other surfaces. Table 4.3 shows the surface emissivities and reflectance ratios and corresponding standard deviations for both ATMS, MHS, and aircraft campaigns and shows ATMS modes range from being 0.004 to 0.02 greater than MHS modes. At 183h GHz, MHS surface emissivities are less than ATMS due to the more strongly absorbed frequencies. The offset between the modes of ATMS at 88v GHz and MHS at 89v GHz are due to the use of skin temperatures from the 183h GHz retrieval. This is also true for the offset between the ATMS at 165h GHz and MHS at 157v GHz.
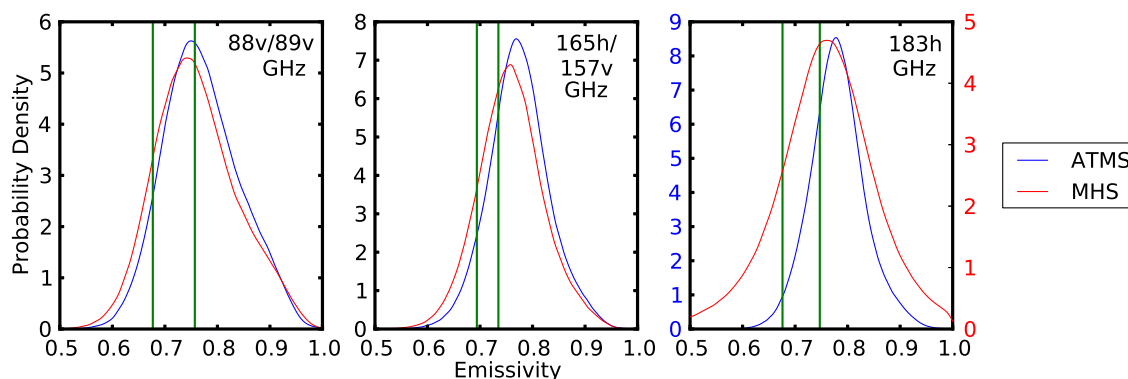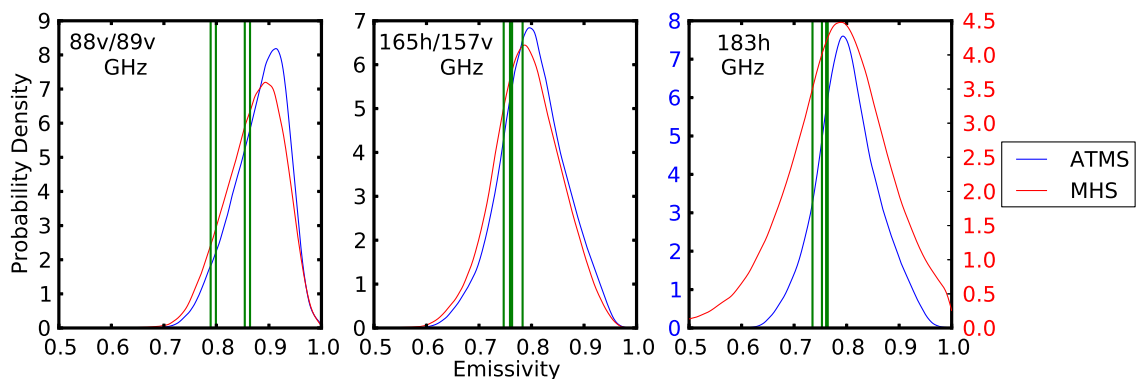

Figure 4.36: Probability densities for the surface emissivity over first year ice surfaces using the ATMS (MHS) on board the Suomi-npp (MetOP-A) for MYI at 88v (89v) GHz, 165h (157v) GHz, and 183h GHz. Overpasses from December 2012 to March 2013 were used for latitudes greater than 60 $°$ and less than $1.5 \ kg\,m^{-2}$ water vapour column. Vertical green lines represent other published results.

Similar to the previous surfaces, the surface emissivity distributions are similar in terms of shape and width between ATMS and MHS except at 183h GHz. The MHS distribution at 183h GHz has a standard deviation twice as large as the ATMS distribution. This is due

to the MHS 183h GHz measurement using more strongly absorbed frequencies.

For the ATMS measurements, instrument noise accounts for about 15% of the distribution width when compared to Table 4.2. For MHS, the instrument noise can account for up to 30% of the distribution width at 89v GHz and 157v GHz, while at 183h GHz it accounts for approximately 50%. The difference between ATMS and MHS is due to the more strongly absorbed frequencies used for the MHS 183h GHz retrieval.

Comparing the distribution widths to open ocean show FYI distributions widths for ATMS are 0.008 larger at 88v GHz, 0.031 larger at 165h GHz, and 0.025 larger at 183h GHz and for MHS are 0.006 larger at 89v GHz, 0.019 larger at 157v GHz, and 0.016 larger at 183h GHz. The larger distribution widths than when compared to open ocean is likely accounted for by geophysical variation. However, the increase in distribution width is small for ATMS (MHS) at 88v (89v) GHz, which is where the largest difference was seen for other surfaces while 165h (157v) GHz showed the largest difference compared to the other frequencies for FYI. As with the previous surfaces, the different polarizations at 165h GHz and 157v GHz for ATMS and MHS respectively likely has a negligible effect on retrieved surface emissivity.

For FYI, there are four different results for surface emissivity from Harlow (2009, 2011) overlaid in Fig. 4.36 and summarized in Table 4.3. The published results were within the retrievals distributions. The published surface emissivity results were within 1 SD or less of the ATMS (MHS) modes at 165h (157v) GHz and 183h GHz. At 88v (89v) GHz, the published results range from 1 to 2.5 SD apart from the ATMS (MHS) modes.

The $\frac{r_{88v}}{r_{165h}}$ ($\frac{r_{89v}}{r_{157v}}$) and $\frac{r_{165h}}{r_{183h}}$ ($\frac{r_{157v}}{r_{183v}}$) probability densities for ATMS (MHS) are shown in Fig. 4.39 and summarized in Table 4.3. The $\frac{r_{88v}}{r_{165h}}$ ($\frac{r_{89v}}{r_{157v}}$) mode is significantly smaller compared to the other surface types. The MHS distribution for $\frac{r_{157v}}{r_{183v}}$ is less than 2 times wider than $\frac{r_{165h}}{r_{183h}}$ for ATMS due to the more strongly absorbed frequencies used in the 183h GHz surface emissivity retrieval. The $\frac{r_{89v}}{r_{157v}}$ mode for MHS is 0.05 greater than $\frac{r_{88v}}{r_{165h}}$ for ATMS and the MHS $\frac{r_{157v}}{r_{183v}}$ mode is 0.096 less than $\frac{r_{165h}}{r_{183h}}$ for ATMS. Most of the ATMS and MHS distributions span the same range in reflectance ratio.

The mean surface emissivities from the published results were used to derive $\frac{r_{89}}{r_{157}}$ and $\frac{r_{157}}{r_{183}}$. The published results are within the ATMS and MHS distributions. For $\frac{r_{88v}}{r_{165h}}$ ($\frac{r_{89v}}{r_{157v}}$) from ATMS (MHS), the modes range from nearly equal to 1.5 SD apart from the published results. For $\frac{r_{165h}}{r_{183h}}$ ($\frac{r_{157v}}{r_{183v}}$), the modes range from nearly equal to 2 SD apart from the published
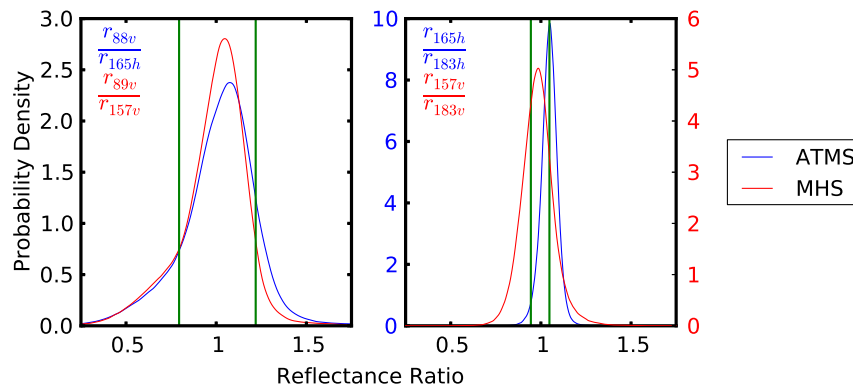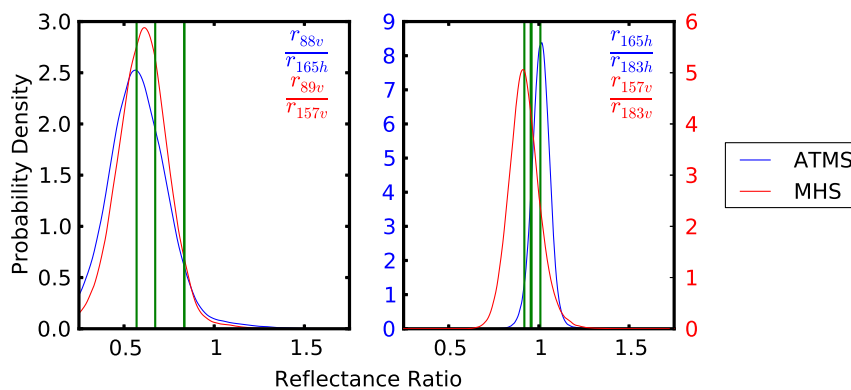
Figure 4.37: Probability densities for the reflectance ratio over first year ice surfaces using the ATMS (MHS) on board the Suomi-npp (MetOP-A) for $\frac{r_{88v}}{r_{165h}}$ ($\frac{r_{89v}}{r_{157v}}$) and $\frac{r_{165h}}{r_{183h}}$ ($\frac{r_{157v}}{r_{183v}}$). Overpasses from December 2012 to March 2013 were used for latitudes greater than 60 $^\circ$ and less than 1.5 kg m^{-2} water vapour column. Vertical green lines represent other published results.

results.

MYI surface emissivity probability densities are shown in Fig. 4.38 for ATMS (MHS) at 88v (89v) GHz, 165h (157v) GHz, and 183h GHz. At each frequency, the surface emissivities span a smaller range of values than FYI. MYI modes are almost equal for all three frequencies for both satellite instruments.

Similar to FYI, surface emissivity distributions are similar in terms of shape and width between ATMS and MHS except at 183h GHz. The MHS distribution at 183h GHz has a standard deviation that is almost three times larger than ATMS. This is due to the MHS 183h GHz measurement using more strongly absorbed frequencies.

For the ATMS measurements, instrument noise accounts for about 25% of the distribution width when compared to Table 4.2. For MHS, the instrument noise can account for up to 50% of the distribution width at 89v GHz, 157v GHz, and 183h GHz. The difference between ATMS and MHS is due to the more strongly absorbed frequencies used for the MHS 183h GHz retrieval. The larger relative contribution from instrument noise for MYI compared to FYI is likely due to there being less geophysical variation for MYI. Newer ice can have a larger range of surface emissivities depending on how it was formed (Hewison and English, 1999).

Comparing the distribution widths for open ocean show MYI distributions widths for ATMS are equal at 88v GHz, 0.009 larger at 165h GHz, and 0.003 smaller at 183h GHz and for MHS are 0.004 smaller at 89v GHz, 0.003 smaller at 157v GHz, and 0.004 smaller

at 183h GHz. The smaller or equal distribution widths for MYI compared to open ocean indicate there is very little geophysical variation, perhaps even less than what is caused by waves. This agrees with the Arctic maps of surface emissivity where the variation was smaller over MYI surfaces than land surfaces. As with the previous surfaces, the difference in polarization at 165h GHz and 157v GHz for ATMS and MHS respectively likely has a negligible effect.
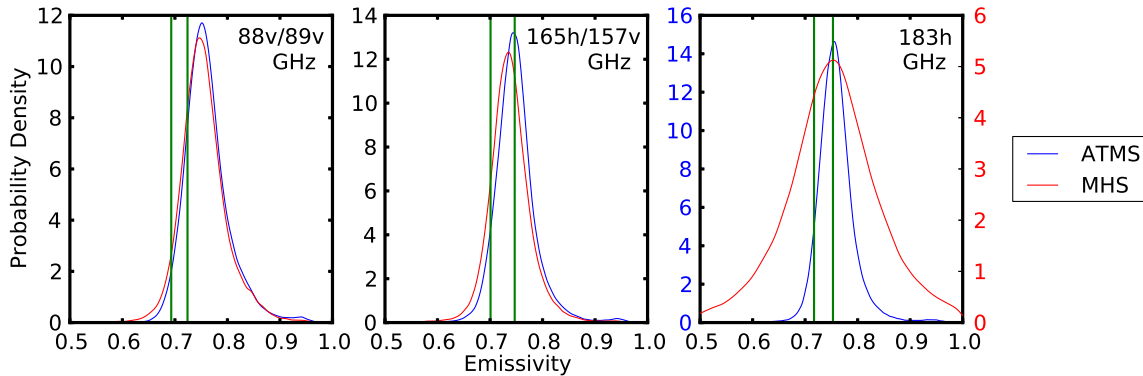
Figure 4.38: Probability densities for the surface emissivity over multi year ice surfaces using the ATMS (MHS) on board the Suomi-npp (MetOP-A) for MYI at 88v (89v) GHz, 165h (157v) GHz, and 183h GHz. Overpasses from December 2012 to March 2013 were used for latitudes greater than 60 $^\circ$ and less than 1.5 $\mathrm{kg\,m^{-2}}$ water vapour column. Vertical green lines represent other published results.

For MYI, there are two different published results shown from Harlow (2011) overlaid in Fig. 4.38 and summarized in Table 4.3. The published results were within the retrieved distributions. All the published results were 1.5 SD or less than the ATMS and MHS modes at all frequencies.

The $\frac{r_{88v}}{r_{165h}}$ ($\frac{r_{89v}}{r_{157v}}$) and $\frac{r_{165h}}{r_{183h}}$ ($\frac{r_{157v}}{r_{183v}}$) probability densities for ATMS (MHS) were calculated using the previous surface emissivity calculations and are shown in Fig. 4.39. The modes for $\frac{r_{88v}}{r_{165h}}$ and $\frac{r_{165h}}{r_{183h}}$ for ATMS are 0.019 and 0.064 greater than $\frac{r_{89v}}{r_{157v}}$ and $\frac{r_{157v}}{r_{183v}}$ for MHS. Similar to the other surface types, the $\frac{r_{157v}}{r_{183v}}$ for MHS has a distribution that is less than three times wider than $\frac{r_{165h}}{r_{183h}}$ for ATMS.

The mean surface emissivities from the published results were used to derive $\frac{r_{89}}{r_{157}}$ and $\frac{r_{157}}{r_{183}}$. The published results are within the ATMS and MHS distributions. For $\frac{r_{88v}}{r_{165h}}$ ($\frac{r_{89v}}{r_{157v}}$) from ATMS (MHS), the modes are 0.5 SD and 2 SD apart from the first published result for ATMS and MHS respectively. For $\frac{r_{165h}}{r_{183h}}$ ($\frac{r_{157v}}{r_{183v}}$), the modes range from being nearly equal to 1 SD greater than both published results.
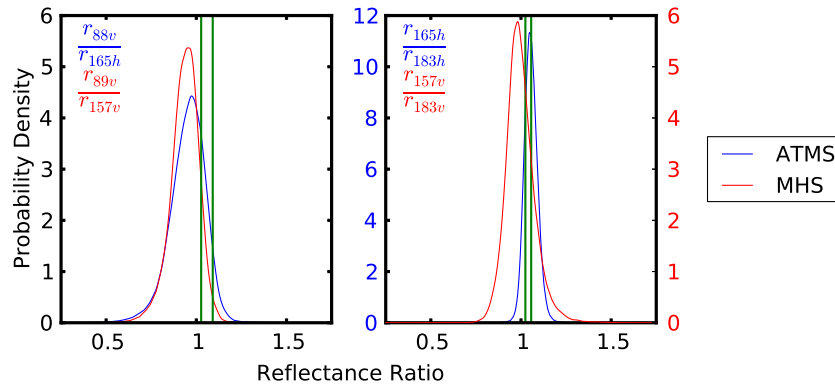
Figure 4.39: Probability densities for the reflectance ratio over multi year ice surfaces using the ATMS (MHS) on board the Suomi-npp (MetOP-A) for MYI at $\frac{r_{88v}}{r_{165h}}$ ($\frac{r_{89v}}{r_{157v}}$) and $\frac{r_{165h}}{r_{183h}}$ ($\frac{r_{157v}}{r_{183v}}$). Overpasses from December 2012 to March 2013 were used for latitudes greater than 60 $^\circ$ and less than 1.5 kg m^{-2} water vapour column. Vertical lines represent other published results.

The surface emissivity and reflectance ratio results for FYI and MYI are significantly different even though they are both sea ice surfaces. For all three frequencies FYI is greater than MYI surface emissivities and the difference between the two ice types decreases with increasing frequency. The $\frac{r_{88v}}{r_{165h}}$ ($\frac{r_{89v}}{r_{157v}}$) from ATMS (MHS) is significantly less for FYI when compared to MYI and any other surface. Similar to the other surface types, $\frac{r_{165h}}{r_{183h}}$ ($\frac{r_{157v}}{r_{183v}}$) are nearly equal for FYI and MYI surfaces.

ATMS and MHS surface emissivity and reflectance ratios modes were similar for all frequencies over FYI and MYI with small differences where ATMS is slightly larger than MHS for all frequencies when comparing surface emissivities. For reflectance ratios, ATMS is larger except for $\frac{r_{88v}}{r_{165h}}$ where MHS $\frac{r_{89v}}{r_{157v}}$ is larger. Published aircraft campaign measurements show good agreement as they were well within the ATMS and MHS distributions for both surface types. This indicates that the retrievals performed on ATMS and MHS measurements were accurate for FYI and MYI.

4.4.3 Discussion

Measurements of surface emissivity and reflectance ratio were shown for five different surfaces which were: open ocean, land, Greenland, FYI, and MYI. When comparing ATMS and MHS results, surface emissivities were frequently larger for ATMS. This is likely due to the use of more strongly absorbed frequencies in the MHS retrieval, which were 183h

$\pm$ 3, 1 GHz, while ATMS used 183h $\pm$ 7, 4.5, 3, 1.8, 1 GHz. The more strongly absorbed frequencies are affected more by retrieval errors than the more weakly absorbed frequencies. The is also the case for when distribution widths are much wider for MHS 183h GHz surface emissivities and $\frac{r_{157v}}{r_{183v}}$. The 165h GHz and 157v GHz retrievals from ATMS and MHS respectively had different polarizations but there was no discernible difference when compared to surface emissivity differences at other frequencies with equal polarization for each surface type. Different polarizations were not expected to have an effect on surface emissivity retrieved near nadir.

Comparing the results from different surfaces shows the land surface emissivity distributions being wider than the other surface types. The change in distribution widths of surface emissivity retrievals is due to geophysical variation. For land, the surface can range from flat and barren to rough and highly vegetated. The surfaces with the smallest distributions were open ocean and MYI. Comparing FYI and MYI showed significant differences in surface emissivity and reflectance ratio when sea-ice ages.

The aircraft results were within the distributions from MHS and ATMS. The majority of aircraft-measured emissivities were within 1 SD of the MHS and ATMS emissivity modes. This is considered to be good agreement. However, the emissivities from ATMS and MHS were frequently greater than the published aircraft results. This may be due to retrieval error associated with the auxiliary profiles needed for satellite measurements. The differences could also be due to the fact that the ATMS and MHS measurements provide a larger statistical representation of different surfaces in the Arctic while the published results used aircraft campaign missions that sampled a small number of areas in comparison. This can also explain the large variation in some of the published results. It is also important to note that the reflectance ratios from published results were derived from the means of the surface emissivity results. This is not ideal, as the mean or mode does not represent individual values. The actual reflectance ratio derived from individual measurements could have a different mean or mode.

4.4.4   *Viewing Angle Dependence*

Depending on the surface type, the type of surface reflection, and polarization, surface emissivity and reflectance ratios can vary with satellite local zenith angle. Polarization has a significant involvement in the viewing angle dependence of surface emissivity for

microwave radiation. In Chapter 2, microwave horizontal and vertical polarization reflectivities varied significantly with viewing angle, except at nadir, for specular reflection. This variation with angle is reduced for ATMS and MHS since the instruments measure mixed polarizations as discussed in Sect 2.4. Note, at 165h GHz, ATMS is horizontally polarized at nadir and at 157v GHz MHS is vertically polarized at nadir. This causes some differences in the retrieved surface emissivities for satellite zenith angles off nadir and will be discussed later in this section.

To evaluate viewing angle dependence, surface emissivity retrievals are binned with respect to satellite local zenith angle with a bin size of $10°$ or less. Surface emissivity retrievals were produced using measurements with water vapour columns less than 1.5 $kg\, m^{-2}$. Figure 4.40 shows the variation of surface emissivity with increasing satellite local zenith angle from ATMS (MHS) at 88v (89v) GHz , 165h (157v) GHz, and 183h GHz frequencies for land, open ocean, FYI, and MYI.

For land, FYI, and MYI surfaces, surface emissivity is nearly equal for all satellite local zenith angles. These surfaces are where Lambertian surface reflection was assumed. However, FYI surface emissivity at 88v (89v) GHz showed a small decreasing trend. For open ocean, where specular surface reflection was assumed, there was an increase in surface emissivity retrieved for larger satellite local zenith angles at 183h GHz for both instruments. At 165h GHz, the ATMS surface emissivity retrieval exhibited the same behavior as 183h GHz. However, at 157v GHz, MHS surface emissivity increased at lower satellite zenith angles and then decreased at the largest binned set of angles. This also occurred at 88v (89v) GHz.
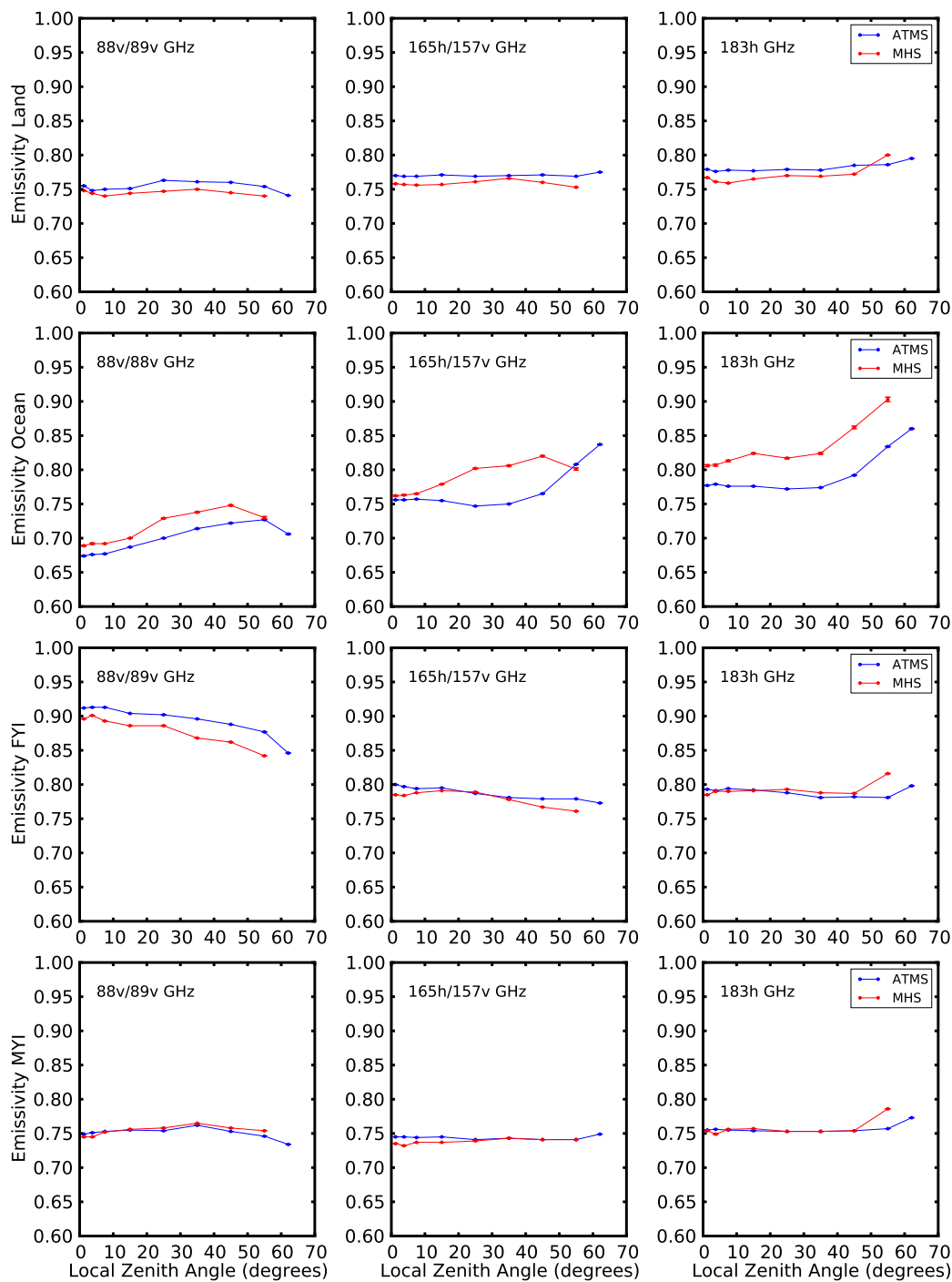
Figure 4.40: Surface emissivity compared to satellite local zenith angle for land, ocean, FYI, and MYI surfaces. Surface emissivity retrievals are produced from ATMS (MHS) measurements at 88v (89v) GHz, 165h (157v) GHz, 183h GHz.

For MYI and FYI, ATMS and MHS surface emissivity retrievals were nearly equal except for FYI at 88 (89) GHz where ATMS was larger MHS. For land surfaces, the ATMS

surface emissivities retrieved were slightly greater than MHS for all frequencies. Surface emissivity retrieved over open ocean were significantly larger for MHS at 183h GHz. At 165h (157v) GHz the surface emissivities were nearly equal at nadir and diverged with increasing angle with the largest difference near 30 °. After 30° the surface emissivity difference between MHS and ATMS decreased until they were nearly equal at the largest satellite local zenith angle bin.

The Lambertian surfaces (FYI, MYI, and land) have nearly constant surface emissivity with satellite local zenith angle since radiation viewed by the satellite is being reflected equally from all directions. As discussed in Sect. 2.2.2, surface emissivity is also depolarized (Maxwell, 1974) for Lambertian surfaces, Fig. 4.40 shows these features for MYI and land surfaces as there is little variation of surface emissivity with viewing angle, even though the instruments polarization varies with viewing angle.

FYI at 88v (89v) GHz was the only Lambertian retrieval to show variation with viewing angle. This could be associated with FYI not being as good of a Lambertian reflector when compared to MYI and land surfaces. Further discussion on types of surface reflection is done in Chapter 5.

For a specular surface, it is expected that the surface emissivity to vary with the satellite local zenith angle. For open ocean at 183h GHz, the surface emissivity increased for the largest satellite local zenith angles for both instruments. At 88v (89v) GHz surface emissivity increased with increasing angle and then began to decrease at larger angles. At 165h GHz, the ATMS surface emissivity retrieval follows the trend seen at 183h GHz, while the MHS retrieval at 157v GHz follows the trend at 88v (89v) GHz. In each of these cases the channels with similar trends have the same polarization.

4.4.5   Water vapour column Dependence

Model results typically showed an increase in error for the surface emissivity retrieved with larger water vapour columns. Producing plots of surface emissivity with variation in water vapour column similar to Sect. 4.3 can give insight on the potential retrieval error for surface emissivity. Measurements are shown for both specular and Lambertian surface reflection assumptions.
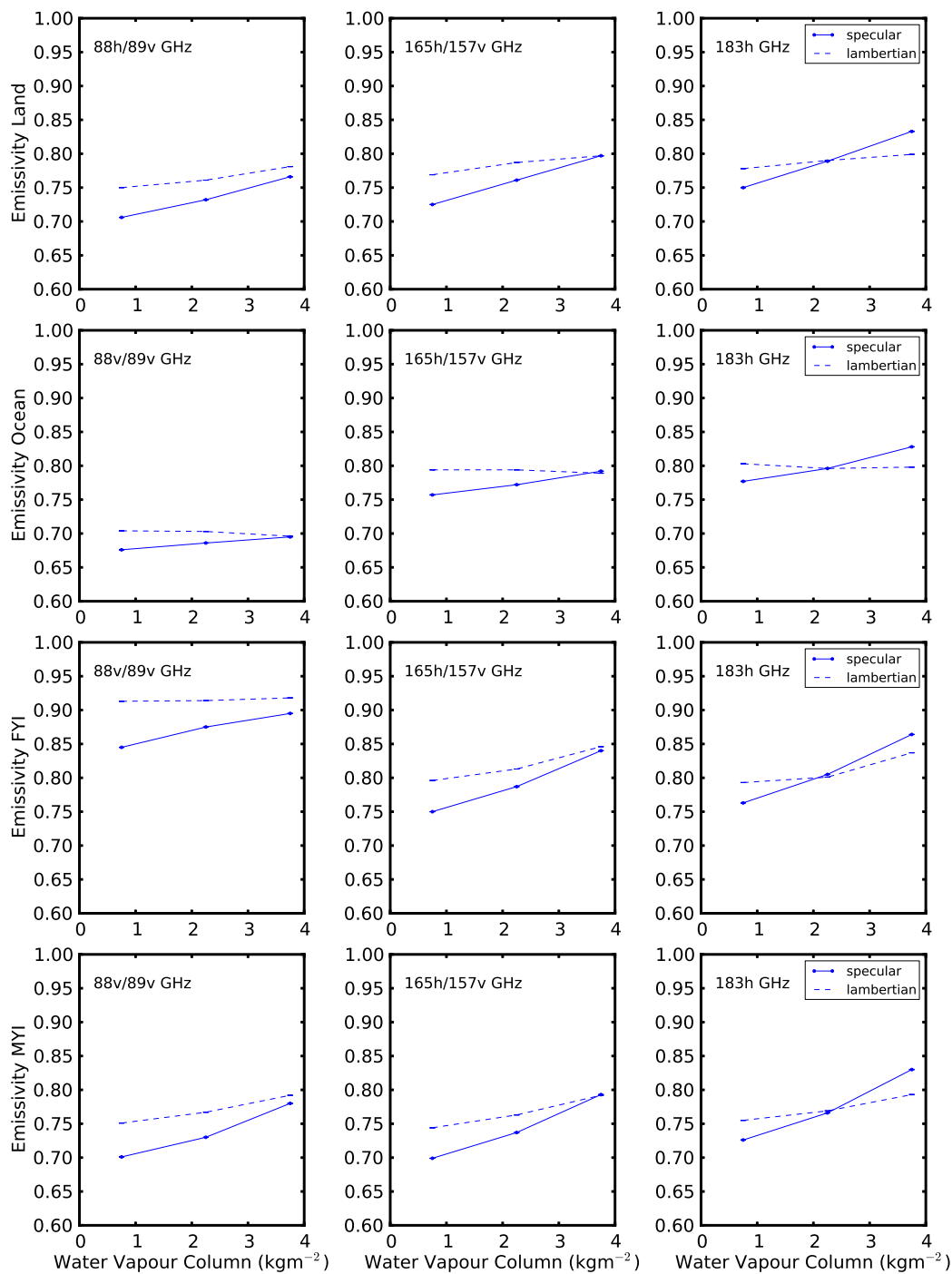
Figure 4.41: Surface emissivity compared to water vapour column $\mathrm{kg\,m^{-2}}$ for land, ocean, FYI, and MYI surfaces. Surface emissivity retrievals are produced using ATMS (MHS) measurements at 88v (89v), 165h (157v), 183h GHz. Results for both specular (solid) and Lambertian (dashed) are shown in each plot.

Figure 4.41 shows surface emissivity retrievals for land, open ocean, FYI, and MYI at

88v GHz, 165h GHz, and 183h GHz for ATMS using specular and Lambertian reflection compared to water vapour column with a bin size of $1.5 \, \mathrm{kg \, m^{-2}}$. The change in surface emissivity for land, FYI, and MYI is smaller for the Lambertian assumption compared to specular. Over open ocean, the surface emissivity variation is smaller for the Lambertian assumption but is also relatively small compared to the other surface types at specular reflection.

From the model results, the surface emissivity retrieval with the least variation for increasing water vapour column should have a smaller error. Therefore, the assumption of Lambertian reflection would be correct for these surfaces. This was expected for the land, FYI, and MYI surfaces. However, over the ocean it is generally assumed that specular reflection occurs.

Using skin temperatures retrieved from the Selbach technique at 183h GHz shows realistic values with a specular reflection assumption as shown in Fig. 4.42. The skin temperatures retrieved with specular reflection assumed has a mean of approximately 270 K while Lambertian reflection has a mean of approximately 260 K. The freezing point of the ocean (depending on salinity) is 271.5 K (Talley et al., 2011) meaning the Lambertian skin temperatures are unphysical.
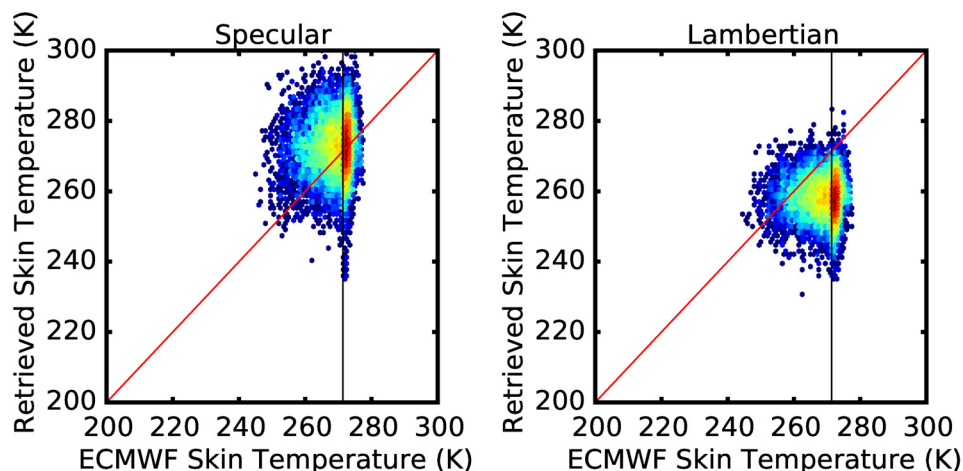
Figure 4.42: Skin temperature retrievals at 183 GHz over open water compared to ERA-interim skin temperatures assuming specular and Lambertian surface reflection. Freezing point of sea water (271.5 K). Note, the unphysical ERA-interim skin temperatures are due to incorrect classification of sea ice and open ocean.

The skin temperature retrievals over the other surfaces show that the assumption of Lambertian reflection was likely the correct choice. Retrieved skin temperature from ATMS

has a larger correlation with ERA-interim skin temperatures when Lambertian reflection was assumed in the retrieval as shown in Fig. 4.43 for land. In Chapter 3, it was stated that skin temperature was variable between different reanalyses and should not be trusted, however, it is likely accurate to a certain degree.
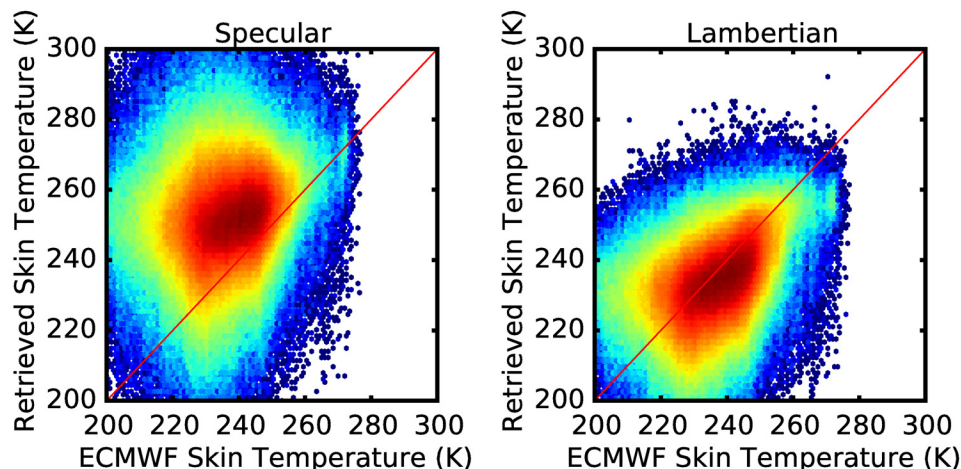
Figure 4.43: Skin temperature retrievals at 183 GHz over land compared to ERA-interim skin temperatures assuming specular and Lambertian surface reflection.

4.5 Summary

A retrieval formulation for determining surface emissivities from microwave brightness temperatures using Lambertian and specular reflection at the surface was introduced. Two methods to retrieve surface emissivity were given. One, the Selbach technique, uses multiple 183 GHz channels to calculate surface emissivity and skin temperature. The second method, the Hewison technique, rearranges Eq. 4.2 and uses a single 183 GHz channel but requires auxiliary skin temperature estimates. For 183 GHz the Selbach technique was used, and at 88 GHz and 165 GHz the Hewison technique was used.

Simulations were performed for several test cases to examine the effects of errors from atmospheric auxiliary information and improper surface assumptions on the surface emissivity retrieved. The results showed that the retrieval error for surface emissivity increased with increasing water vapour column. Retrieval errors were also larger when more strongly absorbed frequencies were used at 183 GHz.

Application of the surface emissivity and reflectance ratio retrievals to real brightness temperatures was initially shown in the form of pan-Arctic maps which were produced

monthly for the 2012/2013 winter season. The $\frac{r_{88v}}{r_{165h}}$ could easily distinguish surface types and also showed variations within a surface type. Structure in $\frac{r_{88v}}{r_{165h}}$ would typically be persistent over multiple months meaning the values seen were not likely due to retrieval errors. The $\frac{r_{165h}}{r_{183h}}$ showed little structure in comparison to $\frac{r_{88v}}{r_{165h}}$ but still had small differences between surface types and small changes during winter season. Maps of reflectance ratio will be used for the PLDC16 water vapour column retrieval in the following chapter.

From the pan-Arctic maps, anomalously large reflectance ratios for $\frac{r_{88v}}{r_{165h}}$ were measured over a large portion of Greenland. The large reflectance ratios coincided with regions where there was minimal melt of glacial ice.

Validation of the surface emissivities and reflectance ratios was done by classifying surfaces as either open ocean, land, Greenland, FYI, and MYI and then producing probability densities for water vapour columns less than $1.5 \, \mathrm{kg\,m^{-2}}$. There were small offsets between MHS and ATMS which were likely due to retrieval error. Some other possible sources of error could be differences in instrument calibrations or the 1-D radiative transfer model, RTTOV. ATMS and MHS retrievals were compared to published aircraft campaigns which measured surface emissivity. The published results fell within the ATMS and MHS distributions of surface emissivity, in many cases less than 1 SD from the mode.

Comparing surface emissivity retrieved with satellite local zenith angle showed little change for retrievals using a Lambertian surface assumption but did show change for the specular assumption over open ocean which was expected. Comparing surface emissivity retrieved with water vapour column showed less variation for the Lambertian assumption than compared to the specular assumption. This confirms that Lambertian was the proper surface assumption. Over open ocean the specular assumption was also confirmed to be correct. Surface reflection will be further discussed in Chapter 5.

CHAPTER 5

PAN-ARCTIC WATER VAPOUR
ANALYSIS

The PLDC16 retrieval may be used to obtain water vapour columns from satellite microwave measurements. Previously, measurements were shown at the single-point location of Barrow, Alaska. The next step is to use the retrieval to produce pan-Arctic maps of water vapour column.

Application of the PLDC16 retrieval for Arctic mapping requires three modifications to the technique used in Chapter 3. It was originally assumed that the surface reflects specularly, but this is not necessarily true. The first modification to the retrieval accounts for specular, Lambertian, or mixed surface reflection.

The second modification involves the reflectance ratios. As discussed in Chapter 3, the retrieval requires an estimate for the reflectance ratio in the mid and extended regimes. Originally a constant value was used at Barrow, Alaska, but this is not sufficient for pan-Arctic retrievals. Reflectance ratio maps from Chapter 4 are applied to the PLDC16 retrieval.

The third modification involves the application of three empirical corrections to the PLDC16 retrieval. They are in the form of offsets to the bias coefficients, reflectance ratio, and water vapour column (TCWV) which vary with surface type and PLDC16 regime. The empirical corrections ensure self-consistency between large and nadir angle measurements.

Using the updated PLDC16 retrieval, pan-Arctic maps of water vapour are presented during a portion of the 2013 winter season. The TCWV is compared to measurements from the GVR at Barrow, Arctic radiosondes, and ERA-interim. Also, pan-Arctic maps of water vapour are used to evaluate ice leads as a water vapour source.

Section 5.1 describes the PLDC16 reformulation. The use of reflectance ratio maps from Chapter 4 is described in Sect. 5.3. Section 5.4 specializes the application of the PLDC16 retrieval to ATMS measurements. Section 5.5 describes a method to validate the surface reflection type. Section 5.6, Sect. 5.7, and Sect. 5.8 describe each of the three empirical corrections and Sect. 5.9 summarizes the corrections used for the PLDC16 retrieval. Comparisons with GVR, Arctic radiosondes, and ERA-interim are shown in Sect. 5.10.2-5.10.4. A case study of the influence ice leads have on water vapour is shown in Sect. 5.11.

5.1 PLDC16 Reformulation

The PLDC16 water vapour column retrieval from Chapter 3 assumed specular reflection from the surface. As stated in Chapter 4, surface reflection may be specular or diffuse. The PLDC16 retrieval is updated using the effective incident angle parameterization from Chapter 4 for Lambertian surface reflection.

To update the PLDC16 retrieval, the brightness temperature formulae from Eq. 4.2 and Eq. 4.3 are used. Following the derivation from Chapter 3, where brightness temperatures T_1, T_2, and T_3 from three channels are combined to take the form of,

$$\frac{\Delta T_{12} - b_{12}}{\Delta T_{23} - (b_{23} + \Delta b_{23})} = \left(\frac{r_1}{r_2} + \Delta \frac{r_1}{r_2}\right) \left(\frac{e^{-\tau_1 \sec \theta_D} e^{-\tau_1 \sec \theta_U} - (\frac{r_2}{r_1} + \Delta \frac{r_2}{r_1}) e^{-\tau_2 \sec \theta_D} e^{-\tau_2 \sec \theta_U}}{e^{-\tau_2 \sec \theta_D} e^{-\tau_2 \sec \theta_U} - (\frac{r_3}{r_2} + \Delta \frac{r_3}{r_2}) e^{-\tau_3 \sec \theta_D} e^{-\tau_3 \sec \theta_U}}\right)$$

$$(5.1)$$

and

$$\begin{aligned}
b_{ij} \approx & \int_0^\infty \left(e^{-\tau_j(z,\infty) \sec \theta_U} - e^{-\tau_i(z,\infty) \sec \theta_U}\right) \frac{\mathrm{d}T(z)}{\mathrm{d}z} \mathrm{d}z \\
& + r\left[e^{-\tau_j \sec \theta_D} e^{-\tau_j \sec \theta_U} \int_0^\infty \left(1 - e^{\tau_j(z,\infty) \sec \theta_D}\right) \frac{\mathrm{d}T(z)}{\mathrm{d}z} \mathrm{d}z \right. \\
& \left. - e^{-\tau_i \sec \theta_D} e^{-\tau_i \sec \theta_U} \int_0^\infty \left(1 - e^{\tau_i(z,\infty) \sec \theta_D}\right) \frac{\mathrm{d}T(z)}{\mathrm{d}z} \mathrm{d}z\right],
\end{aligned}$$

$$(5.2)$$

where Δb_{23} is a bias correction term discussed in Sect. 5.6, $\Delta \frac{r_1}{r_2}$ and $\Delta \frac{r_2}{r_3}$ are reflectance ratio adjustments discussed in Sect. 5.7, θ_D and θ_U are the local zenith angles for downward radiation incident to the surface and for upward radiation from the surface towards the

satellite. The general approach is to tune Δb_{23}, $\Delta\frac{r_1}{r_2}$, and $\Delta\frac{r_2}{r_3}$ to eliminate dependencies on satellite local zenith angle and discontinuities between regimes. For specular reflection, $\theta_D = \theta_U$ and for Lambertian reflection, $\theta_D = \theta_{eff}$. Note, the third correction, a water vapour column offset, is applied post retrieval. The differences between Eq. 5.1 and Eq. 5.2 from Eq. 3.2 and Eq. 3.6 are that the $e^{-2\tau_1 \sec\theta}$ terms split to become $e^{-\tau_1 \sec\theta_D}e^{-\tau_1 \sec\theta_U}$. Also, local zenith angle terms in Eq. 3.6 either become θ_D or θ_U.

5.2   Mixture of Specular and Lambertian Reflection

Surface reflection may be a mixture of specular and Lambertian. Matzler (2005) has represented this as a linear average of brightness temperatures,

$$T_{mix} = ST_{specular} + (S-1)T_{Lambertian} \tag{5.3}$$

where S is the fraction of specular reflection at the surface and $S-1$ is the fraction of Lambertian. $T_{specular}$, $T_{Lambertian}$, and T_{mix} are the brightness temperatures for specular, Lambertian, and mixed reflection (Matzler, 2005).

To apply mixed surface reflection to the PLDC16 retrieval, θ_D is allowed to take on values between θ_U and θ_{eff}. The value θ_D takes depends on the value of S, θ_{eff}, and θ_U.

To determine θ_D, simulations were produced using radiosonde measurements from Barrow, Alaska. The model uses the following settings: surface emissivity of 0.8 for all frequencies, cloud-free, unpolarized radiation, mixed surface reflection ($S=0.5$), and equal surface air and skin temperatures. Simulations were produced for the ATMS instrument. Simulations were produced for a range of θ_U. Note, the simulated value for θ_{eff} (55°) does not vary with τ in the model.

The PLDC16 retrieval is applied to the simulations for each θ_U. θ_D is determined by minimizing the water vapour column bias with respect to the model input for each θ_U. Figure 5.1 shows resulting values of θ_D for each satellite local zenith angle. The value for θ_D is smallest for satellite zenith angles at nadir and increases with increasing satellite zenith angle. A fit is used as a transfer function to retrieve angle of incidence from satellite zenith angle for mixed scattering only.

This parameterization only applies to situations where the surface reflection is a simple mixture of specular and Lambertian. Surface reflection can be complex and in those cases
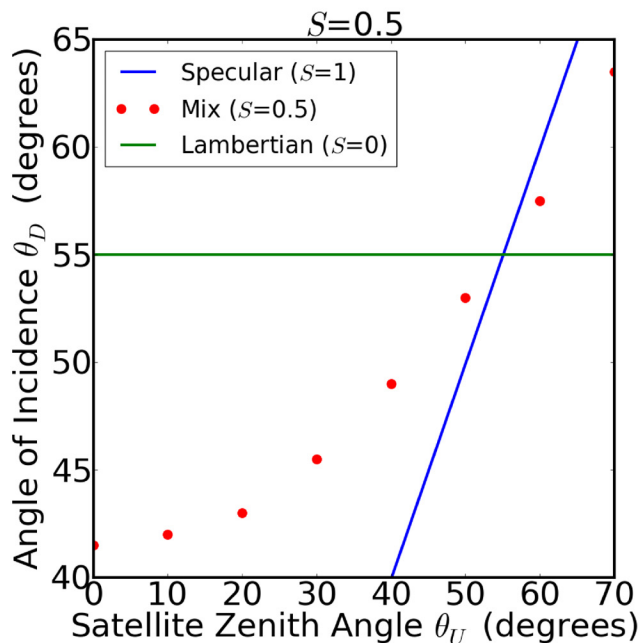
Figure 5.1: θ_D values determined from simulations (S=0.5) by minimizing water vapour column bias of PLDC16 retrievals with varying satellite local zenith angles. θ_{eff} for Lambertian surface reflection and θ_D for specular reflection are also plotted.

this may not produce optimal results.

5.3 Reflectance Ratio Maps

The PLDC16 retrieval requires reflectance ratios for the mid and extended regimes. Depending on the surface type and frequencies, the reflectance ratio substantially varies as shown in Chapter 4. Chapter 4 also showed that reflectance ratios vary spatially and temporally for the same surface type, especially over land surfaces. Temporal variation is seen with FYI where the reflectance ratio increased later in the winter season.

The reflectance ratio maps of Chapter 4 were produced monthly with a bin size of 30 km×30 km for satellite local zenith angles less than 20°. Each bin contained a minimum of 10 measurements and a maximum of 50 measurements.
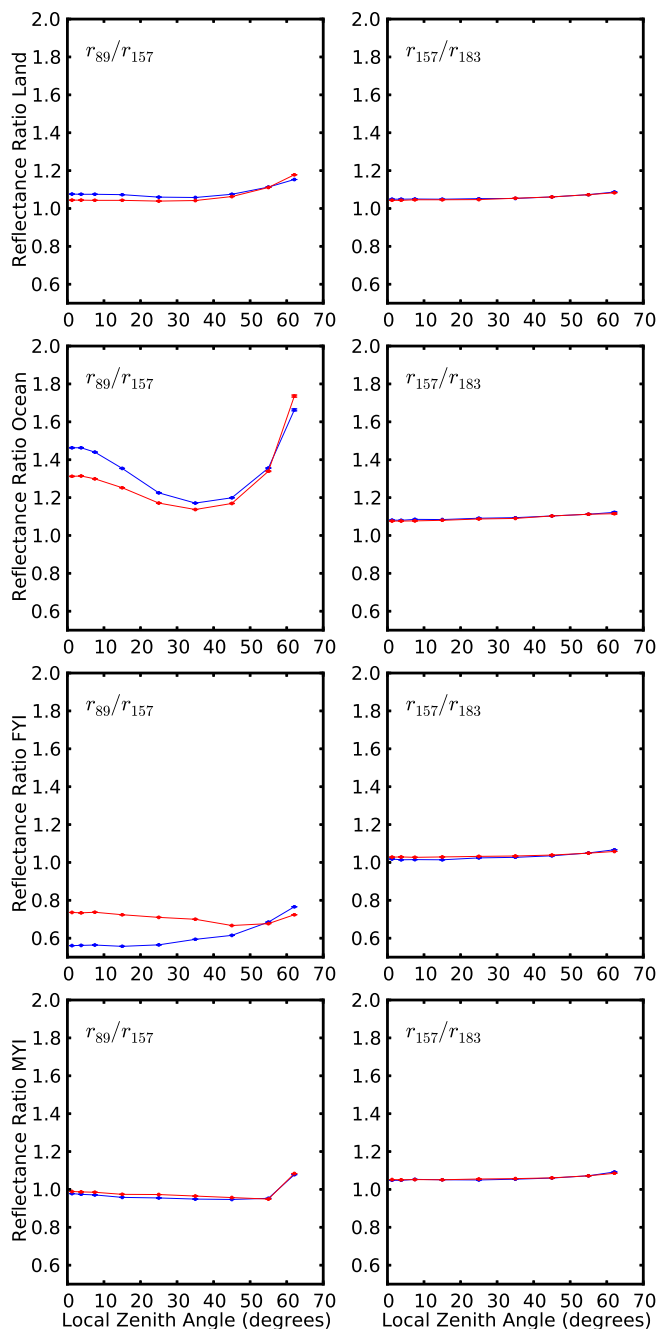
Figure 5.2: Retrieved reflectance ratio compared to satellite local zenith angle for land, ocean, FYI, and MYI surfaces. Reflectance ratio retrievals are produced at 88v, 165h, and 183h GHz for ATMS using both specular (red) and Lambertian (blue) surface reflection assumptions.

For the purposes of water vapour retrievals, the maps are produced weekly, using the surrounding two weeks of overpasses. Maps using less than 2 weeks of measurements do not have enough data for each bin.

To maximize data usage, all satellite local zenith angles from ATMS are used. As shown in Chapter 4, surface emissivity, and therefore reflectance ratio, vary with satellite local zenith angle for some surfaces. To account for this, reflectance ratios were adjusted to nadir viewing. Plots of reflectance ratio with respect to satellite local zenith angle are shown in Fig. 5.2. The reflectance ratios were derived from reflectance data shown in Fig. 4.40.

For open ocean (ice-free), the reflectance ratio is specified from the measurements in Fig. 5.2. The reason for this is that large water vapour columns over open ocean, even during the Arctic winter, can introduce significant error in the reflectance ratio.

Most reflectance ratio maps use all data, regardless of water vapour column; in order to obtain mean values from a statistical sample. However, $\frac{r_{165h}}{r_{183h}}$ is more sensitive to error from larger water vapour columns and so a maximum mean water vapour column threshold of 3.5 $\mathrm{kg\,m^{-2}}$ is applied to each bin. A constant reflectance ratio derived from the measurements of Fig. 5.2 is applied to the bins that cross the threshold.
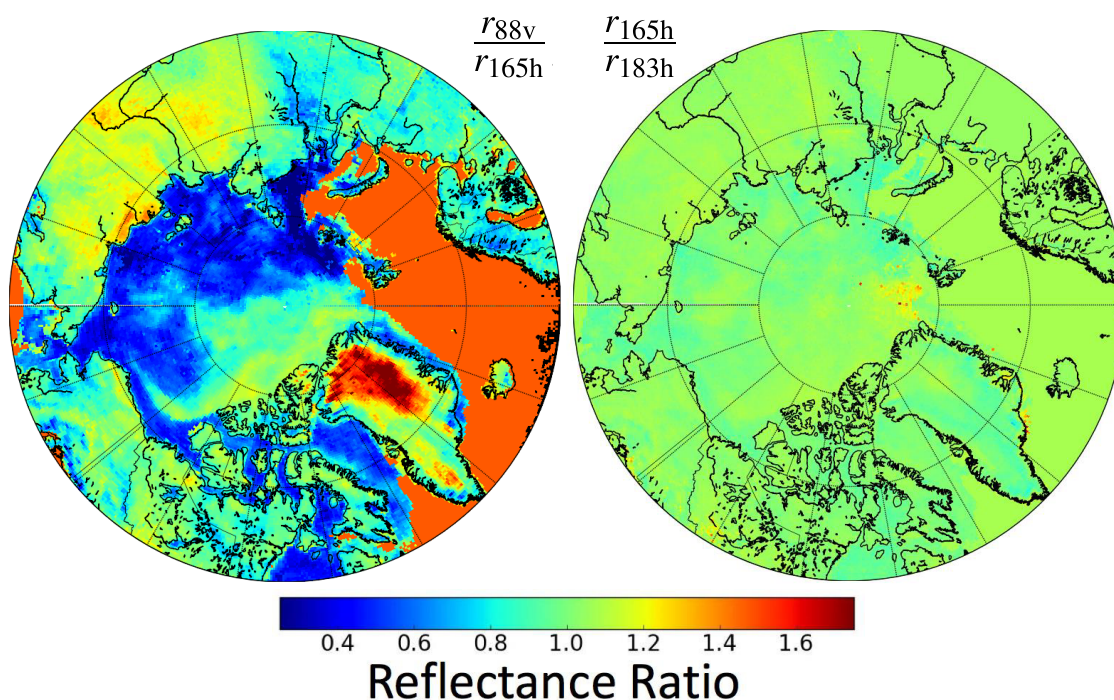
Figure 5.3: Reflectance ratio map over the Arctic for January 1 to January 15, 2012 for nadir $\frac{r_{88v}}{r_{165h}}$ and $\frac{r_{165h}}{r_{183h}}$ using the ATMS instrument.

Sample reflectance ratio maps for $\frac{r_{88v}}{r_{165h}}$ and $\frac{r_{165h}}{r_{183h}}$ used in the PLDC16 retrieval are shown in Fig. 5.3. The specified value for open ocean reaches up to latitudes of 80°N for the

Atlantic Ocean and greater than 60°N for the Pacific Ocean. The 3.5 $\mathrm{kg\,m^{-2}}$ water vapour column threshold for $\frac{r_{165h}}{r_{183h}}$ affects a portion of northern Europe and eastern Russia.

5.4   PLDC16 Retrieval Application to ATMS measurements

The PLDC16 retrieval may be applied to ATMS measurements in a manner similar to the MHS measurements from Chapter 3. Table 5.1 shows the channels used in each regime along with the slant water vapour column ranges. Three regimes are used, which are labeled: low, mid, and extended. The frequencies, v_1, v_2 and v_3 , in each regime are ordered so $\tau_1 < \tau_2 < \tau_3$. The frequencies were chosen to be close to those used in Chapter 3 for MHS. The mid regime range was extended by 1 $\mathrm{kg\,m^{-2}}$ owing to improved performance of the updated retrieval.

Table 5.1: ATMS frequencies for the low, mid, and extended regimes for the retrievals of water vapour column with typical water vapour column (W) ranges. The frequencies v_1, v_2 and v_3 in each regime are ordered so that $\tau_1 < \tau_2 < \tau_3$.

Regime	ATMS frequencies (GHz)			W range ($\mathrm{kg\,m^{-2}}$)
	v_1	v_2	v_3	
Low	183.31 ± 7	183.31 ± 3	183.31 ± 1	0 - 2.5
Mid	165.5	183.31 ± 7	183.31 ± 3	1.5 - 10
Extended	88.2	165.5	183.31 ± 7	9 - 15

ATMS has two extra frequencies near 183 GHz when compared to MHS. These two frequencies could potentially be used in the PLDC16 retrieval, either to create more regimes or replace channels in the pre-existing regimes. Currently, this has not been investigated.

5.5   Surface Reflection Type

A method for determining S for different surfaces is presented in the following section which uses the difference between large and near-nadir angle measurements of water vapour column. Section 5.5.1 gives simulations presenting the effect an incorrect surface reflection assumption has on water vapour column. Section 5.5.2 then describes the application of those results to real measurements for different surface types and presents the surface reflection assumptions that are used in the updated PLDC16 retrieval.

5.5.1 Simulations

Simulations were conducted for the purpose of describing the effect incorrect surface reflection assumptions have on the PLDC16 water vapour column. Simulations were produced for ATMS using radiosonde measurements from Barrow, Alaska from January 2008 to March 2014 for the winter months (December to March). The model uses the following assumptions: surface emissivity of 0.8 for all frequencies, cloud-free, unpolarized radiation, and equal surface air and skin temperatures.
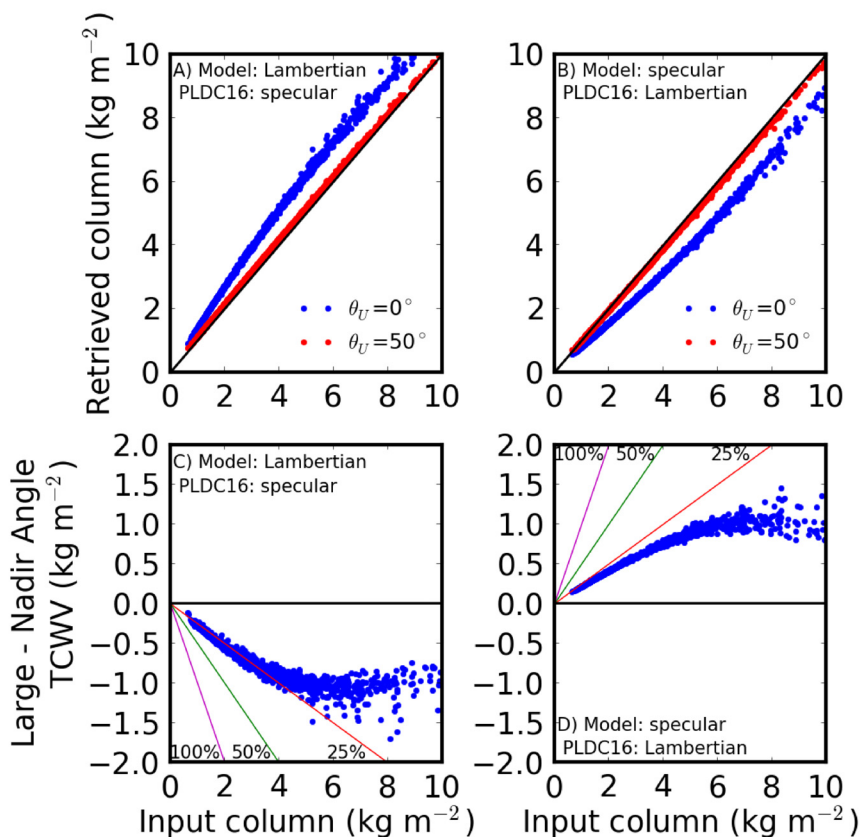
Figure 5.4: PLDC16 retrievals for the mid regime using simulated brightness temperatures are shown for two situations where PLDC16 incorrectly assumes the surface reflection type. A/C) The model assumes Lambertian while PLDC16 assumes specular and B/D) the model assumes specular while PLDC16 assumes Lambertian. The plots show PLDC16 water vapour column for the top row and differences between the PLDC16 water vapour column at 50 and nadir for the second row.

Figure 5.4 shows PLDC16 mid regime simulations compared to model input water vapour column that assume specular (S=1) and Lambertian (S=0) surface reflection while the PLDC16 retrieval assumes Lambertian and specular surface reflection, respectively, for

both nadir and 50° satellite local zenith angles. Simulations show that when there is an incorrect estimate for S, a bias is induced in the PLDC16 water vapour column that is a maximum for nadir satellite local zenith angle. The bias is positive when specular surface reflection is incorrectly assumed by PLDC16 and negative when Lambertian surface reflection is incorrectly assumed by PLDC16.

The figure also shows the differences of the 50° and nadir measurements for each simulation. If the PLDC16 incorrectly assumed the surface reflection to be specular, the difference between water vapour columns is negative and if PLDC16 incorrectly assumed Lambertian reflection, the difference is positive. It can also be inferred that the difference in large and nadir angle water vapour columns for Lambertian surface reflection are greater than the differences for specular surface reflection.

The differences in PLDC16 water vapour column between large and nadir angles can be used to evaluate the surface reflection assumption for each surface type by finding the surface reflection assumption that minimizes the difference.

5.5.2 *Measurements*

To evaluate the surface reflection assumptions, measurements were compiled for 711 locations in the Arctic on a regular grid with a resolution of 2.5 degrees latitude and 5 degrees longitude, as shown in Fig. 5.5. At latitudes greater than 80 °N, the longitude resolution was decreased. Overpasses from the ATMS satellite within 50 km of each location were used. Measurements between January 2012 and March 2015 inclusive during the winter season (December-March) were used. Measurements were split into four different surface types using the OSI-403-c mask: land, open ocean, first-year ice (FYI), and multi-year ice (MYI).

For each surface type, measurements at each location with satellite local zenith angles between 0° and 20° (near-nadir) and between 45° and 65° (large angle) were binned. Overpasses at each location that were within 3 hours in the near-nadir and large angle bins were considered to have the same atmospheric conditions.

PLDC16 retrievals were run with three different types of surface reflection: specular (S=1), Lambertian (S=0), and mixed (S=0.5). For the low regime, the difference in PLDC16 water vapour column for large angle and near-nadir bins for each surface type is shown in Fig. 5.6. For all the surface types, Lambertian surface reflection had the smallest difference
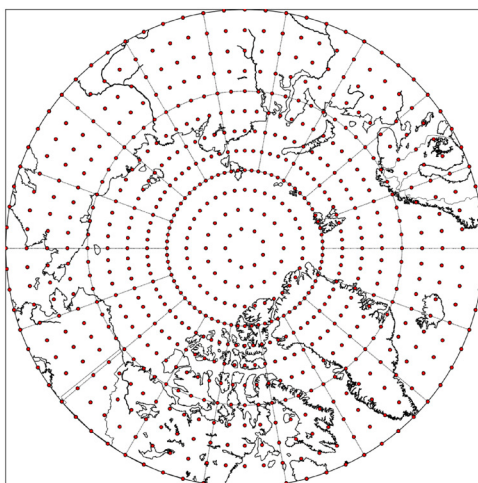
Figure 5.5: Pan arctic map of locations chosen for ATMS water vapour column retrievals.

in water vapour column for large and near-nadir angles. This was unexpected for open ocean which was considered to be specular reflection in Chapter 4. This could be due to the open ocean having fewer measurements at low water vapour columns than the other surface types, producing an erroneous result. Also, the differences are increasingly negative for increasing water vapour column for all types of surface reflection, which was not seen in the simulated results of Fig. 5.4.
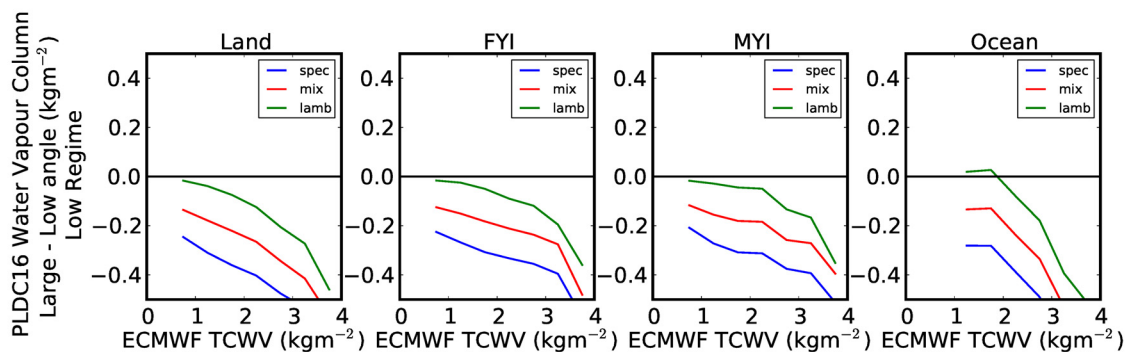
Figure 5.6: Differences in large angle and near-nadir overpasses within 3 hours at each of the 711 locations combined for land, FYI, MYI, and open ocean surfaces assuming specular (S=1), Lambertian (S=0), and mixed (S=0.5) surface reflection for the low regime of the PLDC16 water vapour column retrieval compared to ERA-interim water vapour column.

Figure 5.7 shows the difference in mid regime PLDC16 water vapour column for large
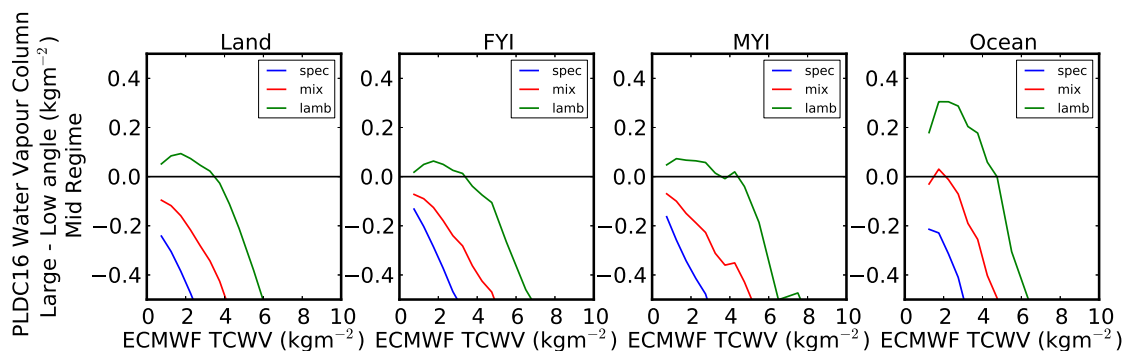
Figure 5.7: Differences in large angle and near-nadir overpasses within 3 hours at each of the 711 locations combined for land, FYI, MYI, and open ocean surfaces assuming specular (*S*=1), Lambertian (*S*=0), and mixed (*S*=0.5) surface reflection for the mid regime of the PLDC16 water vapour column retrieval compared to ERA-interim water vapour column.

angle and near-nadir measurements for each surface type. Similar to the low regime, Lambertian surface reflection minimized the difference for Land, FYI, and MYI water vapour columns. However, in this case, the difference for open ocean was minimized with mixed surface reflection for water vapour columns up to approximately 3 $\mathrm{kg\,m^{-2}}$. Beyond 3 $\mathrm{kg\,m^{-2}}$, the difference becomes increasingly negative, as seen in the low regime. This effect is investigated in Sect. 5.6. Due to there being more measurements in the mid regime for open ocean, this result is expected to be more accurate than the low regime result for open ocean.
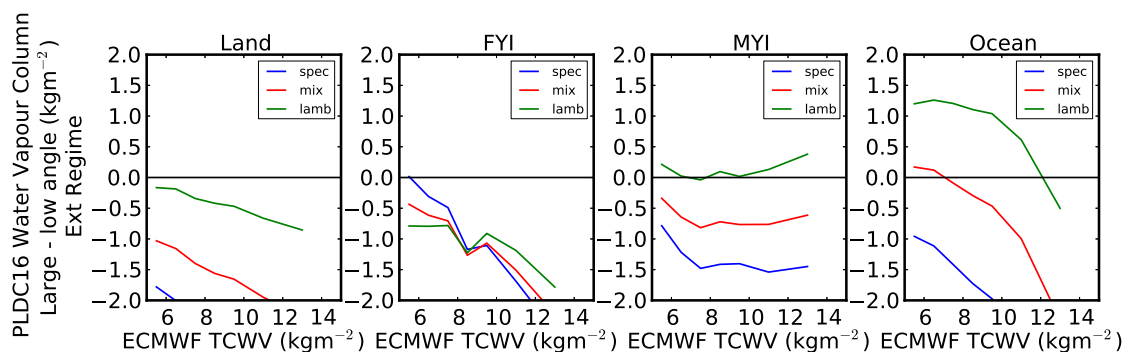
Figure 5.8: Differences in large angle and near-nadir overpasses within 3 hours at each of the 711 locations combined for land, FYI, MYI, and open ocean surfaces assuming specular (*S*=1), Lambertian (*S*=0), and mixed (*S*=0.5) surface reflection for the extended regime of the PLDC16 water vapour column retrieval compared to ERA-interim water vapour column.

Figure 5.8 shows the difference in extended regime PLDC16 water vapour column for large and near-nadir angle measurements for each surface type. For Land and MYI

surfaces, Lambertian was again the result that had the smallest difference. However, the PLDC16 retrieval difference for land was still large. FYI showed specular reflection with the smallest difference for water vapour column up to $8\ \mathrm{kg\,m^{-2}}$, which did not agree with the results of the low and mid regime. The FYI and land results do not match the results from Fig. 5.4 where the difference for specular should be less than the Lambertian retrieval and the specular result should be negative while the Lambertian would result should be positive. These results could be erroneous due to errors in $\frac{r_{88v}}{r_{165h}}$ since it was not seen in the other regimes. This is investigated further in the subsequent sections. Finally, the difference over open ocean was smallest when using mixed surface reflection up to $10\ \mathrm{kg\,m^{-2}}$. Beyond $10\ \mathrm{kg\,m^{-2}}$, the increasingly negative trend in the difference causes Lambertian surface reflection to be smallest. The differences are increasingly negative with increasing water vapour column for every surface except for MYI.

From the results of each regime, Lambertian surface reflection is the optimal choice for land, FYI, and MYI. For open ocean, the optimal choice in the mid and extended regimes optimal solution was a mixture of specular and Lambertian, while the low regime result favoured Lambertian reflection.

Since the low regime has fewer measurements when compared to the mid and extended regimes, therefore a mixed solution is considered optimal for open ocean. This is different from the assumption of specular reflection for open ocean made in other publications. Capillary waves (ripple scale) in the open ocean could be associated with the mixed solution.

An unexpected feature in the results of Fig. 5.6-5.8 was the increasingly negative trend of the difference in large and near-nadir angle PLDC16 water vapour column with increasing water vapour column for each regime and surface reflection assumption. PLDC16 water vapour column biases with respect to ERA-interim water vapour column showed a similar effect (not shown). Another source of error is causing this effect, and will require a separate correction (discussed next).

5.6   Bias Correction

A method for correcting the increasingly negative trend with increasing water vapour column for the PLDC16 retrieval difference of large and near nadir angles is presented in the following section. Section 5.6.1 shows simulations presenting a possible cause of the effect. Section 5.6.2 describes the application of insights from those results to real measurements

for different surface types and presents the corrections that are used in the updated PLDC16 retrieval.

5.6.1 Simulations

Simulations are produced using radiosonde measurements from Barrow, Alaska from January 2008 to March 2014 for the winter months (December to March). The model uses the following assumptions: surface emissivity of 0.8 for all frequencies, cloud-free, unpolarized radiation, specular surface reflection, and equal surface air and skin temperatures. Simulations are produced for the ATMS instrument.

For the low, mid, and extended regimes, 1 K, 1 K, and 3 K were subtracted from the denominators on the left hand side of Eq. 5.1, respectively. Figure 5.9 shows the PLDC16 retrieval for nadir and $50°$ satellite local zenith angles for the low, mid, and extended regimes, as well as the difference of the $50°$ and nadir angle PLDC16 retrievals for each regime. The extended regime had 3 K subtracted since the effect does not influence the extended regime as much as the low and mid regimes.

For all the regimes, the simulations show that when the denominator was adjusted on the left-hand side of Eq. 5.1, a difference in PLDC16 water vapour column for $50°$ and nadir angles was induced showing a similar increasingly negative trend than seen in Sect. 5.5.2. Therefore, the simulations reveal a systematic error likely caused by an error in the bias coefficient.

There are a couple of possible sources of error that could be causing this issue and are listed below:

   i. Model error in RTTOV;

  ii. Calibration error in brightness temperature for satellite-borne instruments (Weng and Yang, 2016); and

 iii. Incorrect distribution with altitude for auxiliary information water vapour profile.

It is difficult to determine which of these is inducing error in the retrieval. Currently the best method to correct this issue is to add or subtract a fixed empirical offset, Δb_{23}, as is done on the left-hand side of Eq. 5.1.
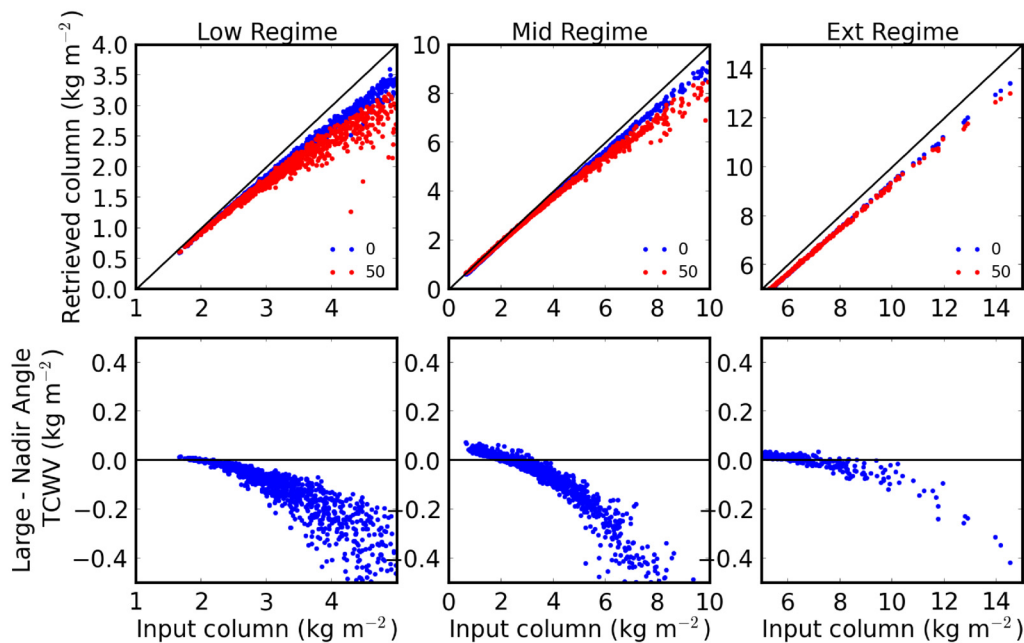
Figure 5.9: PLDC16 retrievals for low, mid, and extended regime using simulated brightness temperatures with specular surface reflection. 1 K, 1 K, and 3 K is subtracted from the bias coefficient in the denominator of the PLDC16 retrieval for low, mid, and extended regime. Differences of the PLDC16 retrieval at 50° and nadir are shown in bottom plots. Blue dots are nadir and red dots are 50° satellite local zenith angle.

5.6.2 Measurements

To determine the empirical offset, measurements were chosen from 711 locations in the Arctic for a regular grid with a resolution of 2.5 degrees latitude and 5 degrees longitude, as shown in Fig. 5.5. At latitudes greater than 80 °N, the longitude resolution was decreased. Overpasses from the ATMS satellite within 50 km of each location were used. Measurements were used between January 2012 and March 2015 inclusive during the winter season (December-March). Measurements were split into four different surface types using the OSI-403-c mask: land, open ocean, first-year ice (FYI), and multi-year ice (MYI).

To determine Δb_{23}, the differences between large and near nadir angle PLDC16 retrievals using ATMS measurements are used, similar to the approach of Sect. 5.5. Figure 5.10 shows the low regime PLDC16 retrieval difference for large and near nadir angles for varying Δb_{23} for all surface types. The Δb_{23} that minimizes the difference up to 2.5 $\mathrm{kg\,m^{-2}}$ over land is 1.5 K, for FYI it is 1.5 K, and for MYI it is 1 K. Over open ocean it is significantly harder to discern which value is optimal. There is no obvious reason for Δb_{23} to

Figure 5.10: Differences in PLDC16 water vapour column for large angle and near-nadir overpasses within 3 hours at each of the 711 locations combined for different Δb_{23} for land, FYI, MYI, and open ocean surfaces for the low regime compared to ERA-interim water vapour column.

be surface type dependent, and so a constant value across each surface is used. Taking the average of the Δb_{23} for each surface type and rounding down to the closest value of Δb_{23} in Fig. 5.10 gives 1.25 K.

At larger water vapour columns the difference becomes increasingly negative, but only for values outside of the low regime (up to 2.5 $\mathrm{kg\,m^{-2}}$ slant column). The increasingly negative difference with increasing water vapour column likely occurs due to the Δb_{23} empirical offset parameterization not completely accounting for the actual source of error in the PLDC16 retrieval when applied to real measurements. There are also fewer measurements with solutions in the low regime at larger water vapour columns since the more strongly absorbed channels are impeded from viewing the entire atmospheric column.

Figure 5.11 shows the mid regime PLDC16 retrieval difference for large and near nadir angles for varying Δb_{23} for all surface types. For land and MYI, the mid regime difference of large and near-nadir angle water vapour columns is positive, except for the largest water vapour columns, for all Δb_{23}. For these surfaces, finding a Δb_{23} that flattens the curves in Fig. 5.11 is optimal. A separate correction to the reflectance ratios is discussed and applied in Sect. 5.7, and will improve the results. Similar to the low regime, at large water vapour columns the difference becomes increasingly negative.

The Δb_{23} that flattens the difference up to 6 $\mathrm{kg\,m^{-2}}$ over land is 1.75 K, for FYI it is 1.5 K, for MYI it is 1 K, and for open ocean it is 1.75 K. Taking the average of the Δb_{23}

Figure 5.11: Differences in PLDC16 water vapour column for large angle and near-nadir overpasses within 3 hours at each of the 711 locations combined for different Δb_{23} for land, FYI, MYI, and open ocean surfaces for the mid regime compared to ERA-interim water vapour column.

for each surface and rounding down to the closest value of Δb_{23} in Fig. 5.11 gives 1.5 K. Beyond 6 $kg\,m^{-2}$, the increasingly negative trend still exists.

The differences are only important up to 6 $kg\,m^{-2}$ due to slant water vapour columns approaching the maximum specified for the mid regime described in Sect. 5.4.

Figure 5.12 shows the extended regime PLDC16 retrieval difference for large and near nadir angles for varying Δb_{23} for all surface types. Similar to the mid regime, some surface types had either a positive or negative bias for the PLDC16 retrieval difference between large and near nadir angle measurements for all values of Δb_{23}. For these surfaces, finding a Δb_{23} that flattens the curve with respect to water vapour column in Fig. 5.12 were chosen instead. The biases will be improved in Sect. 5.7 by a separate reflectance ratio adjustment.

The Δb_{23} that flattens the difference up to 12 $kg\,m^{-2}$ over land is 2.75, for FYI it is 2.5, and for open ocean it is 4. The results for MYI were inconclusive since the difference curves did not significantly change when varying Δb_{23}. This is due to the small number of measurements in the extended regime over MYI. Taking the average of Δb_{23} for each surface and rounding down to the closest value in Fig. 5.12 gives 3.

5.7 Reflectance Ratio Correction

After Δb_{23} values were applied to the PLDC16 retrieval there still was a large difference between the large and near nadir angle water vapour columns for a large number of surface

Figure 5.12: Differences in PLDC16 water vapour column for large angle and near-nadir overpasses within 3 hours at each of the 711 locations combined for different Δb_{23} for land, FYI, MYI, and open ocean surfaces for the extended regime compared to ERA-interim water vapour column.

types. A reason for this is likely due to erroneous reflectance ratios since this was only seen in the mid and extended regimes, where the reflectance ratios are applied. Therefore, a second correction is applied to the mid and extended regimes.

The reflectance ratio adjustment, $\Delta \frac{r_1}{r_2}$, in Eq. 5.1 induces a nearly constant offset in the PLDC16 retrieval with respect to water vapour column. However, the adjustment varies with respect to satellite local zenith angle. This is the reason it was important to adjust Δb_{23} to have PLDC16 differences of large and near nadir angles that were constant with respect to increasing water vapour column.

Another important reason to apply a reflectance ratio adjustment is to make sure the regimes smoothly transition from one regime to another. Without any reflectance ratio adjustments, there are discontinuities when transitioning from the low to mid or the mid to extended regimes. Depending on the size of the difference between large and near nadir PLDC16 water vapour columns, removing the discontinuities can be a greater priority.

The following section describes the results for real measurements from adjusting the reflectance ratios for each surface type and regime. Section 5.7.1 describes and shows the results of introducing a reflectance ratio offset, $\Delta \frac{r_1}{r_2}$, for the mid regime, and Sect. 5.7.2 describes the introduction of two reflectance ratio offsets, $\Delta \frac{r_1}{r_2}$ and $\Delta \frac{r_2}{r_3}$, for the extended regime.

5.7.1 Mid Regime Correction

Figure 5.13 shows the difference in the mid and low regime PLDC16 retrieval for all satellite local zenith angles for various reflectance ratio adjustments. Note, the difference varies with water vapour column; this is likely associated with the Δb_{23} adjustments not fully correcting the error seen in Sect. 5.6. The best water vapour column to have the PLDC16 mid and low regimes be equal would be where they are equally weighted. As described in Chapter 3, weighted averages are used where regimes overlap in order to smooth the transition. For the low-mid regime, this occurs between 1.5 $kg\,m^{-2}$ and 2.5 $kg\,m^{-2}$ slant water vapour column. For the low-mid regime transition, the regimes are equally weighted at 2 $kg\,m^{-2}$ slant water vapour column. For a mid angle from ATMS (approximately $30°$) this translates to a nadir column of approximately 1.7 $kg\,m^{-2}$. From Fig. 5.13, the reflectance ratio adjustment, $\Delta\frac{r_1}{r_2}$, that provides the minimal difference between the mid and low regimes near 1.7 $kg\,m^{-2}$ is -0.025 for land, -0.05 for FYI, -0.05 for MYI, and -0.025 for open ocean. Each surface type has its own adjustment since this correction applies to a surface-derived quantity. The difference between each adjustment is relatively small.

Figure 5.13: Differences in the mid and low regimes for the PLDC16 water vapour column at each of the 711 locations combined for different reflectance ratio adjustments at land, FYI, MYI, and open ocean surfaces compared to ERA-interim water vapour column.

Figure 5.14 shows the difference in mid regime water vapour column for the large and near-nadir angles of the PLDC16 retrieval with varying reflectance ratio adjustments. The results from Fig. 5.14 are not as strongly affected by the reflectance ratio adjustment when compared to the results in Fig. 5.13. For land, FYI, and MYI, the differences in large and near nadir water vapour columns shown in Fig. 5.14 are improved with the reflectance ratio
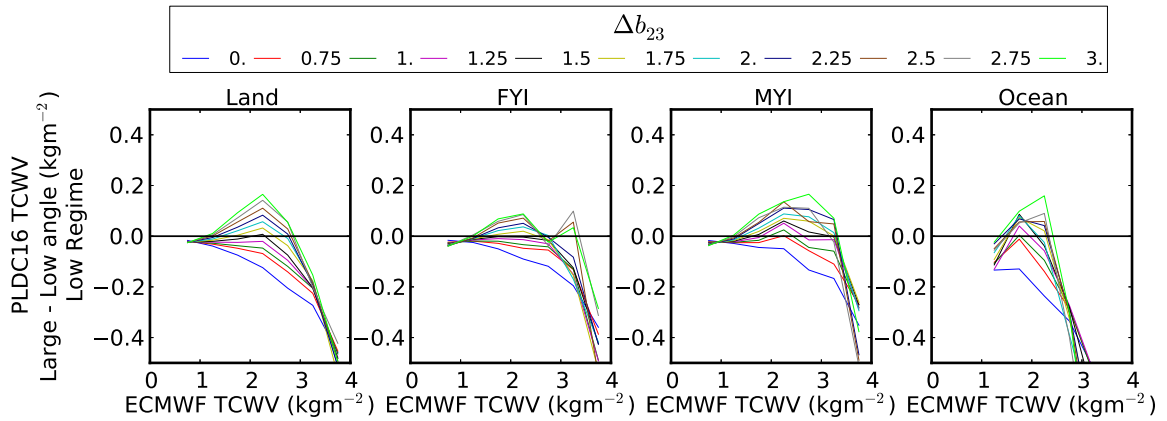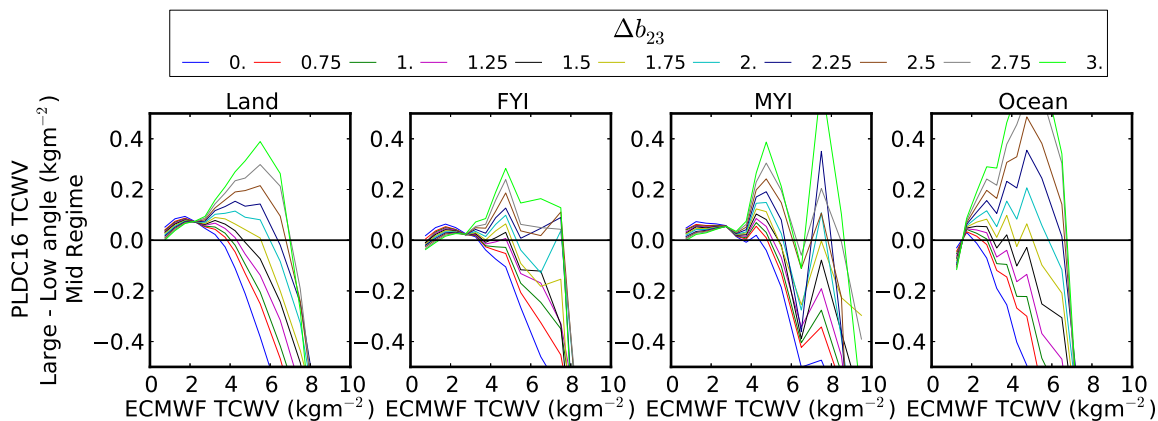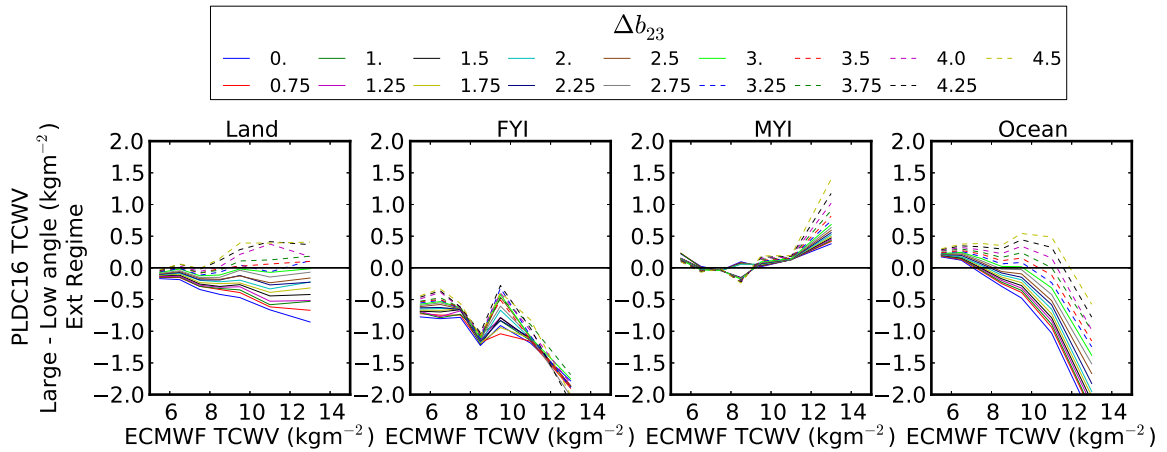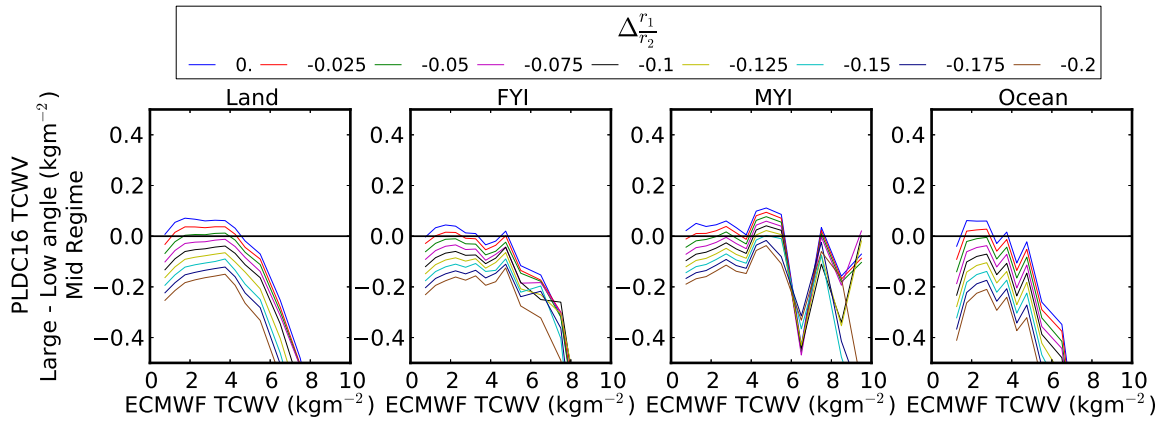
Figure 5.14: Differences in PLDC16 water vapour column for large angle and near-nadir overpasses within 3 hours at each of the 711 locations combined for different reflectance ratio adjustments for land, FYI, MYI, and open ocean surfaces for the mid regime compared to ERA-interim water vapour column.

adjustments listed earlier. The reflectance ratio adjustment for open ocean slightly degrades the result, but for this case, the smooth transition between the low and mid regimes is relatively more important than a small error in the difference between large and near nadir angle measurements.

5.7.2   Extended Regime Correction

Figure 5.15 shows the difference between the extended and mid regime PLDC16 retrieval for all satellite local zenith angles with varying reflectance ratio adjustments to $\Delta\frac{r_1}{r_2}$. Note, $\Delta\frac{r_2}{r_3}$ is equal to $\Delta\frac{r_1}{r_2}$ from the mid regime, therefore the values determined from Sect. 5.7.1 are used for $\Delta\frac{r_2}{r_3}$. The best water vapour column to have the PLDC16 mid and low regimes be equal is where they are equally weighted. For the mid-extended regime, this is between $9\,\mathrm{kg\,m^{-2}}$ and $10\,\mathrm{kg\,m^{-2}}$ slant water vapour column according to the auxiliary water vapour profile. For the mid-extended regime transition, the regimes are equally weighted at 9.5 $\mathrm{kg\,m^{-2}}$ slant water vapour column. For a mid angle from ATMS (approximately $30°$), this translates to a nadir column of approximately 8.2 $\mathrm{kg\,m^{-2}}$. However, none of the curves reduce the difference between the mid and extended regimes to a suitable size near 8.2 $\mathrm{kg\,m^{-2}}$.

Compared to the mid regime results, this was unexpected since the adjustments were no larger than -0.05 and the adjustments needed for the extended regime according to Fig. 5.15

are larger than 0.2. To gain further insight, the difference in large and near nadir angle measurements of PLDC16 water vapour column for the current reflectance ratio adjustments were viewed.
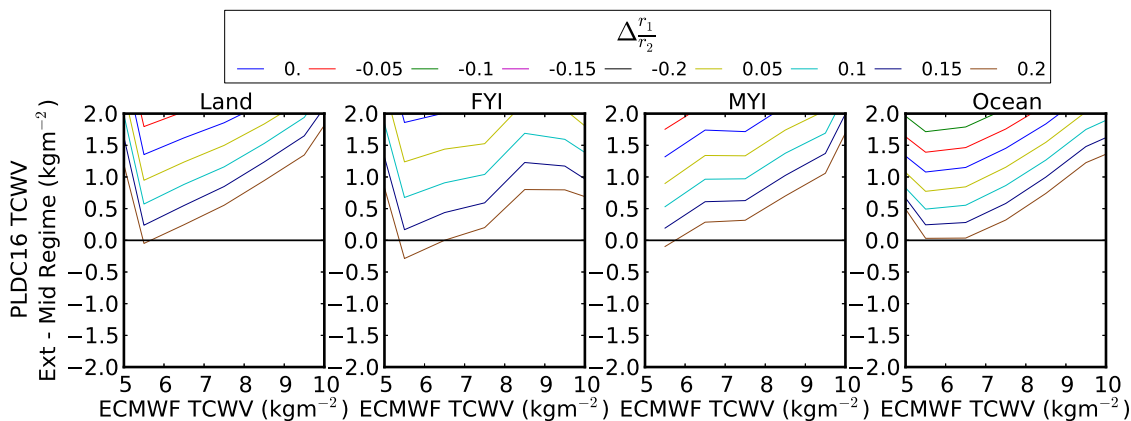
Figure 5.15: Differences in the extended and mid for the PLDC16 water vapour column at each of the 711 locations combined for different reflectance ratio adjustments at land, FYI, MYI, and open ocean surfaces compared to ERA-interim water vapour column.
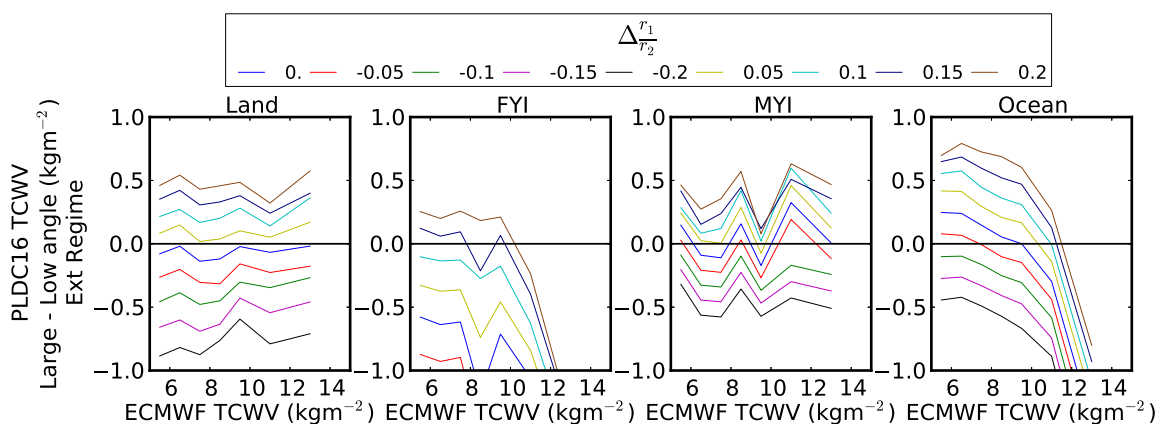
Figure 5.16: Differences in PLDC16 water vapour column for large angle and near-nadir overpasses within 3 hours at each of the 711 locations combined for different reflectance ratio adjustments for land, FYI, MYI, and open ocean surfaces for the extended regime compared to ERA-interim water vapour column.

Figure 5.16 shows the difference in extended regime water vapour column for the large and near nadir angles of the PLDC16 retrieval with varying $\Delta\frac{r_1}{r_2}$. From Fig. 5.16, the reflectance ratio adjustment that provides the minimal difference up to 12 kg m^{-2} between the large and near nadir angle measurements in the extended regime are 0 for land, 0.15 for

FYI, 0 for MYI, and -0.05 for open ocean. The reflectance ratio adjustments are significantly smaller than the results from Fig. 5.15.

Using the optimal reflectance ratio adjustments from Fig. 5.16, the water vapour columns are larger for the extended regime when compared to the mid regime. However, these reflectance ratio adjustments minimize the difference between the large and near nadir angle water vapour column measurements. The difference between the mid and extended regime is improved in Sect. 5.8 by a water vapour column adjustment.

5.8   Extended Regime TCWV Offset

A third correction is needed to align the mid and extended regime water vapour columns. Using the reflectance ratio adjustments derived in Sect. 5.7.2, the difference in large and near nadir angle water vapour column for the extended regime are nearly equal for increasing water vapour column. Therefore, a constant offset in water vapour column that is independent of angle, ΔTCWV, is applied to the extended regime.
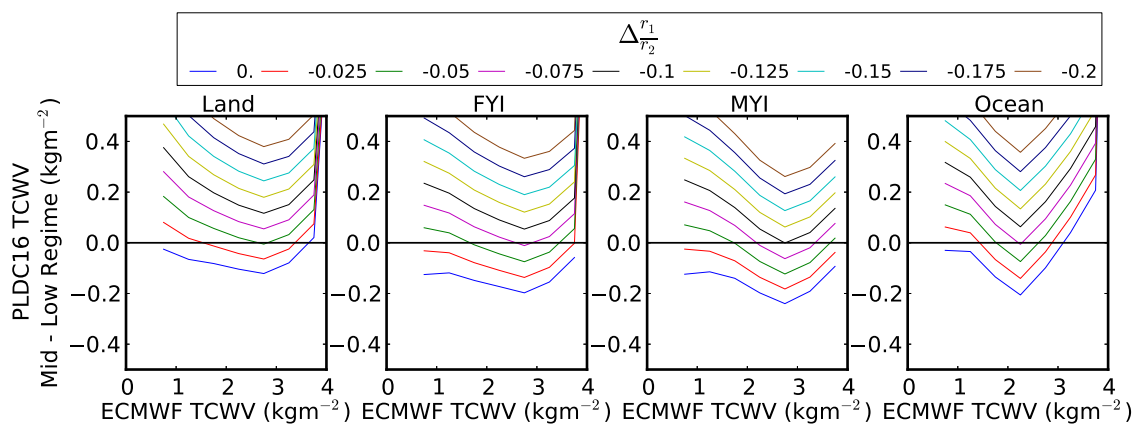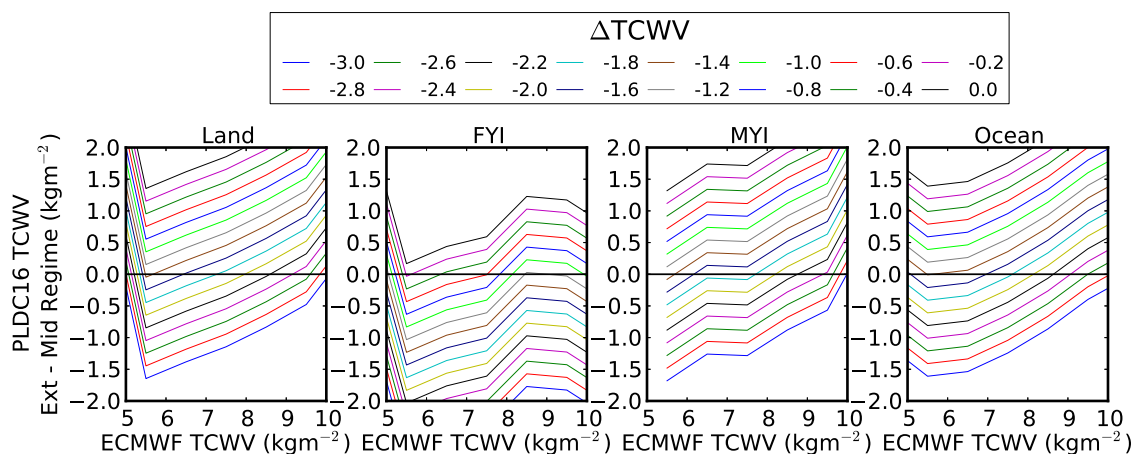

Figure 5.17: Differences in the extended and mid for the PLDC16 water vapour column at each of the 711 locations combined for different water vapour column adjustments at land, FYI, MYI, and open ocean surfaces compared to ERA-interim water vapour column.

Figure 5.17 shows the difference in the extended and mid regimes water vapour column for various water vapour column offsets applied to the extended regime. The water vapour column offsets to the extended regime that minimize the difference in water vapour column near 8.2 $\mathrm{kg\,m}^{-2}$ are -2 $\mathrm{kg\,m}^{-2}$ for land, -1 $\mathrm{kg\,m}^{-2}$ for FYI, -2 $\mathrm{kg\,m}^{-2}$ for MYI, and -2 $\mathrm{kg\,m}^{-2}$ for open ocean.

The source of error is for this offset between the extended and mid regimes is unknown. The offsets for the surfaces are equal except for over FYI. Since FYI is smaller, individual offsets are applied to each surface type since the offset could be a surface dependent error in the PLDC16 retrieval.
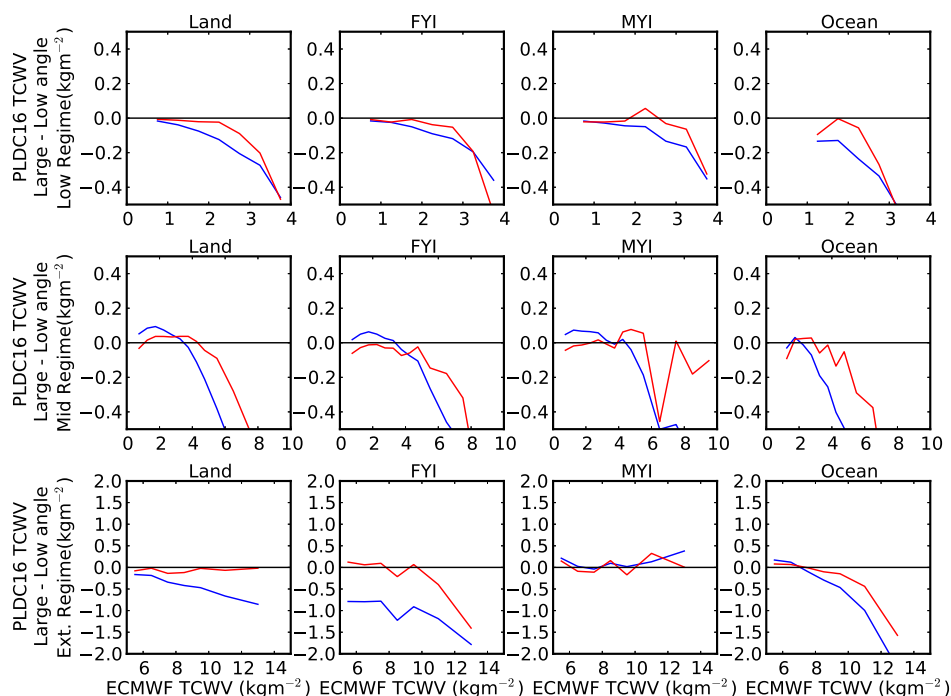
Figure 5.18: PLDC16 differences of large and near nadir angle measurements of water vapour column for all regimes and surface types before and after Δb_{23}, reflectance ratio adjustments, and water vapour column offsets are included. Blue line is without corrections and red line is with corrections.

5.9 PLDC16 Correction Summary

Figure 5.18 shows the differences in large and near-nadir angle water vapour column for the PLDC16 retrieval compared to ERA-interim water vapour column with and without the Δb_{23}, reflectance ratio adjustments, and water vapour column offsets. Overall, the PLDC16 water vapour column difference in large and near nadir angles was significantly reduced. There is still a residual increasingly negative trend with increasing water vapour column.

The increasingly negative difference grows significantly near 6 $\mathrm{kg\,m^{-2}}$, however the mid regime transitions from the mid regime and extended regime at 9 $\mathrm{kg\,m^{-2}}$ slant water vapour column. This is not an issue, according to Fig. 5.9, large angle measurements are

more strongly effected by the bias coefficient error. Larger angle measurements switch regimes at smaller nadir water vapour columns, which is before the difference grows to a significant size.

The Δb_{23}, reflectance ratio adjustments, and water vapour column offsets are summarized for each regime and surface type in Table 5.2.

Table 5.2: Summary of Corrections applied to ATMS PLDC16 retrievals

Surface	Regime	Surface Reflection	Δb_{23} (K)	$\Delta \frac{r_1}{r_2}$	ΔTCWV (kg m^{-2})
	Low		1.25	0	0
Land	Mid	Lambertian (S=0)	1.5	-0.025	0
	Ext.		3	0	-2
	Low		1.25	0	0
FYI	Mid	Lambertian (S=0)	1.5	-0.05	0
	Ext.		3	0.15	-1
	Low		1.25	0	0
MYI	Mid	Lambertian (S=0)	1.5	-0.05	0
	Ext.		3	0	-2
	Low		1.25	0	0
Land	Mid	Mix (S=0.5)	1.5	-0.025	0
	Ext.		3	-0.05	-2

5.10 PLDC16 Pan Arctic Water Vapour Column

The following section shows pan Arctic maps of water vapour column for a series of days. Comparisons of the PLDC16 water vapour column to the GVR instrument at Barrow, Alaska, the Arctic radiosonde network, and ERA-interim are subsequently give.

5.10.1 Pan Arctic Maps

Pan-Arctic water vapour maps are produced using the updated PLDC16 retrieval for the 2012/2013 winter season using the corrections shown in Table 5.2 for the ATMS instrument. Similar to the reflectance ratio maps, a 30km×30km grid is used for measurements north of 60°N. For the ATMS, maps are produced daily and grid cells with multiple overpasses are averaged.
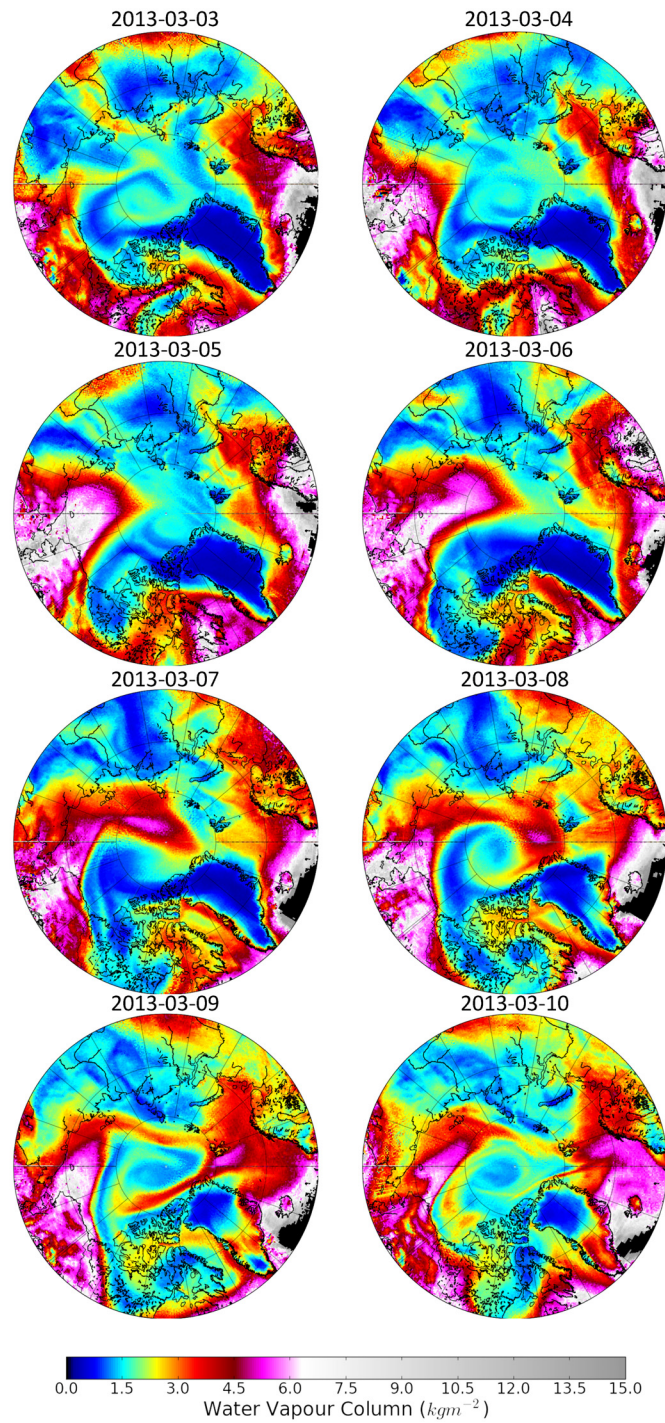
Figure 5.19: Pan-Arctic water vapour maps for March 3 to March 10, 2013. Maps were produced using ATMS measurements and the PLDC16 water vapour column retrieval.

Figure 5.19 shows a sample series of pan-Arctic maps from March 3-10, 2013. One of the most notable events in the time series is a lobe of water vapour being transported from the Pacific Ocean to the North pole. As it travels north, it begins to circulate around the pole. The maps of water vapour column also show a large amount of structure in water vapour column on March 5, 2013 and March 10, 2013 near the pole where there are several thin strands of water vapour. Another feature is the low water vapour column over Greenland. This is associated with Greenland's high surface elevation.
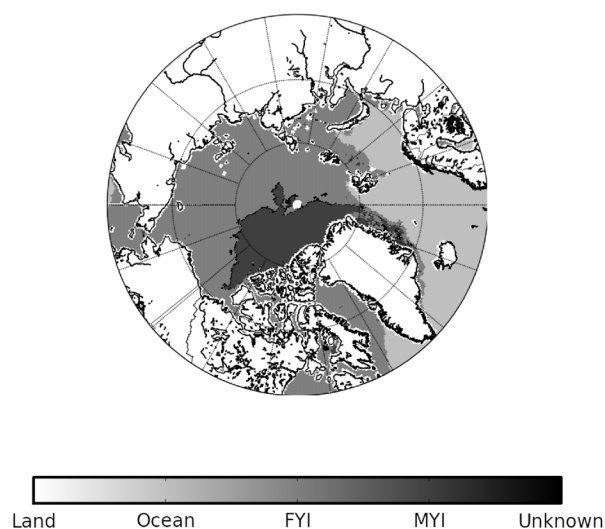
Figure 5.20: Pan-Arctic surface type map for March 6, 2013. The map was produced using the OSI-403-c retrieval.

Due to there being different corrections for different surface types, it is important to determine whether there are any discontinuities between the types of surfaces. Figure 5.20 shows an ice type map for March 6, 2013. Comparing the boundaries of surface type with Fig. 5.19 shows there are no discernible discontinuities in water vapour. One example is the lobe of water vapour transported northward on March, 7, 2013. The land and FYI boundary shows no discontinuity north of Barrow or north of Russia. Between Russia and Alaska, there are differences over FYI compared to the eastern Russia land mass, but this is likely the transport path of the water vapour. Near the pole, there is a boundary between MYI and FYI, but there is no noticeable change in water vapour column. Also, water vapour transport from the Atlantic ocean shows no discontinuity when the water vapour

mass moves over FYI.

5.10.2 Barrow TCWV Evaluation

To evaluate the updated retrieval, PLDC16 water vapour column is compared with the GVR at Barrow, Alaska as done in Chapter 3. Figure 5.21 shows the PLDC16 retrieval compared to the GVR from January 2012 to March 2015 during the winter season (December to March). The RMS deviation and bias with respect to the GVR measured water vapour columns less than $6 \, \mathrm{kg} \, \mathrm{m}^{-2}$ are 0.40 and $-0.01 \, \mathrm{kg} \, \mathrm{m}^{-2}$, respectively.
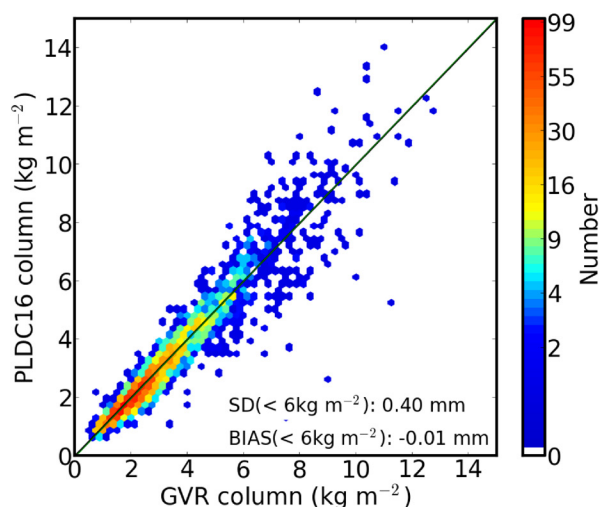
Figure 5.21: PLDC16 retrieval of water vapour column from ATMS brightness temperatures compared to GVR retrievals at Barrow, Alaska for water vapour columns less than 6 $\mathrm{kg} \, \mathrm{m}^{-2}$.

Compared to the Chapter 3 results, the RMS deviation is $0.01 \, \mathrm{kg} \, \mathrm{m}^{-2}$ larger, however, the bias is essentially eliminated. The high level of agreement between the two measurements provides a measure of validation for the PLDC16 retrieval.

5.10.3 Radiosonde Comparison

A comparison between the PLDC16 retrieval and Arctic radiosonde measurements can be made. Measurements from 62 stations across the Arctic were employed. PLDC16 overpasses within 50 km and 3 hours from a radiosonde launch were used between January 1, 2012 and March 31, 2015 for the winter months (December to March).
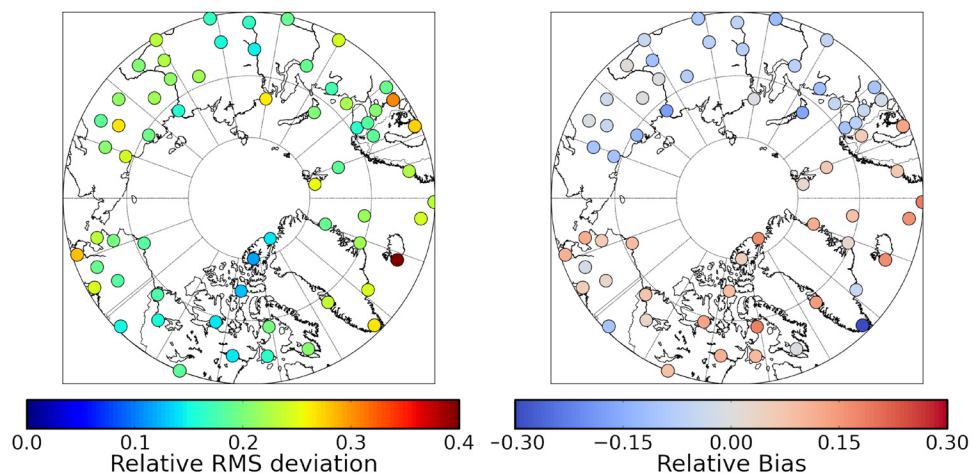
Figure 5.22: PLDC16 retrieval compared to 62 Arctic radiosonde stations in the form of relative RMS deviation and relative bias for water vapour columns less than 6 $\mathrm{kg\,m^{-2}}$.

Figure 5.22 shows the PLDC16 comparison to radiosonde measurements north of 60°N in terms of the relative RMS Deviation and relative bias. The relative RMS deviation is fairly consistent across the Arctic. Northern Canada shows small relative RMS deviations when compared to other locations. The reason for this is that the average water vapour column for the Canadian measurements are less than other radiosonde stations. This is shown in Fig. 5.23.

An outlier from the rest of the results is station 04018 on Iceland. This station has a large relative RMS deviation. This is likely associated with a large number of the overpasses being over open ocean where there are relatively larger water vapour columns in comparison to the rest of the Arctic. For the 0 to 6 $\mathrm{kg\,m^{-2}}$ interval there are a small number of measurements due to the predominantly larger water vapour columns, which could influence the accuracy of the RMS deviation.

The relative bias in Fig. 5.22 shows the radiosondes having a dry bias for most stations in Northern Canada, Alaska, and Greenland, while most stations in Europe and Russia have a wet bias. A possible reason for this is the use of different instrumentation for radiosonde launches in other regions or countries. Different countries tend to use different brands of instruments, but due to poor metadata, specifics are difficult to determine. Another reason could be associated with errors in the reflectance ratio maps used for the PLDC16 retrieval.
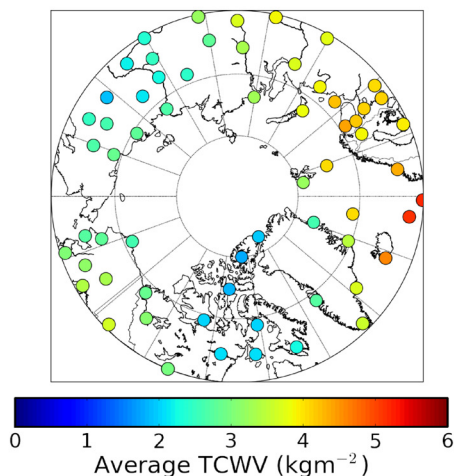
Figure 5.23: Average PLDC16 water vapour column at 62 Arctic radiosonde stations for overpasses that are within 50 km and 3 hours of a radiosonde launch.

However, the evaluation with the GVR at Barrow, Alaska, showed an almost zero bias. A ground truth network in the Arctic would help more fully evaluate the PLDC16 retrieval.

One measurement that is an outlier in terms of the bias is station 04270 near the southern tip of Greenland. This station has a large negative bias in comparison to other stations. A likely reason for this is the large variability in surface elevation. The standard deviation of surface elevation derived from topography data for the surrounding area is over 700 metres. This could have a couple different effects on the comparison between satellite and ground station measurements. First, the satellite could be measuring a different quantity than the ground based instrument, owing to footprint size (ATMS is 15 km to 45 km in diameter). Since the surface elevation standard deviation is large, certain parts of the footprint will measure more atmosphere than the other parts which could induce a bias relative to a ground-based instrument at a single point location. Second, the surface reflection type may be influenced by the varying slopes of the surface creating a type of reflection that is more complex than specular, Lambertian, or a mixture of the two.

5.10.4 ERA-Interim Comparison

A comparison between the PLDC16 retrieval and ERA-interim can also be made. Measurements were chosen from 711 locations in a regular grid with 2.5° latitude and 5° longitude

north of 60°, except for latitudes greater than 80°N where the longitudinal resolution is reduced, which are shown in Fig. 5.5. PLDC16 overpasses within 50 km were used between January 1, 2012 and March 31, 2015 for the winter months (December to March).
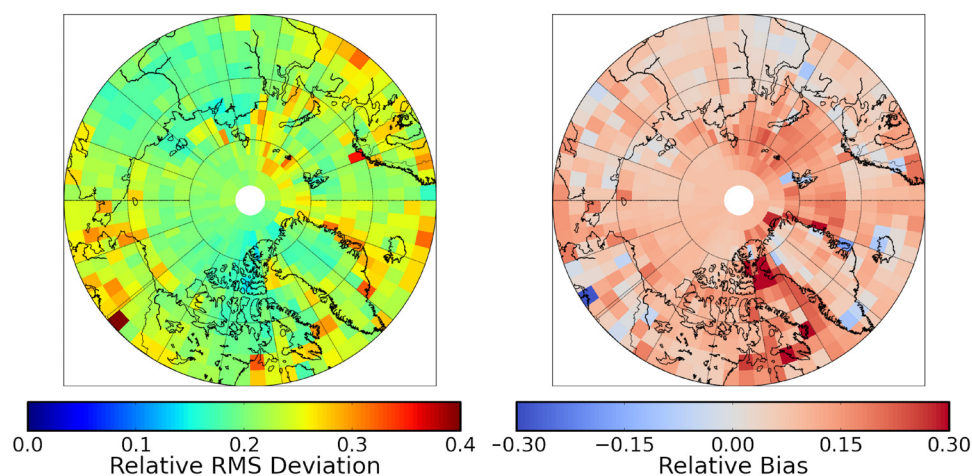
Figure 5.24: PLDC16 retrieval compared to ERA-interim at 711 locations in the form of relative RMS deviation and relative bias for water vapour column less than $6\,\mathrm{kg\,m^{-2}}$.

Figure 5.24 shows the PLDC16 comparison to ERA-interim north of 60°N in terms of the relative RMS Deviation and relative bias. The RMS deviation is fairly constant over most of Russia, Greenland, Canada, and sea ice. There are larger values in Alaska, along the coast of Greenland, Europe, and near the boundary of sea ice and open ocean.

The elevated values in Alaska, coastal Greenland, and Europe coincide with large surface elevation variability as shown in Fig. 5.25. However, the enhanced RMS deviations over the open ocean and western Russia are not associated with surface elevation variability. Also, there are regions with larger surface variability that don't show relatively large RMS deviations, such as part of eastern Russia. The larger RMS deviations near the boundary of open ocean and sea ice in the Atlantic Ocean are likely due to miss-classification of surface types in the PLDC16 retrieval or perhaps a similar issue within ERA-interim.

The relative bias shows that ERA-interim is about 10% to 15% dryer than PLDC16 over all surfaces. Comparing to the relative biases for radiosondes from Fig. 5.22, North America and Greenland radiosonde biases were equal to or smaller than what is shown in Fig.
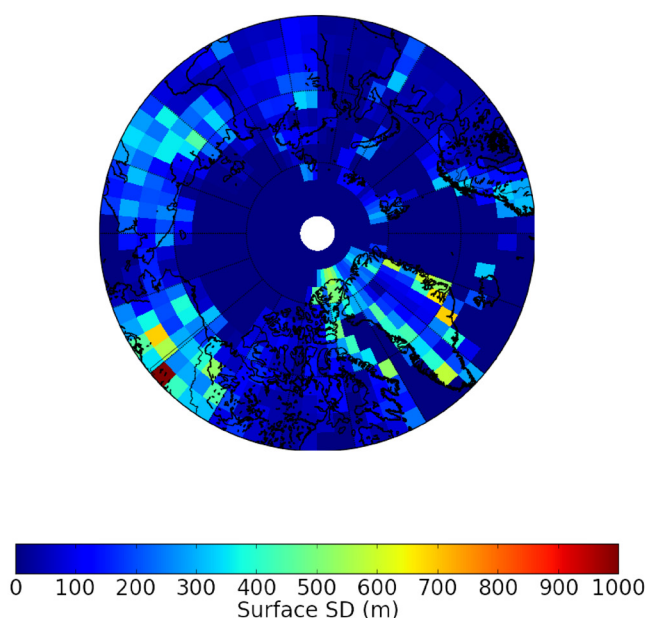
Figure 5.25: Surface elevation variability in the form of a standard deviation for the 711 locations PLDC16 and ERA-interim are compared.

5.24. However, over Russia and Europe, the water vapour column measured by radiosondes would be significantly larger than ERA-interim. The relative bias for the comparison of PLDC16 to ERA-interim is slightly smaller over Russia when compared to North America. This could be associated with the radiosonde measurements being relatively wetter in this region when compared to PLDC16 since ERA-interim uses radiosonde data as part of its reanalysis.

The relative bias also has some outlaying values in some regions. The coast of Greenland and Southern Alaska has several locations with relatively low biases which coincide with surface variability in Fig. 5.25. Similarly, northern Canada has relatively large biases which coincide with surface variability. However, some of the regions with elevated values are not over land. Near the boundary of sea-ice and open ocean in the Atlantic ocean there are elevated biases which could also be due to miss-classification sea ice and open ocean.

Figure 5.26 shows pan-Arctic maps of PLDC16 and ERA-interim water vapour column for February 25 and March 23, 2013. In general, ERA-interim and PLDC16 both show the same general water vapour features. The fine structure in water vapour column is where
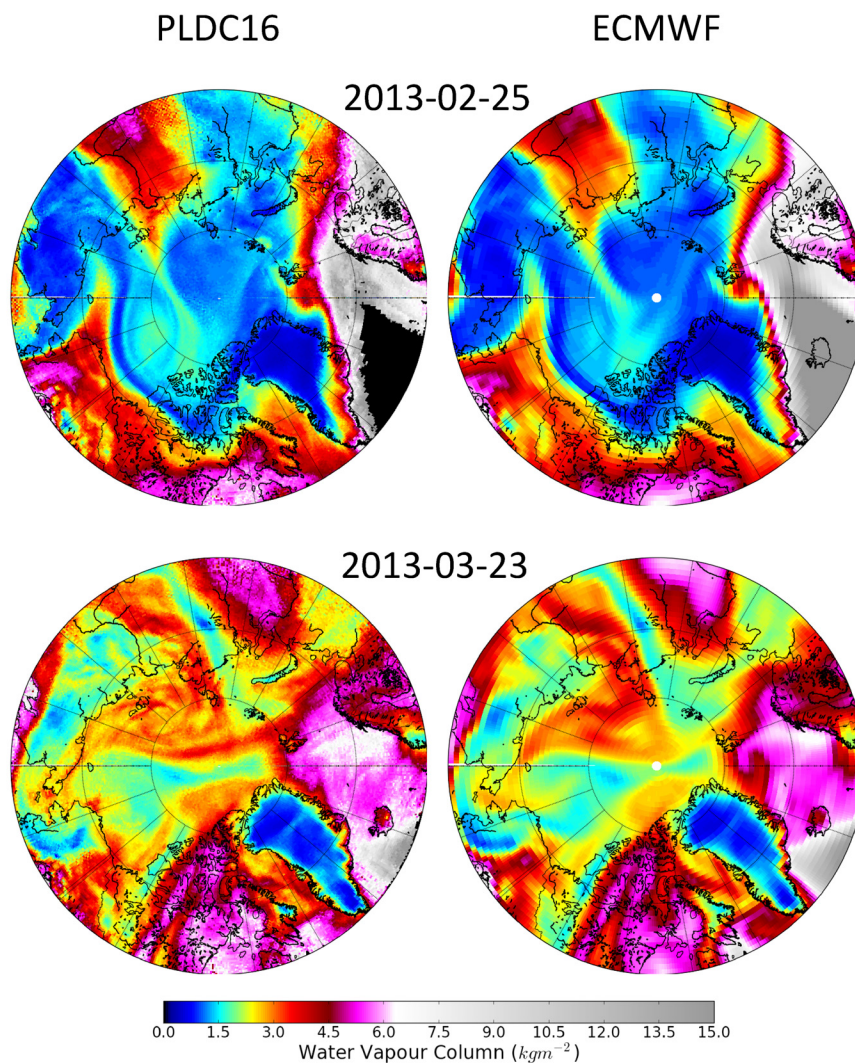
Figure 5.26: Pan Arctic maps of water vapour column for PLDC16 and ERA-interim on February 25, 2013.

differences in the retrievals are apparent.

For example, on February 25, 2013, a small mass of water vapour north of Alaska and west of Canada for ERA-interim shows a larger enhancement near the top of the feature, but in general is constant. However, PLDC16 shows the same enhancement at the top of the water vapour mass and another filament at the bottom of the distribution. A minimum separates the main mass of water vapour in the centre and the filaments north and south of it.

Another example is the case on March 23, 2013. North of Russia is a mass of water vapour that shows a large amount of structure in the PLDC16 retrieval while ERA-interim

smooths a large portion of the finer details.

5.11 Water Vapour and Ice Leads

Ice leads are areas of open ocean that form within closed areas of sea ice. Ice leads frequently occur during the Arctic winter season. The area of ice leads within sea ice is generally considered to be up to 5% during the Arctic winter (Gloersen et. al , 1993). Ice leads expose the open ocean to the relatively cold atmosphere and therefore are a source of water vapour and heat to the atmosphere (Weeks, 2010). The following section provides a case study comparing PLDC16 water vapour column to 11.5-12.5 μm AVHRR infrared measurements near the beginning of March, 2013 for the purpose of measuring water vapour in the vicinity of ice leads.
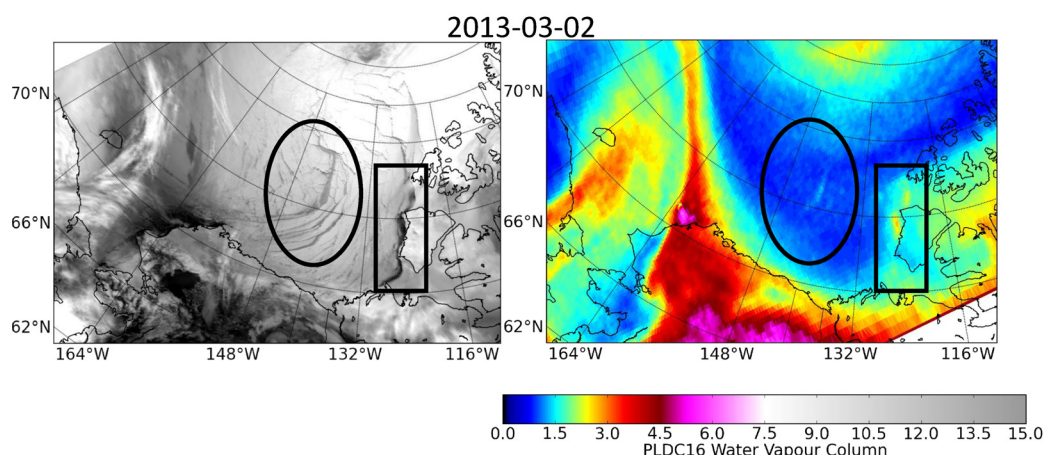
Figure 5.27: Map of AVHRR infrared measurements at 11.5-12.5 μm and PLDC16 water vapour column for March 2, 2013 over ice leads, potentially showing enhanced water vapour.

Measurements were chosen during the 2013 winter season, which had a relatively large occurrence frequency of leads (Willmes and Heinemann, 2015) in the Beaufort Sea compared to other years. Leads were detected using AVHRR raw measurements. PLDC16 retrievals of water vapour column were produced for the same location and time as AVHRR showed leads.

Figure 5.27 shows AVHRR infrared and PLDC16 water vapour column measurements for March 2, 2013 over the Beaufort Sea. These leads are relatively old since they were seen forming one week prior. This case was also shown in Sect. 3.2.1. A small enhancement in

water vapour column is shown north of Alaska (circled) where there are a few large leads according to AVHRR.

Figure 5.28: Longitudinal Cross section of AVHRR infrared measurements at 11.5-12.5 μm and PLDC16 water vapour column for March 2, 2013 over ice leads averaged between 73°N and 76°N.

To determine if the reflectance ratios were causing the effect, low regime PLDC16 water vapour column was compared to the full PLDC16 results from Fig. 5.27 (not shown). The low regime does not use reflectance ratios. The features were still visible with no discernible change in water vapour column in that region.

Figure 5.28 shows a longitudinal cross sectional image of PLDC16 water vapour column and AVHRR infrared measurements averaged between 73°N and 76 °N for the March 2, 2013 case. A small enhancement of approximately 0.1 $\mathrm{kg\,m^{-2}}$ in PLDC16 water vapour column is coinciding with a depression in the AVHRR infrared measurement near 140°W which is where the first lead in the Beaufort Sea is located. This shows that the PLDC16 water vapour column retrieval is at least sensitive to changes of approximately 0.1 $\mathrm{kg\,m^{-2}}$.

Figure 5.27 shows another lead along the coast of the Canadian archipelago (boxed), there is a larger enhancement in water vapour column compared to the lead in the Beaufort sea. There is a surrounding layer of water vapour as well but it is difficult to tell if it is part of the water vapour mass over the Canadian archipelago. The lead near the Canadian archipelago has an enhancement of almost 1 $\mathrm{kg\,m^{-2}}$ in PLDC16 water vapour column coinciding with an AVHRR depression according to Fig. 5.28.

Figure 5.29 shows AVHRR infrared and PLDC16 water vapour column for March 4,

2013-03-04
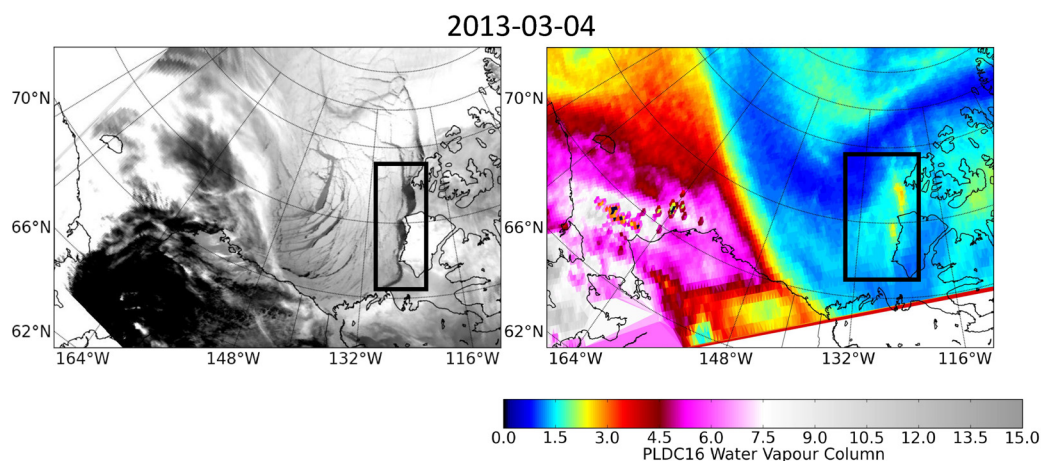
Figure 5.29: Map of AVHRR infrared measurements at 11.5-12.5 μm and PLDC16 water vapour column for March 4, 2013 over an ice lead, potentially showing enhanced water vapour.

2013, a couple days after Fig. 5.27 over the same region. The circled water vapour feature in Fig. 5.27 is no longer visible, but the feature along the Canadian archipelago is still visible (boxed). There is a larger enhancement of water vapour in the vicinity of the lead than was seen in Fig. 5.27. The enhancement of water vapour is more isolated than compared to a couple days earlier. The water vapour column from the PLDC16 low regime was also produced for this time period (not shown) and did not show a noticeable difference when compared to the full PLDC16 retrieval.

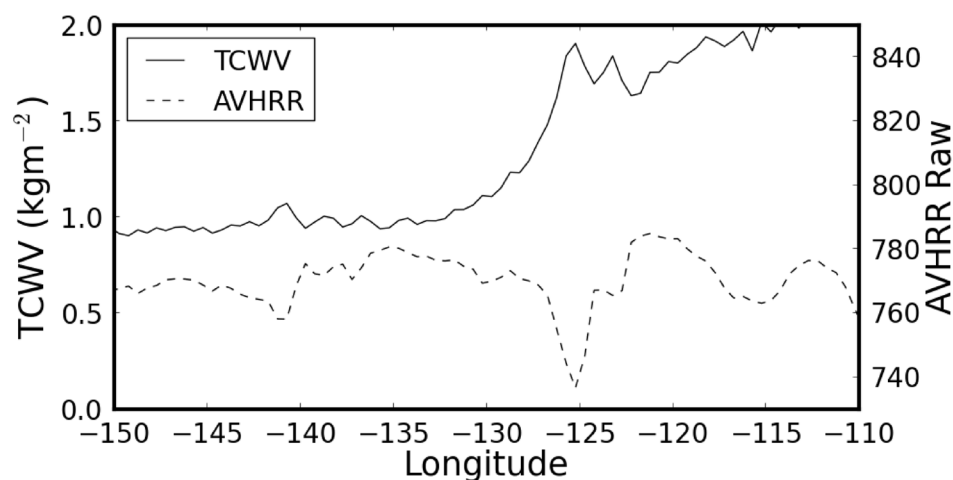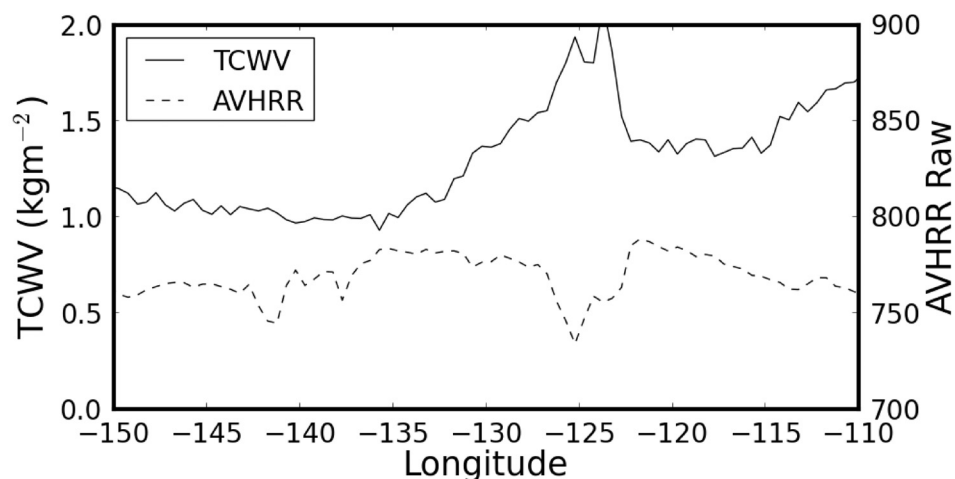Figure 5.30: Longitudinal Cross section of AVHRR infrared measurements at 11.5-12.5 μm and PLDC16 water vapour column for March 4, 2013 over ice leads averaged between 73°N and 76°N.

A longitudinal cross sectional image of PLDC16 water vapour column and AVHRR infrared measurements is shown in Fig. 5.30. Similar to Fig. 5.29, there are some depressions in AVHRR near 140°W but there is no water vapour column visible from the lead in the Beaufort Sea. The lead at the Canadian archipelago near 125°W shows a greater than $1 \, \mathrm{kg\,m^{-2}}$ enhancement compared to the water vapour columns further west which also coincides with an AVHRR depression. The enhancement of water vapour west of the lead is approximately $0.5 \, \mathrm{kg\,m^{-2}}$ compared to its surroundings and there is no corresponding depression in the AVHRR measurement. The water vapour column east of the lead shows a depression of at least $0.2 \, \mathrm{kg\,m^{-2}}$ compared to both enhancements which agrees with the interpretation of the lead being relatively isolated.

To test if the water vapour enhancement observed over leads was an artifact owing to high surface temperature over open ocean, additional simulations were performed. Assuming a surface temperature over the lead of -1.8°C (freezing point of ocean water) and that the dry adiabatic lapse rate is 9.8 K/km, temperature profiles were adjusted at the surface until the dry adiabatic temperature profile aligned with the original temperature profile. This is tested using typical arctic winter temperature profiles with large surface temperature inversions as in input into the model.
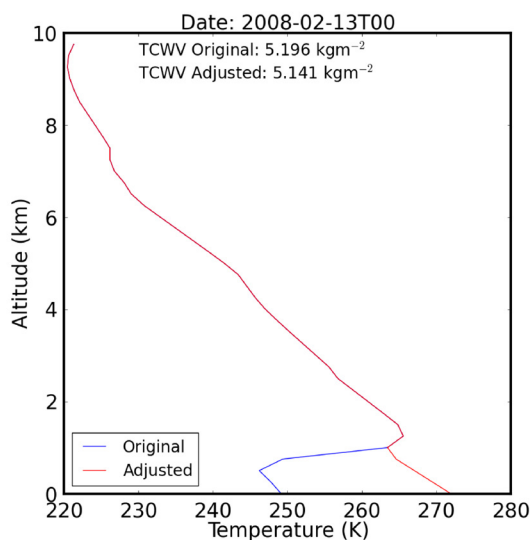
Figure 5.31: Temperature column before and after it was adjusted to simulate an increase in temperature due to an ice lead. Original and Adjusted PLDC16 TCWV are for the cases where the simulation used the adjusted temperature profile and the auxiliary was either the original or adjusted temperature profile. This was taken from a radiosonde at Barrow, Alaska on Feb. 13, 2008.

Figure 5.31 shows a sample simulation where the adjusted temperature profile was used to retrieve brightness temperature and both the original temperature profile and adjusted temperature profile were used as auxiliary information for the PLDC16 retrieval. The difference in water vapour column retrieved is approximately 0.05 $\mathrm{kg\,m^{-2}}$ which is significantly smaller than the enhancement of water vapour seen over the lead for the March 4, 2013 case. Other cases showed similar results.
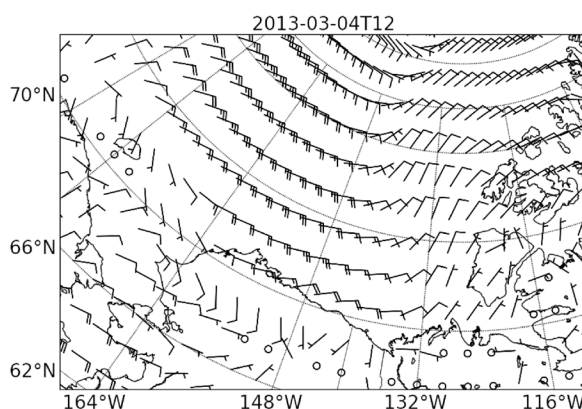
Figure 5.32: Map of ERA-interim 10 metre wind speed for the A) and B) meridional wind velocities over the Beaufort Sea region on March 4, 2013.

Figure 5.32 shows a surface wind barb plot on March 4, 2013 from ERA-interim. From wind velocities, it can be determined if the enhanced of water vapour around the lead is being transported in the same direction as the surface winds. This would indicate the water vapour could be near the surface, which is what would be expected of water vapour from an ice lead. Comparing the wind velocities to the water vapour column in Fig. 5.29, the directions of the surface wind indicate it is possible the water vapour enhancement is tracking in the same direction since the winds are pointing south-west while the water vapour column is west of the lead.

Figure 5.33 shows the ERA-interim water vapour column on March 2, 2013 and March 4, 2013 for the same Beaufort sea region. There is no enhancement near the first series of

ice leads on March 2, 2013. The water vapour enhancement directly along the coast of the Canadian archipelago was not seen, however, there still was a small enhancement of water vapour from the surrounding area of the ice lead.
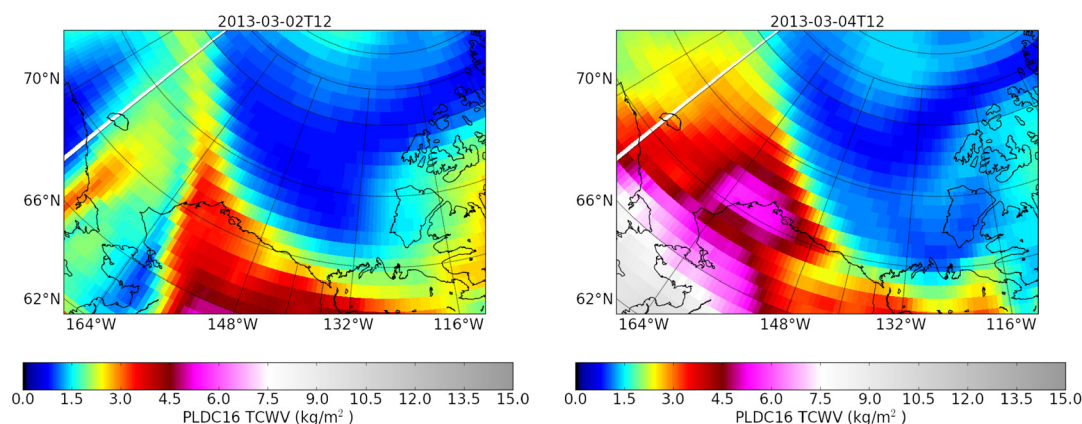
Figure 5.33: Map of ERA-interim water vapour column for A) March 2, 2013 and B) March 4, 2013 over the Beaufort Sea region.

5.12   Summary

Several changes in the PLDC16 retrieval were implemented when compared to Chapter 3. A change in the PLDC16 retrieval formulation allowed different surface reflection assumptions, which include specular, Lambertian, and a mixture of specular and Lambertian. Reflectance ratio maps replace the constant reflectance ratios used for the mid and extended regimes. Also, ATMS measurements were used instead of MHS for this chapter to reduce any effect caused by the MHS having different polarizations for the 183 GHz frequencies.

Three corrections were applied to reduce differences between water vapour columns for different regimes and different satellite local zenith angles. The first correction was to the bias coefficient/brightness temperatures, Δb_{23}, which caused an increasingly negative difference in large and near nadir angle water vapour column with increasing water vapour column.

The second correction was an offset applied to the reflectance ratios, which varied with surface type. This was implemented to further reduce differences in large and near nadir

angle water vapour column for the mid and extended regime, which were not fully corrected by Δb_{23}. The same ATMS measurements used for Δb_{23} were used to determine the reflectance ratio adjustments. The reflectance ratio adjustment also reduced a bias between the PLDC16 mid and low regimes.

The final correction was an offset to the extended regime water vapour column to align the mid and extended regimes. Similar to the other corrections, ATMS measurements were used to determine the offset.

The updated PLDC16 retrieval was compared with three different data sets, which include: GVR measurements from Barrow, Alaska, 62 Arctic radiosonde stations, and the ERA-interim reanalysis. The comparison with the GVR showed excellent agreement reducing the bias significantly when compared to the results of Chapter 3. The Arctic radiosondes also compared well, although there was a wet bias over Russia and a dry bias over North American. PLDC16 and ERA-interim also compared well, but ERA-interim was 10-15% drier than PLDC16.

A brief case study was shown for March 2-4, 2013, investigating the influence of ice leads as a local source of water vapour. The results suggest the PLDC16 retrieval has the sensitivity to measure water vapour from leads, although it is not conclusive.

CHAPTER 6

CONCLUSION

A new retrieval of water vapour column from microwave satellite measurements, PLDC16, was developed for Arctic winter conditions. The strong water vapour absorption line at 183 GHz is used for this purpose. PLDC16 replaces parameterizations that were included in its predecessor, MH08 with auxiliary water vapour and temperature profiles. PLDC16 was evaluated using both simulations and real brightness temperature measurements from the Microwave Humidity Sounder (MHS). The simulations showed that in the worst case scenario, where climatological profiles were used as an auxiliary, the PLDC16 retrieval is nearly as accurate as its predecessor, MH08. MHS brightness temperatures applied to PLDC16 show smaller RMS deviations compared to AIRS and MH08 water vapour columns with respect to a ground truth, in this case, the G-band Vapor Radiometer (GVR) at Barrow, Alaska. PLDC16 RMS deviations were comparable to reanalyses with respect to the GVR, but swath measurements of PLDC16 water vapour column showed spatial structure that was reduced or did not exist in reanalyses.

Several uncertainties were detailed that pertain to the PLDC16 retrieval. Some of these were evaluated, including: cloud contamination, removal of the second bias term, constant reflectance in the bias coefficient, and satellite dependencies. Clouds induced small increases in PLDC16 RMS deviation when comparing cloud free conditions with measurements including ice or super-cooled thin water clouds with respect to radiosonde measurements. The removal of the second bias term and constant reflectance also induced small increases in the bias and scatter respectively, which were small in comparison to the effect of clouds. There was also an insignificant difference between MHS instruments onboard MetOP-A and NOAA-18.

Some uncertainties for reflectance ratio, specular surface reflection, and instrument

channel polarization could not be directly evaluated. Reflectance ratio and the assumption of specular reflection were investigated for the purpose of reducing errors on the PLDC16 water vapour column.

Polarization was not considered in the retrieval. The effect of polarization on the PLDC16 retrieval could be investigated using a couple of methods. First, instrument channels with similar frequencies but different polarizations could be simulated over different surface types to compare the differences in brightness temperature and PLDC16 water vapour column. However, RTTOV does not currently provide a workable treatment of polarization. Once polarization is treated in radiative transfer codes, this could help advance the PLDC16 retrieval. Similarly, real measurements of instrument channels with similar frequencies but different polarizations could be used to compare the effects of polarization on brightness temperature and PLDC16 water vapour column.

In the initial PLDC16 retrieval of Chapter 3, constant reflectance ratios were used. This is not optimal as surfaces have varying properties that influence surface emissivity over time, especially in the Arctic and for microwave radiation. Therefore, surface emissivity and reflectance ratio were measured across the Arctic to reduce the error associated with a constant reflectance ratio. Two techniques were used to calculate the surface emissivity and reflectance ratio: the Hewison technique and the Selbach technique. The main difference between the two techniques is the Selbach technique uses multiple instrument channels while the Hewison technique uses a single instrument channel. The Selbach technique was used at 183 GHz since it also provides skin temperature, while Hewison does not. At 165 GHz and 88 GHz, the Hewison technique was used while employing skin temperatures obtained from the Selbach technique.

The retrieved surface emissivity was evaluated using simulations and measurements. Simulations showed that the surface emissivity should be retrieved at small water vapour columns to reduce retrieval error. Simulations also showed that the Selbach technique retrieval error was reduced when more weakly absorbed frequencies near 183 GHz were used or when an increase in the number of 183 GHz channels were used. For real brightness temperatures, maps of reflectance ratio and surface emissivity were produced and

showed significant variation across surface types, particularly over Greenland. The Greenland anomaly, which has not been previously reported, is associated with glacial ice. Surface emissivities and reflectance ratios were validated using aircraft campaign measurements and showed good agreement over the different Arctic surfaces. Aircraft campaigns over regions with anomalous values, such as were observed in Greenland and eastern Russia, would help determine the accuracy of the measurements over these locations.

Earlier, it was assumed that specular reflection occurs for microwave radiation (Guissard and Sobieski, 1994; Selbach, 2003; Hewison and English, 1999). More recently, Lambertian surface reflection has been assumed to occur over land and sea ice (Harlow, 2009). A method to determine the correct choice was investigated using the PLDC16 retrieval. Simulations showed that the difference between large and nadir angle water vapour columns increased if the incorrect surface reflection was assumed in the retrieval. Taking advantage of this, the PLDC16 retrieval was applied using specular, Lambertian, and a mixture of both. It revealed Lambertian was the best choice for land and sea ice surfaces while a mixture was best for open ocean. The result for open ocean is unique in the literature.

Other issues with PLDC16 were discovered while investigating surface reflection. The difference in PLDC16 water vapour column for large and nadir angles was increasingly negative with increasing water vapour column, and for some cases the difference was large for all types of surface reflection. Corrections were applied to the bias coefficients, reflectance ratios, and extended regime water vapour column to reduce or remove these effects on the PLDC16 water vapour column.

Comparisons of the the updated PLDC16 retrieval with the GVR, Arctic radiosondes, and ERA-interim showed good agreement overall. Arctic radiosondes showed varying biases depending on geographical location which are likely associated with the type of radiosonde instrument used. ERA-interim showed a dry bias in comparison to PLDC16 which has implications for our understanding of radiative transfer and climate in the Arctic. Further validation is needed to confirm this result. The Extended Atmospheric Emitted Radiance Interferometer (E-AERI) in Eureka, Nunavut, will be used in future work.

PLDC16 was finally used to investigate the influence ice leads have on local water vapour for a single case with the aid of AVHRR infrared measurements. The results suggest an enhancement of water vapour near an ice lead. More cases need to be investigated for the purpose of validation.

Some other projects the PLDC16 retrieval could be applied to include: measuring the dehydration of the atmosphere, producing a water vapour climatology, developing an Arctic water budget, and improving reanalyses.

The PLDC16 retrieval is versatile as it can be applied to several microwave instruments which include the Microwave Humidity Sounder (MHS), Advanced Technology Microwave Sounder (ATMS), MicroWave Humidity Sounder (MWHS), Special Sensor Microwave Imager/Sounder (SSMIS), Advanced Microwave Sounding Unit-B (AMSU-B), and Special Sensor Microwave/Temperature 2 (SSM/T-2). Each instrument is on board multiple satellites and combined can provide 25 years of water vapour column measurements.

BIBLIOGRAPHY

Aaboe, S., Breivik, L., and Eastwood, S.: Algorithm Theoretical Basis Document for the OSI SAF Global Sea Ice Edge and Type product - v1.2 Technical Report SAF/OSI/CDOP2/MET˙Norway/SCI/MA/208, EUMETSAT OSI SAF - Ocean and Sea Ice Satellite Application Facility, 2015.

Bohren, C. and Huffman, D.: Absorption and Scattering of Light by Small Particles, John Wiley and Sons, New York, USA, 1983.

Bourdages, L., Duck, T., Lesins, G., Drummond, J., and Eloranta, E.: Physical properties of High Arctic tropospheric particles during winter, Atmos. Chem. Phys., 9, 6881–6897, 2009.

Boukabara, S., Garrett, K., and Chen, W.: Global Coverage of Total Precipitable Water Using a Microwave Variational Algorithm, IEEE T. Geosci. Remote, 48, 3608–3621, 2010.

Boukabara, S., Garrett, K., Chen, W., Iturbide-Sanchez, F.,Grassotti, C., Kongoli, C., Chen, R., Liu, Q., Yan, B., Weng, F., Ferraro, R., Kleespies, T., and Meng, H.: MIRS: An All-Weather 1DVAR Satellite Data Assimilation and Retrieval System, IEEE T. Geosci. Remote, 49, 3249–3272, 2011.

Breivik, L., Eastwood, S., and Lavergne, T: Use of C-Band Scatterometer for Sea Ice Edge Identification, IEEE T. Geosci. Remote, 50, 2669–2677, 2012.

Bromwich, D., Kuo, Y., Serreze, M., Walsh, J., Bai, L., Barlage, M. Hines, K., and Slater, A.: Arctic system reanalysis: call for community involvement, EOS T. Am. Geophys. Un., 91, 13–14, 2010.

Behler, S., Östman, S., Melsheimer, C., Holl, G., Eliasson, S., John, V., Blumenstock, T., Hase, F., Elgered, G., Raffalski, U., Nasuno, T., Satoh, M., Milz, M., and Mendrok, J.: A multi-instrument comparison of integrated water vapour measurements at a high latitude site, Atmos. Chem. Phys., 12, 10925–10943,2012.

Cadeddu, M., Turner, D., and Liljegren, J.: A neural network for real-time retrievals of PWV and LWP from Arctic millimeter wave ground based observations, IEEE T. Geosci. Remote, 9, 1887–1900, 2009.

Cadeddu, M., Liljegren, J., and Turner, D.: The Atmospheric radiation measurement (ARM) program network of microwave radiometers: instrumentation, data, and retrievals, Atmos. Meas. Tech., 6, 2359–2372, 2013.

Chuvieco, E. and Huete, A.: Fundamentals of Satellite Remote Sensing, CRC Press, USA, 2009.

Cormier, J., Hodges, J. and Drummond, J.: Infrared water vapor continuum absorption at atmospheric temperatures, J. Chem. Phys., 122, 114309, 2005.

Curry, J., Schramm, J., Serreze, M., and Shramm, J.: Water vapor feedback over the Arctic Ocean, J. Geophys. Res., 100, 223–229, 1995.

Curry, J., Rossow, W., Randall, D., and Schramm, J.: Overview of Arctic Cloud and Radiation Characteristics, J. Climate, 9, 1731–1764, 1996.

Dee, D., Uppala, S., Simmons, A., Berrisford, P., Poli, P., Kobayashi, S., Andrae, U., Balmaseda, M., Balsamo, G., Bauer, P., Bechtold, P., Belijaars, A., van de Berg, L., Bidlot, J., Bormann, N., Delsol, C., Dragani, R., Fuentes, M., Geer, A., Haimberger, L., Healy, S., Hersbach, H., Hólm, E., Isaksen, L., Kållberg, P., Köhler, M., Matricardi, M., McNally, A., Monge-Sanz, B., Morcrette, J., Park, B., Peubey, C., de Rosnay, P., Tavolato, C., Thépaut, J., and Vitart. F.: The ERA interim reanalysis: configuration and performance of the data assimilation system, Q. J. Roy. Meteor. Soc., 137, 553–597, 2011.

Devasthale, A., Sedlar, J., and Tjernstrom, M.: Characteristics of water-vapour inversions observed over the Arctic by Atmospheric Infrared Sounder (AIRS) and radiosondes, Atmos. Chem. Phys., 11, 9813–8323,2011.

Divakarla, M., Barnet, C., Goldberg, M., McMillin, L., Maddy, E., Wolf, W., Zhou, L., and Liu, X.: Validation of atmospheric infrared sounder temperature and water vapor retrievals with matched radiosonde measurements and forecasts, J. Geophys. Res., 111, D09S15,2006.

Fuhrhop, R., Grenfell, T., Heygster, G., Johnsen, K., Schliissel, P., Schrader, M., and Simmer, C.: A combined radiative transfer model for sea ice, open water, and atmosphere, Radio Sci., 33, 303–316, 1998.

Ghatak, D. and Miller, J.: Implications for Arctic amplification of changes in the strength of the water vapor feedback, J. Geophys. Res., 118, 7569–7578, 2013.

GISTEMP Team: GISS Surface Temperature Analysis (GISTEMP),NASA Goddard Institute for Space Studies. Dataset accessed 2017-05-16 at https://data.giss.nasa.gov/gistemp, 2017.

Gloersen, P., Campbell, W., Cavalieri, D., Comiso, J., Parkinson, C., and Zwalley, H.: Arctic and Antarctic Sea Ice, 1978-1987, Ann. Glaciol., 149–154, 1993.

Guedj, S., Karbou, K., Rabier, F., and Bouchard, A.: Toward a Better Modeling of Surface Emissivity to Improve AMSU Data Assimilation Over Antarctica, IEEE T. Geosci. Remote, 48, 1976–1985, 2010.

Guissard, A. and Sobieski, P.: A simplified radiative transfer equation for application in ocean microwave remote sensing, Radio Sci., 29, 881–894, 1994.

Haggerty, J. and Curry, J.: Variability of sea ice emissivity estimated from airborne passive microwave measurements during FIRE SHEBA, J. Geophys. Res., 106, 15265–15277, 2001.

Haall, D., Nghiem, S., Schaaf, C, DiGirolamo, N., and Neumann, G.: Evaluation of surface and near-surface melt characteristics on Greenland ice sheet using MODIS and QuikSCAT data, J. Geophys. Res., 114, F04006, 2009.

Hansen, J., Ruedy, R., Sato, M., and Lo, K.: Global surface temperature change, Rev. Geophys., 48, RG4004,doi:10.1029/2010RG000345, 2010.

Harlow, R.: Millimeter Microwave Emissivities and Effective Temperatures of Snow-Covered Surfaces: Evidence for Lambertian Surface Scattering, IEEE T. Geosci. Remote, 47, 1957–1970, 2009.

Harlow, R.: Sea Ice Emissivities and Effective Temperatures at MHS Frequencies: An Analysis of Airborne Microwave Data Measured During Two Arctic Campaigns, IEEE T. Geosci. Remote, 49, 1223–1237, 2011.

Hasted, J., Husain, S., Frescura, F., and Birch, J.: The temperature variation of the near millimetre wavelength optical constants of water, Infrared Phys., 27, 11–15, 1987.

Hewison, T. and English, S.: Airborne retrievals of snow and ice surface emissivity at millimeter wavelengths, IEEE T. Geosci. Remote, 37, 1871–1879, 1999.

IPCC, 2014: Climate Change 2014: Synthesis Report. Contribution of Working Groups I, II, and III to the Fifth Assessment Report of the Intergovernmental Panel of Climate change [Core Writing Team, R.K. Pachauri and L.A. Meyer (eds.)], IPCC, Geneva, Switzerland, 151 pp. in IPCC AR5 Synthesis Report website.

Kakar, R.: Retrieval of Clear Sky Moisture Profiles using the 183 GHz Water Vapor Line, J. Clim. Appl. Meteoral., 22, 1282–1289, 1983.

Kalnay, E., Kanamitsu, M., Kistler, R., Collins, W., Deaven, D., Gandin, L., Iredell, M., Saha, S., White, G., Woollen, J., Zhu, Y., Leetmaa, A., Reynolds, R., Chelliah, M., Ebisuzaki, W., Higgins, W., Janowiak, J., Mo, K., Ropelewski, C., Wang, J., Jenne, R., and Joseph, D.: The NCEP NCAR 40 year reanalysis project, B. Am. Meteorol. Soc., 77, 437–470, 1996.

Karbou, F., Rabier, F., and Prigent, C.: The Assimilation of Observations from the Advanced Microwave Sounding Unit over Sea Ice in the French Global Numerical Weather Prediction System, Mon. Weather. Rev., 142, 125–140, 2014.

Kim, E., Lyu, C-H., Anderson, K., Leslie, V., and Blackwell, W.: S-NPP ATMS instrument prelaunch and on-orbit performance evaluation, J. Geophys. Res-Atmos., 119, 5653–5670, 2014.

Kleepsies, T. and Watts, P.: Comparison of simulated radiances, Jacobians and linear error analysis for the microwave humidity sounder and the advanced microwave sounding unit B, Q. J. Roy. Meteor. Soc., 3001–3010, 2006.

Kneifel, S., Lohnert, U., Battaglia, A., Crewell, S. and Siebler, D.: Snow scattering signals in ground-based passive microwave radiometer measurements, J. Geophys. Res., 115, D16214, 2010.

Kobayashi, S., Ota, Y., Harada, Y., Moriya, M., Onoda, H., Onogi, K., Kamahori, H., Kobayashi, C., Endo, H., Miyaoka, K., and Takahashi, K.: The JRA 55 reanalysis: general specifications and basic characteristics, IEEE T. Geosci. Remote, 93, 5–48, 2015.

Kongoli, C., Boukabara, S., Yan, B., Weng, F., and Ferraro, R.: A New Sea-Ice Concentration Algorithm Based on Microwave Surface Emissivities Application to AMSU Measurements, IEEE T. Geosci. Remote, 49, 175–189, 2011.

Lesins, G., Duck, T., and Drummond, J.: Climate trends at Eureka in the Canadian high Arctic, Atmos. Ocean, 48, 59–80, 2010.

Lesins, G., Duck, T., and Drummond, J.: Surface energy balance framework for Arctic amplification of climate change, J. Climate, 25, 8277–8288, 2012.

Lindsay, R., Wensnahan, M., Schweiger, A., and Zhang, J.: Evaluation of Seven Different Atmospheric Reanalysis Products in the Arctic, J. Climate, 27, 2588–2606, 2013.

Liou, K.: An Introduction to Atmospheric Radiation, University of California, USA, 2002.

Liu, G.: A database of microwave single-scattering properties for nonspherical ice particles, B. Am. Meteorol. Soc., 89, 15631570, 2008.

Martin, S.: An introduction to Remote Ocean Sensing - Second Edition, Cambridge University Press, Cambridge, UK, 2014.

Mathew, N., Heygster, G., Melsheimer, C., and Kaleschke, L.: Surface Emissivity of Arctic Sea Ice at AMSU Window Frequencies, IEEE T. Geosci. Remote, 46, 2298–2306, 2008.

Matricardi, M. and Saunders, R.: Fast radiative transfer model for simulation of infrared atmospheric sounding interferometer radiances, Appl. Optics, 38, 5679–5691, 1999.

Matzler, C.: Applications of the interaction of microwaves with the natural snow cover, Remote Sens. Rev., 2, 259-392, 1987.

Matzler, C.: On the Determination of Surface Emissivity From Satellite Observations, IEEE T. Geosci. Remote Letters, 2, 160–163, 2005.

Maxwell, J.: Polarized Emittance. Volume 1: Polarized Bidirectional Reflectance with Lambertian or Non-Lambertian Diffuse Components, Environmental Research Institute of Michigan, Prepared for Ballistic Research Laboratories, 1974.

McGowan, W.: Water Processing Third Edition, Water Quality Association, Lisle, Illinois, USA, 2000.

McGrath, A. and Hewison, T.: Measuring the Accuracy of MARSS - An Airborne Microwave Radiometer, J. Atmos. Ocean Tech., 18, 2003–2012, 2001.

Melsheimer, C. and Heygster, G.: Improved retrieval of total water vapor over polar regions from AMSU-B microwave radiometer data, IEEE T. Geosci. Remote, 46, 2307–2322, 2008.

Mernild, S.: Greenland ice sheet surface melt extent and trends: 1960-2010, J. Glaciol., 57,621–628, 2011.

Miao, J.: Retrieval of Atmospheric Water Vapor Content in Polar Regions Using Spaceborne Microwave Radiometry, Alfred Wegener Inst. Polar Marine Res., Bremerhaven, Germany, 1998.

Miao, J., Kunzi, K., Heygster, G., Lachlan-Cope, T., and Turner, J.: Atmospheric water vapor over Antarctica derived from special sensor microwave/temperature 2 data, J. Geophys. Res., 106, 10187–10203, 2001.

Nicodemus, F.: Directional Reflectance and Emissivity of an Opaque Surface, Appl. Optics, 4, 767–775, 1965.

All about Sea Ice. National Snow and Ice Data Center. Accessed 25 June 2017.

Payne, V., Mlawer, E., Pereira, C. and Moncet, J.: Water Vapor Continuum Absorption in the Microwave, IEEE T. Geosci. Remote, 49, 2194–2208, 2011.

Pazmany, A.: A compact 183 GHz radiometer for water vapor and liquid sensing, IEEE T. Geosci. Remote, 45, 2202–2207, 2007.

Perro, C., Lesins, G., Duck, T., and Cadeddu, M.: A microwave satellite water vapour column retrieval for polar winter conditions, Atmos. Meas. Tech., 9, 2241–2252, 2016.

Petty, G.: A First Course In Atmospheric Radiation, Sundog Publishing, Madison, Wisconsin, 2006.

Pithan, F. and Mauritsen, T.: Arctic amplification dominated by temperature feedbacks in contemporary climate models, Nat. Geosci., 7, 181–184, 2014.

Przybylak, R.: The Climate of the Arctic second edition, Kluwer Academic Publishers, Norwell, MA, USA, 2015.

Rodgers, C.: Inverse Methods for Atmospheric Sounding: Theory and Practice, World Scientific, Singapore, 2000.

Seinfeld, J. and Pandis, S.: Chemistry and Physics: From Air Pollution to Climate Change, John Wiley and Sons Inc., New Jersey, USA, 2016.

Selbach, N.: Determination of Total Water Vapor and Surface Emissivity of Sea Ice at 89 GHz, 157 GHz and 183 GHz in the Arctic Winter, PhD thesis, University of Bremen, Bremen, Germany, 2003.

Serreze, M. and Barry, R.: The Arctic Climate System, Cambridge University Press, Cambridge, UK, 2005.

Serreze, M., Barry, R., and Walsh, J.: Atmospheric water vapor characteristics at 70 N, J. Climate, 8, 719–731, 1995.

Serreze, M. and Barry, R.: Processes and impacts for Arctic amplification: A research synthesis, Global Planet. Change,77, 85–96,2011.

Serreze, M., Barrett, A., and Stroeve, J.: Recent changes in tropospheric water vapor over the Arctic as assessed from radiosondes and atmospheric reanalyses, J. Geophys. Res.,117, D10104,2012.

Shokr, M. and Sinha, N.: Sea Ice: Physics and Remote Sensing, John Wiley and Sons Inc., New Jersey, USA, 2015.

Spinhirne, J.: Micro Pulse Lidar, IEEE T. Geosci. Remote, 31, 48–55, 1993.

Stamnes, K., Ellingson, R., Curry, J., Walsh, J., and Zak, B.: Review of science issues, deployment strategy, and status for the ARM north slope of Alaska-Adjacent Arctic Ocean Climate Research Site, J. Climate, 12, 46–63, 1998.

Seinfeld, J. and Pandis, S.: Practical Meteorology: An Algebra-based Survey of Atmospheric Science, University of British Columbia, Canada, 2016.

Talley, L., Pickard, G., Emery, W., and Swift, J.: Descriptive Physical Oceanography, Elsevier, Boston, USA, 2011.

Tobin, D., Revercomb, R., Knuteson, R., Lesht, B., Strow, L., Hannon, S., Feltz, W., Moy, L., Fetzer, E., and Cress, T.: Atmospheric Radiation Measurement site atmospheric state best estimates for Atmospheric Infrared Sounder temperature and water vapor retrieval validation,, J. Geophys. Res.,111, D09S14,2006.

Willmes, S. and Heinemann, G.: Sea-Ice Wintertime Lead Frequencies and Regional Characteristics in the Arctic, 2003-2015,Remote Sens.,8, 2015.

Wallace, J. and Hobbs, P.: Atmospheric Science: An introductory Survey - Second Edition, Academic Press Publications, Cambridge, Massachusetts, USA, 2006.

Weeks, W.: On sea ice, University of Alaska Press, Alaska, USA, 2010.

Weng, F. and Yang, H.: Validation of ATMS Calibration Accuracy Using Suomi NPP Pitch Maneuver Observations, Remote Sens.,8, 1–14, 2016.

Yan, B., Weng, F., and Meng, H.: Retrieval of snow surface microwave emissivity from advanced microwave sounding unit, J. Geophys. Res., 113, 1–23, 2008.

APPENDIX A

For the brightness temperature formulation derived in Chapter 2 and used in the retrievals of Chapter 3, Chapter 4, and Chapter 5, algebraic manipulation of Eq. 2.21 is done to derive the form in Eq. 2.24 and Eq. 2.25.

To begin, Eq. 2.22 and Eq. 2.23 are modified to replace the absorption coefficient and transmittance terms with a partial derivative of transmittance with respect to altitude as shown below,

$$T_u = \int_0^H T_a(z) \frac{\partial t(z,H)}{\partial z} dz \tag{A.1}$$

and

$$T_D = -\int_0^H T_a(z) \frac{\partial t(0,z)}{\partial z} dz + t(0,H)T_c \tag{A.2}$$

where $t(0,z)$ is the transmittance from the surface to altitude, z, $t(z,H)$ is the transmittance from altitude, z, to the satellite at altitude, H, and $t(0,H)$ is the transmittance of the entire atmosphere from the surface, 0, to the satellite at altitude, H.

Integration by parts is applied to T_U in Eq. A.1 to become,

$$T_u = T_a(z)t(z,H)\big|_0^H - \int_0^H t(z,H) \frac{dT_a(z)}{dz} dz \tag{A.3}$$

where T_0 is the surface atmospheric temperature. The first term on the right hand side is evaluated to get,

$$T_u = T_a(H) - t(0,H)T_0 - \int_0^H t(z,H) \frac{dT_a(z)}{dz} dz \tag{A.4}$$

where $T_a(H)$ is the atmospheric temperature at satellite. The next step is to add and subtract $\int_0^H \frac{dT_a(z)}{dz}$ to the right hand side and bring the positive term into the integral and evaluate the negative term. With some rearrangement $T_U(\hat{r})$ becomes,

$$T_u = [1 - t(0,H)]T_0 + \int_0^H [1 - t(z,H)] \frac{dT_a(z)}{dz} dz$$
$$= [1 - t(0,H)]T0 - I_1 \tag{A.5}$$

where $I_1 = -\int_0^H [1 - t(z,H)] \frac{dT_a(z)}{dz} dz$.

Next, similar manipulations are applied to T_D. First, integration by parts is applied to

T_D in Eq. A.2 and the first term on the right hand side is evaluated to become,

$$T_D = T_0 - t(0,H)T_a(H) - \int_H^0 t(0,z)\frac{dT_a(z)}{dz}dz] + t(0,H)T_c. \tag{A.6}$$

The following term, $t(0,z) = \frac{t(0,H)}{t(z,H)}$ is substituted into the integral and $t(0,H)$ leaves the integral as shown below,

$$T_D = T_0 - t(0,H)T_a(H) - t(0,H)\int_H^0 \frac{1}{t(z,H)}\frac{dT_a(z)}{dz}dz + t(0,H)T_c. \tag{A.7}$$

Also, similar to the upwelling derivation, the addition and subtraction of a term is applied, except in this case it is $t_i(0,H)\int_H^0 \frac{dT_a(z)}{dz}$. The positive term is evaluated and the negative term is combined with the integral in Eq. A.7 to get,

$$T_D = T_0 - t(0,H)T_a(H) -$$
$$\left(t(0,H)[T_0 - T_a(H)] - t(0,H)\int_H^0 \frac{dT_a(z)}{dz}(1 - \frac{1}{t(z,H)})dz \right) + t(0,H)T_c. \tag{A.8}$$

Rearrangement of the terms outside the integral and substituting $I_2 = \int_H^0 \frac{dT_a(z)}{dz}(1 - \frac{1}{t(z,H)})dz$, T_D gives,

$$T_D = T_0[1 - t(0,H)] - t(0,H)I_2 + t(0,H)T_c. \tag{A.9}$$

The new forms of $T_U(\hat{r})$ and $T_D(\hat{i}_r)$ from Eq. A.5 and Eq. A.9 respectively are substituted into the satellite brightness temperature formula for T_i from Eq. 2.21 to give,

$$T_i = [1 - t(0,H)]T_0 - I_1$$
$$+ t(0,H)[\varepsilon T_S + (1 - \varepsilon)(T_0[1 - t(0,H)] - t(0,H)I_2 + t(0,H)T_c)] \tag{A.10}$$

After each term is expanded individually, rearrangement is done for the purpose of combining I_1 and I_2 to get $I_p = I_1 + (1 - \varepsilon)t^2(0,H)I_2$ which produces,

$$T_i = T_0 - t(0,H)T_0 + t(0,H)\varepsilon T_S + t(0,H)T_0 -$$
$$\varepsilon t(0,H)T_0 - I_P - (T_0 - T_c)(1 - \varepsilon)t^2(0,H). \tag{A.11}$$

Extracting the skin temperature, T_S from every term except for the last on the right hand

side and canceling $t(0,H)T_a(0)$ gives,

$$T_i = T_S \left((1 - t(0,H)\varepsilon)\frac{T_0}{T_S} + t(0,H)\varepsilon - \frac{I_P}{T_S} \right) - (T_0 - T_c)(1 - \varepsilon)t^2(0,H). \qquad \text{(A.12)}$$

Finally, the addition and subtraction of $\frac{T_S}{T_S}$ is applied inside the large brackets giving,

$$T_i = T_S \left((1 - t(0,H)\varepsilon)\frac{T_0}{T_S} + t(0,H)\varepsilon + \frac{T_S}{T_S} - \frac{T_S}{T_S} - \frac{I_P}{T_S} \right) -$$
$$(T_0 - T_c)(1 - \varepsilon)t^2(0,H), \qquad \text{(A.13)}$$

and after some manipulation of the $\frac{T_S}{T_S}$ terms, T_i becomes,

$$T_i = T_S \left(1 + (1 - t(0,H)\varepsilon)\frac{T_0 - T_S}{T_S} - \frac{I_P}{T_S} \right) - (T_0 - T_c)(1 - \varepsilon)t^2(0,H)$$
$$= T_S m_p - (T_0 - T_c)(1 - \varepsilon)t^2(0,H), \qquad \text{(A.14)}$$

where $mp = 1 + (1 - t(0,H)\varepsilon)\frac{T_0 - T_S}{T_S} - \frac{I_P}{T_S}$. Expanding the transmittance terms and substituting in I_P, I_1, and I_2 provide Eq. 2.24 and Eq. 2.25 from Chapter 2 (Guissard and Sobieski, 1994).

APPENDIX B

The following appendix shows my publications pertaining to atmospheric science:

O'Neill, N., Baibakov, K., Hesaraki, S., Ivanescu, L., Martin, R., Perro, C., Chaubey, J., Herber, A., and Duck, T.: Temporal and spectral cloud screening of polar winter aerosol optical depth (AOD): impact of homogeneous and inhomogeneous clouds and crystal layers on climatological-scale AODs, Atmos. Chem. Phys., 16, 12753-12765, 2016.

Perro, C., Lesins, G., Duck, T.: A microwave satellite water vapour column retrieval for polar winter conditions, Atmos, Meas. Tech., 9, 2241-2252, 2016.

Baibakov, K., O'Neill, N., Ivanescu, L., Duck, T., Perro, C., Herber, A., Schulz, K., and Schrems, O.: Synchronous polar winter starphotometry and lidar measurements at a High Arctic station, Atmos. Meas. Tech., 8, 3789-3809, 2015.

O'Neill, N., Perro, C., Saha, A., Lesins, G., Duck, T., Eloranta, E., Nott, G., Hoffman, A., Karumudi, M., Ritter, C., Bourassa, A., Abboud, I., Carn, S., Savastiouk, V.,: Properties of Sarychev sulphate aerosols over the Arctic, J. Geophys. Res.-Atmos., 117, 10.1029/ 2011JD016838 2012.

Nott, G., Duck, T., Doyle, J., Coffin, M., Perro, C., Thackray, C., Drummond, J.: A Remotely Operated Lidar for Aerosol, Temperature, and Water Vapor Profiling in the High Arctic, J. Atmos. Ocean. Tech., 29, 221-234, 2012.

Lindenmaier, R., Strong, K., Batchelor, R., Chipperfield, M., Daffer, W., Drummond, J., Duck, T., Fast, H., Feng, W., Fogal, P., Kolonjari, F., Manney, G., Manson, A., Meek, C., Mittermeier, R., Nott, G., Perro, C., Walker, K.: Unusually low ozone, HCl, and HNO_3 column measurements at Eureka, Canada during winter/spring 2011, Atmos. Chem. Phys., 12, 3821–3835, 2012.

Doyle, J., Lesins, G., Thackray, C., Perro, C., Nott, G., Duck, T., Damoah, R., Drummond, J.: Water vapor intrusions into the High Arctic during winter, Geophys. Res. Lett., 38, 10.1029/2011GL047493, 2011.

APPENDIX C

Section 3.1 contains a published article which I wrote in the Journal of Atmospheric Measurement Techniques. The journal states that I, the author, retain the copyright for this article. More information on the copyright can be viewed at the following website:

```
https://publications.copernicus.org/for_authors/licence_
and_copyright/license_and_copyright_2007-2017.html
```

Below is a couple sections of the copyright information for the journal of Atmospheric Measurement Techniques.

License and copyright agreement

The following license and copyright agreement is valid for any article published by Copernicus Publications whose original manuscript was received from 10 December 2007 on.

Authors certification

In submitting the manuscript, the authors certify that:

- They are authorized by their co-authors to enter into these arrangements.

- The work described has not been published before (except in the form of an abstract or as part of a published lecture, review or thesis), that it is not under consideration for publication elsewhere, that its publication has been approved by all the author(s) and by the responsible authorities tacitly or explicitly of the institutes where the work has been carried out.

- They secure the right to reproduce any material that has already been published or copyrighted elsewhere.

- They agree to the following license and copyright agreement:

Copyright

- Copyright on any article is retained by the author(s). Regarding copyright transfers please see below.

- Authors grant Copernicus Publications a license to publish the article and identify itself as the original publisher.

175

- Authors grant Copernicus Publications commercial rights to produce hardcopy volumes of the journal for sale to libraries and individuals.

- Authors grant any third party the right to use the article freely as long as its original authors and citation details are identified.

- The article is distributed under the Creative Commons Attribution 3.0 License. Unless otherwise stated, associated published material is distributed under the same licence:

Copyright transfers

Many authors have strict regulations in their contract of employment regarding their works. A transfer of copyright to the institution or company, as well as the reservation of specific usage rights, is typical. Please note that in the case of open-access publications in combination with a Creative Commons License, a transfer of the copyright to the institution is possible, as it belongs to the author anyway and is not subject to the publisher.

Any usage rights are regulated through the Creative Commons License. As Copernicus Publications uses the Creative Commons Attribution 3.0 License, anyone (the author, his/her institution/company, the publisher, as well as the public) is free to copy, distribute, transmit, and adapt the work as long as the original author is given credit (see above). Therefore, specific usage rights cannot be reserved by the author or his/her institution/company, and the publisher cannot include a statement "all rights reserved" in any published paper.

A copyright transfer from the author to his/her institution/company will be expressed in a special "Copyright Statement" at the end of the publication rather than on the first page in the article citation header. Authors are asked to include the following sentence: "The author's copyright for this publication is transferred to institution/company".